(3)

1

UNIVERSITY OF BRADFORD

Author Anastassios Dimitriou Papatsoris

Title Improvements to the modelling of radiowave propagation at millimetre wavelengths.

Degree P.R.D. Year 1993.

IMPROVEMENTS TO THE MODELLING OF RADIOWAVE PROPAGATION AT MILLIMETRE WAVELENGTHS

In-depth studies are reported on resonance phenomena in the scattering of spherical ice particles, extinction and backscattering properties of clouds and on the absorption and dispersion spectra of atmospheric gases

Anastassios Dimitriou PAPATSORIS

submitted for the degree
of Doctor of Philosophy

Department of Electrical and Electronic Engineering
University of Bradford

1993

Anastassios Dimitriou PAPATSORIS

"Improvements to the modelling of radiowave propagation at millimetre wavelengths"

Keywords: *radiowave propagation, resonant scattering, millimetre waves, extinction and backscattering, clouds, gaseous absorption.*

ABSTRACT

Various physical mechanisms that affect radiowave propagation at millimetre wavelengths are considered. Current modelling weaknesses are highlighted and new improved models or more appropriate modelling approaches are suggested.

Interference and resonance phenomena in the scattering of spherical ice and water particles are reviewed. The long standing problem of the numerous resonances observed in the scattering diagrams of dielectric spheres is answered.

The spatial structure and the physical characteristics of non-precipitable ice and water clouds are reviewed. Extinction and back scattering calculations for a wide variety of cloud models over the entire millimetre frequency spectrum are given. Multiple scattering and the effects of super-large drops in clouds are also dealt with. The potential of a spaceborne instrument in deducing information about the vertical structure of various cloud types is examined. Attenuation and reflectivity profiles resulting from various cloud types are calculated for a nadir pointing fixed beam millimetre wave radar operating at 94 GHz.

The physics and application of the equation of radiative transfer to millimetre wave propagation in the earth's atmosphere are given and also is the solution of this equation for a typical millimetre wave remote sensing application. The theory of gaseous absorption at millimetre wavelengths is presented and an improved modelling approach is proposed for the calculation of the absorption and dispersion spectra of atmospheric gases. The effects of trace gases on communication systems operating at high altitudes are for the first time reported.

Finally the use of the 60 GHz oxygen absorption band for top-side air traffic control/navigation and broadband transmission purposes is studied.

CONTENTS

ACKNOWLEDGEMENTS

I would like to address my deepest thanks to my supervisor Professor P.A.Watson, whose mental and financial support enabled me to complete this thesis.

I thank Dr. John Ballard at R.A.L. for the fruitful and stimulating discussions we shared, as well as for the advice and interest with which he engulfed my efforts in spectroscopic modelling.

I appreciate the encouragement and assistance given by all colleagues and members of staff of the University, in particular Dr. Neal McEwan and Mrs. Freda Hewitson.

I would also like to thank my family and my fiancee, whose unconditional love, support and understanding enabled me to achieve the highest level of dedication.

My special thanks go to all those that helped me realize how invaluable a good sense of humour is.

To my mother Vasiliki, my father Dimitrios,
my sister Paraskevi and my fiancee Athanasia.

CHAPTER 1

INTRODUCTION.

The propagation of electromagnetic radiation through the earth's atmosphere is governed by the characteristics of the propagating wave (wavelength, polarization), the physical characteristics of the atmosphere (temperature, pressure, suspended particles) and the atmospheric composition. These physical mechanisms are complex to model because of the three dimensional nature of the propagation medium and the multiplicity of the interaction mechanisms: scattering, absorption, emission and refraction.

At microwave frequencies these interactions are relatively simple and the modelling of radiowave propagation greatly simplifies. Over the past three decades radiowave propagation at microwave frequencies has been exhaustively studied and the existing models are well supported by experimental data and measurements. However, the ever increasing demand for new telecommunication services and environmental monitoring have resulted in growing interest in the millimetre wave propagation. It is this interest and the recent technological advances that reduced the cost of millimetre wave systems which shape investigative studies currently being designed or taking place on data collection, propagation modelling or atmospheric modelling [Brussaard, Watson et al 1991].

Millimetre wave communications systems, have already been proposed or are currently being developed for a range of applications including:

- millimetre wave multichannel multipoint video distributions (M^3VDS),
- point-multipoint networks (ISDN or broadband),
- broadband and narrowband mobile applications,
- satellite networks (eg. VSAT's),
- satellite mobile systems,
- acronautical-satellite communications systems.

Of course, before any such systems can be put into operation, theoretical radiowave

propagation modelling along with experimental studies are required to enable the system designer to model sufficiently accurate performance predictions for radio links.

Furthermore, millimetre waves can be used for a wide variety of atmospheric remote sensing applications [e.g. Atlas et al 1981, Fujita et al 1984, Gibbins et al 1988, Gasiewski 1990a, 1990b]. Such applications currently focus on the determination of the concentration and global distribution of atmospheric water vapour, liquid water, ice and various trace gases -particularly ozone. It is the author's conviction, however, that in the next few years the worldwide ever growing environmental awareness will lead to the development of more sophisticated and complex remote sensing applications. Such applications will be on a continuous basis aiming to globally monitor the concentration and distribution of those atmospheric gases that control the physics and the chemistry of the atmosphere, including trace constituents (ie. CO_x, NO_x, SO_2, NH_3). The accuracy with which measurements can be achieved using various remote sensing techniques depends on models for radiowave propagation, which in turn depend upon spectroscopic predictions for various atmospheric gases. Consequently, radiowave propagation modelling at millimetre wavelengths is a subject of great importance both for communication and remote sensing applications.

In this thesis we consider various physical mechanisms -some of them usually ignored at microwave frequencies- and assess their influence on radiowave propagation at millimetre wavelengths. Current modelling weaknesses are highlighted and new improved models or more appropriate modelling approaches are suggested. Generally, this thesis can be divided in four parts. In part I the long standing problem of the numerous resonances present in the scattering diagrams of dielectric spheres is answered. Although this phenomenon does not noticeably affect the attenuation and reflectivity calculations resulting from a polydispersive medium, it had always been a serious academic challenge. In part II the effect of clouds and other associated factors such as the presence of super-large drops and multiple scattering on radiowave propagation are investigated. In part III the derivation of the equation of radiative

transfer and the theory of gaseous absorption are reviewed and later employed to produce a comprehensive atmospheric propagation model (A.P.M.). The model calculates the absorption and dispersion spectra of atmospheric gases and gives improved modelling accuracy over other prediction techniques. Finally, in part IV some novel aeronautical-satellite communication applications are proposed and investigated using the Atmospheric Propagation Model (A.P.M.).

More specifically, in chapter 2 the absorption and scattering cross sections of spherical ice and water particles at millimetre wavelengths are calculated using Mie theory. Various interference and resonance phenomena are distinguished and brief physical explanations wherever available are given. The in-depth study of the numerous fluctuations observed in the scattering of dielectrics is the main subject of chapter 3. A detailed survey of the so-far proposed explanations is given and a new physical mechanism is nominated to explain the resonance effects.

The effects of clouds on radiowave propagation at millimetre wavelengths are analyzed in chapter 4. A useful description of the spatial structure and physical characteristics of various cloud types is given in the introductory part of this chapter and in the following the effects of multiple scattering and super-large drops in clouds are considered. The chapter concludes with tabulated values and detailed graphical illustrations of the extinction and back scattering cross sections of various cloud types calculated over the entire millimetre frequency range. These calculations appear for the first time in the literature. In chapter 5 the potential of a spaceborne instrument in deducing information about the vertical structure of various cloud types is investigated. Attenuation and reflectivity profiles for various cloud types are calculated for a nadir pointing fixed beam millimetre wave radar operating at 94 GHz. In fact, these calculations represent the feasibility study submitted to a UK scientific team which examined the possible development of a millimetre wave spaceborne radar as part of the UK contribution to the international Global Energy and Water Experiment (GEWEX).

In chapter 6 the physics and the derivation of the equation of radiative transfer are given. Also

given is the solution of the equation of radiative transfer for a typical remote sensing application. This chapter has a review character and the main objective is to describe the physical basis of the millimetre remote sensing. In chapter 7 the theory of gaseous absorption at millimetre wavelengths is presented and an improved modelling approach is proposed for the calculation of the absorption and dispersion spectra of atmospheric gases. The effects of trace gases on communication systems operating at high altitudes are for the first time reported. Finally, in chapter 8 the use of the 60 GHz oxygen absorption band for top-side air traffic control/navigation and broadband transmission purposes is studied.

"Παντα χωρει και ουδεν μενει, ποταμω ουκ εστιν εμβηναι δις. - Ειμεν και ουκ ειμεν"

Ηρακλειτος, 500 B.C.

CHAPTER 2

SCATTERING PROPERTIES OF SPHERICAL ICE AND WATER PARTICLES AT MILLIMETRE WAVELENGTHS.

2.1 Introduction.

The scattering of a plane wave by a sphere of arbitrary size and material has been rigorously treated by Mie [1908]. Since then, Mie's formulation has been proved an invaluable tool for a variety of applications related to meteorology, astronomy, physics, chemistry and telecommunications. In this chapter, Mie theory is briefly reviewed and later employed to characterize the absorption and scattering properties of spherical ice and water particles at millimetre wavelengths. Various resonance and interference phenomena appearing in the scattering of ice and water particles are recognized and then further discussed.

2.2 Mie Theory.

Scattering of a plane wave by a homogeneous sphere is the subject of Mie theory. A sphere of radius a and complex refractive index **m** is embedded in an infinite homogeneous medium (vacuum in our case). A plane wave whose electric vector is linearly polarised in the **x**-direction, is propagated in the direction of the positive **z**-axis. The incident wave (of unit amplitude) is then described by:

$$E = a_x\, e^{-ikz+iwt}, \qquad H = a_y\, e^{-ikz+iwt},$$

where a_x and a_y are unit vectors along the **x**- and **y**-axes. It can be proved that these fields may be written in terms of the scalar solutions u and v of the scalar wave equation

$$\Delta\psi + k^2m^2\psi = 0\ ,$$

which is separable in spherical coordinates and has elementary solutions of the following type:

$$\psi_{ln} = \begin{matrix}\cos l\phi \\ \sin l\phi\end{matrix}\ \Big\}\ P_n^l(\cos\theta)\ z_n(mkr)\ ,$$

where n and l are integers with $n \geq l \geq 0$, P is an associated Legendre polynomial and z is any

spherical Bessel function. So, for the incident outside wave we have

$$u = e^{i\omega t} \cos\phi \sum_{n=1}^{\infty} (-i)^n \frac{2n+1}{n(n+1)} P_n^1(\cos\theta)\, j_n(kr) ,$$

$$v = e^{i\omega t} \sin\phi \sum_{n=1}^{\infty} (-i)^n \frac{2n+1}{n(n+1)} P_n^1(\cos\theta)\, j_n(kr) ,$$

where j_n is the spherical Bessel function derived from the Bessel function of the first kind, $J_{n+1/2}$.

The induced secondary field must be constructed in two parts, the one applying to the interior of the sphere and the other valid at all external points with the necessary regularity at infinity. So for the outside scattered field we have

$$u = e^{i\omega t} \cos\phi \sum_{n=1}^{\infty} -a_n(-i)^n \frac{2n+1}{n(n+1)} P_n^1(\cos\theta)\, h_n^{(2)}(kr) ,$$

$$v = e^{i\omega t} \sin\phi \sum_{n=1}^{\infty} -b_n(-i)^n \frac{2n+1}{n(n+1)} P_n^1(\cos\theta)\, h_n^{(2)}(kr) ,$$

where a_n and b_n are coefficients to be determined and $h_n^{(2)}(kr)$ is a spherical Bessel function derived directly from the Bessel function of the second kind $H_{n+1/2}^{(2)}(kr)$. It has been chosen because its asymptotic behaviour,

$$h_n^{(2)}(kr) \sim \frac{i^{n+1}}{kr} e^{-ikr}$$

when combined with the factor $\exp(i\omega t)$, represents an outgoing spherical wave, as it is required for the scattered wave.

In a similar way, the field inside the sphere can be represented by:

$$u = e^{i\omega t} \cos\phi \sum_{n=1}^{\infty} mc_n(-i)^n \frac{2n+1}{n(n+1)} P_n^1(\cos\theta)\, j_n(mkr) ,$$

$$v = e^{i\omega t} \sin\phi \sum_{n=1}^{\infty} md_n(-i)^n \frac{2n+1}{n(n+1)} P_n^1(\cos\theta)\, j_n(mkr) ,$$

where c_n and d_n are another pair of coefficients to be determined. The choice of $j_n(mkr)$ is justified by the fact that the refractive index inside the sphere is **m** and the fields are finite at its centre.

In order to find the undetermined coefficients the boundary conditions have to be considered.

The well known boundary conditions for the tangential components of the fields

$$(7) \quad n \times (H_m - H_0) = 0, \qquad n \times (E_m - E_0) = 0 ,$$

result to the following set of equations:

$$\psi_n(x) - a_n\zeta_n(x) = mc_n\psi_n(y) ,$$

$$\psi_n'(x) - a_n\zeta_n'(x) = c_n\psi_n'(y) ,$$

$$\psi_n(x) - b_n\zeta_n(x) = d_n\psi_n(y) ,$$

$$\psi_n'(x) - b_n\zeta_n'(x) = md_n\psi_n'(y) ,$$

where $x=ka=2\pi a/\lambda$ is the ratio of the circumference of the sphere to the wavelength (also known as size parameter), $y=mx$ and $\psi_n(z)=zj_n(z)$, $\zeta_n(z)=zh_n^{(2)}(z)$ are the Riccati-Bessel functions which differ from the spherical Bessel functions by a factor z. The primes denote derivatives with respect to the relevant argument. Eliminating c_n and d_n from the above set of equations we obtain the solutions

$$a_n = \frac{\psi_n'(y)\psi_n(x) - m\psi_n(y)\psi_n'(x)}{\psi_n'(y)\zeta_n(x) - m\psi_n(y)\zeta_n'(x)} ,$$

$$b_n = \frac{m\psi_n'(y)\psi_n(x) - \psi_n(y)\psi_n'(x)}{m\psi_n'(y)\zeta_n(x) - \psi_n(y)\zeta_n'(x)} .$$

For the coefficients c_n and d_n we find fractions with the same respective denominators and

$$\psi_n'(x)\zeta_n(x) - \psi_n(x)\zeta_n'(x)$$

as common numerator. This completes the solution of the problem. The field at any point, either inside or outside the sphere, is now fully determined.

2.3 Amplitude functions, cross sections and efficiency factors.

The scattered field is generally described by the amplitude matrix $S(\theta,\phi)$, with θ and ϕ the

Fig. 1. Decomposition of electric vectors of incident and scattered waves.

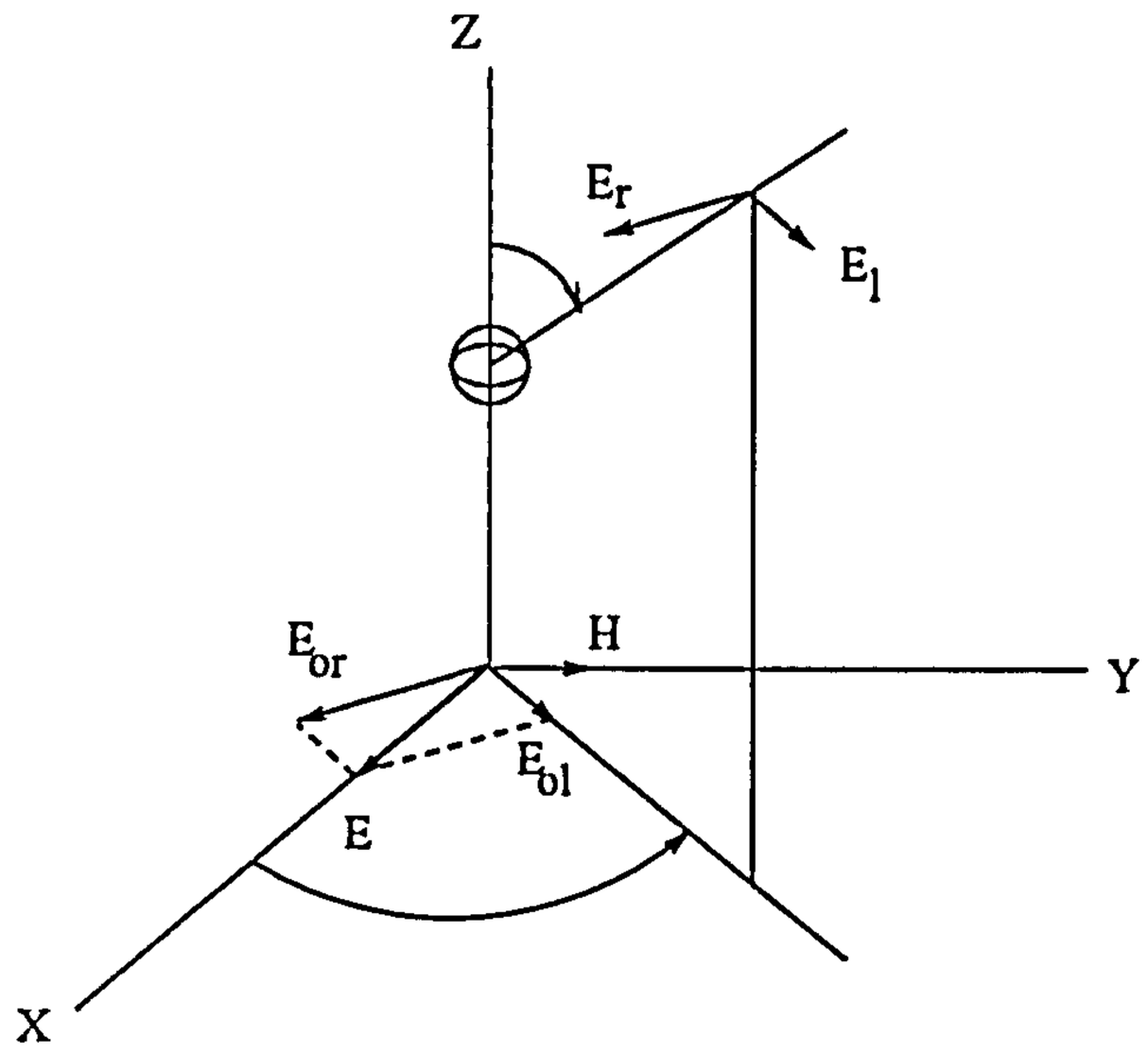

scattering angles in spherical coordinates. So the field at any point is given by:

$$\begin{bmatrix} E_l \\ E_r \end{bmatrix} = \begin{bmatrix} S_2 & S_3 \\ S_4 & S_1 \end{bmatrix} \cdot \frac{e^{-ikr+ikz}}{ikr} \begin{bmatrix} E_{l0} \\ E_{r0} \end{bmatrix},$$

where S_1, S_2, S_3 and S_4 are the elements of the amplitude matrix, E_{l0} and E_{r0} are the components of the incident field, and E_l and E_r the components of the scattered field. The indices r and l refer to the electric fields perpendicular to and parallel with the plane of scattering (see figure 1).

Especially for spherical particles $S_3=S_4=0$ and S_1, S_2 depend only on the scattering angle θ.

So, for spherical particles the general formula reduces to the following simple relations

$$E_r = S_1(\theta)\ \frac{e^{-ikr+ikz}}{ikr}\ E_{r0}\ ,$$

$$E_l = S_2(\theta)\ \frac{e^{-ikr+ikz}}{ikr}\ E_{l0}\ ,$$

where the amplitude functions are given by:

$$S_1(\theta) = \sum_{n=1}^{\infty}\ \frac{2n+1}{n(n+1)}\ [a_n\pi_n(\cos\theta) + b_n\tau_n(\cos\theta)]\ ,$$

$$S_2(\theta) = \sum_{n=1}^{\infty}\ \frac{2n+1}{n(n+1)}\ [b_n\pi_n(\cos\theta) + a_n\tau_n(\cos\theta)]\ ,$$

and

$$\pi_n(\cos\theta) = \frac{1}{\sin\theta}\ P_n^1(\cos\theta)\ ,$$

$$\tau_n(\cos\theta) = \frac{d}{d\theta}\ P_n^1(\cos\theta)\ .$$

Using the above set of formulae, it is possible to describe the intensity and state of polarisation of the scattered wave in any direction, if radiation with an arbitrary intensity and state of polarisation is falling on the sphere. Of particular interest is the case for which $\theta=0°$ (forward scattering). In forward scattering we have $S_1(0)=S_2(0)$ and the expression for the scattered field is further reduced to

$$S(0) = \frac{1}{2}\sum_{n=1}^{\infty}(2n+1)(a_n+b_n)\ ,$$

because of the relations

$$\pi_n(1) = \tau_n(1) = \frac{1}{2}n(n+1).$$

The total extinction cross section for a single particle is then given by:

$$C_{ext} = \frac{\lambda^2}{\pi} Re\{S(0)\} .$$

The extinction cross section may be defined as follows. If a plane wave is incident on a particle, currents induced in it will set up a reradiated field. The scattering cross section C_{sca} multiplied by the incident power density gives the total power in this re-radiated field alone. Similarly, power dissipated within the particle is defined as an absorption cross section C_{abs} multiplied by the incident flux. The extinction cross section is then defined as $C_{ext}=C_{sca}+C_{abs}$ and is a measure of the total power that the particle can remove from the coherent forward travelling plane wave. The scattering cross section for a single particle is given by:

$$C_{sca} = \frac{\lambda^2}{2\pi} \sum_{n=1}^{\infty} (2n+1) \{ |a_n|^2 + |b_n|^2 \} ,$$

and the absorption cross section may be simply calculated as $C_{abs}=C_{ext}-C_{sca}$. The scattering cross sections are measured in area units. If we want to measure how efficiently a spherical particle of radius a absorbs, scatters or removes the incident electromagnetic radiation, then the corresponding absorption, scattering and extinction efficiency factors will have to be considered. These factors are dimensionless and defined as $Q_{abs}=C_{abs}/G$, $Q_{ext}=C_{ext}/G$ and $Q_{sca}=C_{sca}/G$, where $G=\pi a^2$. The former definitions refer to a single particle. If someone wants to find the attenuation resulted by a medium containing N similar particles, then the specific resultant attenuation is

$$\gamma = 4.343 \cdot N \cdot C_{ext} \quad [\frac{dB}{unit\ distance}] .$$

If the particles have different radii, but the size distribution is given, that is N(a)da particles with radii between a and a+da per unit volume, then the specific attenuation is given by:

$$\gamma = 4.343 \cdot \int_0^{\infty} C_{ext} N(a) da \quad [\frac{dB}{unit\ distance}] .$$

2.4 Scattering calculations for spherical ice and water particles.

Using a Mie scattering program (Papatsoris [1990], see also appendix A), the scattering cross sections of spherical ice and water particles have been calculated. For ice, calculations have been performed over the 10-300 GHz frequency range for particles with 0.1, 0.2, 0.5, 1.0, 2.0 and 5.0 mm radii. Similar calculations have been repeated for water drops. The index of refraction of ice is calculated using Ray's [1972] model and that of water using Manabe's [1987] model. For the ice crystals the temperature is assumed to be -10 °C and for water drops 10 °C. The calculations fall into two categories. The first refers to the forward scattering case and is directly related to the resultant attenuation; the second refers to the back scattering case and is directly related to radar observations of rain and cloud structures.

2.4.1 Forward scattering.

2.4.1.1 Scattering cross sections of ice and water spheres.

Fig. 2. Scattering cross sections of spherical ice particles.

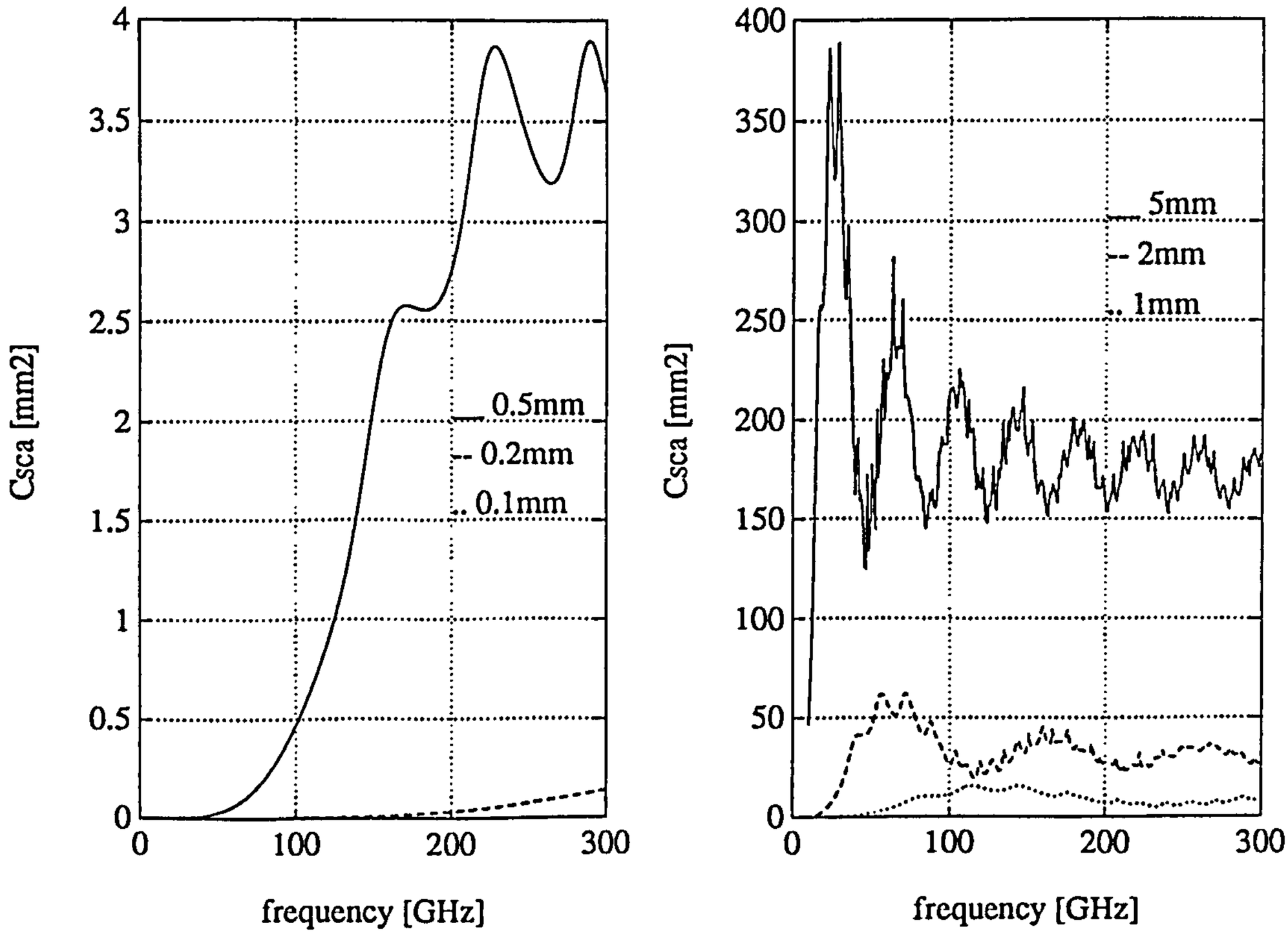

Figure 2 illustrates the scattering cross sections of spherical ice particles. Regarding the ice scattering cross section curves, one interesting feature is revealed; the occurrence of a sequence of peak and valley regions which is dependent upon the size of the particle. The peak and valley regions for different particle sizes are tabulated in table I. Generally speaking, big particles exhibit more and sharper peak-valley configurations than smaller ones. We may

Table I. Frequencies for which the extinction cross sections of spherical ice particles of various sizes maximize or minimize.

radius [mm]	Peaks [GHz]	Valleys [GHz]
1	105-155	220-250
2	55-75, 155-175, 250-270	110-130, 205-225
5	25-35, 60-70, 100-110, 140-150, 175-185, 215-225, 255-265	45-55, 80-90, 120-130, 160-170, 195-205, 235-245, 275-285

seek the explanation to this, in terms of constructive and destructive interference between diffracted and transmitted radiation. Since the two fields (diffracted and transmitted) simply add together to give the total resultant field in the shadow area behind the particle, we may say that the peaks occur when the fields interact constructively and the valleys when they interact destructively.

But the most striking feature of all, is the existence of numerous small scale fluctuations in the ice scattering curve. This peculiar behaviour of ice has been verified by Pendorf [1960], Herman and Battan [1961], Kerker [1969], Ruck [1970] and others who have published similar scattering calculations for ice and other dielectric materials. A similar pattern -but severely more pronounced- is revealed, when bistatic or back scattering cross sections are calculated (see section 2.4.2.1). Why this is happening, it is not so simple to explain. A complete treatment and a rigorous explanation for this phenomenon will be given in the next chapter. Figure 3 shows the scattering cross sections of spherical water particles. Similar resonance effects to those that Holt and Evans [1977] found are here observed. The water scattering cross sections reach a peak value and then oscillates but the oscillation quickly damps with increasing

Fig. 3. Scattering cross sections of spherical water particles.

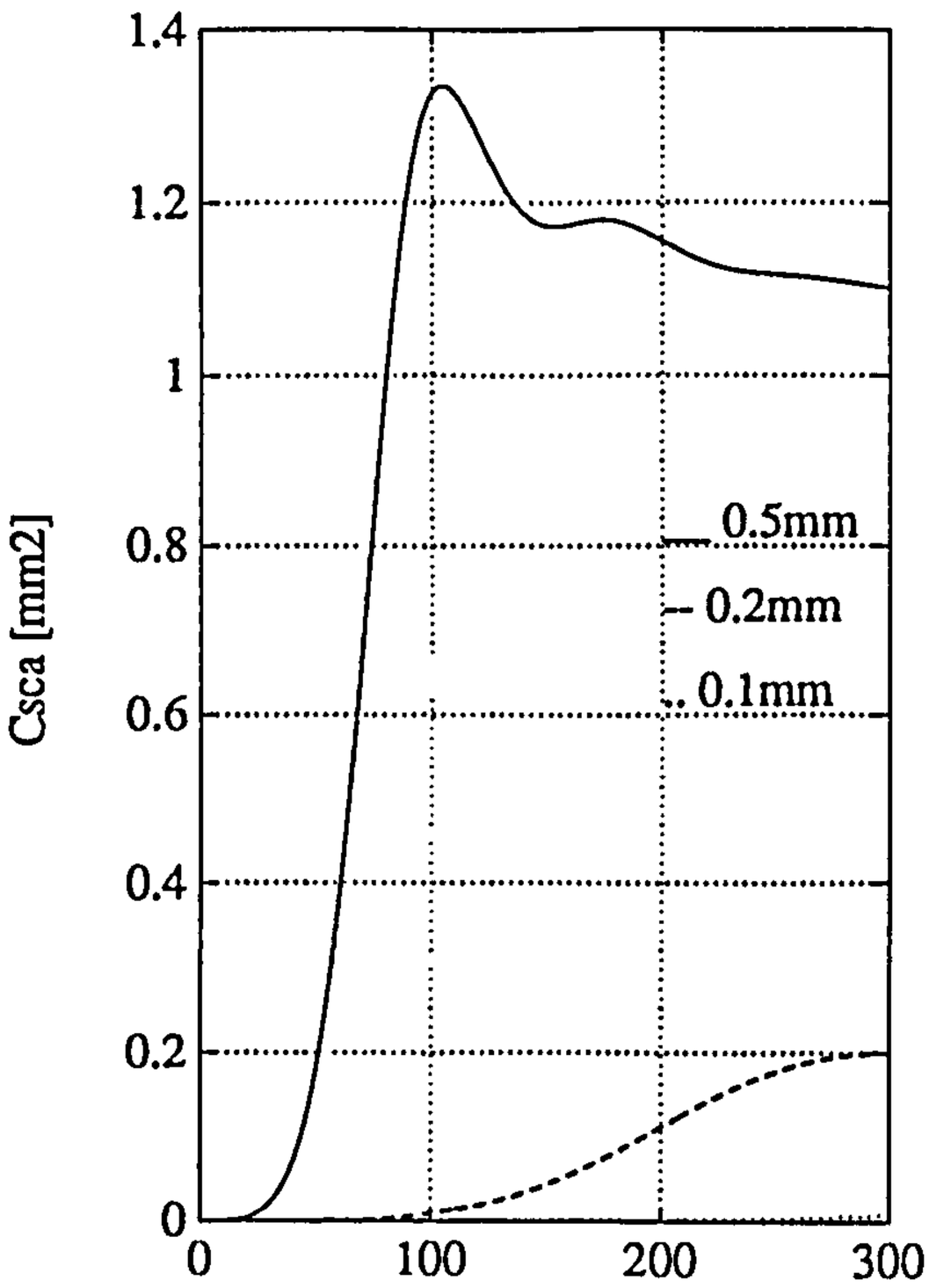

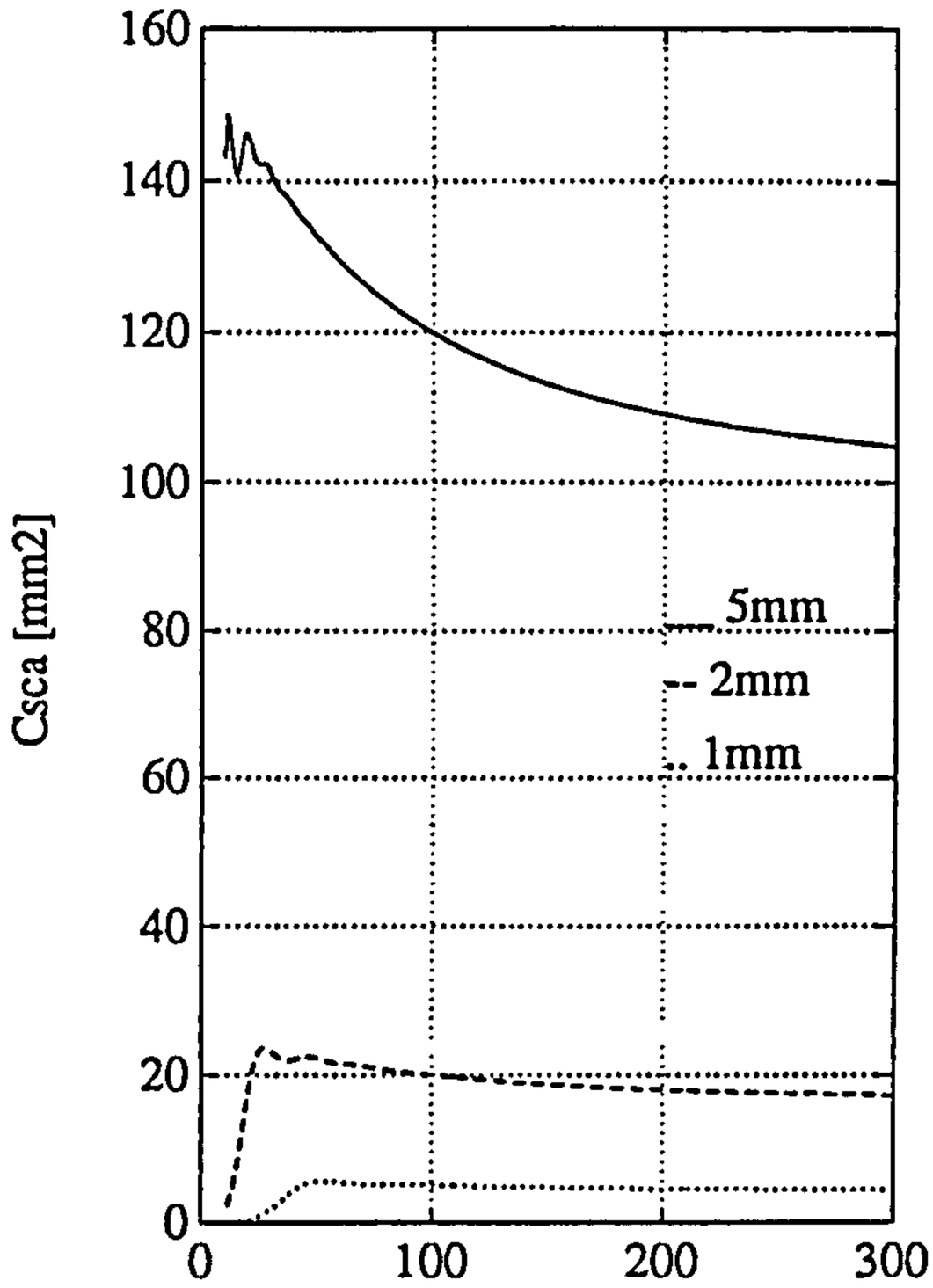

frequency. The peak is dependent upon the size of the particle and occurs at lower frequencies for the larger particles. The frequencies that the peaks occur for various particle sizes are tabulated in table II. As frequency increases, the scattering curve tends asymptotically towards

Table II. Frequencies for which the scattering cross sections of spherical water particles of various sizes maximize.

radius [mm]	Peak value [GHz]
1	52.4
2	27.3
5	11.3

the Mie optical limit. Compared with the ice scattering cross sections, water cross sections are always smaller, but become comparable to ice cross sections in the valley regions. Nevertheless, it is apparent that ice particles scatter the incident radiation twice as efficiently as water drops. This can be verified in figure 4 where both scattering cross sections for spherical water and ice particles of the same size are illustrated.

Fig. 4. A comparison between the scattering cross sections of ice and water particles.

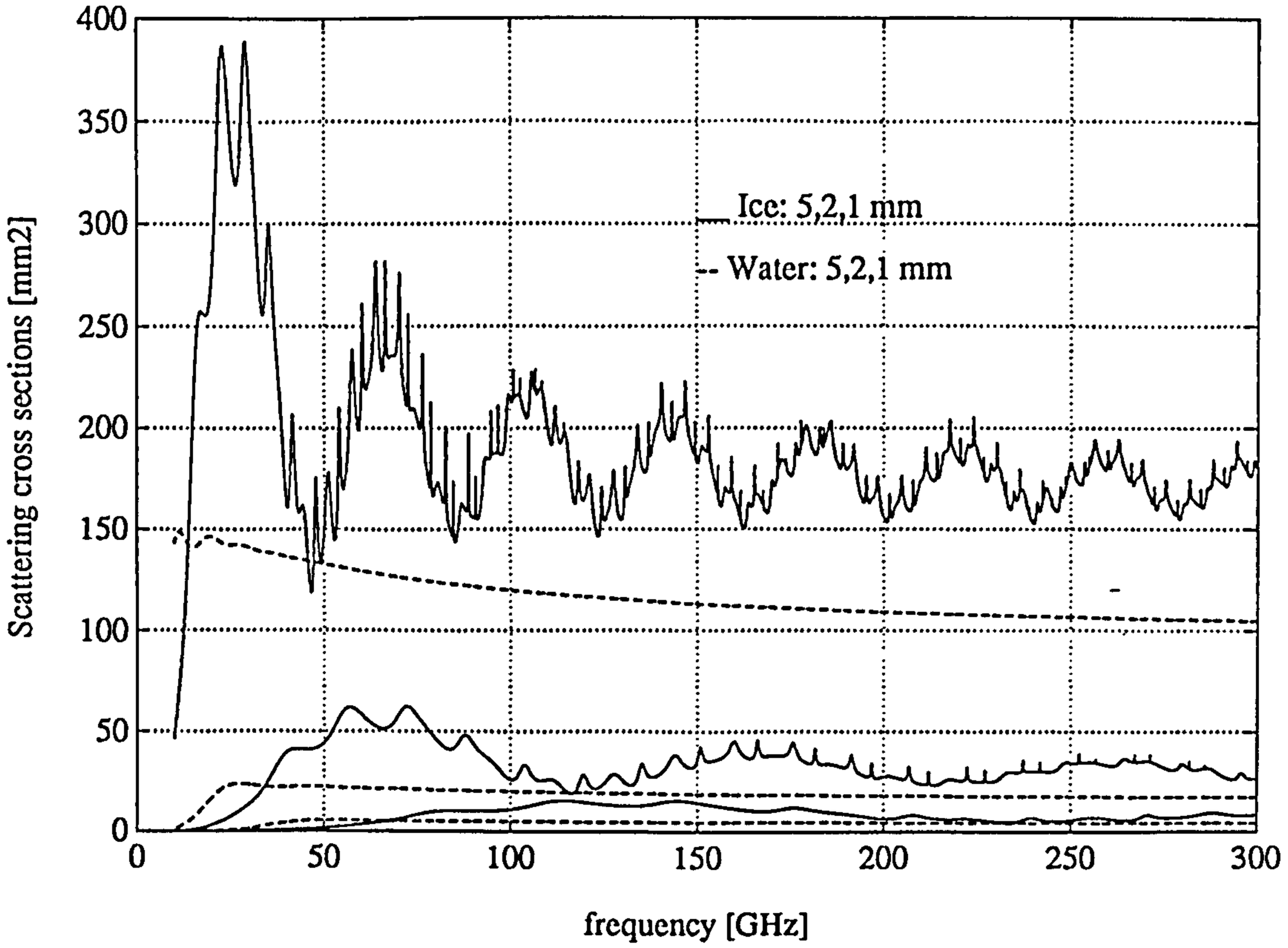

2.4.1.2 Absorption cross sections of ice and water spheres.

Figure 5 shows the absorption cross sections for ice. As expected, the ice absorption cross sections are much smaller than the scattering cross sections (ie 300 times on the average in the Mie optical region). Therefore, their contribution to the total extinction cross section is almost negligible. It is interesting to note though, that the ice absorption cross sections fluctuate strongly with frequency in a way similar to that observed in the scattering cross sections. A closer examination reveals that the numerous local minima and maxima occur at the same frequency positions for both absorption and scattering curves.

The absorption cross sections for water can be seen in figure 6. Again the water absorption cross sections reach a peak value and then oscillate but the oscillation quickly damps with increasing frequency. This phenomenon which is also present in the scattering cross sections of water drops (see section 2.4.1.1) can be explained in terms of the same physical mechanism deployed to physically translate the scattering diagrams of spherical ice particles. The only

Fig. 5. Absorption cross sections of spherical ice particles.

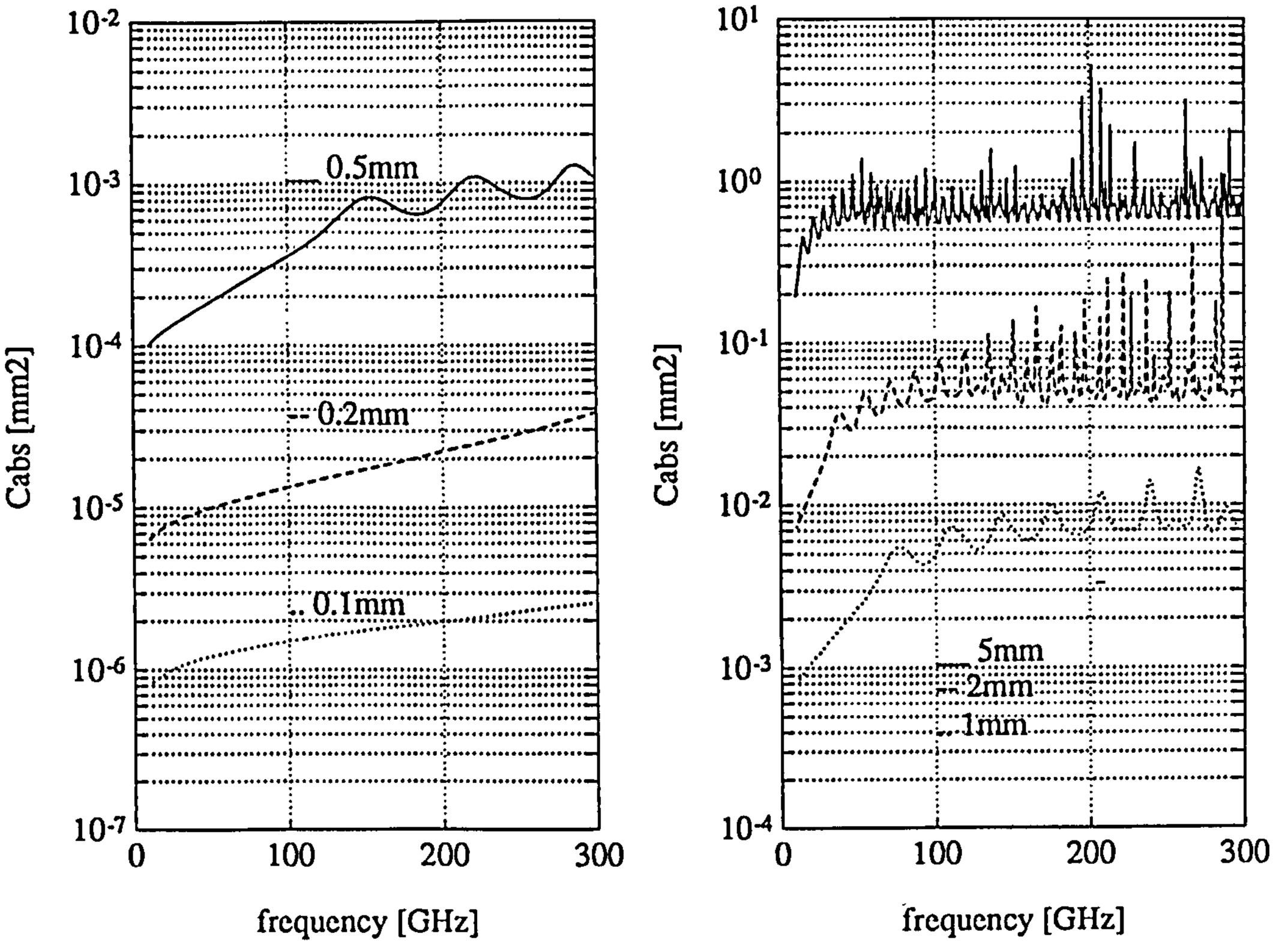

Fig. 6. Absorption cross sections of spherical water particles.

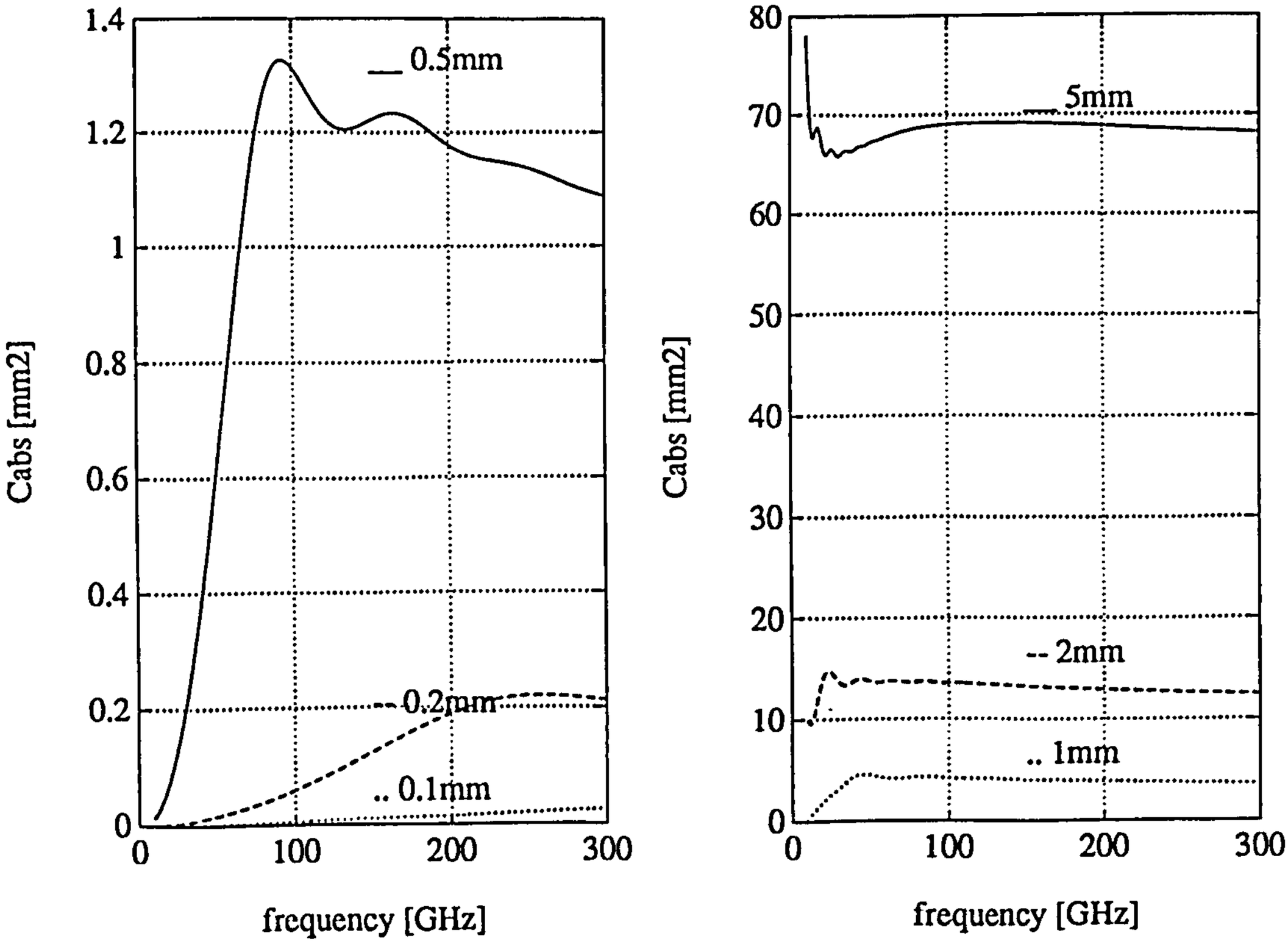

difference here is that the transmitted field is heavily attenuated because of the large imaginary part of the refractive index of water, and as a result the oscillation damps quickly. Regarding figures 3 and 6, we see that the absorption and the scattering cross sections of spherical water particles are of the same order of magnitude over much of the millimetre wave spectrum. Therefore, at millimetre wavelengths the intensity of a radiowave which propagates through an ensemble of water particles suffers attenuation which is due both to scattering and absorption.

2.4.1.3 Distinction between scattering and absorption regions for ice.

Figure 7 shows the ratio of the scattering cross section to the extinction cross section (also known as the scattering albedo) as a function of frequency for various sizes of ice spheres.

Fig. 7. Scattering albedo for ice particles with various radii.

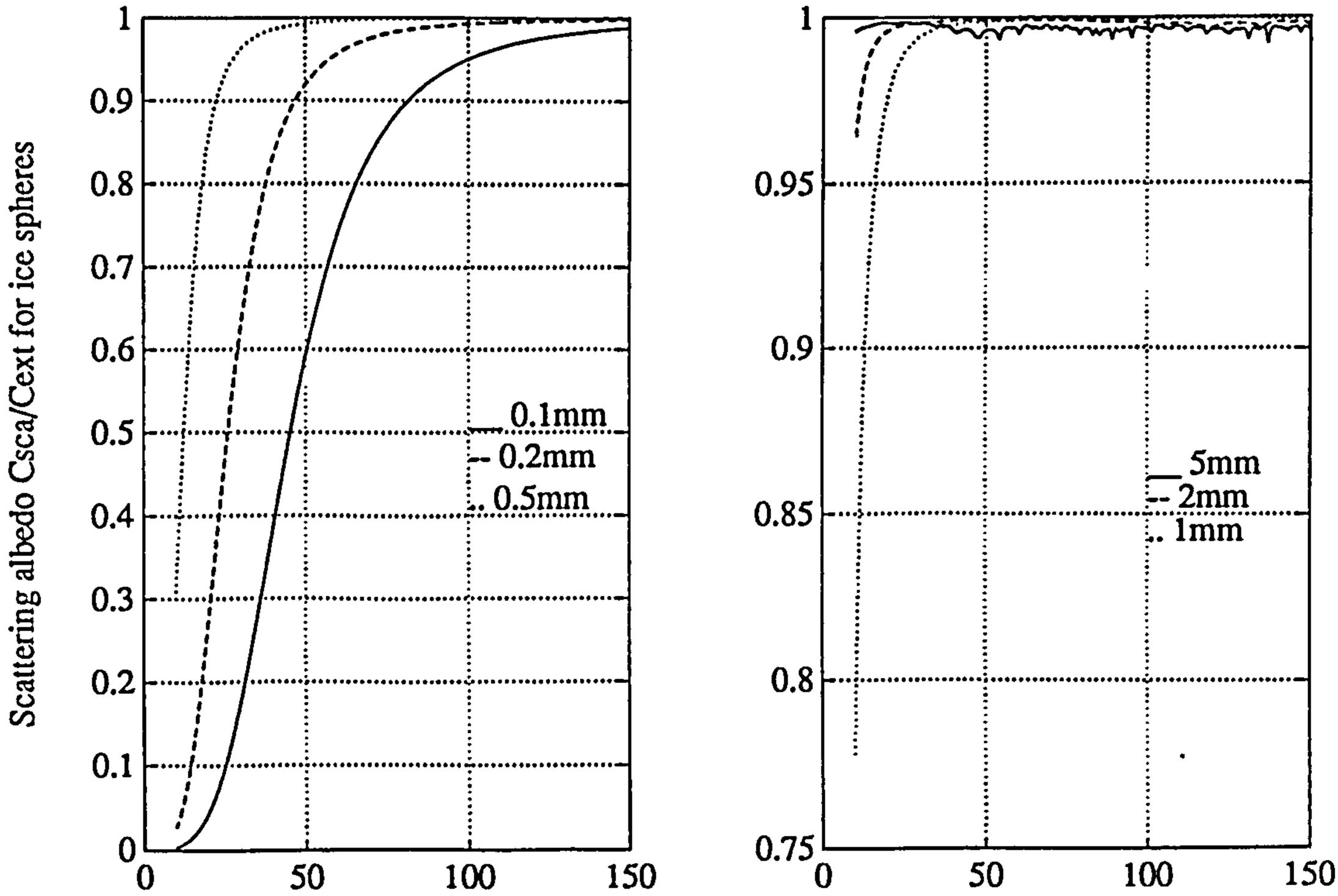

Regarding carefully figure 7, we see that smaller particles absorb a much more significant percentage of the incident energy than the larger ones for frequencies up to 30 GHz. This is

shown better in figure 8 where the values of the scattering and absorption cross sections for ice spheres of various sizes are depicted. For a particle with radius r=0.1mm, the absorbed energy is greater than the scattered for frequencies up to approximately 44 GHz, where the two energies are equal. Although the proportion of energy absorbed is much greater (orders

Fig. 8. Absorption and scattering cross sections of spherical ice particles with radii r=0.1, 0.2, 0.5 and 1 mm.

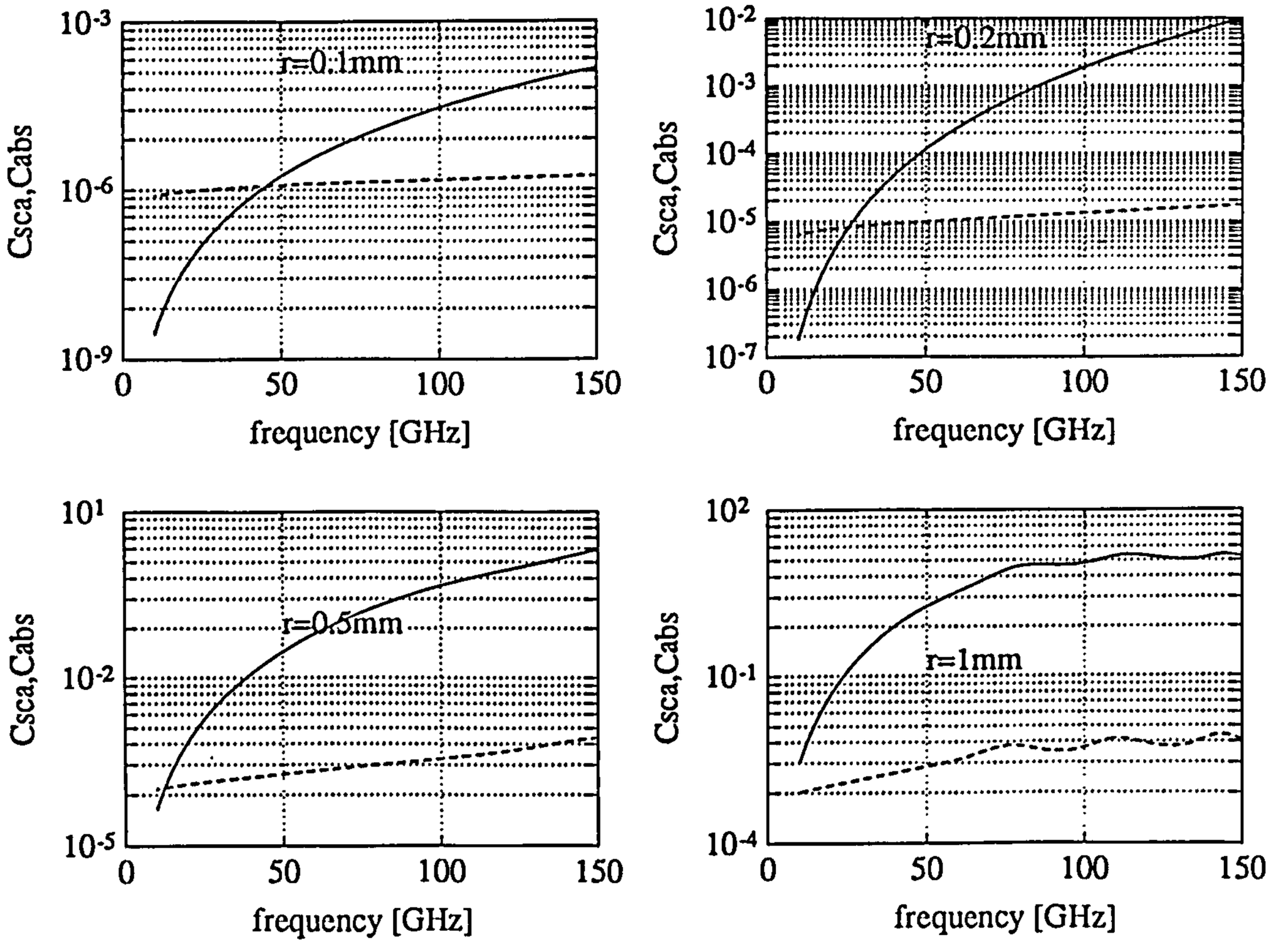

of magnitude) than that scattered at lower frequencies, the absolute values are of course very small and usually negligible. As the size of ice particles increases, the cross-over point moves fast to lower frequencies. The cross-over points for various particle sizes may be found in table III.

Table III. Frequencies for which the absorption and scattering cross sections of spherical ice particles are the same.

radius [mm]	frequency [GHz]
0.1	44
0.2	25
0.5	12

So, we can safely say that for frequencies above 60 GHz the ice resultant attenuation is almost exclusively due to scattering even for quite small ice crystals.

2.4.1.4 Distinction between scattering and absorption regions for water.

Figure 9 shows the ratio of the scattering albedo $\omega_o=C_{sca}/C_{ext}$ for various sizes of water drops as a function of frequency. Careful inspection of figure 9 reveals that small particles absorb a much more significant percentage of the incident energy than the larger particles even for frequencies up to 300 GHz. Nevertheless, the magnitude of the absorption cross sections of

Fig. 9. Scattering albedo for water spheres with various radii.

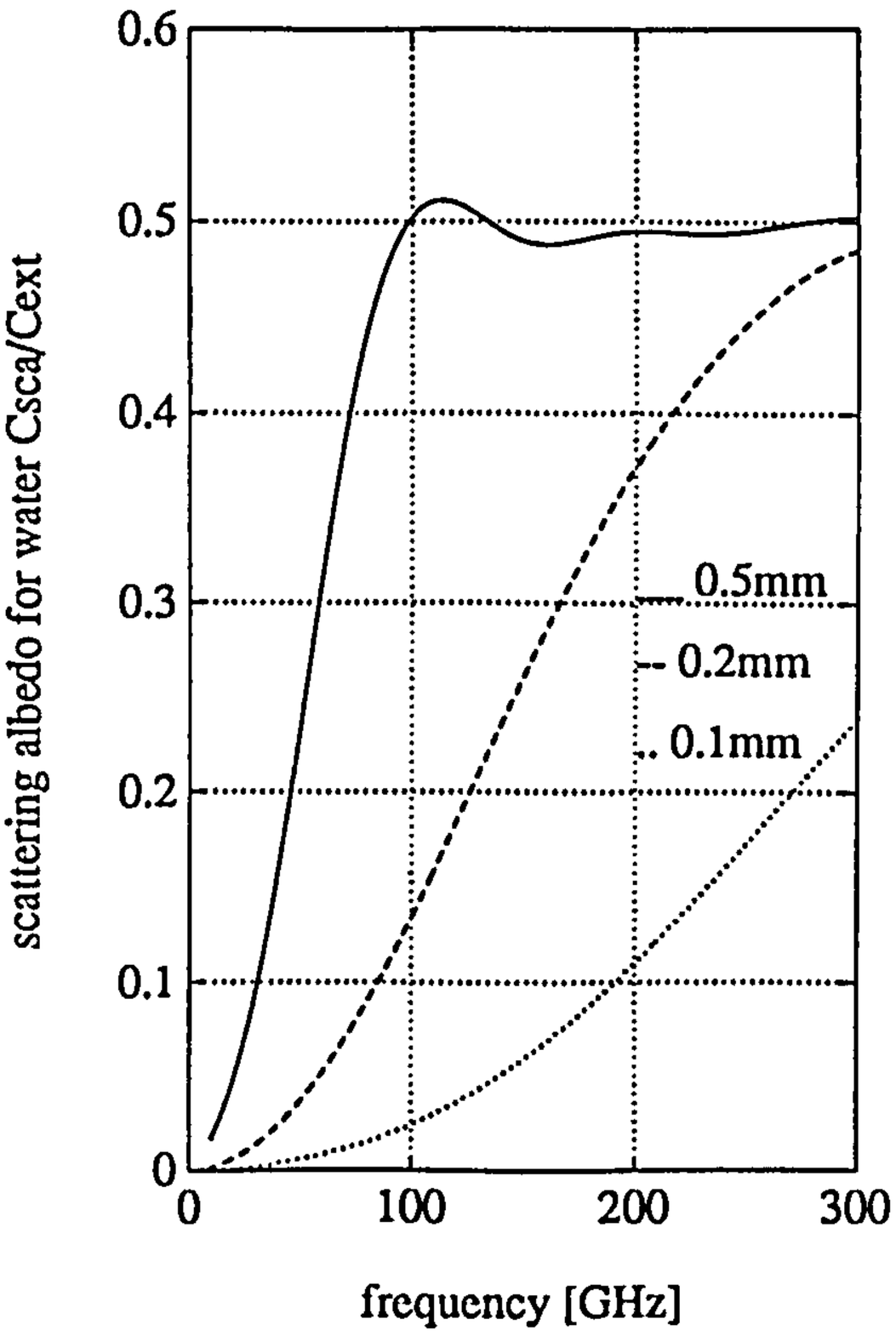

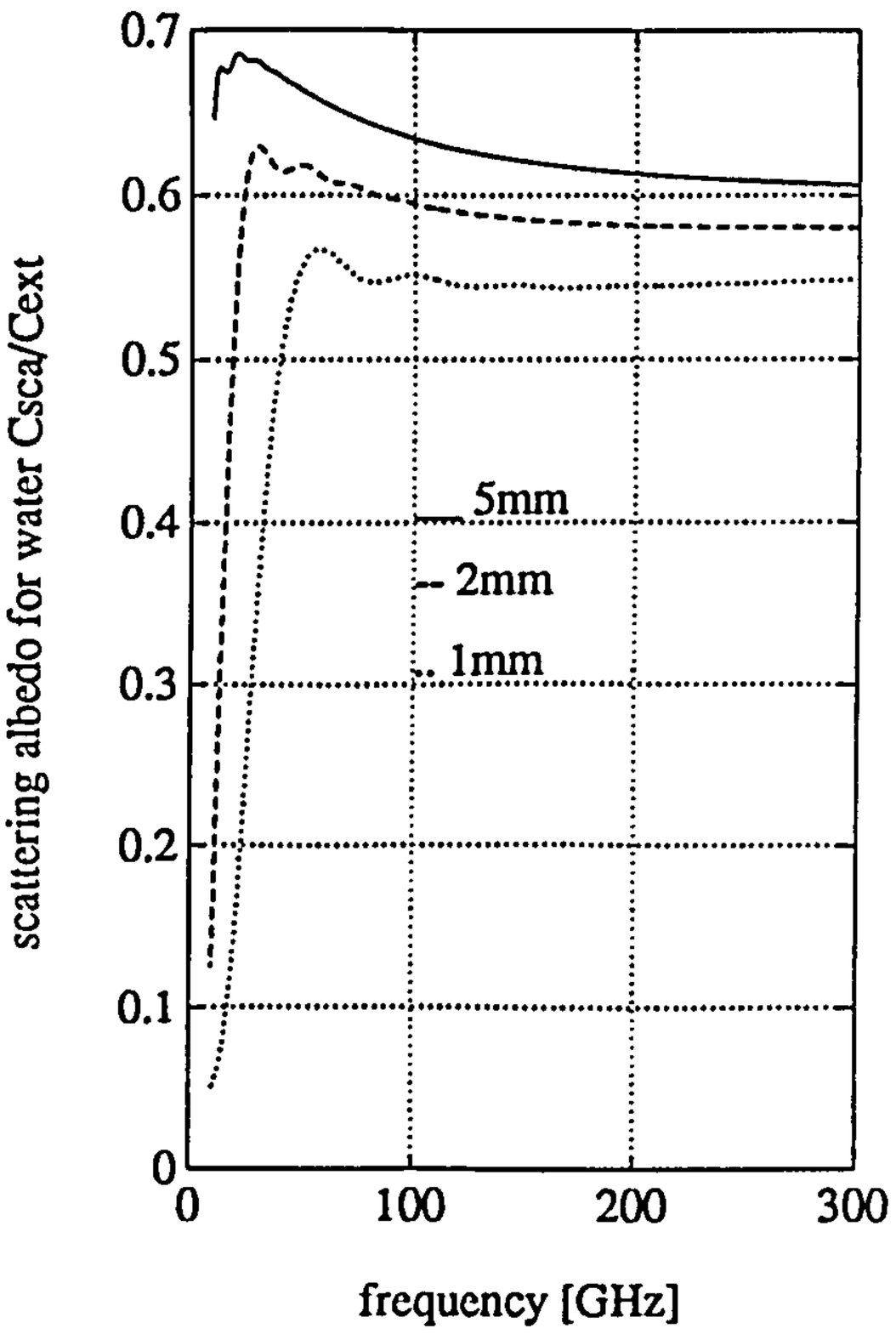

small water drops is too small and usually negligible. For medium sized particles (i.e. 0.5mm in radius) absorption dominates over scattering for frequencies up to 100 GHz, but as we move to higher frequencies both become soon level. For particles greater than 1mm in radius, scattering becomes more important than absorption even at microwave frequencies and contributes about 60% to the total extinction throughout the rest of the millimetre wave

spectrum. A comparison between the scattering and absorption cross sections of water spheres of various radii over the frequency range 10-300 GHz may be seen in figure 10.

Fig. 10. Absorption and scattering cross sections of ice spheres with radii r=0.1, 0.2, 0.5 mm and 1mm.

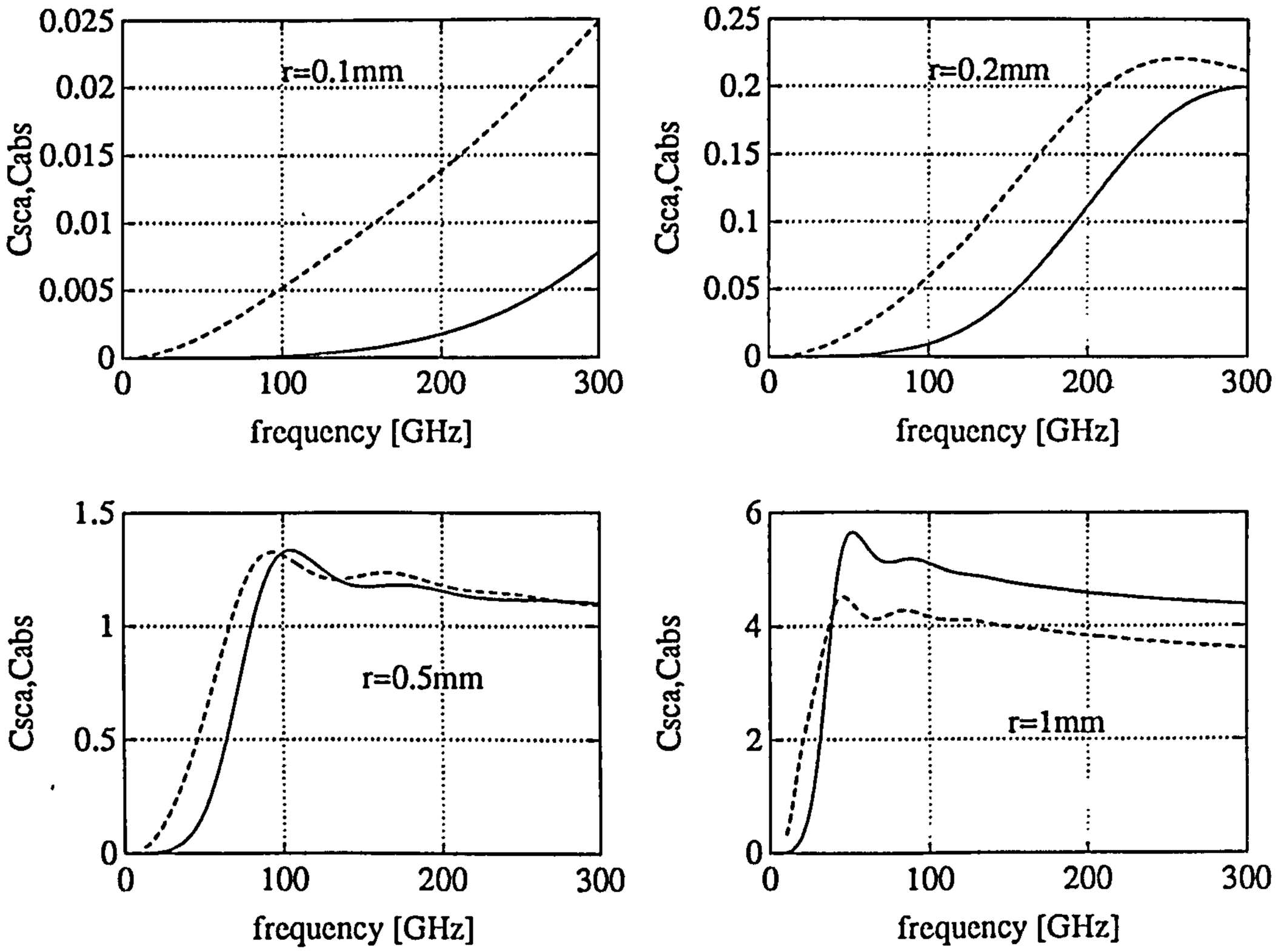

2.4.1.5 Extinction cross sections of ice and water spheres.

Finally the extinction cross sections of spherical ice and water particles of various sizes are illustrated in figure 11. At microwave frequencies the water extinction cross sections are always greater than the ice extinction cross sections. The smaller the particles the bigger the ratio of the water extinction cross sections to the ice extinction cross sections becomes. However, as frequency increases and the particles become bigger in size, the ice extinction cross sections become comparable or greater than those of water. The variation of the ratio C_{ext} (water) / C_{ext} (ice) with frequency and particle size can be seen in table IV, below. Also shown is the frequency for which the two cross sections become equal.

Fig. 11. Extinction cross sections of spherical ice and water particles with radii r=0.1, 0.2, 0.5, 1, 2 and 5 mm.

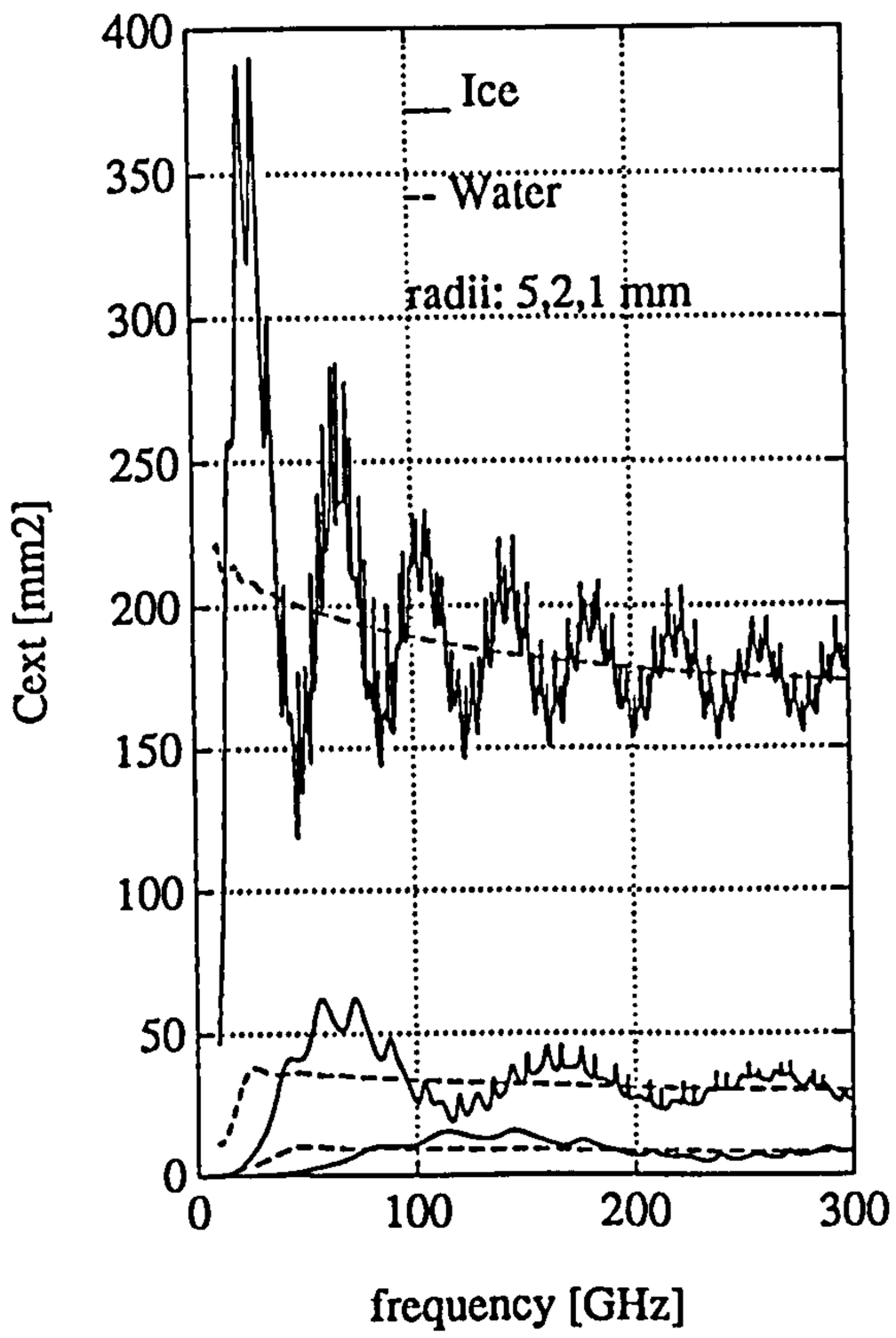

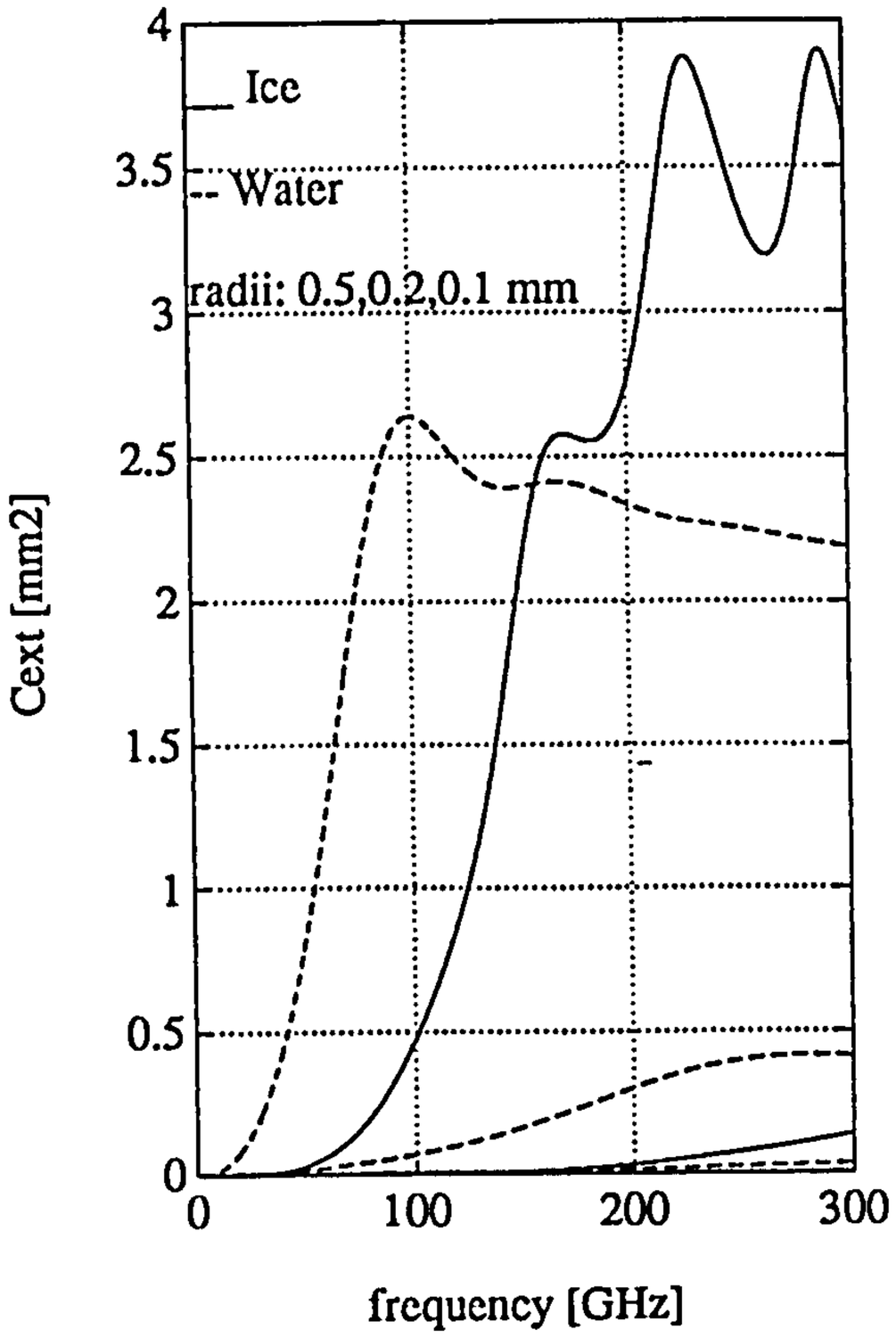

Table IV. Variation of the C_{ext} (water) / C_{ext} (ice) ratio with frequency and size particle.

	f [GHz]	30	60	100	150	300	$C_w/C_i=1$
r [mm]	0.1	507	459	176	66	13	-
	0.2	254	94.5	35.5	16.5	2.97	-
	0.5	57.7	19.6	5.64	1.15	0.60	158
	1.0	19.37	2.57	0.84	0.60	0.89	78
	2.0	2.66	0.60	1.29	0.89	1.12	38
	5.0	0.57	0.88	0.88	1.00	0.95	15

In conclusion ice becomes important for particles bigger than 1 mm in diameter for frequencies greater than 150 GHz. For smaller particles ie 0.4 mm in diameter the ice extinction cross sections are very small so the resultant attenuation is expected to be very low. For even smaller particles the ice extinction cross sections are too small and even at 300 GHz they are 13 times less than those of water.

2.4.2 Back scattering.

According to Mie theory the back scattering cross section σ is given by:

$$\sigma = \frac{\lambda^2}{\pi}|S_1(180°)|^2 = \frac{\lambda^2}{2\pi}\left|\sum_{n=1}^{\infty}(-1)^n(2n+1)(a_n-b_n)\right|^2,$$

where λ the wavelength of the incident radiation and a_n and b_n are the Mie scattering coefficients, expressed in terms of spherical Bessel and Hankel functions, dependent upon the size and the refractive index of the particle.

2.4.2.1 Back scattering cross sections of ice and water spheres.

The back scatter efficiency factor $Q=\sigma/\pi a^2$ (or normalized radar cross section) versus size parameter x for ice and water spheres are plotted in figure 12. The frequency of the incident wave is 30 GHz and the temperature for ice is -10 °C and for water 10 °C. The size parameter ranges from 0.30 to 15.7 with an increment step of 6.28×10^{-4}. Fluctuations similar

Fig. 12. Radar cross sections of spherical ice and water particles.

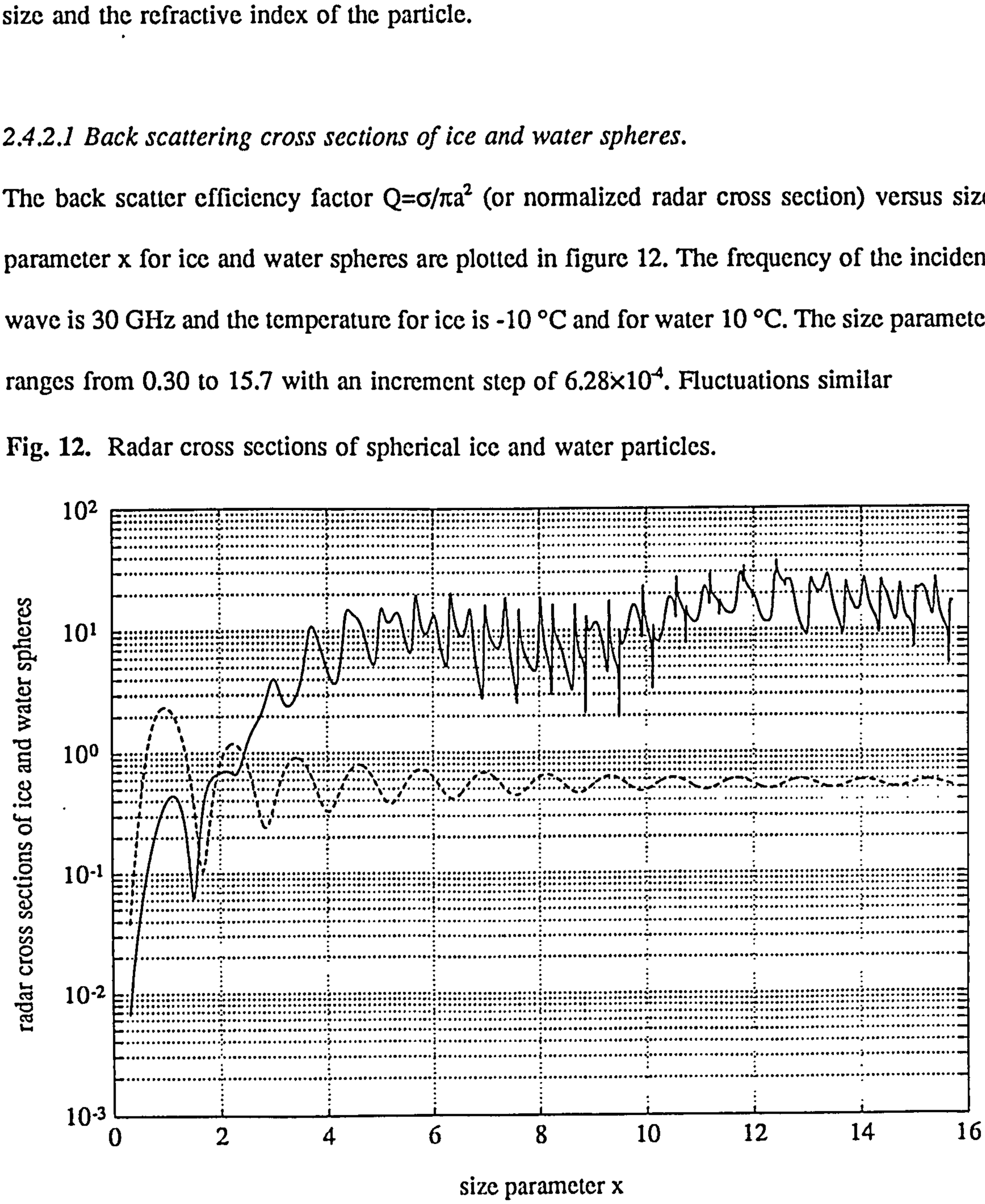

to those in the extinction curve but severely more pronounced are now observed. Careful comparison between figures 4 and 12 reveals, that the sharp minima and maxima appearing in the extinction or the back scattering curves for ice, occur at the same values of the size parameter. This observation will be proved very useful in the next chapter, where these resonance phenomena are rigorously treated. The striking effect of the numerous strong resonances depicted in figure 12 does not only appear in theoretical calculations, but has been experimentally verified by Atlas et al [1963]. Results from their experiments along with theoretical calculations from Herman and Battan and Kerker and Matijevic (from the same paper) can be seen in figure 13.

Fig. 13. Theoretically calculated and experimentally measured radar cross sections of dielectric spheres (from Atlas et al [1963]).

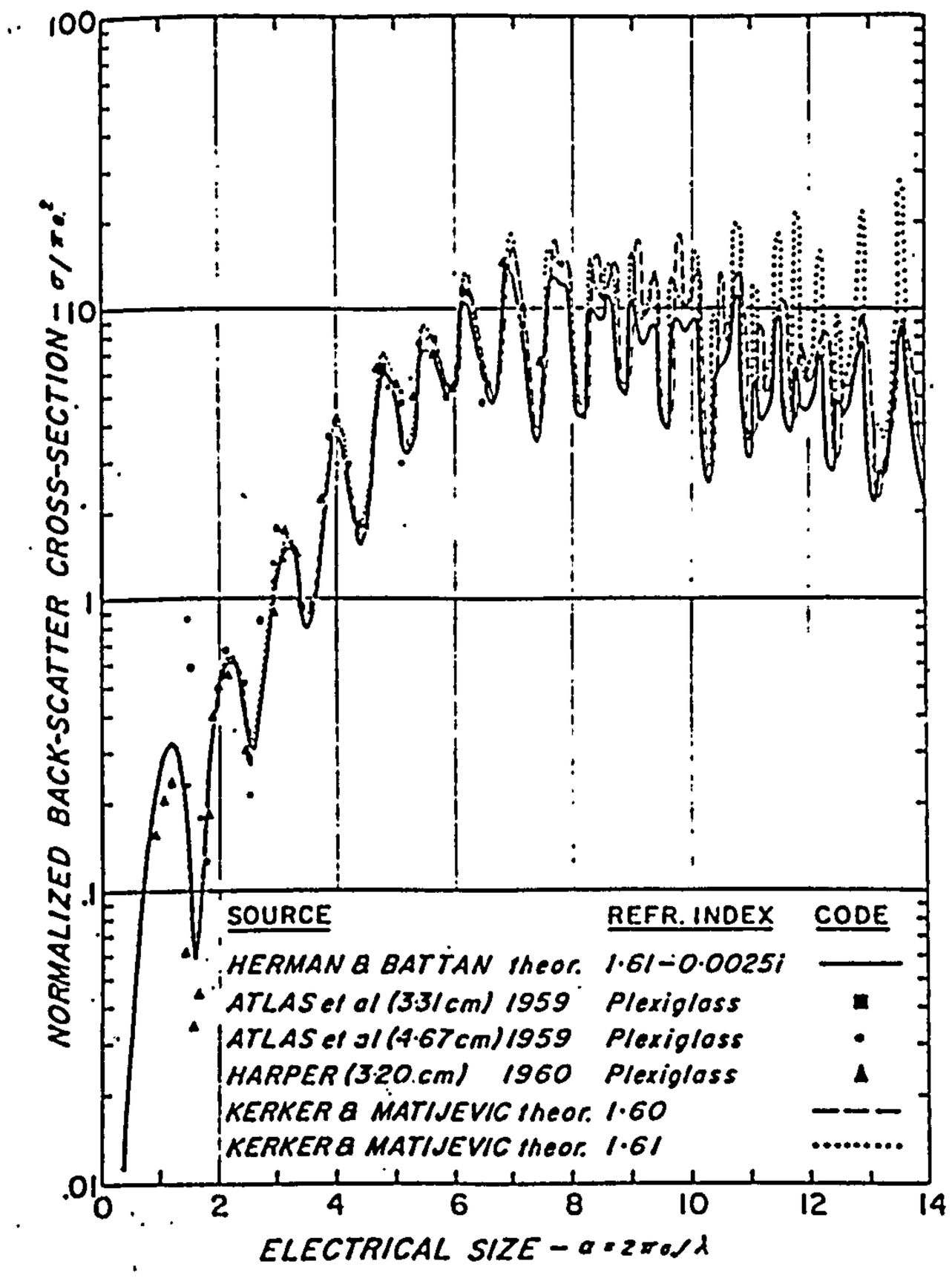

The radar cross sections of water spheres are also plotted in figure 12. The unusual oscillation

of the water radar cross section with size parameter have been experimentally verified by Aden [1951] and theoretically calculated by Haddock [1956] (see figure 14). Theory and experiment thus check very well but still an explanation for the extremely strong fluctuations is needed. According to Van de Hulst [1957], the correct explanation is that a surface wave excited by the grazing incidence near the edge travels around the sphere 1/2, 3/2, 5/2 times, etc., and gives off radiation which interferes either constructively (maxima in the back scattering curve) or destructively (minima in the back scattering curve) with the axially reflected wave. An empirical expression for the induced surface waves has been given by Probert-Jones [1963] and an exact expression rigorously deduced by Senior and Goodrich [1964]. The suggested expressions have been compared with exact theoretical computations

Fig. 14. Radar cross section σ computed for back scattering by water drops and totally reflecting spheres at λ=3mm (after Haddock [1956]).

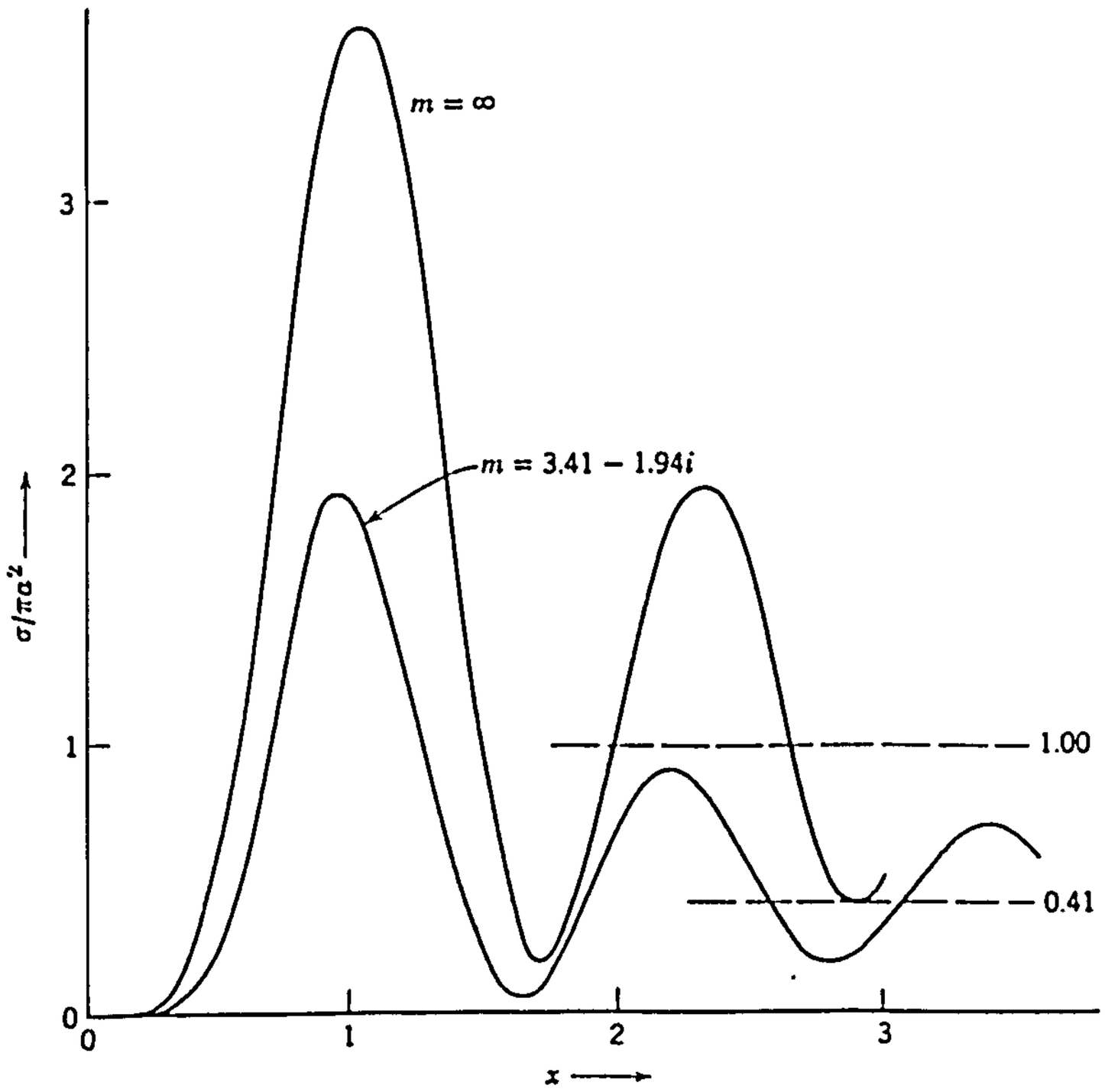

for totally reflecting spheres. Excellent agreement was revealed, indicating that interference between axial rays and surface (creeping) waves is the physical mechanism responsible for the

strong fluctuations observed in the back scattering of absorptive or conducting spheres.

2.5 Conclusions.

In this chapter various resonance and interference phenomena in the scattering from spherical ice and water particles have been reviewed. In the forward direction the scattering process is determined by interference between diffracted and transmitted fields. It is the constructive and destructive interference between those fields that causes the oscillation of the extinction cross sections of ice and water particles. In the backward direction the scattering process is determined by interference between reflected fields and surface waves (external or "creeping" waves for water and internal surface waves for ice). The constructive or destructive interference between these fields leads to oscillations of the radar cross sections of spherical ice and water particles. However, the occurrence of numerous small scale fluctuations in the ice extinction curve which become quite more pronounced in the back scattering case has not been satisfactorily explained yet. A closer look at this problem is taken in the next chapter, where a new physical mechanism is nominated to explain this intriguing phenomenon.

CHAPTER 3

A RIGOROUS EXPLANATION FOR THE RESONANCES OBSERVED IN THE SCATTERING OF DIELECTRIC SPHERES.

3.1 Introduction.

In the previous chapter we employed Mie theory to calculate the absorption and scattering cross sections of spherical ice and water particles at millimetre wavelengths. We also identified and explained the physical mechanisms lying behind the theoretically derived results. However, not all phenomena in the numerical results have been satisfactorily explained.

One such phenomenon, is the existence of numerous fluctuations in the scattering of dielectric spheres. This phenomenon appears as a tiny ripple structure in the forward scattering curve ($\theta=0°$) and becomes progressively more pronounced for increasing scattering angles. For $\theta=180°$ (back scattering case), the fluctuations are so strong, that the radar cross sections may oscillate by an order of magnitude for adjacent values of the size parameter. This is illustrated

Fig. 1. Forward extinction cross sections (exaggerated 5 times for the sake of better visual observation) and radar cross sections of ice spheres versus size parameter.

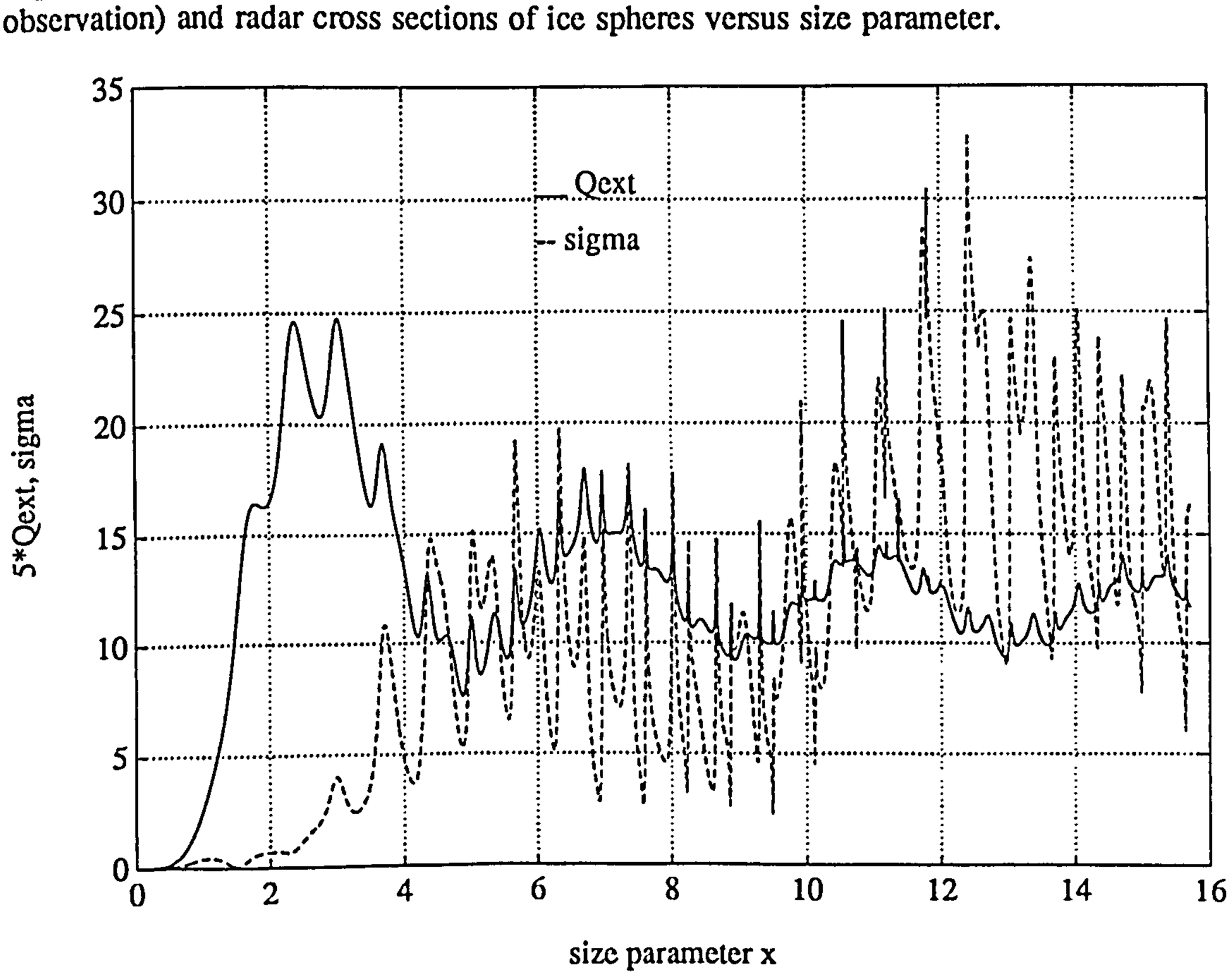

in figure 1, where the scattering cross sections of ice spheres for θ=0° and θ=180° versus size parameter have been plotted.

In order to explain the peculiar behaviour of dielectric spheres ,several physical mechanisms have been proposed by various researchers. The existence of the ripple in the forward scattering has been attributed to internal surface waves. Internal rays from the theory of geometrical optics along with diffracted fields have been suggested as the principal contributors to the back scattering. With none of the above mechanisms being absolutely convincing, a new physical process is nominated for the interpretation of the resonance phenomena present in the scattering of dielectric spheres. The identification and the rigorous mathematical description of this process is the subject of this chapter. Before the details of the derivation are given, a brief review of the already suggested mechanisms will be presented.

3.2 The ripple structure in the extinction curve.

The existence of the ripple structure in the extinction curve was revealed when powerful computers capable of performing large scale computations became available. Before then, most other computations had been made with steps in the size parameter x too big to reveal the fine structure. Van de Hulst was amongst the first to analyze such revealing data provided by the Cambridge Air Force Research Centre (CAFRC). The calculations were performed on an IBM 701 computer, covering the range x=0 to 30 with narrow intervals of x and for real values of the refractive index m=1.33, 1.40, 1.44, 1.486 and 1.50. A graphical representation of some of these data may be seen in figure 2, where the extinction efficiency factors versus size parameter for m=1.5, 1.33, 0.93 and 0.8 are depicted. Based on a series of extensive studies for material bodies with m real, Van de Hulst suggested the following empirical formula

$$S(x,0)=\frac{1}{2}x^2 - x\frac{2m^2}{(m+1)(m^2-1)}ie^{-2ix(m-1)} + (0.46-0.80i)x^{4/3} + ripple\ ,$$

in order to approximate Mie's complex but exact analytical expression. The terms in the former expression are given in order of importance. The first term describes the diffracted and

Fig. 2. Extinction curves computed from Mie's formulae for m=1.5, 1.33, 0.93, and 0.8 (after Van de Hulst [1957]).

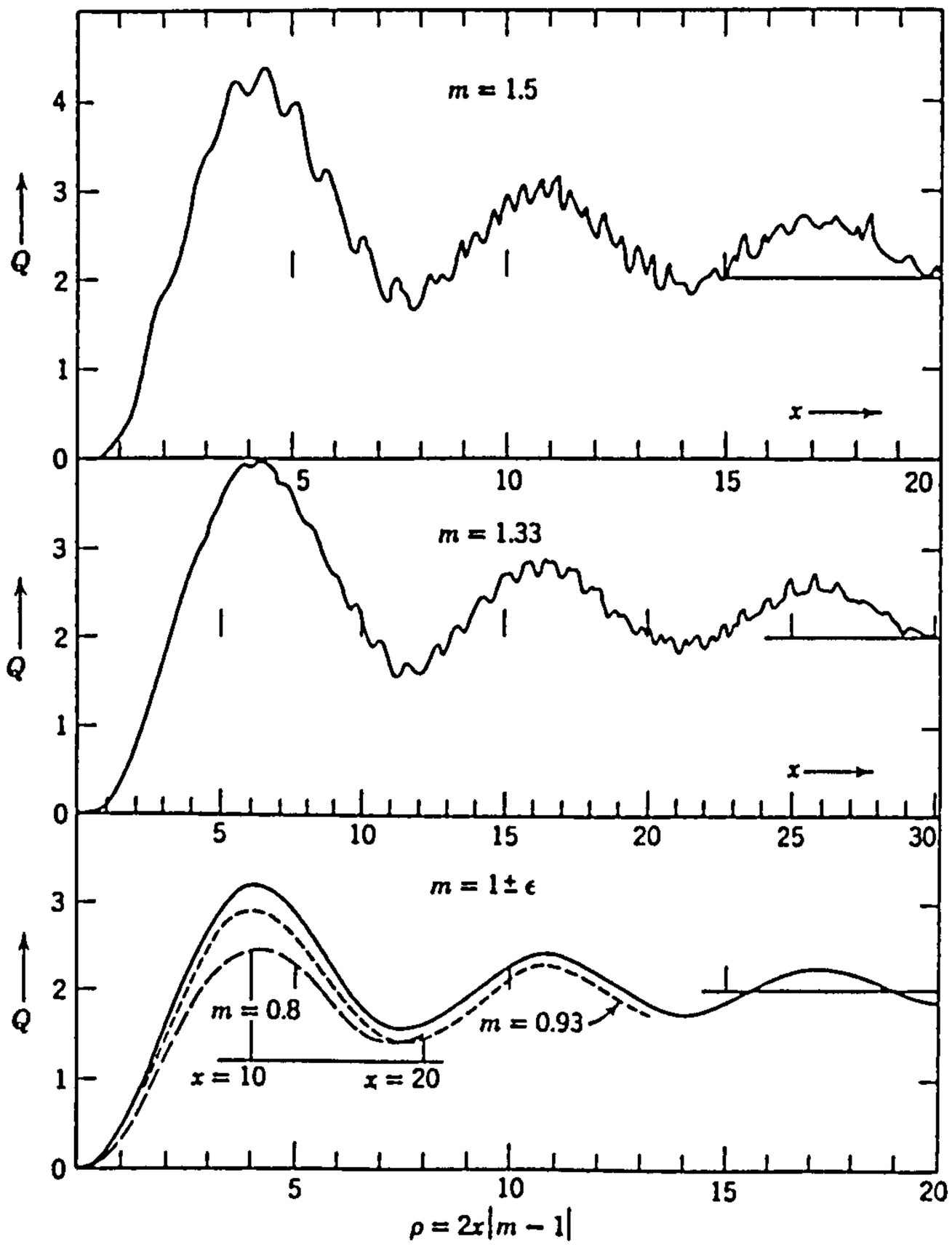

the second the refracted field. In the refraction term, provision is taken only for the contribution due to the central rays that leave the sphere after having covered a path equal to a single diameter. The remaining terms which correspond to the central rays that cover the diameter of the sphere 3,5 or more times have been omitted, as they are numerically insignificant in the range of m considered (m=1 to 2). The third term describes grazing reflection effects, ensuring that the extinction curve lies above Qext=2. It also decreases less rapidly with increasing x than the refraction term does, indicating so its importance for large sizes of the size parameter. The suggested formula and Mie's exact solution are both depicted

in figure 3.

Fig. 3. Van de Hulst's empirical formula for the approximation of the forward extinction cross sections of dielectric spheres.

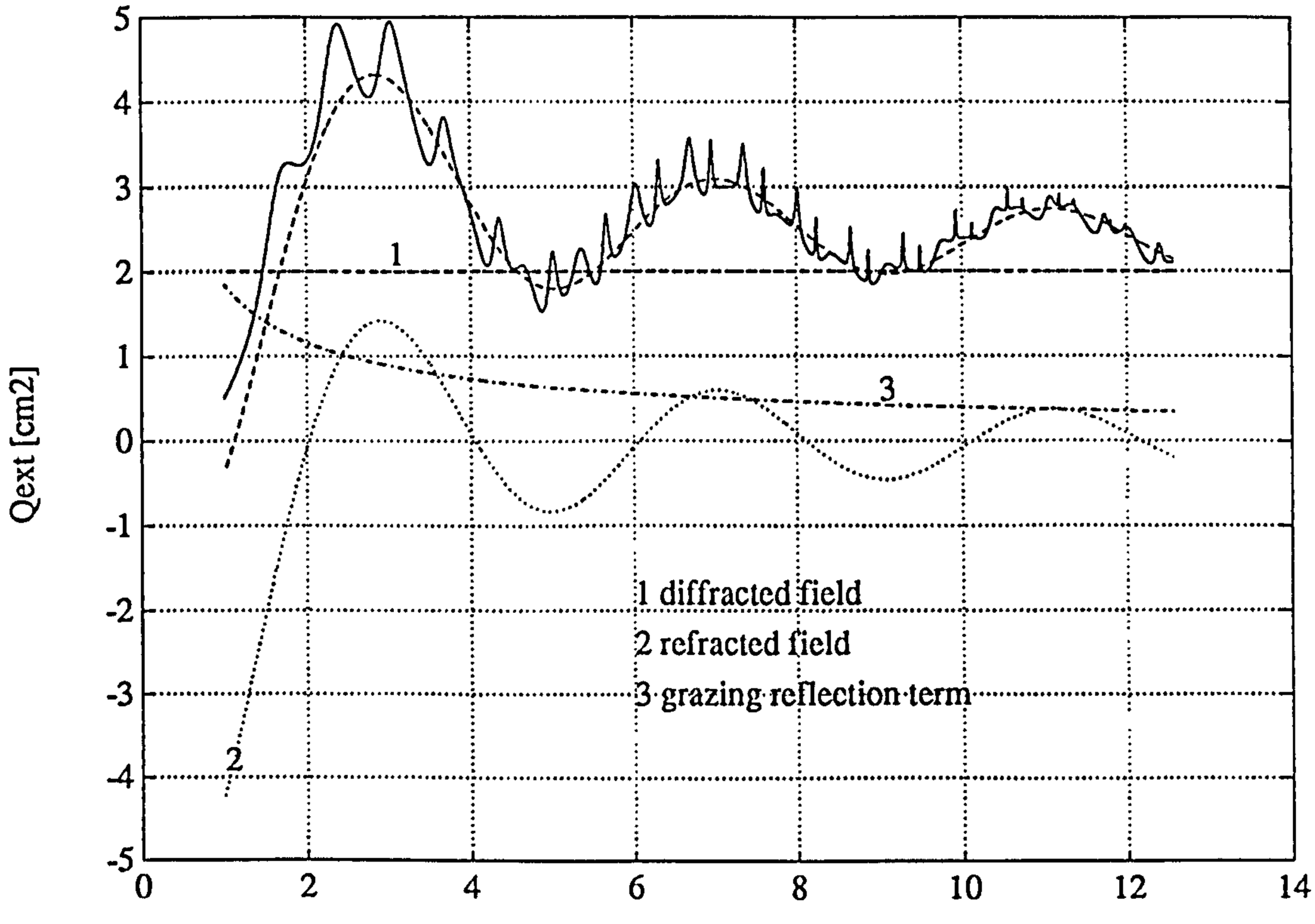

It can be seen that the agreement is quite good apart from the numerous small scale fluctuations observed only in the analytically calculated curve. To account for these fluctuations a fourth term was added in the approximate formula, denoted as 'ripple'. Examining carefully the CAFRC data for all five real values of the refractive index **m** (see above), Van de Hulst was able to assess some general properties of the ripple, which are summarised below:

a) The ripple is not confined to any particular value of **m**. It appears with approximately equal strength in all five curves.

b) The ripple has a definite periodicity: peaks or valleys recur at intervals about 0.80 in x for all values of **m** concerned.

c) The ripple is not a pure sine wave. It resembles somewhat the beat pattern of two sine

waves of slightly different periods, but this is too coarse a description. In some regions it shows double peaks in the interval 0.8, and in some it shows single ones, as indicated below

Table I. Single and double peaks of the ripple.

Refractive index	Double peaks of equal amplitude near	Single peaks near
m=1.33	x=20.5	x=30
m=1.40	x=17.5	x=27.5
m=1.44	x=14	x=23.5
m=1.48	x=12	x=20
m=1.50	x=12	x=19.5

d) Since these values of x are nearly proportional to 1/(m-1), the character of the ripple (double or single hump) has a tendency to recur at the same value of $\rho=2x(m-1)$, i.e., at a fixed position in the major fluctuations.

e) The ripple also has an imaginary component.

3.2.1 Van de Hulst's tentative explanation by means of surface waves.

Let us suppose that a ray bundle is striking the dielectric sphere at grazing incidence (see figure 4). Then a surface wave is generated which begins to circumnavigate the sphere. At any point along the surface the wave will lose energy by two effects; the refraction into the sphere along AB or A'B' as indicated by Ott's [1942] theory of the surface waves for dielectrics, and the spray in the forward direction along AP and A'P', etc. It is very unlikely that the original surface wave will travel all the way around the sphere and still produce a noticeable effect.

The increase in optical length due to taking the 'short cut' through the sphere, rather than travelling on the surface is

$$hr = 2r\tan\alpha_c - 2r\alpha_c ,$$

where r the radius of the sphere and $m=1/\sin a_c$ with a_c the critical angle of incidence.

Fig. 4. Reinforcement of the surface wave on a dielectric sphere by waves travelling through the body.

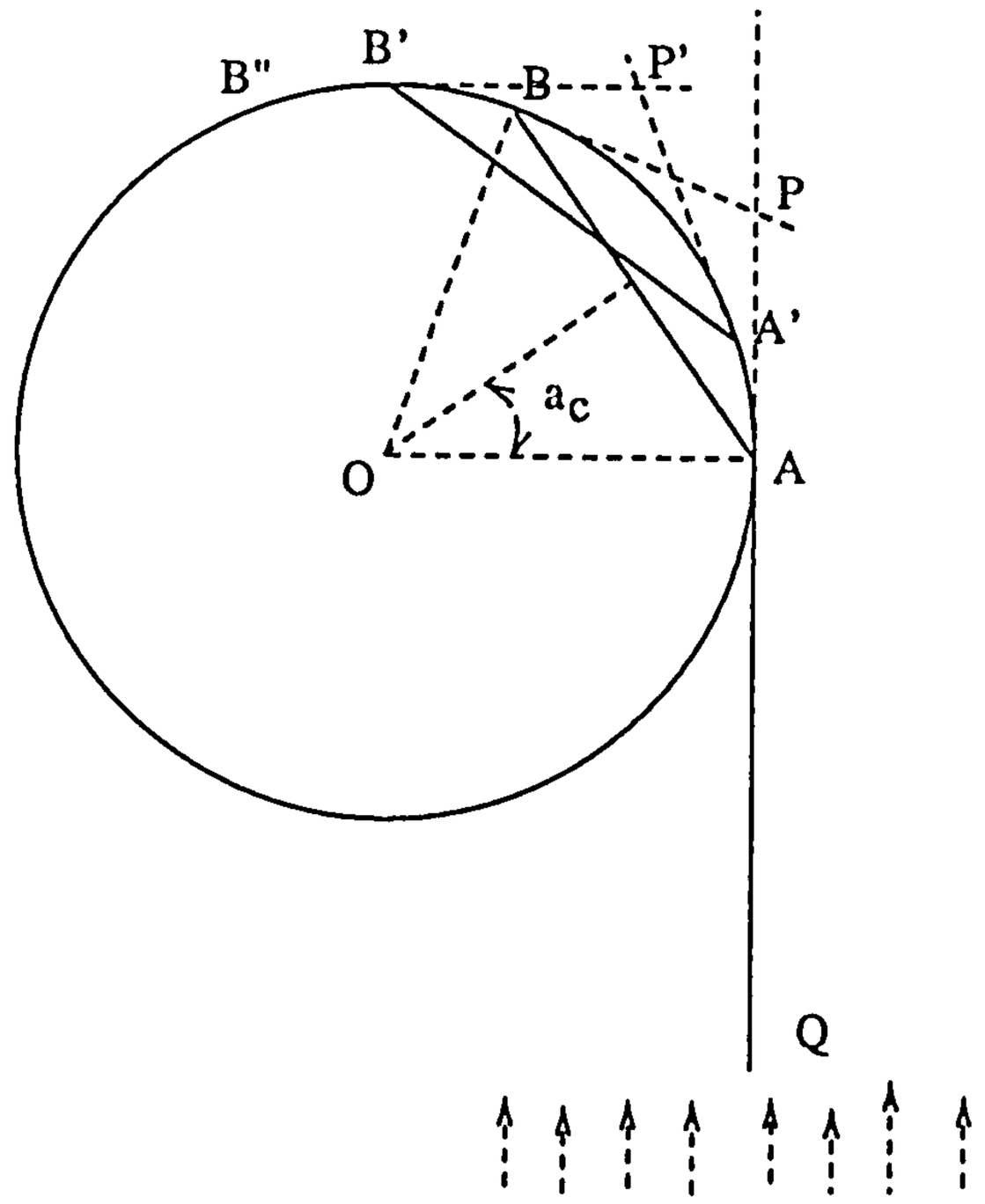

In travelling around the sphere, the surface wave will take N short cuts and each time will suffer a phase decrease corresponding to an optical path hr. The full optical path around the body will then be $2\pi r+Nhr$. It is more likely that N will be close to the maximum number of possible short cuts, for example 3 in the case of ice, where m=1.78. Constructive or destructive interference with the diffracted wave will occur, if this optical path is increased by a full wavelength. Therefore, the peaks observed into the extinction curve should be given by:

$$\Delta(2\pi r + Nhr) = \lambda \ ,$$

and so

$$\Delta x = \frac{1}{1+Nh/2\pi} \ ,$$

would normally give the distance between consecutive peaks. Solving for m=1.78 and N=3 short cuts, one finds $\Delta x=0.67$. This is in good agreement with the calculated data and lends support to the suggested explanation. Not all peaks can be predicted utilizing this theory, but

certainly Van de Hulst's treatment suggested that a more rigorous approach for the ripple structure could be based on the nature of surface waves, already discussed here.

3.2.2 The electric and magnetic multipoles of Metz and Dettmar.

Another explanation was suggested by Metz and Dettmar [1963] who wrote the Mie expression for the extinction efficiency factor as

$$Q_{ext} = \sum_{n=1}^{\infty} q_n^e + q_n^m ,$$

where $q_n^e=2(2n+1)Re\{a_n\}/x^2$, $q_n^m=2(2n+1)Re\{b_n\}/x^2$ with q_n^e and q_n^m called electric and magnetic multipoles of order n. The electric and magnetic multipoles for n=1 to 10 and for real refractive index m=2 versus size parameter x are depicted in figure 5. Careful inspection

Fig. 5. The electric and magnetic multipoles of Metz and Dettmar for size parameter x=0-7 and index of refraction m=2 (after Metz and Dettmar [1963]).

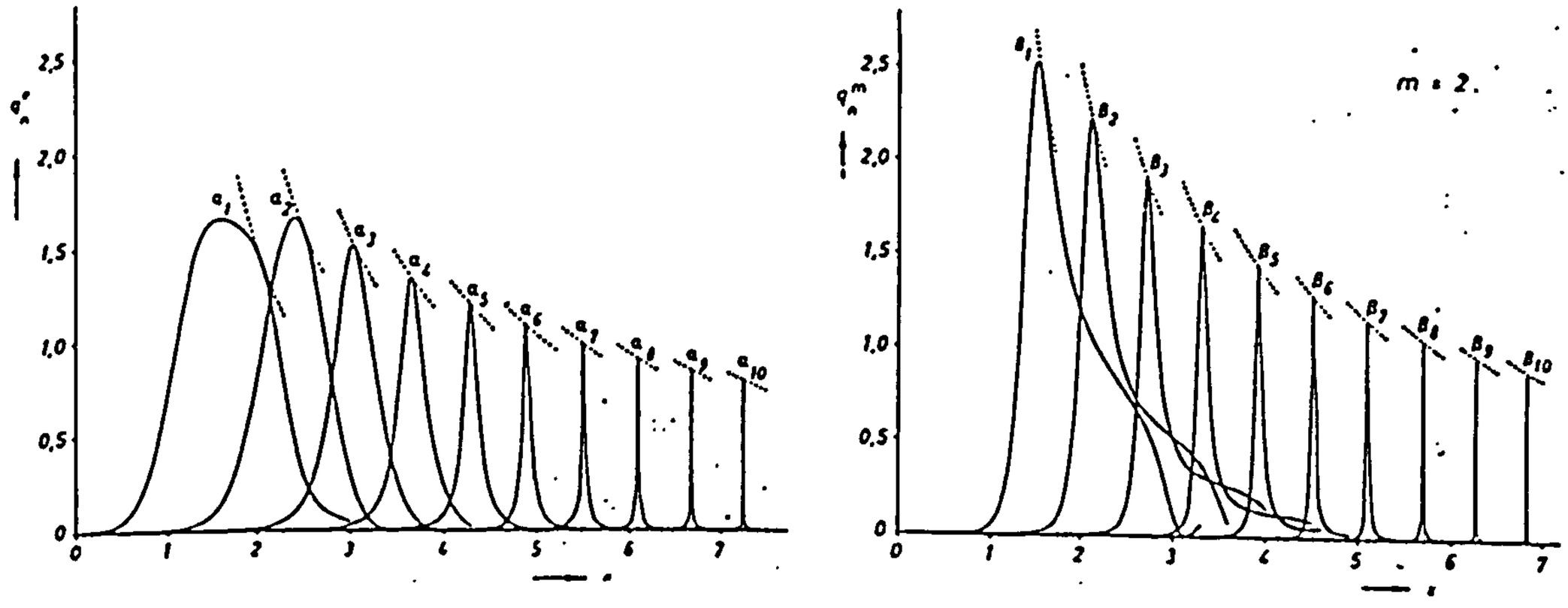

of figure 5 and figure 6 in which the forward efficiency factor Q_{ext} versus size parameter x for m=2 has been plotted, reveals that the local maxima in the extinction curve occur where the electric or magnetic multipoles take their peak values.

For higher values of the refractive index (m>2), the peaks become sharper, giving rise to

strong resonance phenomena. At the other end, that is when **m** approaches unity, the peaks smooth out and finally disappear for **m** less than or equal to unity.

Fig. 6. Extinction cross sections of dielectric spheres with m=2 (after Metz and Dettmar [1963]).

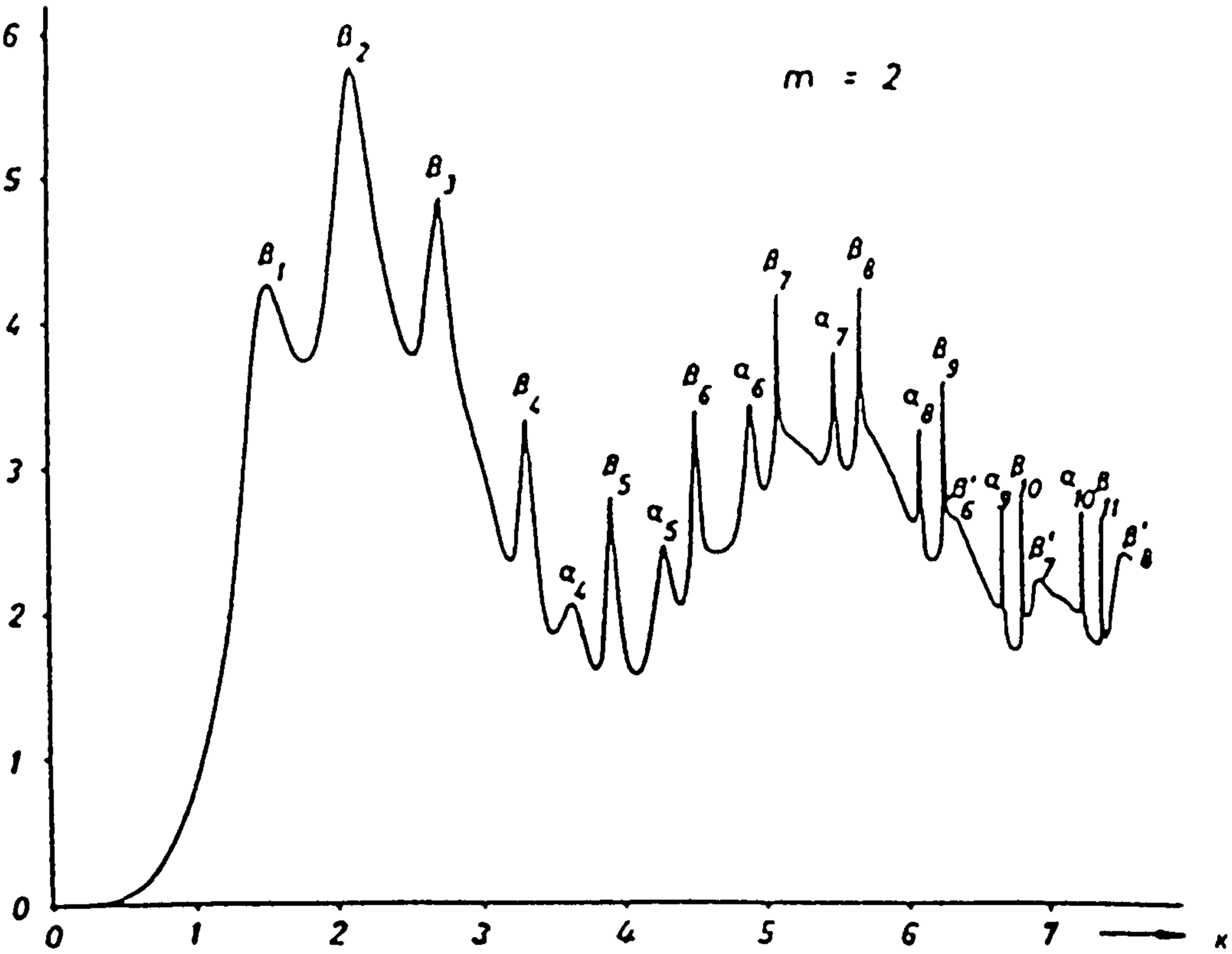

So, Metz and Dettmar's multipoles give at least some explanation for the occurrence of the numerous peaks in the extinction curve. But apart from being useful mathematical entities, the electric and magnetic multipoles fail to support a physical mechanism involved in the scattering process.

3.3 The back scattering of dielectric spheres.

Various electromagnetic techniques and theories have been applied to interpret the back scattering of dielectric spheres. In general, comparisons between the numerical results of Mie and the suggested theories have been carried in the frequency and more recently in the time

domain.

3.3.1 Geometrical optics

The first ever attempts to interpret the back scattering of dielectric spheres employed geometrical optics methods. Kouyoumjian [1963] made use of ray optics to consider refraction and reflection of various significant rays by the dielectric body. The major modification of the theory of the classical geometrical optics, is the inclusion of the fields of the glory ray and the rainbow ray in the back scattered field. The fields of these rays are not included in the classical geometrical optics treatment because the field of the glory ray is

Fig. 7. Radar cross section of a dielectric sphere with m=1.61 as a function of the size parameter, calculated by the use of modified geometrical optics (after Peters [1965]).

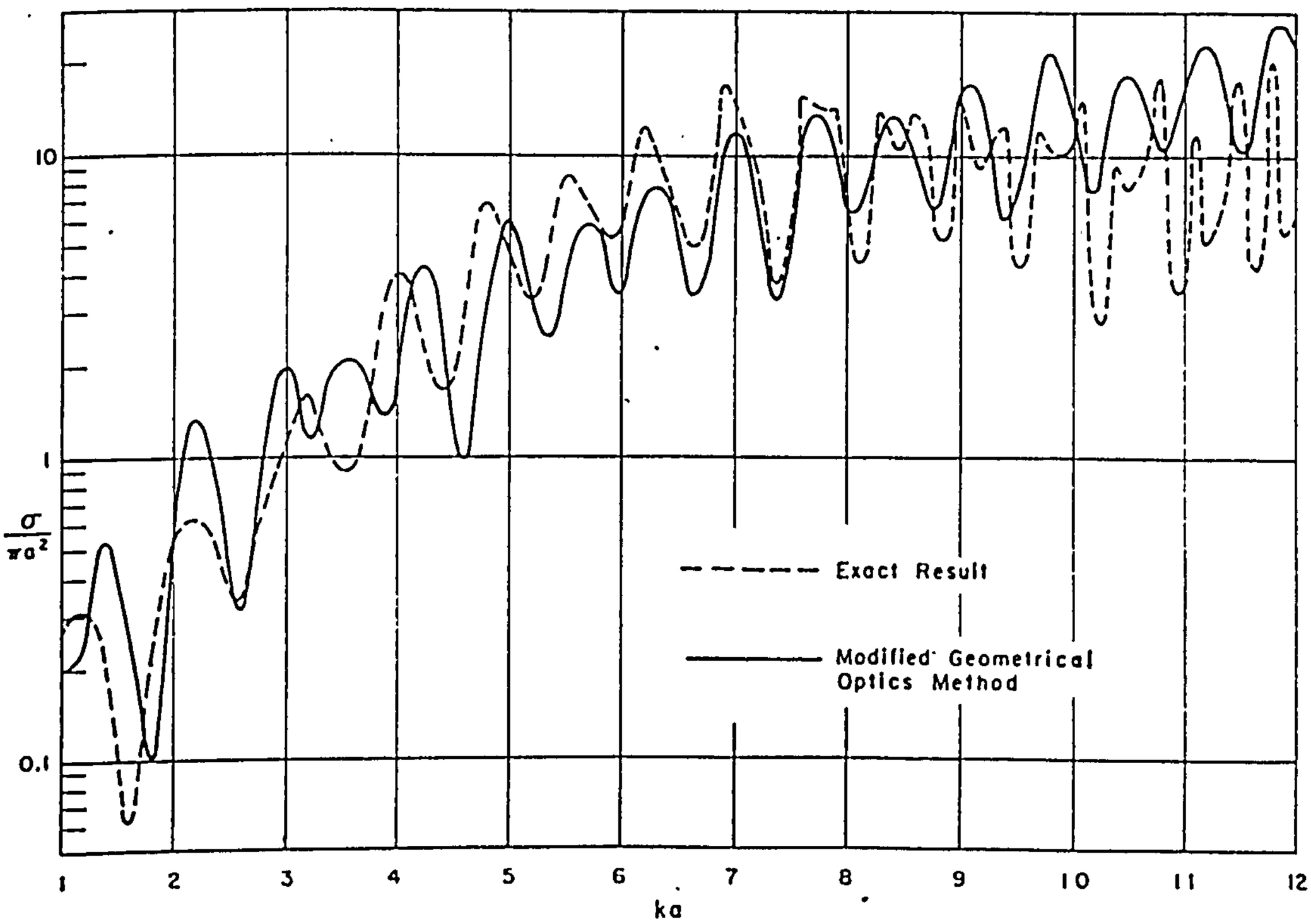

found to be infinite, and the path of the rainbow ray does not pass through the path of observation. Kouyoumjian used concepts from physical optics and the method of stationary

phase to obtain proper field contributions from these rays. Following the principles of his modified geometrical optics method, Peters [1965] calculated the radar cross sections of dielectric spheres. The results for a dielectric sphere with m=1.61 may be seen in figure 7. Thus the geometrical optics method seems to be relatively successful in representing the mechanisms involved in the back scattering of dielectric spheres. However, the validity of the modified geometrical optics method was questioned by Rheinstein [1968], who considered the back scattering from dielectric spheres in the time domain.

3.3.2 The back scattering of dielectric spheres in the time domain.

Another potential approach to the problem of back scattering from dielectric spheres is the impulse response in the time domain. Utilising rigorously computed values of the amplitude and phase of the continuous wave backscatter, short pulses of electromagnetic waves are synthesized by Fourier series. The resultant response is examined as a function of time and the individually resolvable returns are attributed to some approximate theories.

Rheinstein [1968], suggested that relatively simple ray tracing considerations suffice to predict the position of at least a portion of the observed returns. So, the front axial as well as other axial returns of higher order, stationary rays and the glory would contribute to the backscatter. However, he discovered a discrepancy between the predicted amplitude and that observed in the short pulse response for one of the returns, viz., the glory ray. The short pulse response also indicated the presence of a series of returns not predicted by geometrical optics. Rheinstein related these returns to surface waves -similar in nature to those considered previously by Van de Hulst-, which might take short cuts through the sphere at the critical angle of internal reflection. In his final conclusions Rheinstein suggested that further study was necessary to improve the understanding of these surface waves and of the ray optics as well. A few years later Ray and Stephens [1974] utilized again the impulse response technique in an attempt to give sufficient understanding to the scattering by ice spheres. Contributions from

the glory, front and rear axial and stationary rays in combination with an internal surface wave of one cut and the electric dipole model are all summed up together to compose a complex model for ice back scatter. The total model is depicted in figure 8, where various individual contributions can be distinguished. The front axial, rear axial, glory and stationary ray contributions are combined for x>1 and labelled geometric optics. The geometric optics contribution is combined with the internal surface wave contribution and labelled total. An electric dipole approximation is used for x<1.

Fig. 8. Analytically and empirically calculated radar cross sections of an ice sphere with radius 2 cm at a temperature of 0° C (after Ray and Stephens [1974]).

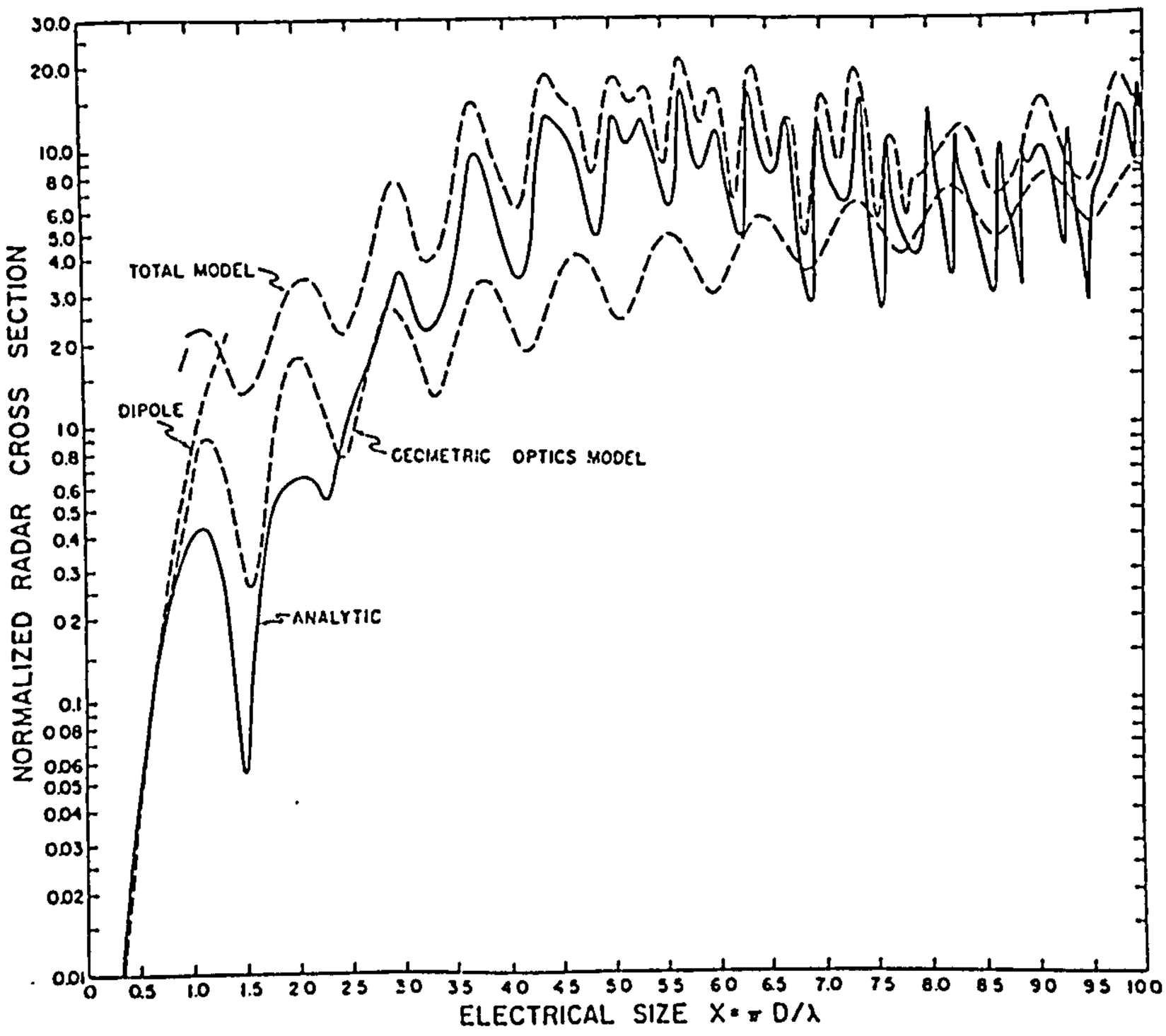

In conclusion, internal rays and diffracted fields are the principal contributors to the backscatter by ice spheres. However, the failure of the suggested model to account for the fine structure, clearly indicates the lack of sufficient understanding in the phenomena involved in the scattering process.

3.3.3 Surface waves.

Inada and Plonus [1970a, 1970b], applied the Watson transformation to split the exact Mie solution into the geometrical optics fields and the diffracted fields. The fields corresponding to the geometrical optics back scattered rays were asymptotically evaluated from the line integral of the transformed Mie series by a saddle point method. The diffracted fields were evaluated by finding the poles of the integrand and computing the residues. The authors connected -rather arbitrarily- the residue contributions with two different types of surface waves; "creeping waves" or D-type waves analogous to those of a perfectly conducting sphere which encircle the sphere, and internally reflected surface waves or E-type waves. In their analysis they ignored the contributions of creeping waves because for a dielectric material these waves are strongly damped. Only the contributions of the internally reflected surface waves were taken into account. Utilizing this approach, Inada and Plonus found that the contributions of the geometrical optics fields are negligible and suggested that the major contributors to the back scattering are the diffracted fields which give rise to surface waves. This conclusion is of course in clear disagreement with the modified geometrical optics theory. Furthermore, the contribution of the diffracted fields (surface waves), seems not to be the dominant return in the time domain of the impulse response technique.

Murphy et al [1980] also expressed the infinite Mie series into a convenient form to attribute the resonances observed in the backscatter curve to surface or "creeping waves". They showed that these resonances may be thought as originating through a mechanism in which families of attenuated circumferential waves are generated during the scattering process which repeatedly circumnavigate the scattering object. At one of the eigenfrequencies (or equivalently the poles which appear in the Watson transformation of the Mie series) of the sphere, the wavelength of one of the surface waves is such that the wave repeats itself after successive circumnavigations ("phase matching"), and a resonant reinforcement occurs.

3.4 A new physical mechanism responsible for the resonances of dielectric spheres.

In the preceding sections we reviewed various explanations for the resonances of dielectric spheres. Generally, two approaches have been adopted so far. One, which appeals to geometrical optics methods and another which involves mathematical manipulations to relate the scattering coefficients a_n and b_n of the infinite Mie series to more understandable physically interpreted entities. With none of them being able to convincingly answer the problem, a new physical mechanism is proposed for the interpretation of the resonance phenomena in the scattering of dielectric spheres.

We saw in chapter 2, that the numerous fluctuations occur for a dielectric sphere at exactly the same positions of the size parameter for all scattering angles. It is logical therefore to assume, that at these points the dielectric sample removes the incident energy more efficiently. This excessively removed energy can not be dissipated within the particle, because it has an almost real index of refraction. Instead, this energy is reradiated towards all directions and can be furthermore enhanced by the externally applied field according to the scattering direction. This was verified by Gastine et al [1967], who studied the resonances of dielectric spheres in an experimental setup which is illustrated in figure 9. The recordings of the dimensional resonances of two dielectric spheres 3.9mm and 4mm in diameter are shown in figures 10 and 11, respectively. The dimensional resonances can be easily recognized from the points where the transmitted power is heavily attenuated. When the frequency of the incident field lies close to some mode of free oscillation of the dielectric sphere a large portion of the energy of the propagating field is removed by the sphere which acts as a dielectric resonator. A large portion of this removed energy is reflected back to the opposite direction where it is eliminated by the isolator. The remaining portion of the energy is eventually transmitted towards the direction of propagation and is recorded at the crystal detector. Thus, the presence of the numerous resonances in the scattering from dielectric spheres must be closely related to the behaviour of dielectric resonators.

Fig. 9. Experimental setup in order to observe the dimensional resonances: 1)sweep generator; 2)oscilloscope or recorder; 3) dielectric sphere 4)isolator; 5)crystal detector; and 6)waveguide.

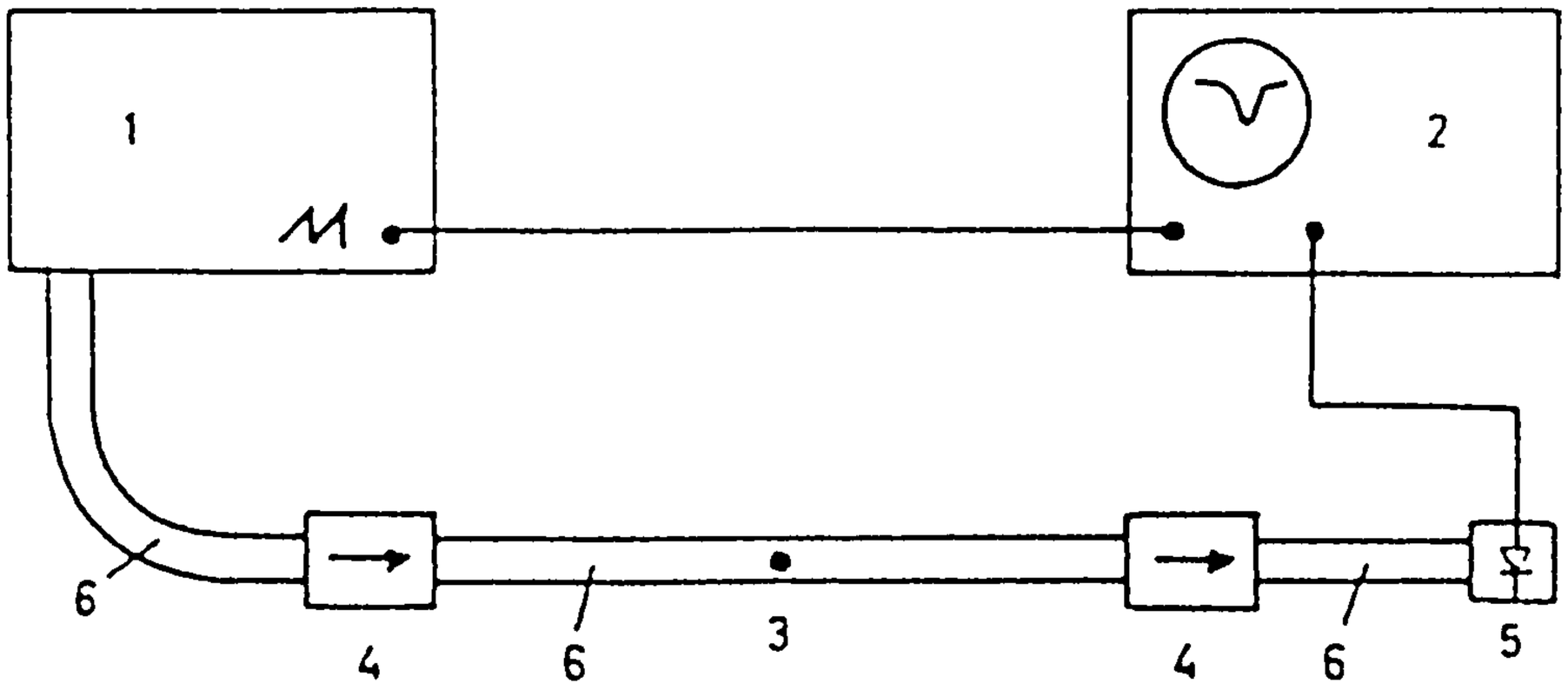

Fig. 10. Recording at the X band of the dimensional resonances of a dielectric sphere, 3.9mm in diameter, ε=86.

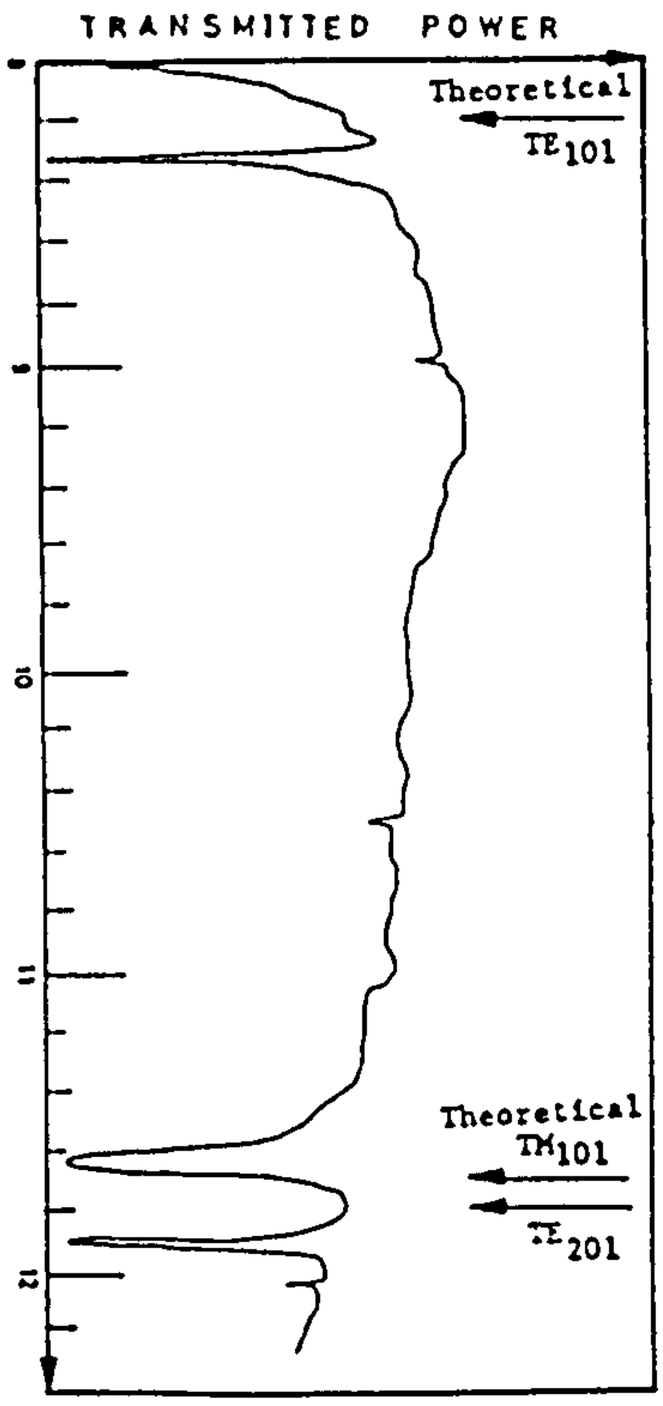

Fig. 11. Recording at the Ku band of the dimensional resonances of a dielectric sphere, 4mm in diameter, ε=86.

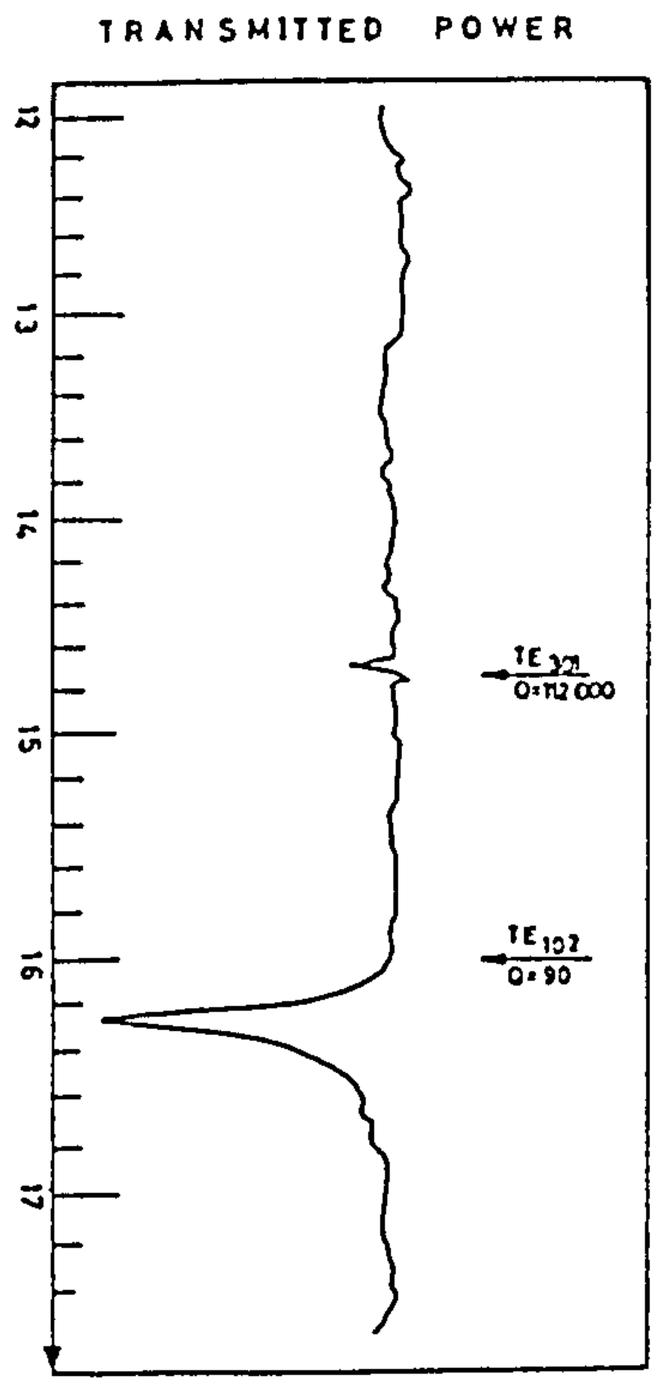

In the following, we will show that the excitation of the modes of free oscillations of the spherical ice particles are responsible for the resonances observed in the scattering curves. Whenever the frequency of the externally applied field approaches a characteristic frequency

of the free oscillations, resonance phenomena will occur.

3.4.1 Modes of free oscillations of a sphere.

Let us suppose that a sphere with radius a and complex index of refraction m is placed in an infinite homogeneous medium, free space in this case. Charge is displaced from the equilibrium distribution on the surface of the sphere and then released. The resulting oscillations of charge are accompanied by oscillations of the surrounding field, which can be represented as a superposition of characteristic wave functions [Stratton 1941a]

$$E=-\sum_{n=1}^{\infty}(a^{e}_{omn}M^{e}_{omn}+b^{e}_{omn}N^{e}_{omn}) ,$$

$$H=-\frac{k}{i\omega\mu}\sum_{n=1}^{\infty}(a^{e}_{omn}N^{e}_{omn}+b^{e}_{omn}M^{e}_{omn}) .$$

The functions may be odd or even, while m and n represent the number of nodes with respect to the spherical angles ϕ and θ. The coefficients a_n and b_n represent the amplitudes of the oscillations of magnetic and electric type, respectively. These oscillations are also known as transverse magnetic modes (TM), or transverse electric modes (TE).

3.4.2 TM modes.

Let us consider an oscillation of magnetic type:

$$E=-(A_{emn}M_{emn}+A_{omn}M_{omn}),$$

$$H=-\frac{k}{i\omega\mu}(A_{emn}N_{emn}+A_{omn}N_{omn}) .$$

Solving Maxwell's equations in a system of spherical coordinates under the restriction that the field is finite at the origin and regular at infinity, we have for r<a (inside the sphere) according to Stratton [1941b]

$$E_r^i=0,$$

$$E_\theta^i=-\frac{1}{\sin\theta}\frac{\partial Y_{mn}^i}{\partial\phi}j_n(k_s r)e^{-i\omega t},$$

$$E_\phi^i=\frac{\partial Y_{mn}^i}{\partial\theta}j_n(k_s r)e^{-i\omega t}$$

$$H_r^i=-\frac{n(n+1)}{i\omega\mu_s}Y_{mn}^i\frac{1}{r}j_n(k_s r)e^{-i\omega t},$$

$$H_\theta^i=-\frac{1}{i\omega\mu_s}\frac{\partial Y_{mn}^i}{\partial\theta}\frac{1}{r}[k_s r j_n(k_s r)]'e^{-i\omega t},$$

$$H_\phi^i=-\frac{1}{i\omega\mu_s}\frac{1}{\sin\theta}\frac{\partial Y_{mn}^i}{\partial\phi}\frac{1}{r}[k_s r j_n(k_s r)]'e^{-i\omega t}\ ,$$

where Y_{mni} is the tesseral harmonic

$$Y_{mn}^e=(A_{emn}^e\cos m\phi+A_{omn}^e\sin m\phi)P_n^m(\cos\phi)\ ,$$

and the prime in denotes differentiation with respect to $k_s r$.

Outside the sphere, that is for r>a, the solutions are obtained in a similar manner by replacing Y_{mn}^i by Y_{mn}^e,k_s and μ_s by k_0 and μ_0, and $j_n(k_s r)$ by $h_n^{(2)}(k_0 r)$.

The continuity conditions on the separation surface of the sphere must be satisfied, so

$$E_\theta^i=E_\theta^e,\quad E_\phi^i=E_\phi^e,\quad H_\theta^i=H_\theta^e,\quad H_\phi^i=H_\phi^e\quad (r=a)\ ,$$

leading to a characteristic equation which is both complex and transcendental

$$\frac{[mxj_n(mx)]'}{\mu j_n(mx)}=\frac{[xh_n^{(2)}(x)]'}{\mu_0 h_n^{(2)}(x)}\ ,$$

where $x=k_0 a$ denotes the size parameter. The roots of this equation belong to a discrete set of characteristic values x_{ns} which result to a set of natural frequencies, or TM modes of oscillation.

3.4.3 TE modes.

These modes of oscillation are quite independent of the magnetic modes, but the fields and the natural frequencies are determined in exactly the same manner. We now have

$$E=-(B_{emn}N_{emn}+B_{omn}N_{omn}),$$

$$H=-\frac{k}{i\omega\mu}(B_{emn}M_{emn}+B_{omn}M_{omn}) \ ,$$

with appropriate expressions for the fields inside and outside the sphere. Finally the continuity of the tangential components of the fields at the separation surface lead to the transcendental equation

$$\frac{[mxj_n(mx)]'}{m^2 j_n(mx)}=\frac{\mu_0[xh_n^{(2)}(x)]'}{\mu_s h_n^{(2)}(x)} \ ,$$

which is also satisfied only by a discrete set of characteristic values, resulting to a set of natural frequencies, or TE modes of oscillation.

3.4.4 Solution of the transcendental equations.

The former transcendental equations can not be solved analytically and therefore numerical analysis methods have to be employed in order to determine the complex roots. An algorithm based on the NAG supplied C05NCF routine [Numerical Algorithms Group Ltd. 1988] was designed, to solve numerically these equations (see appendix B). This routine chooses the correction at each step as a convex combination of the Newton and scaled gradient directions. It converges rapidly and guarantees very accurate results even if the starting points lie far from the solution.

3.4.5 Solutions for ice particles.

For each integer order of the transcendental equation there is a corresponding discrete set of roots. Figures 12 and 13 illustrate the real and imaginary parts of the first three complex roots of the transcendental equations which result to various TM and TE modes of oscillation. The index of refraction of ice m= 1.775-6.574×10^{-4}i has been calculated at 30 GHz and -10° C using Hufford's model [1987].

Of particular interest are the roots with very small imaginary parts, since these give rise to the resonance peaks. Whenever the real frequency of an externally applied field approaches the real part of a complex natural mode, the sphere removes the incident energy more efficiently. This energy may be either scattered and/or absorbed by the material depending on the index of refraction. In order to accurately resolve the local maxima, Mie calculations both for forward and back scattering cases have been performed (see figure 1), with a very fine

Fig. 12. Real parts of the electric (TE) and magnetic (TM) modes of free oscillations of ice particles.

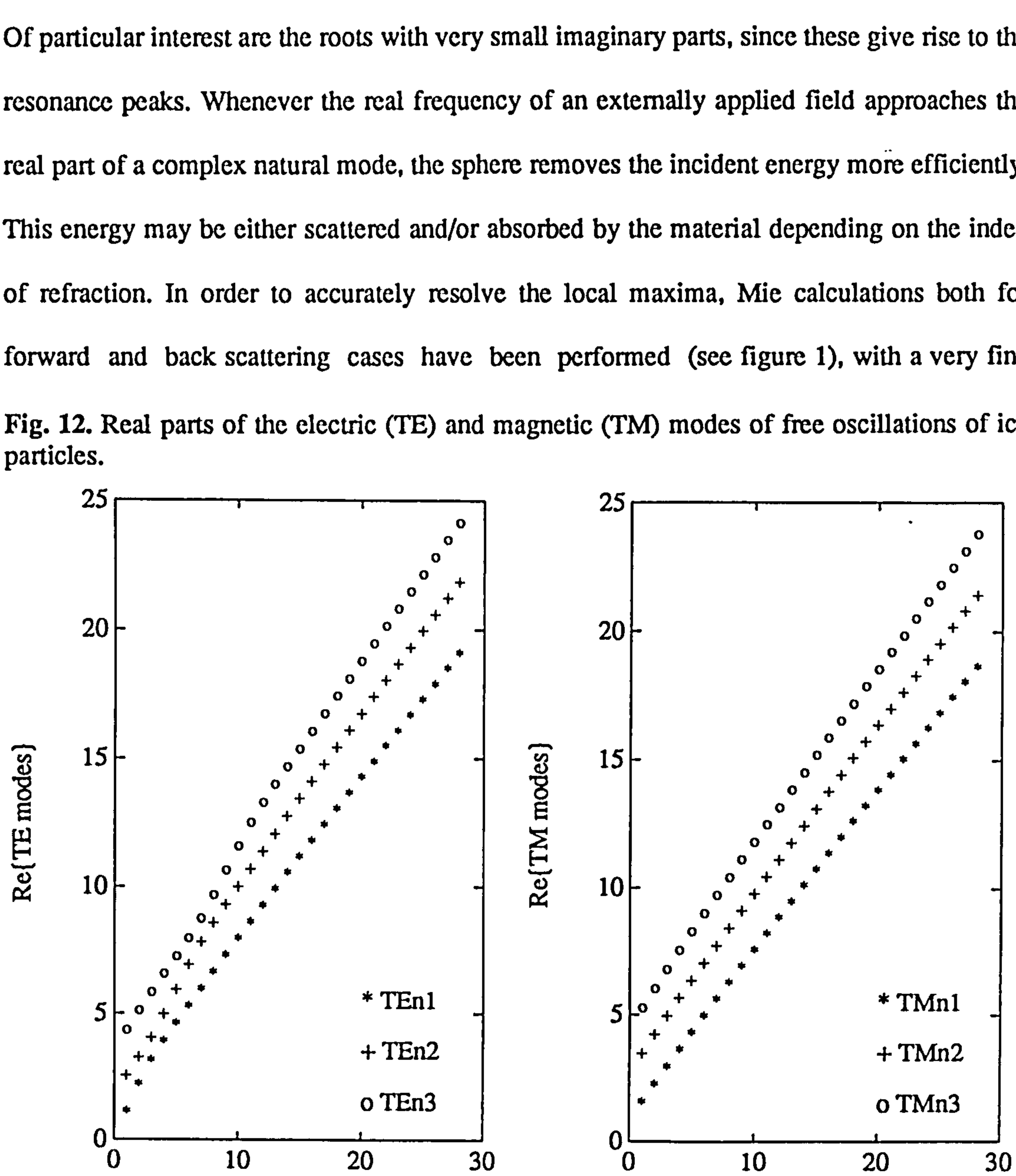

Fig. 13. Imaginary parts of the electric (TE) and magnetic (TM) modes of free oscillations of ice particles.

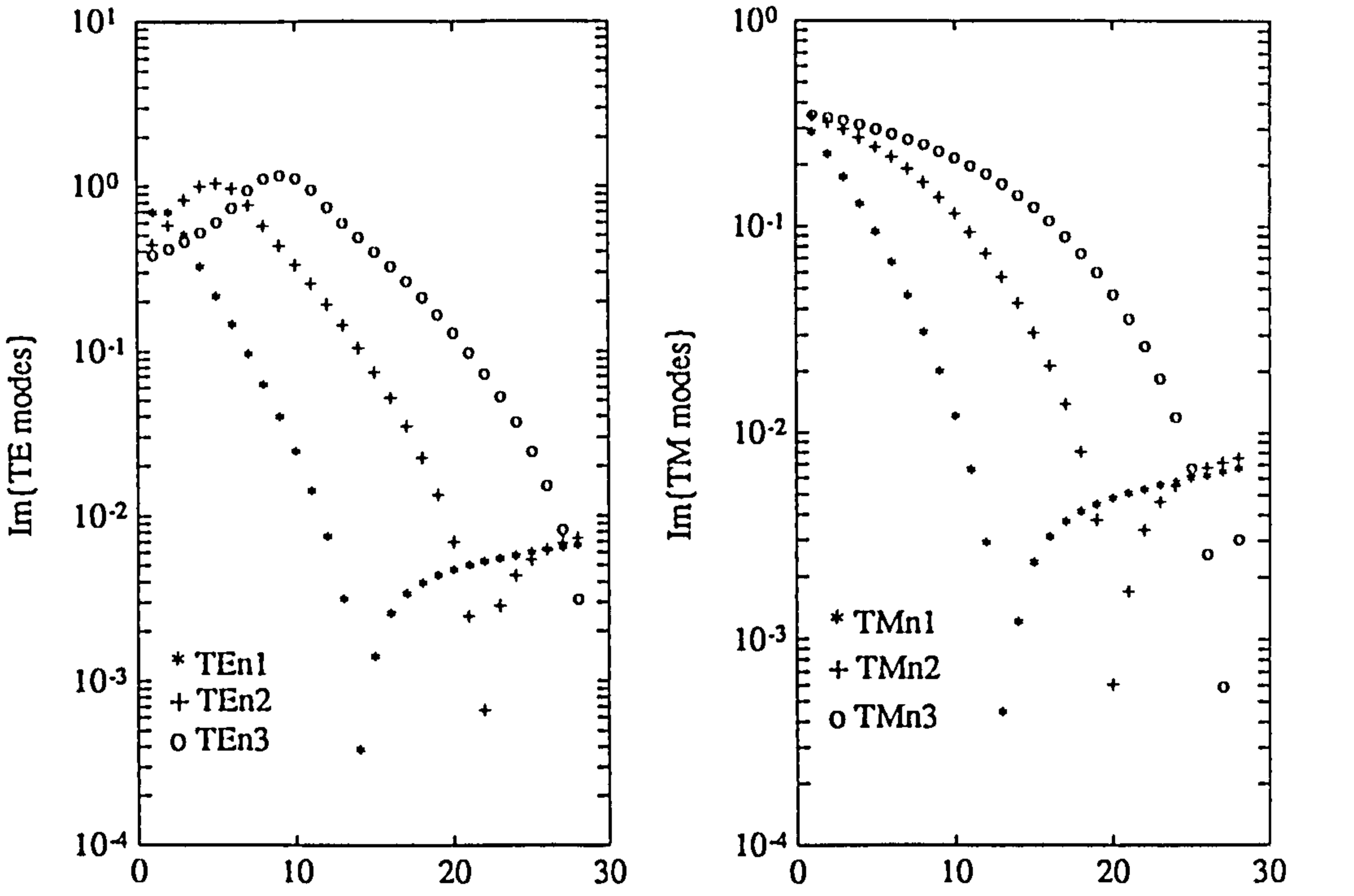

Fig. 14. Detailed view of the extinction cross section and radar cross section of ice spheres (extinction cross sections exaggerated 5 times for comparison purposes).

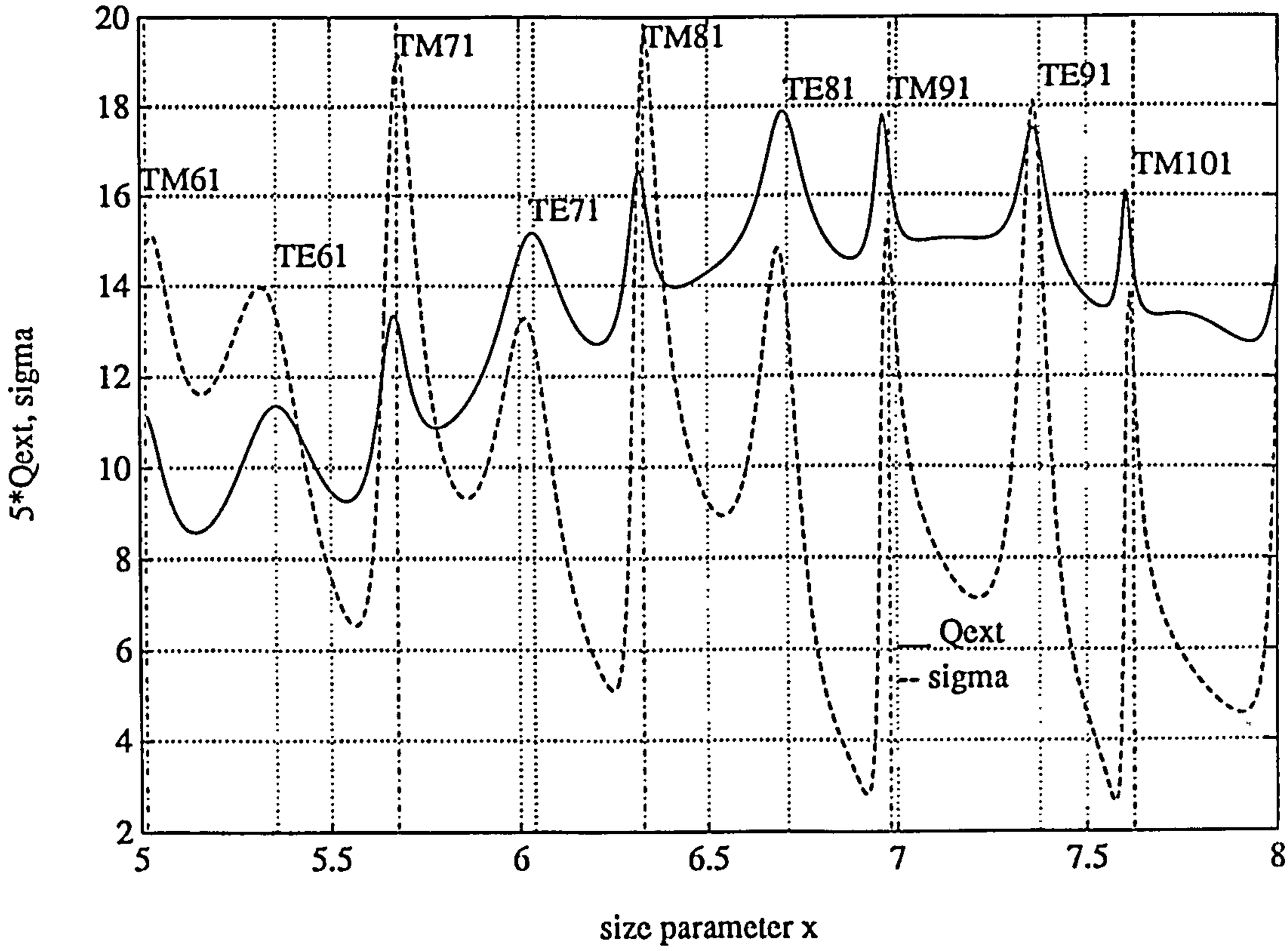

Table II. Maxima in the Mie scattering calculations for the forward and backward scattering cases and responsible mode of free oscillations.

Mie maxima θ=0°	Mie maxima θ=180°	Re{egf}	TM mode	Mie maxima θ=0°	Mie maxima θ=180°	Re{egf}	TE mode
3.036	3.007	2.993	3 1	4.638	4.664		5 1
3.693	3.724	3.673	4 1	5.369	5.325	5.357	6 1
4.359	4.441	4.347	5 1	6.048	6.026	6.039	7 1
5.024	5.043	5.015	6 1	6.714	6.701	6.712	8 1
5.682	5.639	5.676	7 1	7.375	7.375	7.376	9 1
6.334	6.348	6.330	8 1	8.031	8.037	8.032	10 1
6.981	6.995	6.981	9 1	8.680	8.686	8.680	11 1
7.625	7.634	7.624	10 1	9.322	9.327	9.322	12 1
8.263	8.271	8.263	11 1	9.958	9.963	9.958	13 1
8.448		8.401	8 2	10.590	10.595	10.589	14 1
8.897	8.906	8.897	12 1	10.706		10.675	11 2
9.141	9.075	9.078	9 2	11.216	11.220	11.216	15 1
9.527	9.536	9.527	13 1	11.352		11.364	12 2
9.816	9.792	9.752	10 2	11.839	11.842	11.839	16 1
10.153	10.160	10.153	14 1	12.458		12.459	17 1
10.462	10.475	10.422	11 2	12.726	12.668	12.733	14 2
10.775	10.784	10.776	15 1	13.077	13.108	13.076	18 1
11.109	11.121	11.091	12 2	13.412	13.401	13.411	15 2
11.395	11.404	11.395	16 1		13.693	13.691	19 1
11.765	11.784	11.757	13 2	14.086	14.090	14.084	16 2
12.013	12.019	12.013	17 1		14.305	14.303	20 1
12.425	12.462	12.420	14 2	14.753	14.760	14.753	17 2
12.628	12.635	12.627	18 1	14.913	14.917	14.914	21 1
13.241	13.248	13.240	19 1				
13.740	13.759	13.738	16 2				
	13.855	13.851	20 1				
14.393	14.414	14.392	17 2				
15.044	15.073	15.068	22 1				

resolution. The increment step for the size parameter is 6.28E-4. Table II shows the values of the size parameter x for which the local maxima occur for both forward and backward scattering cases and the corresponding size parameter of oscillation. It also clearly indicates that the real parts of the modes of free oscillations lie very close to the observed Mie local maxima, suggesting their responsibility for the numerous fluctuations observed in the scattering of ice particles. A graphical display over the size range x=5 to x=8 may be also seen in figure 14, where both back (dashed line) and forward (continuous line) scattering efficiency factors along with the relevant TE and TM modes of free oscillations have been plotted. (The forward scattering efficiency factors have been exaggerated by 5 times for the sake of better observation.) Further graphical illustrations over the size parameter range x=8 to x=10 have been given by Papatsoris and Watson [1992a].

3.5 Conclusions.

A periodic external field incident upon a sphere gives rise to a forced oscillation of free and bound charges, synchronous with the applied field. This leads to the excitation of a secondary field both inside and outside the sphere, which has to be vectorially added to the primary field in order to determine the total resultant field. The continuity of the tangential components of the fields at the separation surface lead to a transient term constructed from the natural modes of oscillation with suitable amplitudes. If the frequency of the applied field lies very close to an eigenfrequency or mode of free oscillation of the material body of the sphere, resonance phenomena will occur. Whether these oscillations will be damped or increased, depends on the index of refraction of the material and the scattering direction. Here we must note that even for a dielectric sphere the eigenfrequencies are always complex, whereas the frequency of the applied field is real, so the case of infinite amplitudes can be safely avoided. For ice, which is almost a pure dielectric the excited oscillations are not significantly damped, giving rise to numerous fluctuations. Such oscillations therefore are responsible for the numerous

peaks observed when ice scattering cross sections versus size parameter are plotted.

Finally we conclude this chapter by saying that the same physical mechanism could be easily extended to explain the presence of similar resonance phenomena in the scattering of dielectric bodies of other shapes, ie. cylinders or ellipsoids.

CHAPTER 4

EXTINCTION AND BACKSCATTERING PROPERTIES OF CLOUDS AT MILLIMETRE WAVELENGTHS.

4.1 Introduction.

Suspended ensembles of water and ice particulates affect the propagation of millimetre waves in the earth's atmosphere. As a consequence, the characteristics of a transmitted signal suffer a degradation which may be thought as favourable or unfavourable according to the application context within it is considered. For example, the presence of clouds between a satellite transmitter and a ground based receiver would result in loss of power and distortion of the characteristics of the originally transmitted signal. In this case, the effect of clouds is clearly undesirable. On the other hand, meteorologists and atmospheric physicists may use favourably the degradation that the back scattered signal suffers. The back scattered signal can be monitored by ground or space based instruments and then analyzed to provide information about the spatial structure and other characteristics of the illuminated sample.

So, the scattering properties of clouds at millimetre wavelengths are subjects of significant importance to the systems designer of earth-satellite links, the meteorologist, the atmospheric physicist and lately to all those environmentally conscious. In this chapter, we will assess the impact of non-precipitable clouds on millimetre wave propagation. In doing so, a description of the spatial structure and the physical properties of various cloud types is needed.

4.2 Spatial structure of clouds.

4.2.1 Cloud frequencies.

Frequencies of total cloud cover, lower-level clouds and clouds of vertical extent over continents and oceans can be found in climatic handbooks and atlases [Valley 1965, Visher 1966, Agafonova 1970, Dubrovina 1975]. Most of the compiled data though, were obtained from observations on the ground, so information about the frequencies of clouds in the middle

and upper levels are practically non-existent. Only by incorporating the results from aircraft sounding it is possible to estimate the frequencies of clouds in the middle and the upper levels [Zak 1962, Dubrovina 1975]. For large regions the total cloud cover and the amount of any cloud present can be estimated with the aid of satellite measurements [Dubrovina 1975]. The cloud frequency is closely related to the general circulation of the atmosphere, the nature of the underlying surface and the isolation. In addition, the cloud frequency is affected by site elevation, orography and other factors. The global distribution of the cloud frequency can be divided into four climatic zones: a polar zone from 70° to 90° latitude; a temperate zone from 30° to 70°; a tropical zone from 10° to 30° , and an equatorial zone from 0° to 10° latitude.

Fig. 1. Latitude dependence of cloud frequency along the 20° W meridian for month January (after Lobanova [1968]).

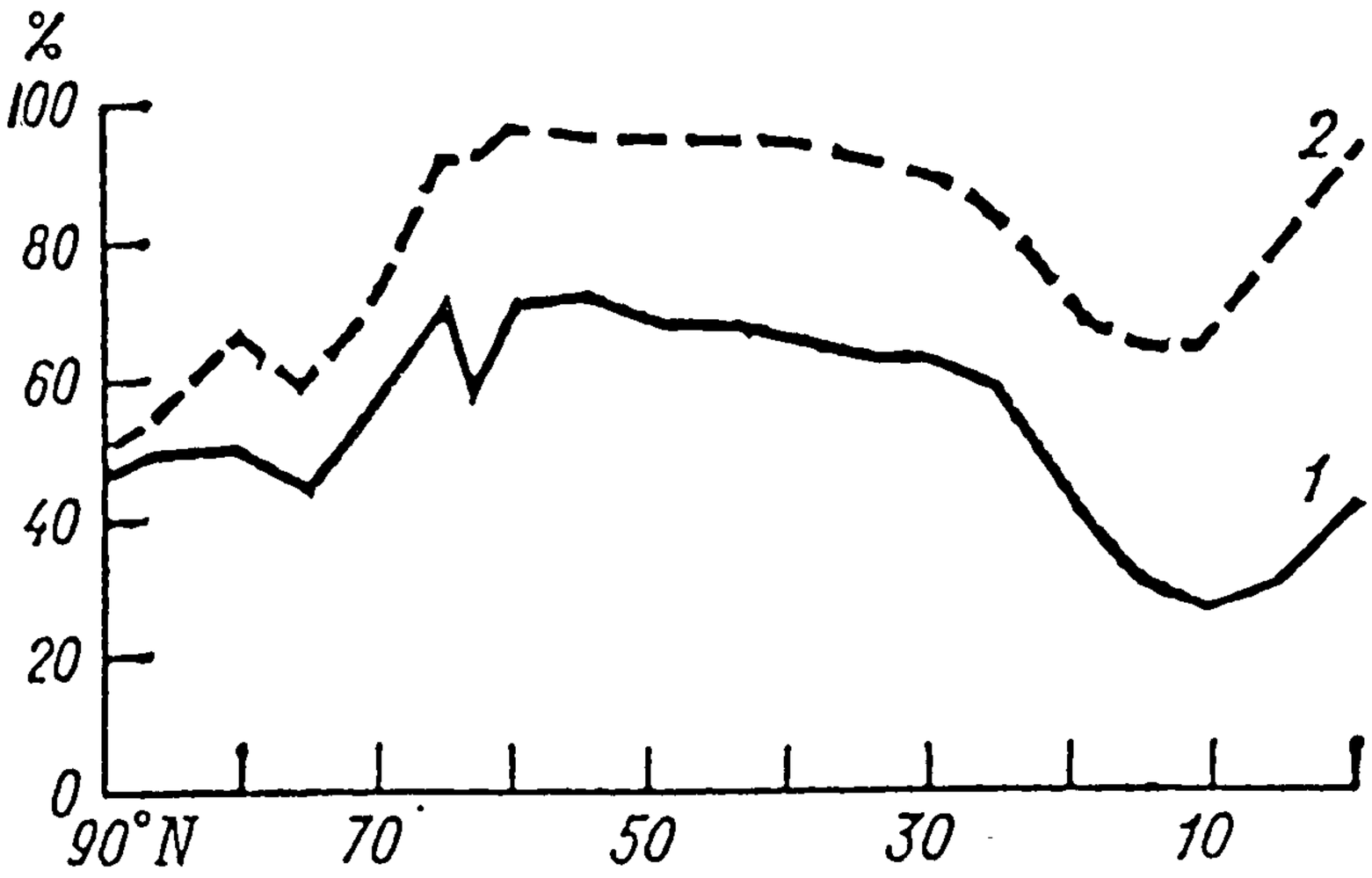

These zones are clearly distinguishable in figure 1, where the latitude dependence of cloud frequencies along the 20° W meridian for the month January is illustrated. The solid line in figure 1 gives the frequency of overcast skies (cloud cover 8-10). The dashed line gives the total frequency of overcast and partly cloudy skies (cloud cover 3-7). The region above the dashed curve characterizes frequency of clear skies (cloud cover 0-2).

Cloud frequency is also dependent upon season. In summer there is a northward shift in the zone boundaries, because the circulation conditions vary and the underlying surface becomes

moistened. In the polar zone there is a sharp increase in both the total cloudiness and the low-lying cloudiness. The southern part of the temperate zone moves downward under the influence of subtropical anticyclones and accordingly the amount of cloud cover is sharply reduced. The intertropical convergence zone shifts northward, increasing the area of the equatorial zone. Consequently, in summer in the northern hemisphere three large zones are discernible in the distribution of the cloudiness frequency: a polar zone combined with a temperate zone, a tropical zone and an equatorial zone.

Furthermore, tendency can be detected in the relative variation of the frequencies of certain cloud families. As we approach the equator the relative frequency of cumuliform to stratiform clouds increases (see figure 2).

Fig. 2. Ratio of frequency of cumuliform (n_c) to stratiform (n_s) cloudiness along the 20° W meridian for month January (after Lobanova [1968]).

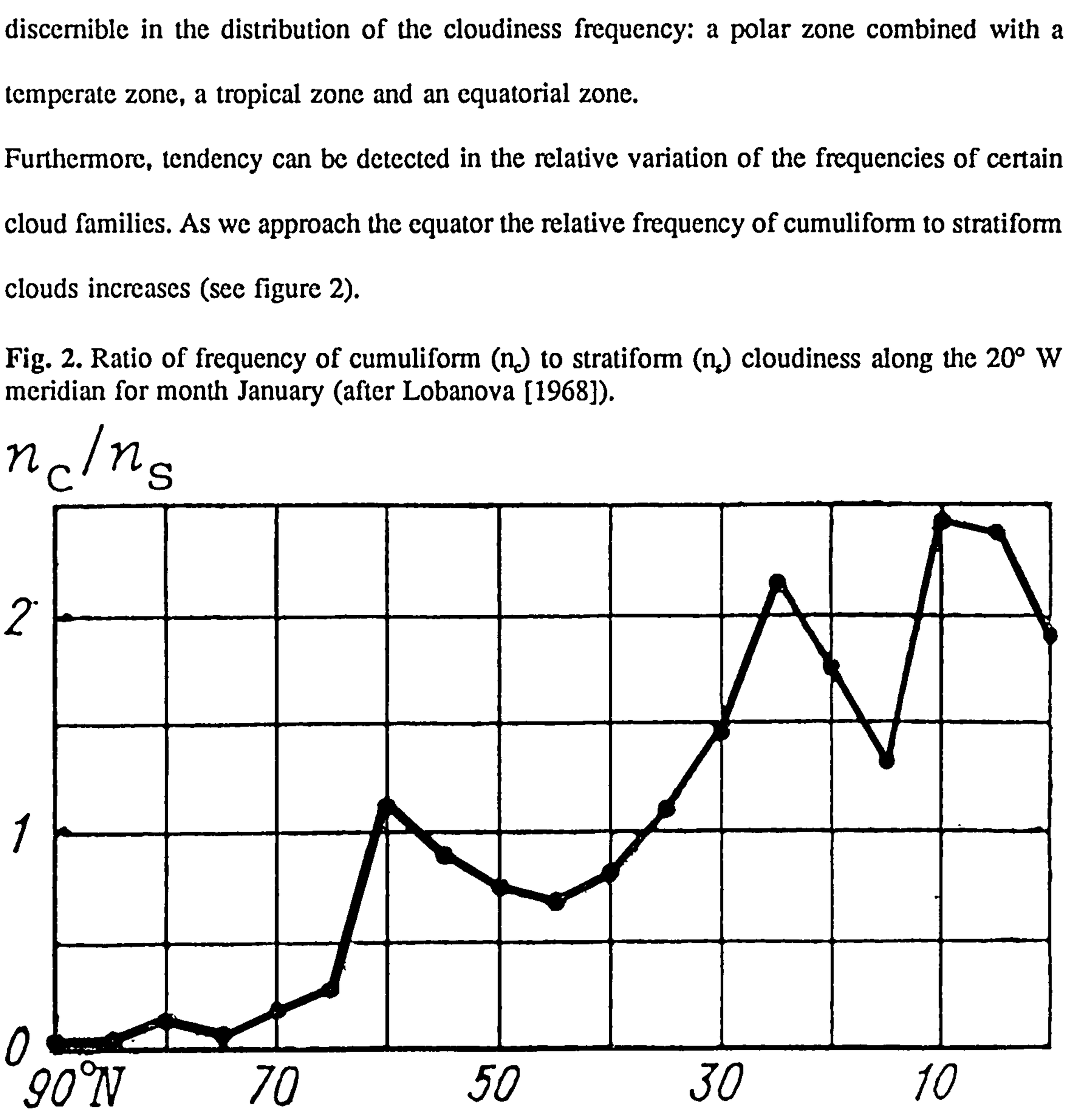

4.2.2 Stratiform clouds.

Stratiform clouds are defined as clouds whose horizontal extent is orders of magnitude greater

than their vertical extent. These include: stratus (St), stratocumulus (Sc), nimbostratus (Ns), altocumulus (Ac), altostratus (As) and cirrostratus (Cs), as well as Ns-As, As-Cs and Ns-As-Cs frontal cloud systems.

Stratiform clouds can stretch over huge areas. Satellite photographs of clouds have revealed that fields of solid cloud cover can in the northern hemisphere encompass areas as great as about 50 million km^2 [Dubrovina 1975]. The mean area of solid cloud cover fluctuates from 5 to 15 million km^2. The mean and also the maximum areas of the cloudless space in these same regions are about twice as large. In extra tropical latitudes the cyclonic activity and the frontal cloud systems associated with it, are one of the main factors influencing the frequency of stratiform clouds and their horizontal extent. Satellite photographs [Gottwald 1976] show that the width of a frontal zone in central Europe can be as great as 1000 km and the length 7000 km.

4.2.2.1 Height distribution of stratiform clouds.

Table I shows the predominant heights of the lower, middle and upper cloud levels for the various geographical zones.

Table I. Heights of stratiform cloud levels (from Feigelson [1984]).

Level	Zone		
	Polar	Temperate	Tropical
Lower	<2	<2	<3
Middle	2 ... 4	2 ... 7	3 ... 8
Upper	3 ... 8	5 ... 13	7 ... 18

The height of the lower boundary of stratiform clouds in summer is generally greater than in winter [Khrgian 1977]. However, in some regions, such as the maritime territory the lower boundary becomes lower in summer because of the arrival of moist air from the sea. The

height of the lower boundary of stratiform clouds is also dependent upon latitude. On the average the cloud base of stratiform clouds increases from north to south [Borovikov 1963]. Meridional and diurnal variations in clouds base related to the conditions of the atmospheric circulation are also expected.

4.2.3 Clouds of vertical extent.

Clouds with considerable vertical extent include convective clouds of various depths: cumulus of various types (ie. Cu-hum, Cu-med, Cu-cong) and cumulonimbus (Cb). The depth of these clouds decreases in winter and increases in summer. They also become 1-2 km deeper upon transition from temperate to tropical latitudes. Typical cloud depths for cumuliform clouds at middle latitudes are given in table II.

Table II. Typical depths of cumuliform clouds (from Feigelson [1984]).

Cloud type	Depth [km]
Cu-hum.	1
Cu-med.	1 ... 2
Cu-cong.	2 ... 3.5
Cb	3 ... 4 (or more)

4.3 Physical characteristics of clouds.

4.3.1 Temperature and phase.

Cloud temperatures usually differ from the temperature of the surrounding air by some tenths of a degree. Only in the case of dense cumuli can this difference be more than a degree. On the whole, convective clouds tend to heat up the surrounding atmosphere somewhat. Within the cloud mass itself, the temperature fluctuations may be considerable, up to 3° C. On the average, these clouds stay a little cooler than the ambient air [Dubrovina 1968]. Inside the

clouds the temperature gradients are typically close to moist-adiabatic.

Many physical characteristics of clouds, in particular the cloud phase make-up and water content are temperature dependent. This dependence is the dominant factor in determining the seasonal and latitudal variation of the physical parameters of clouds. Consequently, once we know the mean atmospheric temperatures, we can deduce information about the characteristics of certain cloud types. Mean temperatures as a function of latitude for the northern hemisphere are given by Baravov [1960]. At temperatures greater than 0° C clouds can naturally be assumed to be droplet clouds. At negative temperatures may be droplet, crystal or mixed phase clouds. The proportion of drops and crystals in a mixed cloud generally varies in time and from place to place. Individual parts of the cloud may consist wholly of droplets or only of crystals, while droplets and crystals coexist in other regions. However, experimental data on the proportions of droplets and crystals in various cloud types are practically non-existent. The

Fig. 3. The distribution of freezing temperatures of water drops of 1mm diameter containing foreign particles (after Mason [1971]).

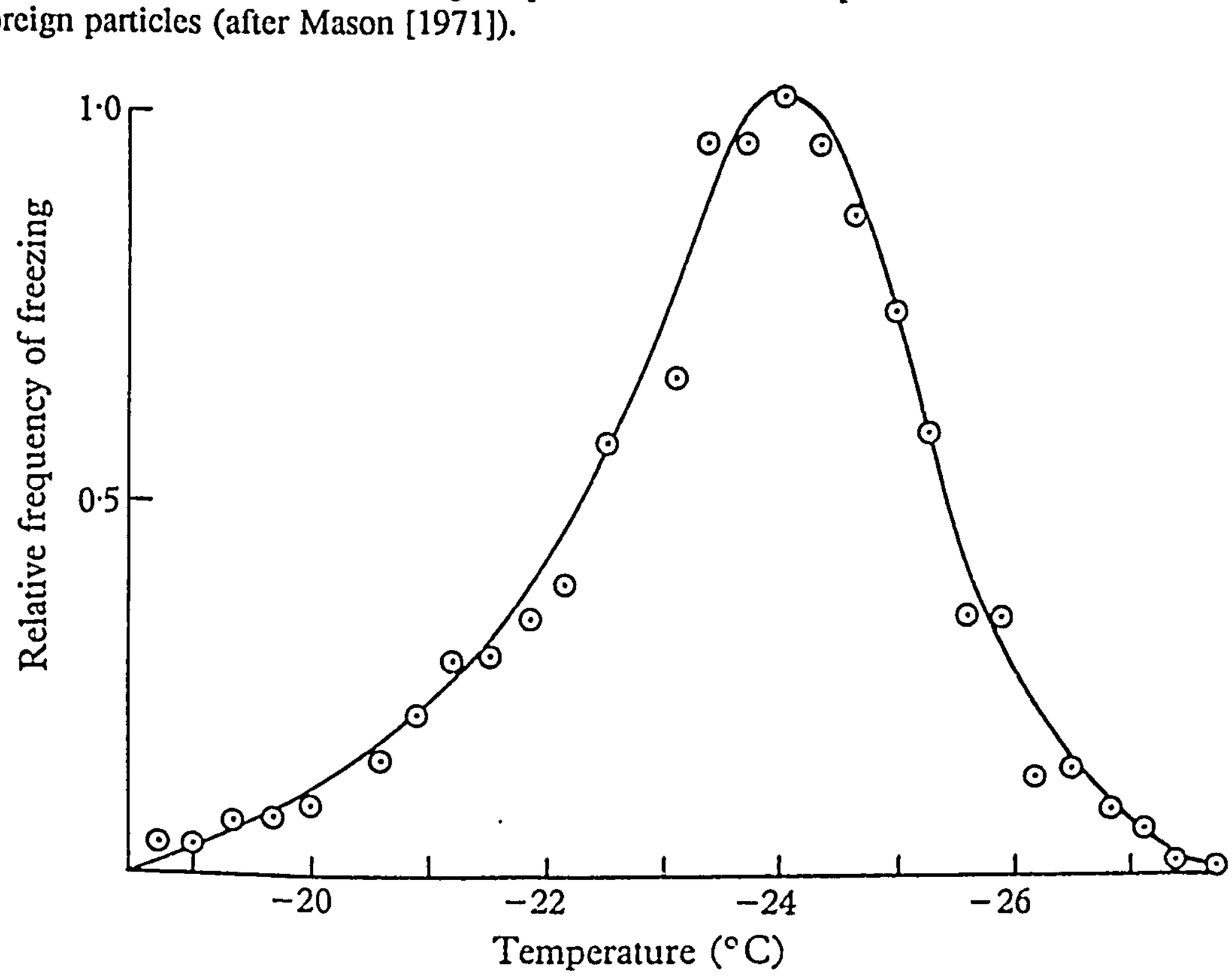

Fig. 4. The freezing temperatures of water samples as a function of their equivalent drop diameter (from Mason [1971]).

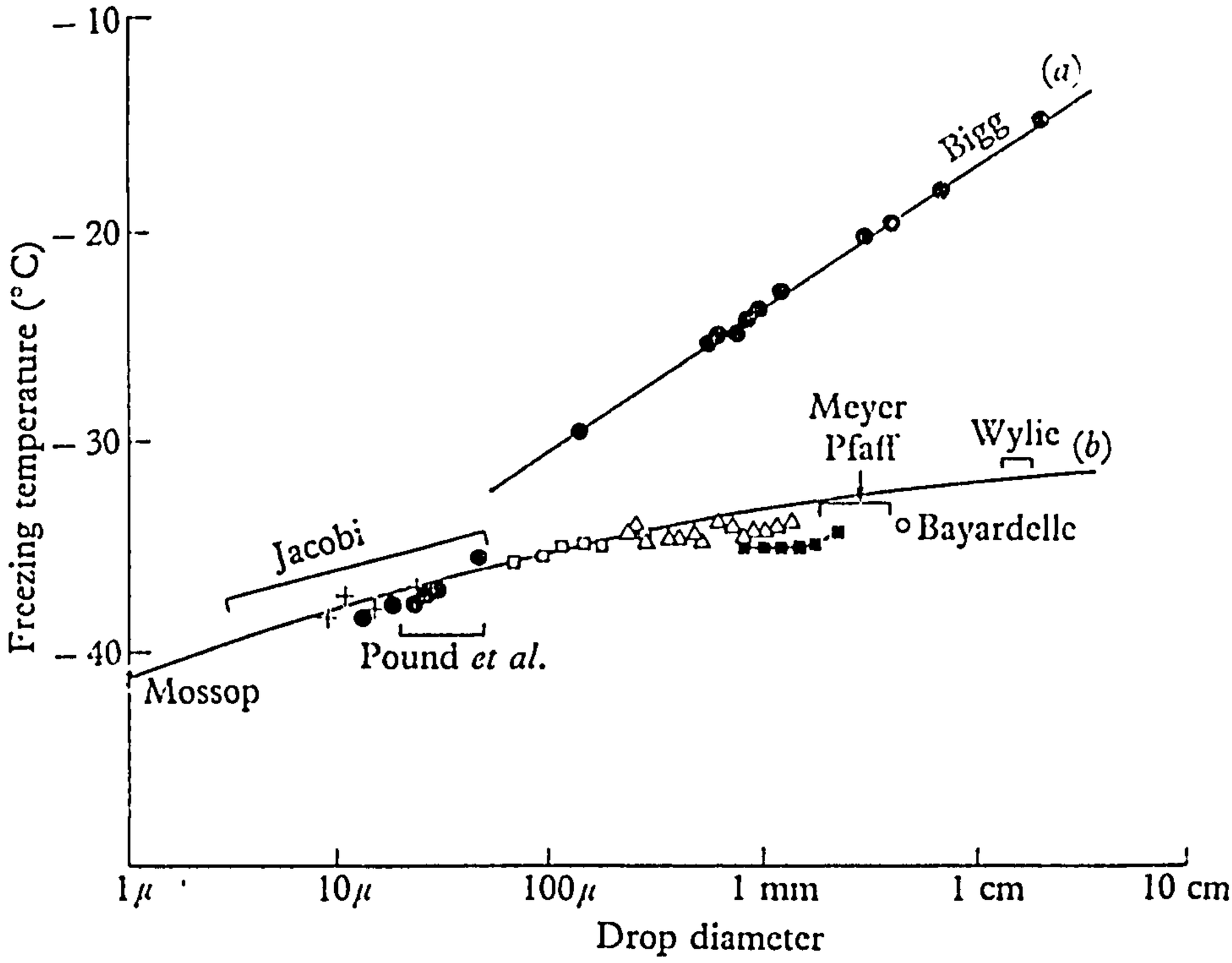

only definite thing is that the relative proportion of crystals increases as the temperature decreases. Mason [1971], has studied in detail the effect of temperature on the freezing of cloud droplets. The behaviour of the freezing temperature of droplets in clouds may be seen in figure 3, where the distribution of freezing temperatures of 1127 drops of 1mm diameter is depicted. Temperature is the main factor in determining the probability that supercooled droplets are present in a cloud.

The next most important factor is the size of the droplet. Figure 4 illustrates the median freezing temperatures of water droplets as a function of their equivalent drop diameter, as reported by different experimenters, [Mason 1971]. The smaller the droplets the more likely it is that unfrozen droplets will be present in the cloud at a given temperature. Finally, important roles also plays the seeding of lower-lying layers with crystals falling from higher layers at a lower temperature, as well as by the secondary multiplication of crystals.

Frequencies of occurrence of pure water, pure ice and mixed phase clouds have been reported

Fig. 5. Frequencies of phases in clouds of various types at a negative temperature (after Borovikov and Mazin [1975]).

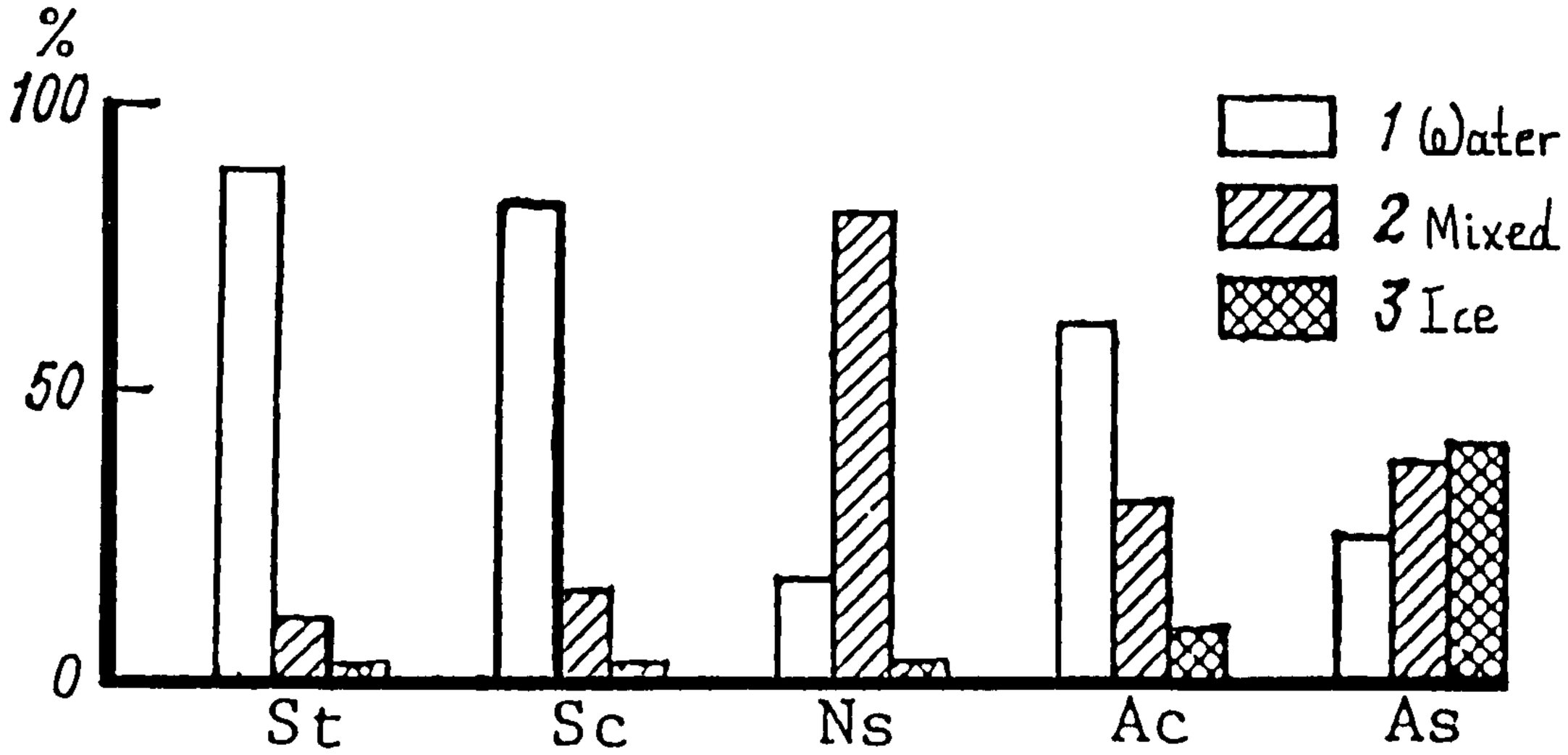

by Borovikov [1975]. Collecting data from regular aircraft sounding carried out over several years in the Soviet Union, he analyzed more than 41500 middle latitude clouds in all. The results are illustrated in figure 5. In these latitudes high-level clouds are almost always crystal clouds.

Table III, gives the mean frequencies of the various phases at various temperatures for clouds of all forms. These data are practically independent of the season of the year. The dependence of the phase on the cloud form is actually determined by the temperature regime of the clouds.

Table III. Frequencies of different phases of clouds as function of temperature over the Soviet Union. (after Feigelson [1984].)

Phase of cloud	Temperature (from - to), °C											
	0 -2	-4 -6	-8 -10	-12 -14	-16 -18	-20 -22	-24 -26	-28 -30	-32 -34	-36 -38	-40 -42	-44 -46
Droplet	84	69	54	37	23	17	10	6	3	2	1	0
Mixed	14	26	35	42	40	35	31	25	17	11	7	6
Crystal	2	5	11	21	37	48	59	69	80	87	92	94

4.3.2 Cloud water content.

The water content of a cloud is defined as the mass of water in the condensed state per unit cloud volume and is usually measured in g/m^3.

4.3.2.1 Water content of stratiform clouds.

Generally, for all types of stratiform clouds at middle latitudes the average water content as a function of temperature is given by the empirical relation [Borovikov and Mazin 1975]:

$$\omega_{av} = \omega_0 e^{(\epsilon/\omega_0)} \approx \omega_0 + \epsilon ,$$

where the parameters ω_0 and ε are temperature dependent. This temperature dependence is depicted in figure 6. The parameter ω_0 is also dependent on cloud type. Figure 7 gives the temperature dependence of ω_0 for stratiform clouds of various types. The lowest values of ω_0 correspond to Ac and As clouds and the highest to Ns clouds. The depths of stratiform clouds of types St and Sc do not exceed 500-600 m, and the mean water content increases with height right up to the cloud summit. For deeper clouds, beginning at a height of 600-700 m,

Fig. 6. Temperature dependence of water content for stratiform clouds (after Borovikov and Mazin [1975]).

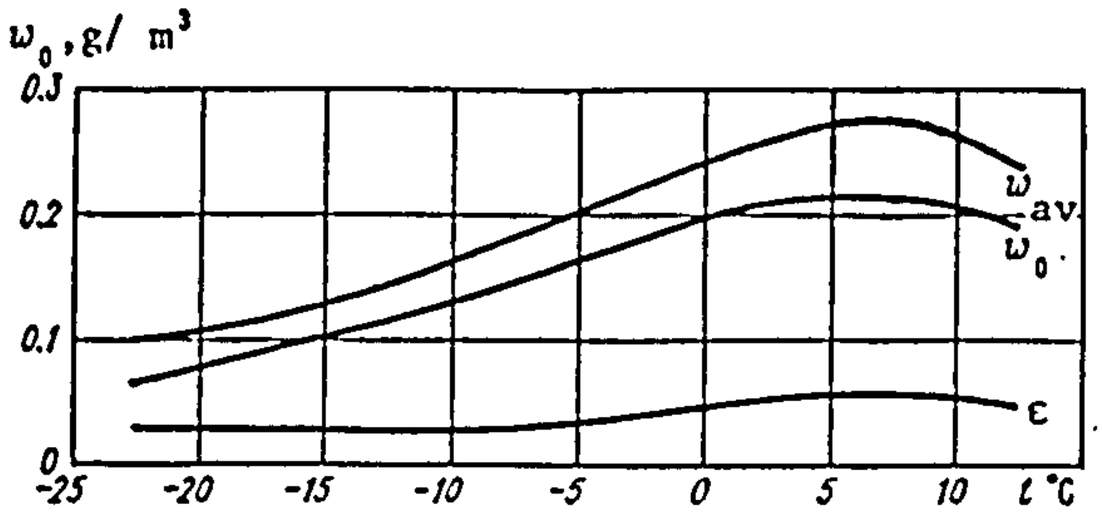

Fig. 7. Temperature dependence of ω_0 for various types of stratiform clouds (after Borovikov and Mazin [1975]).

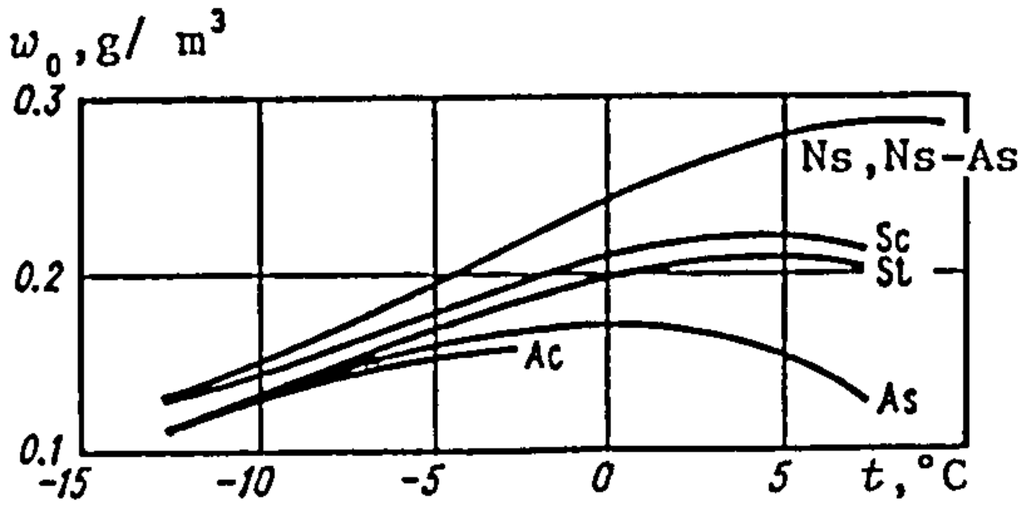

the mean water content gradually decreases. This is illustrated in figure 8. For Ns and Ns-As clouds, the mean water content of the droplet fraction of the clouds at first increases with height but then beginning at 200-300 m remains practically unchanged. In As clouds, the

Fig. 8. Average variation of water content with height in Stratiform clouds for different temperatures; 1) -10° to -5°C, 2)-5° to +5°C, 3) +5° to +10°C (after Feigelson [1984]).

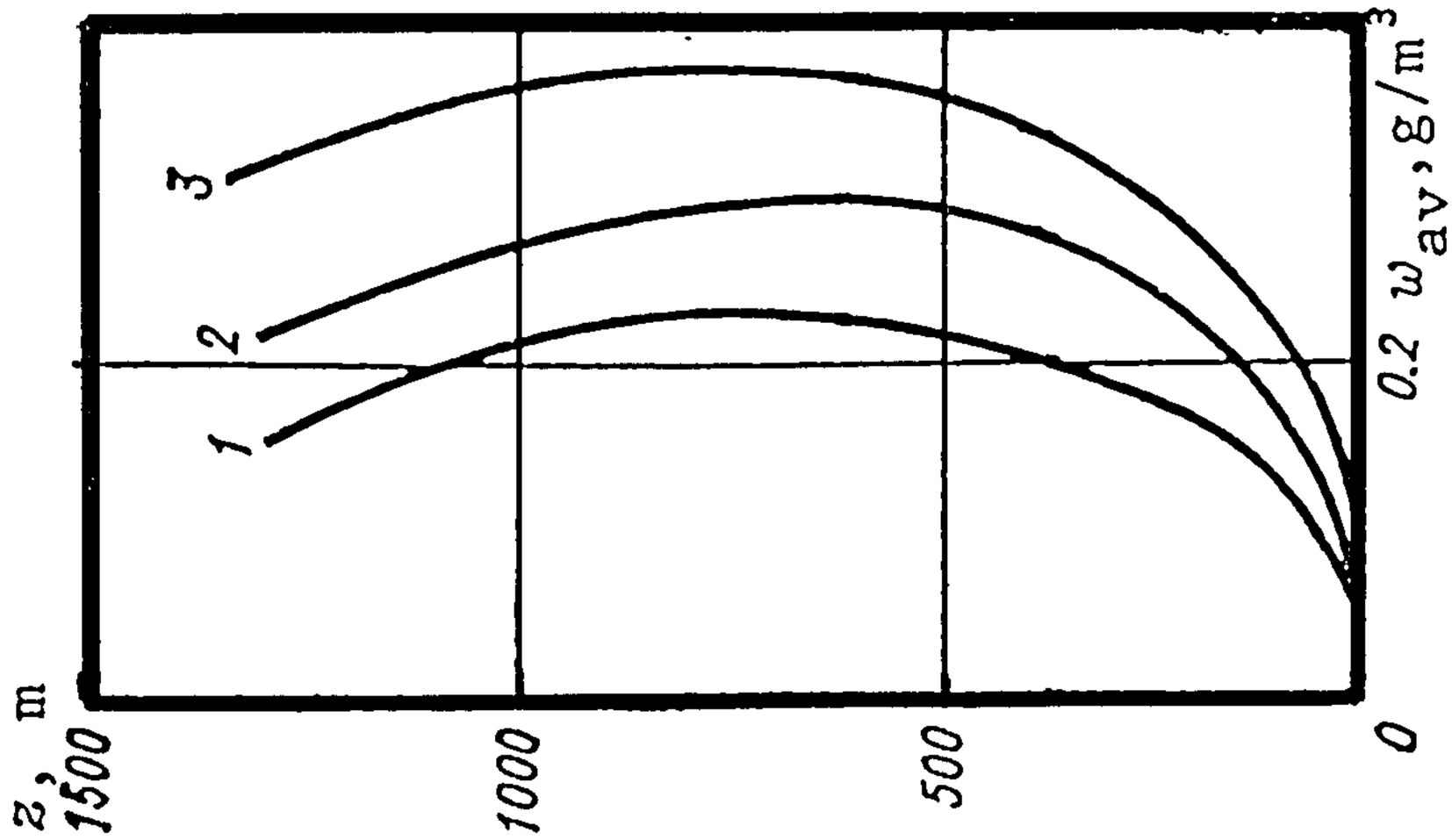

height variation of the droplet part of the water content is the same as in Ns, that is independent of height.

4.3.2.2 Water content of cumuliform clouds.

In vertically extensive clouds, the mean water content over the cloud section increases with the distance from the cloud base, reaching the highest value in the upper part of the cloud, usually at a height of about 80% of the total depth of the cloud. Figure 9 shows a typical water content distribution for a cloud 2 km deep, the variation of the adiabatic water content being plotted as well. The vertical variation of the water content with increasing height may be well described by the expression [Mazin 1983]:

$$\omega(h) = \omega_{max} \left(\frac{h}{h_0}\right)^m \left(\frac{H-h}{H-h_0}\right)^n ,$$

where h_0 is the relative altitude at which the maximum value of water content occurs ($\omega(h_0)=\omega_{max}$), H is the depth of cloud and m,n suitably specified constants depending upon season and geographical location. Generally, the mean water content is expected to vary considerably with geographical location. For example cumulus clouds may have a typical

mean water content from 0.5 to 1.0 g/m^3 at New England, whereas at Florida they may reach values as high as 4 g/m^3 [Falcone et al 1979].

Fig. 9. Typical distribution of the average water content in a typical cumuliform cloud (from Feigelson [1984]).

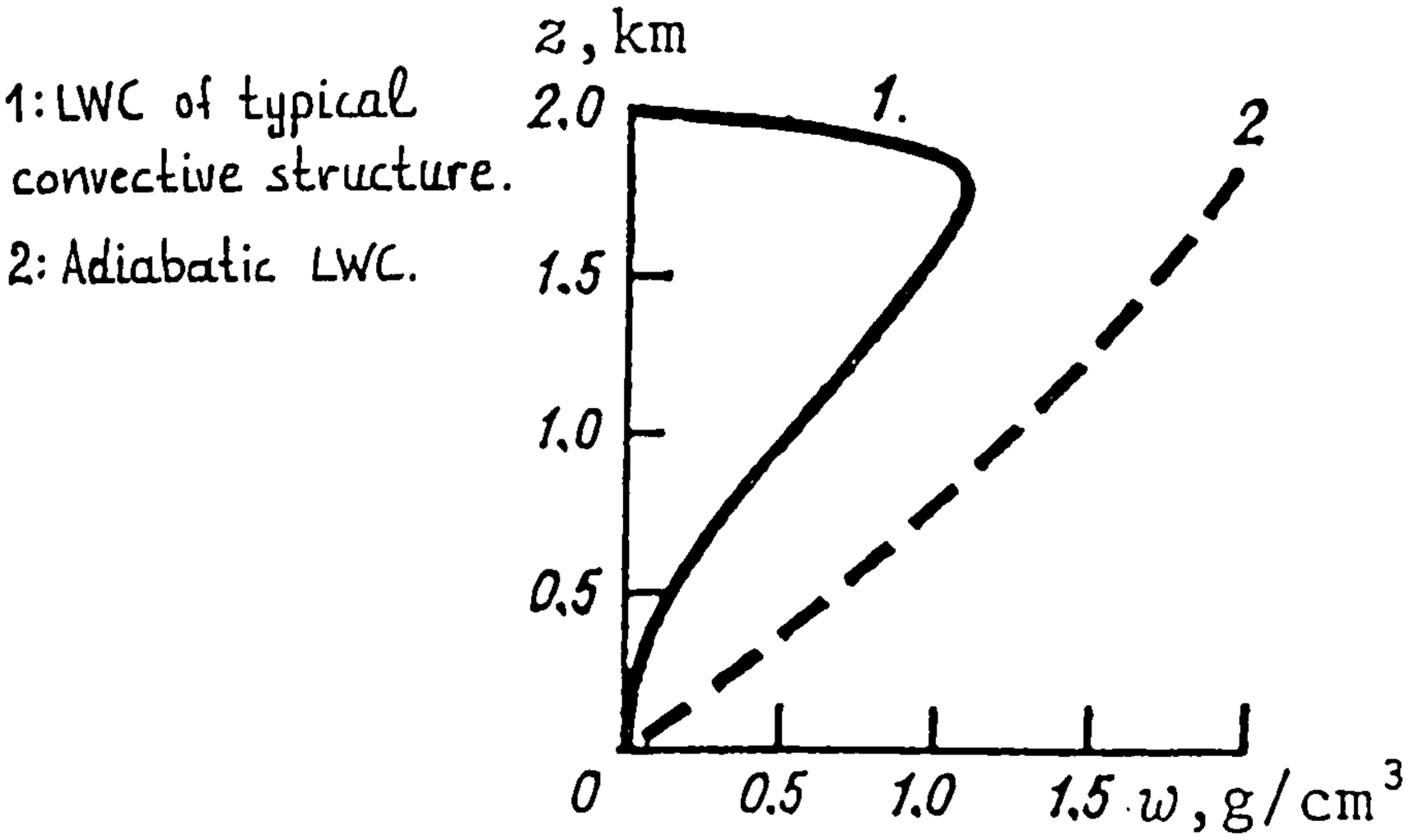

4.3.3 Concentrations and size distributions of water droplets in clouds.

The radii of most cloud droplets range from a few micrometers to some tens of micrometers. The concentration varies from tens to thousands per cubic centimetre. The concentration of large drops (radii greater than 100 μm) is usually 0.1 to 10 per litre. In the presence of precipitation the rain droplet concentration (radii greater than 100-200 μm) may reach 10 to 100 per litre.

The concentration and size of cloud droplets can vary greatly but if we consider averages over large volumes of cloud and over many cases, then definite regularities appear. Generally, the size spectra of water droplets in a cloud of any type have the form shown in figure 10.

The portion of the spectrum with radii less than r_{min} are very small water coated condensation nuclei which take the form of tiny droplets about 1 μm or less in radius and are in equilibrium with the cloud material. This portion of the cloud spectrum ranging from r=0.1 μm to r_{min} can be well approximated by an exponential relation [Aleksandrov and Yudin 1979]:

$$n_S(r) = A\left(\frac{r_0}{r}\right)^{\nu},$$

where usually r_0=1μm and A is a suitably specified constant depending upon cloud type and relative position within the cloud.

Fig. 10. Typical density of droplet size distribution (from Feigelson [1984]).

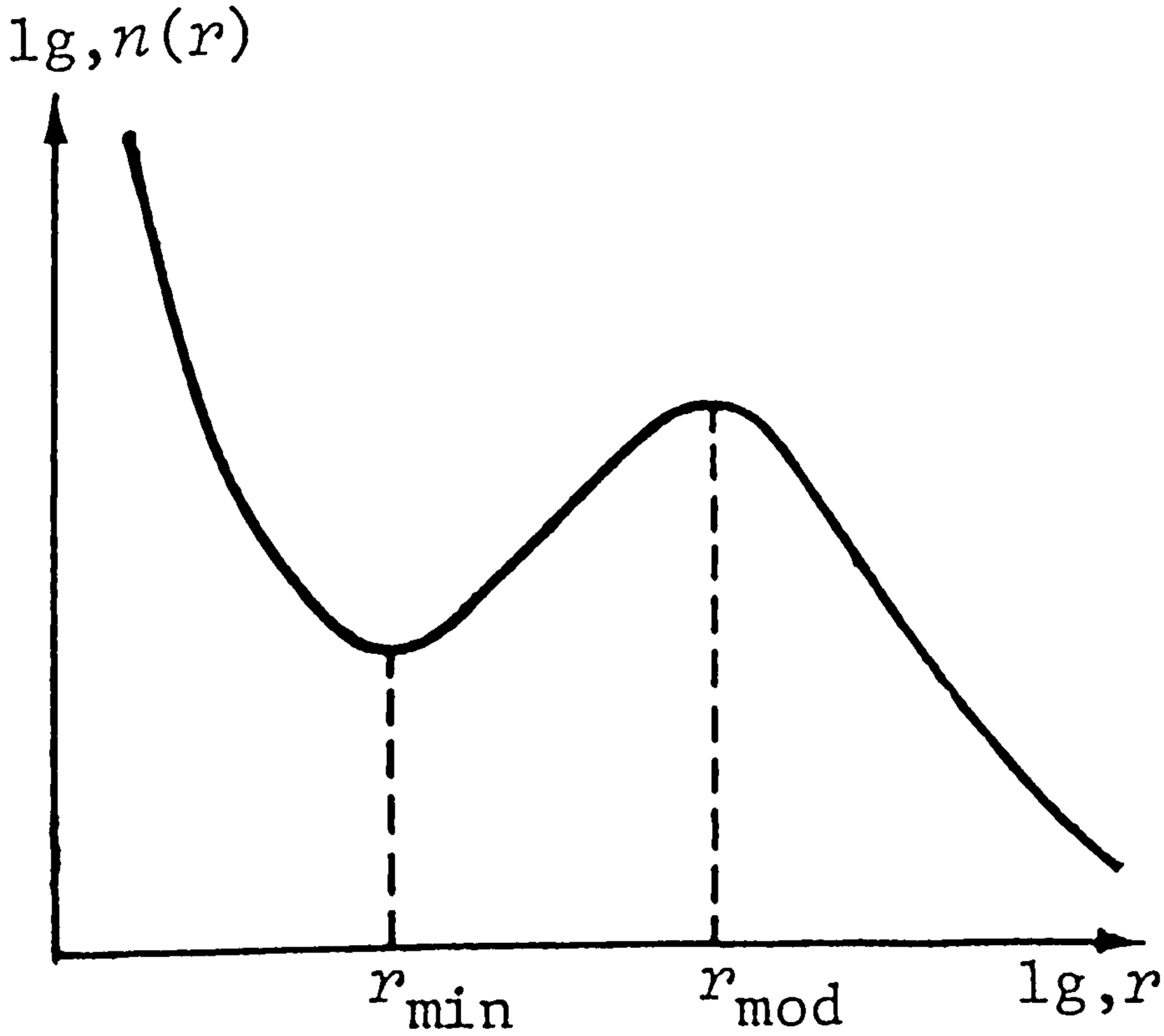

The middle portion of the spectrum is usually a unimodal curve which can be approximated by a lognormal or gamma distribution. For simplicity of analysis and convenience of processing, a gamma distribution is more often used. This distribution has the form:

$$n_M(r) = \frac{N_0}{\Gamma(m+1)r_0^{m+1}}\, r^m\, e^{-\frac{r}{r_0}},$$

where N_0, m, r_0 depend on the cloud type, the averaging scale and other factors. The mode radius r_{mod} is related to the distribution parameters by the relation:

$$r_{mod} = m\, r_0,$$

and the mean radius r_1 by the relation:

$$r_1 = (m+1)\, r_0 \, .$$

In stratiform clouds the size of droplets increase with increasing height h above the lower boundary of the cloud in proportion to $h^{1/3}$, on the average. In convective clouds, the variation of droplet sizes with height is not so definite. Although on the whole the sizes of these droplets also increase with height, mixing with dry ambient air especially in the lower half of the cloud, may cause a great number of tiny droplets to appear, leading to a number of cases in a bimodal distribution [Warner 1969].

The onset of precipitation may also appreciably change the size distribution of the cloud droplets and the height variation of the distribution parameters. Khgrian and Mazin [1952], studied a large number of cloud samples and proposed a universal value of m=2 to describe the size spectra of all cloud types that bear drops in the radius range between 2-3 to 20-30 μm. In the range of droplet sizes from r=50-100 μm to some maximum value r_{max}, which in non-precipitating clouds may range from 100 to 1000 μm, the droplet distribution is described by an exponential relation [Mazin 1983]:

$$n_L(r) = \frac{N_L\,(1-\beta)}{A} \left(\frac{A}{r}\right)^{\beta},$$

where A, β depend on the cloud type and N_L is a normalization constant such that

$$\int_{r_{cut}}^{r_{max}} n_L(r)dr = N_{max} \, ,$$

where N_{max} is the concentration of the large drops.

Borovikov and Mazin [1975] analyzed collected data on the microstructure of droplet clouds to obtain a diagram, which characterizes the possible droplet concentration in a cloud. This can be seen in figure 11. In an overwhelming majority of cases real cloud-droplet concentrations do not lie outside the shaded region and are practically never beyond the upper

curve. If precipitation falls from the clouds then the concentration of the large drops usually

Fig. 11. Generalized diagram of possible distribution of cloud droplets (from Mazin [1983]).

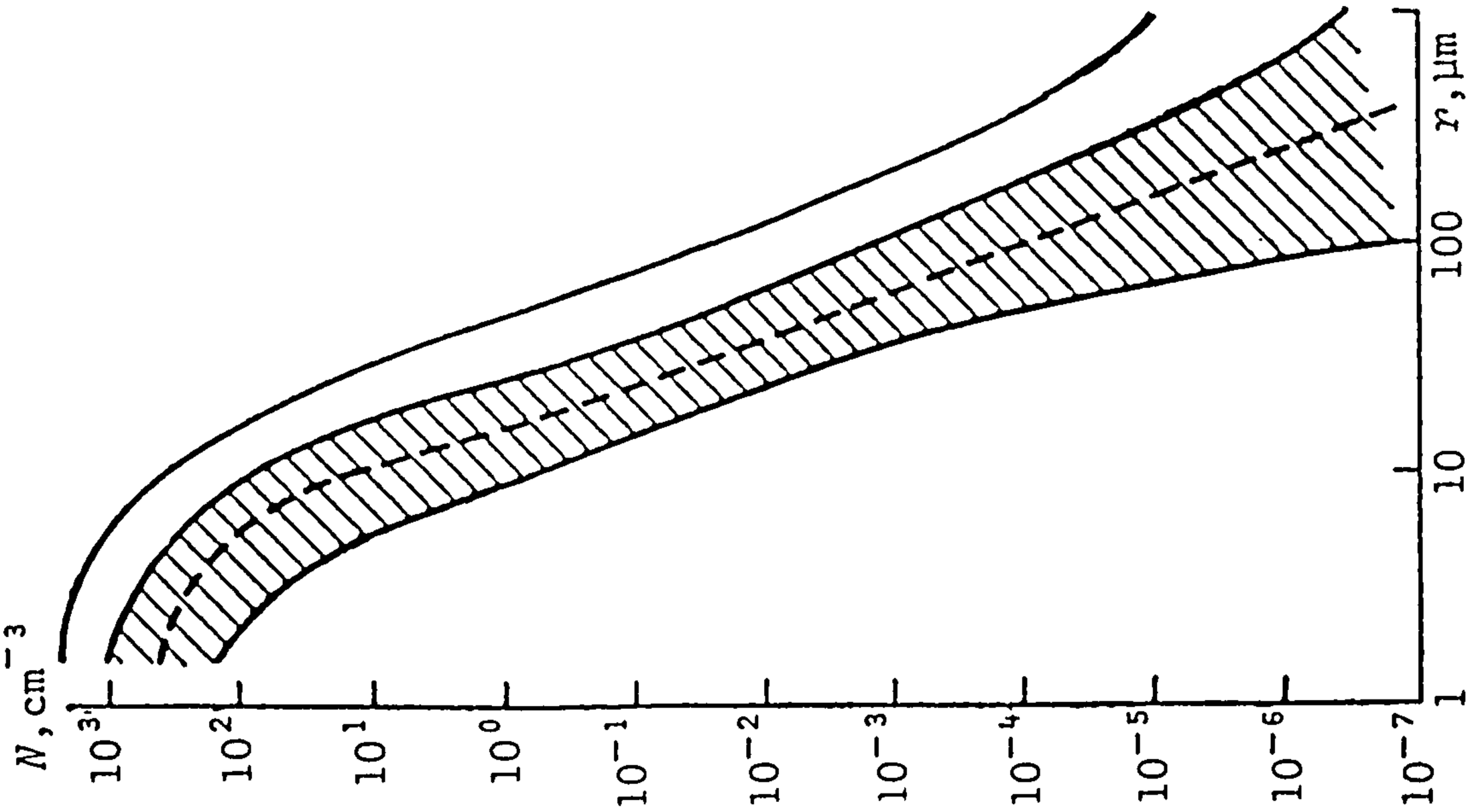

lies in the unshadowed region between the curves. Precipitable clouds have also liquid water contents about an order of magnitude greater than non-precipitable clouds. Typically, the lwc of non-precipitable clouds has values between 0.1 to 1.0 g/m^3, whereas precipitable clouds usually have lwc much greater than 1 g/m^3 (Blau and Fouler [1972]).

Summarizing, the following general model represents the size spectrum of any water cloud:

$$n(r) = \begin{cases} A\left(\frac{r_0}{r}\right), & for \quad 0.1\mu m < r < r_{\min}, \\ \frac{mN_0}{\Gamma(m+1)r_0^{m+1}}\, r^m\, e^{-\frac{r}{r_0}}, & for \quad r_{\min} \le r < r_{cut}, \\ \frac{N_L(1-\beta)}{A}\left(\frac{A}{r}\right)^{\beta}, & for \quad r_{cut} \le r \le r_{\max}, \\ 0, & for \quad r > r_{\max}. \end{cases}$$

Cloud droplet size distributions are given in many original research papers. Here, the most

representative collection of typical middle latitude cloud models has been compiled. Table IV summarizes Silverman and Sprague's [1970] fog and cloud drop size distributions.

Table IV. Silverman's cloud models: Distribution parameters and liquid water content (as later adapted by AFGL).

$n(r) = a\, r^m \exp[-br]$						
Cloud Type	Model Number	m	b	N_0 [cm^{-3}]	$a=C_1 b^{m+1} \Gamma^{-1}(m+1)$	M [g/m^3]
Heavy fog I	1	3	0.3	20	0.027	0.37
Heavy fog II	2	3	0.375	20	0.06592	0.19
Moderate fog I	3	6	1.5	100	2.37305	0.06
Moderate fog II	4	6	3.0	200	607.5	0.02
Cumulus	5	3	0.5	250	2.604	1.00
Altostratus	6	5	1.11	400	6.268	0.41
Stratocumulus	7	5	0.8	200	0.4369	0.55
Nimbostratus	8	1	0.333	100	11.089	0.61
Stratus	9	3	0.667	250	8.247	0.42
Stratus	10	2	0.6	250	27.00	0.29
Stratus-Stratocumulus	11	2	0.75	250	52.734	0.15
Stratocumulus	12	2	0.5	150	9.375	0.30
Nimbostratus	13	2	0.425	200	7.676	0.65
Cumulus-Cumulus Congestus	14	2	0.328	80	1.4115	0.57

All included models are described by a gamma distribution of the form $n_M(r)=ar^m e^{-br}$. N_0 is the concentration of cloud droplets in cm^{-3} and M the amount of water per unit volume in g/m^3. It is interesting to note that the liquid water contents (mesoscale parameter M) of fog and clouds are the same order of magnitude, whereas the concentrations (microscale parameter N_0) differ by an order of magnitude. So, fogs and clouds are distinguishable on the microscale level. Typical cloud heights of occurrence and thicknesses for the cloud models of Silverman can be seen in table V.

Table V. Cloud tops and bases of Silverman's cloud models.

Silverman's cloud model number	Base [m]	Top [m]	Depth [m]
1	0	150	150
2	0	150	150
3	0	75	75
4	0	75	75
5	660	2700	2040
6	2400	2900	500
7	660	1320	660
8	160	1000	840
9	160	660	500
10	330	1000	770
11	660	2000	1340
12	660	2000	1340
13	160	660	500
14	660	3400	2740

Again, we must note that the range of values of thickness may be large for these models. For example, advective fog can be from 30 to 300 meters thick depending on the meteorological conditions and geographic location.

Other sources for cloud droplet size distributions may be found in the literature. Mason [1971], Fletcher [1962], Borovikov [1973], Carrier [1967], Mazin [1983] and Feigelson [1984] give also drop size distributions for various cloud types. Table VI summarizes Carrier's et al [1967] observations which are in disagreement with the data quoted by Silverman in table IV. Thus, it may be seen how difficult it is to model clouds with representative drop size spectra and liquid water content.

Table VI. Carrier et al's water cloud models: Distribution parameters and liquid water content.

Cloud type	Model No	N_0 [cm^{-3}]	m	$\Delta x=\Delta r/r_{mod}$	b	a	M g/m^3
Stratus I	1	464	8	0.85714	2.286	19.61	0.16
Altostratus	2	450	5	1.0	1.33	4.6	0.40
Stratocumulus	3	350	3.5	1.257	1.0	30.09	0.24
Nimbostratus	4	330	1.0	2.7	0.28	26.7	1.4
Fairweather C_u	5	300	8	0.85714	2.286	12.68	0.1
Stratus II	6	260	3.5	1.2667	0.777	7.182	0.37
Cumulus Congestus	7	207	1.5	1.914	0.428	18.71	0.43
Cumulonimbus	8	72	3	1.4	0.6	1.555	0.16

Finally, tables VII and VIII summarize Ajvazyan's [1991] compilation of drop size distributions of small and large drops in various cloud types, originally quoted by Feigelson [1981], Mazin [1983] and Pruppacher and Klett [1978].

Table VII. Ajvazyan's small drop size distributions of water clouds.

No	Cloud type	r_{min} [μm]	r_{cut} [μm]	b	m	N_0 [cm^{-3}]	M [g/m^3]
1	Sc	1.0	20.0	0.639	2	188	0.2140
2	St	1.0	20.0	0.667	2	248	0.2085
3	Ns	1.0	20.0	0.462	2	117	0.2682
4	Ac	1.0	20.0	0.639	2	155	0.1477
5	As	1.0	20.0	0.545	2	116	0.1724
6	medi	1.0	20.0	0.667	2	472	0.3968
7	maxi	1.0	20.0	0.300	2	1000	5.1590
8	Cu hum	1.0	20.0	1.000	2	1987	0.4990
9	Cu med	1.0	20.0	0.750	2	1677	0.9953
10	Cu cong	1.0	20.0	0.500	2	925	1.7350
11	(max)	1.0	35.0	0.600	6	247	2.4040
12	(min)	1.0	35.0	0.600	6	247	2.4040
13	Cb (max)	1.0	45.0	0.286	5	55	2.9650
14	Cb (min)	1.0	45.0	0.286	5	55	2.9650

Table VIII. Ajvazyan's super-large drops distribution parameters in various clouds.

No	Cloud type	r_{cut} [μm]	r_{max} [μm]	β	N_L [m^{-3}]	LWC [g/m^3]	A
1	Sc	85	500	6.3	2000	1.165E-2	85
2	St	85	400	7.6	1000	4.698E-3	85
5	Ns	85	1000	5.0	1000	9.415E-3	85
6	medi	85	500	6.3	2000	1.165E-2	85
7	maxi	85	1000	5.0	1000	9.415E-3	85
8	Cu-hum	85	300	10.0	20	7.713E-5	85
9	Cu-med	85	600	4.0	100	1.512E-3	85
10	Cu-cong	85	1000	5.0	400	3.766E-3	85
11	(max)	200	1200	2.7	1000	4.265E-1	85
12	(min)	200	1100	2.3	100	4.929E-2	85
13	Cb (max)	100	700	3.0	20000	1.026E+0	85
14	Cb (min)	100	400	3.0	3000	8.042E-2	85

4.3.4 Crystals in clouds.

In contrast to the case of water droplets, when considering crystals in clouds it is important to know their shape and orientation as well as their size and number.

4.3.4.1 Crystal shapes and sizes.

Ice particles in clouds can be divided into three groups according to their shape: rounded, laminar and acicular. The first group includes particles whose dimensions are about the same in any direction. The second and third groups include particles which are appreciably smaller in one direction than in a perpendicular direction. Ice crystals have extremely diverse shapes, but as a rule they all posses a definite hexagonal symmetry which manifests itself as a variety of hexagonal prisms, hexagonal plates, and six-ended dendrites. Rounded crystals may contain various air inclusions.

Fig. 12. Relation of shape of ice crystals to conditions of crystal growth (after Magono and Lee [1966]).

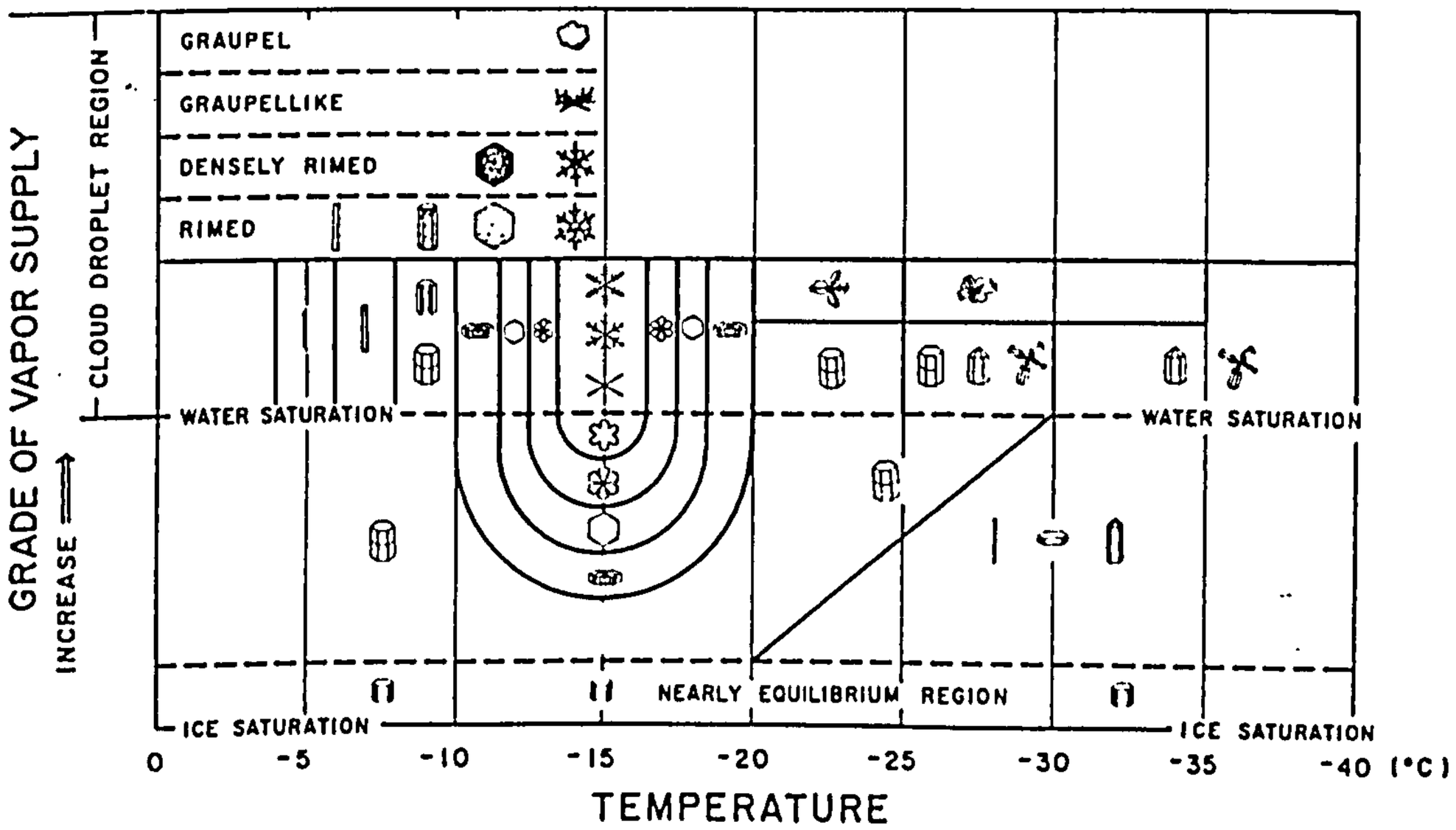

The shape of the cloud crystals depends on the temperature and humidity. Since when crystals originate in clouds, the humidity is close to the saturation value over water, the shape of a crystal being formed may -as a first approximation- be related to the temperature. Figure 12 juxtaposes the shapes of ice crystals with the conditions under which they are formed. As we see from figure 12 high level clouds, where the temperature is below -18°C, the crystals can be expected to take the form of columns, prisms, thick plates and bundles of often hollow crystals. In the -15 to -3°C region, crystals usually take the form of dendritic starlets or thin plates. At -10 to -2°C solid columns and thick plates reappear, while around -5°C the crystals have the form of needles.

Weickman [1947] also reports on the variety of shapes and sizes found in clouds. High altitude isolated cirrus clouds, which are usually associated with temperatures below -30 C, are composed of six-sided columns (prisms), typically 0.5 mm long, and containing pronounced funnel shaped cavities as shown in figure 13a and 13b. In cirrostratus, where the

Fig. 13. (b) Individual hollow prismatic ice columns and (a) clusters collected from cirrus clouds at -40 C. (c) Solid prismatic columns from cirrostratus at -26 C. (d) Thin hexagonal ice plates. (photographs by H.K. Weickman.)

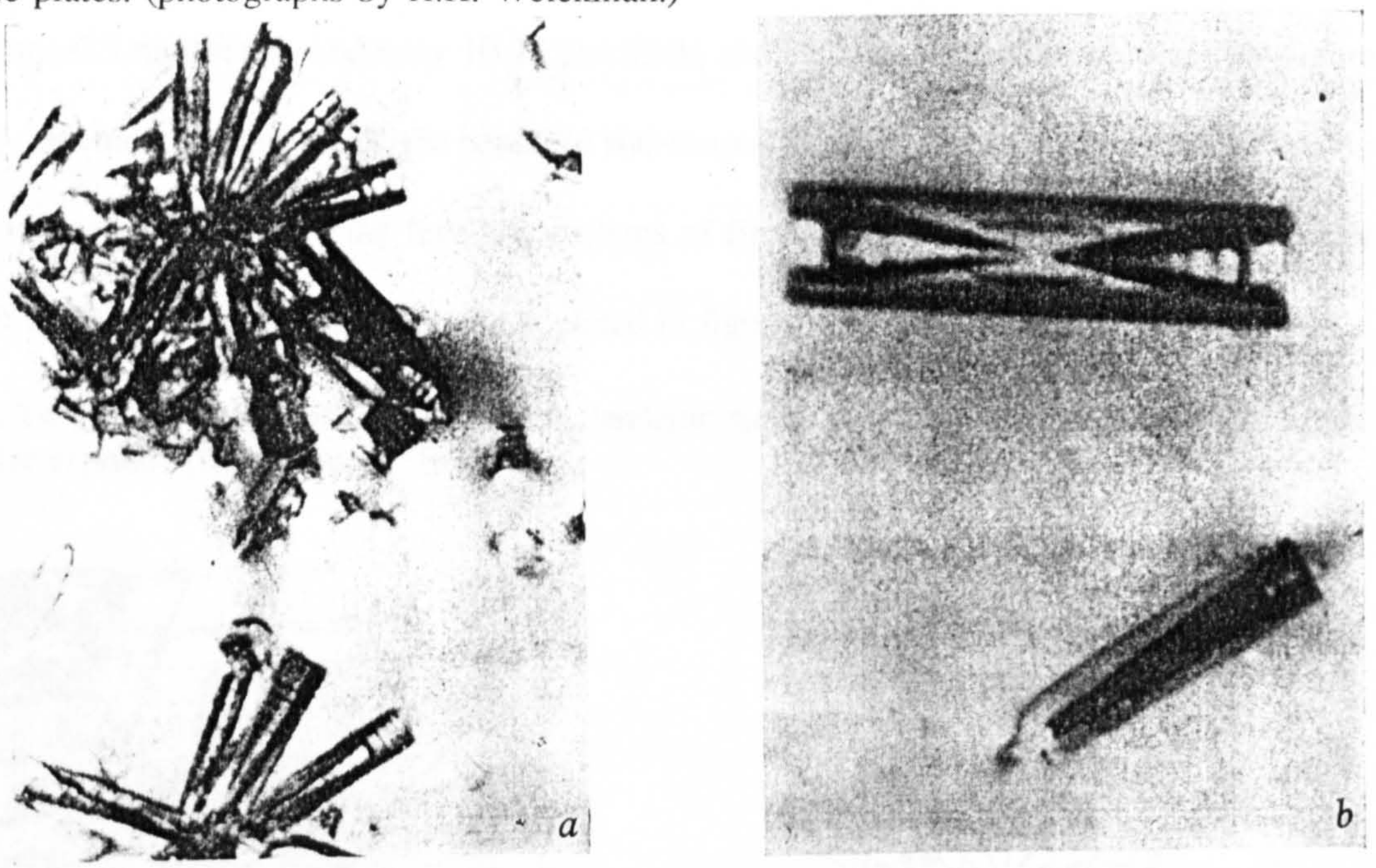

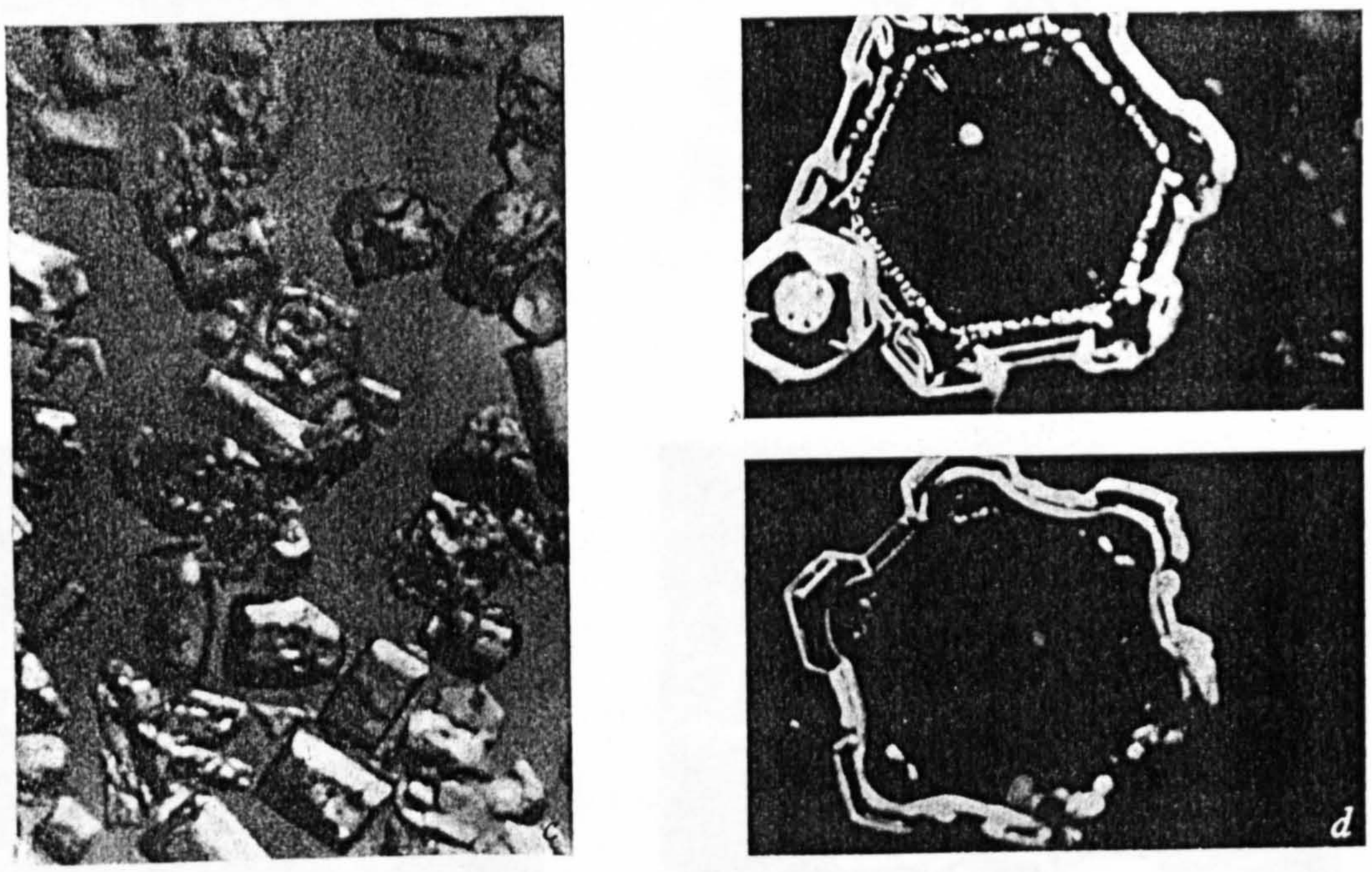

air is only slightly supersaturated relative to ice, the prisms are short and solid as shown in figure 13c. The medium altitude clouds, occurring at temperatures -15 and -30 C, contain both prisms and thin six sided plates, as shown in figure 13d, with the prisms dominant at the lower

temperatures. The greatest variety of crystal shapes is to be found in the lower altitude supercooled clouds, at temperatures between 0 and -15 C. Here we find hexagonal plates, perhaps 0.5 mm across and only 10-20 μm thick, short prisms, long thin needles (see figure 14a), and most striking of all, the beautiful star-shaped crystals, whose six arms often develop side branches to produce the fern-like patterns of figure 14b. Other common crystal shapes such as dendritic stellar crystals, are depicted in figures 14c and 14d.

Fig. 14. (a) A sector plate crystal. (b) A dendritic stellar snow crystal. (c) and (d) Dendritic stellar crystals. (from Mason [1975]).

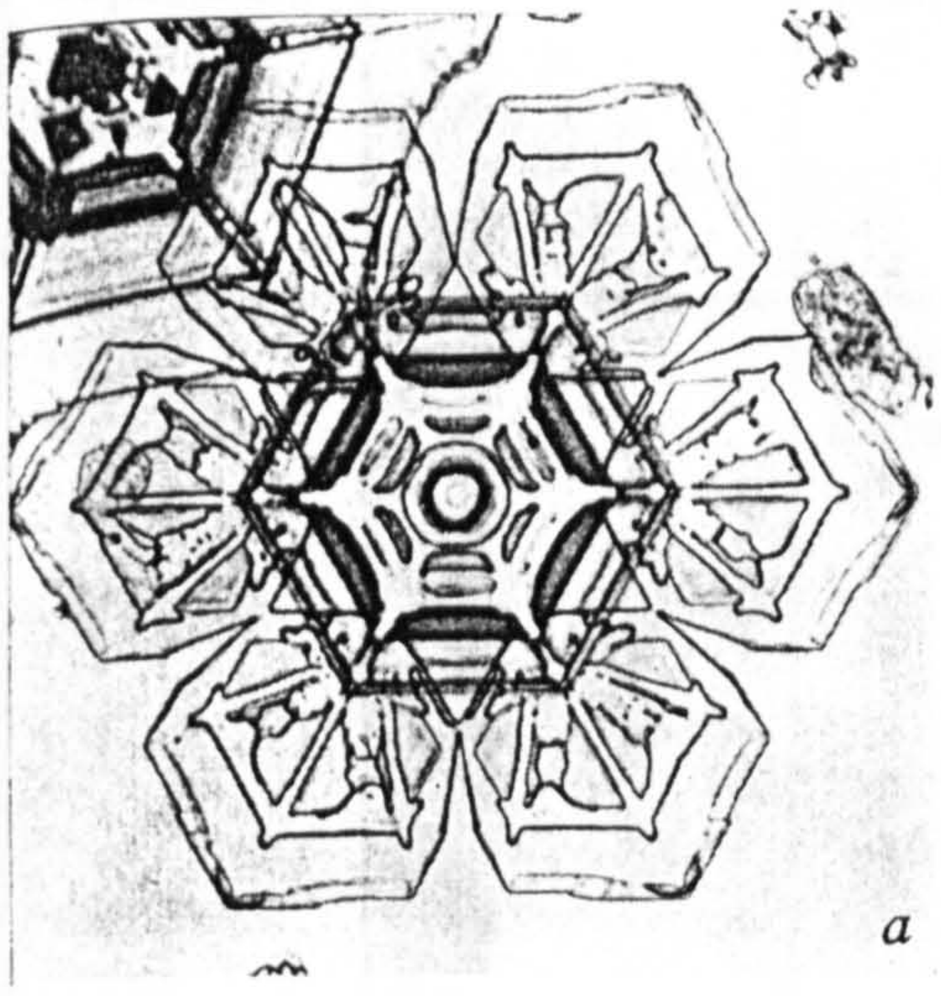

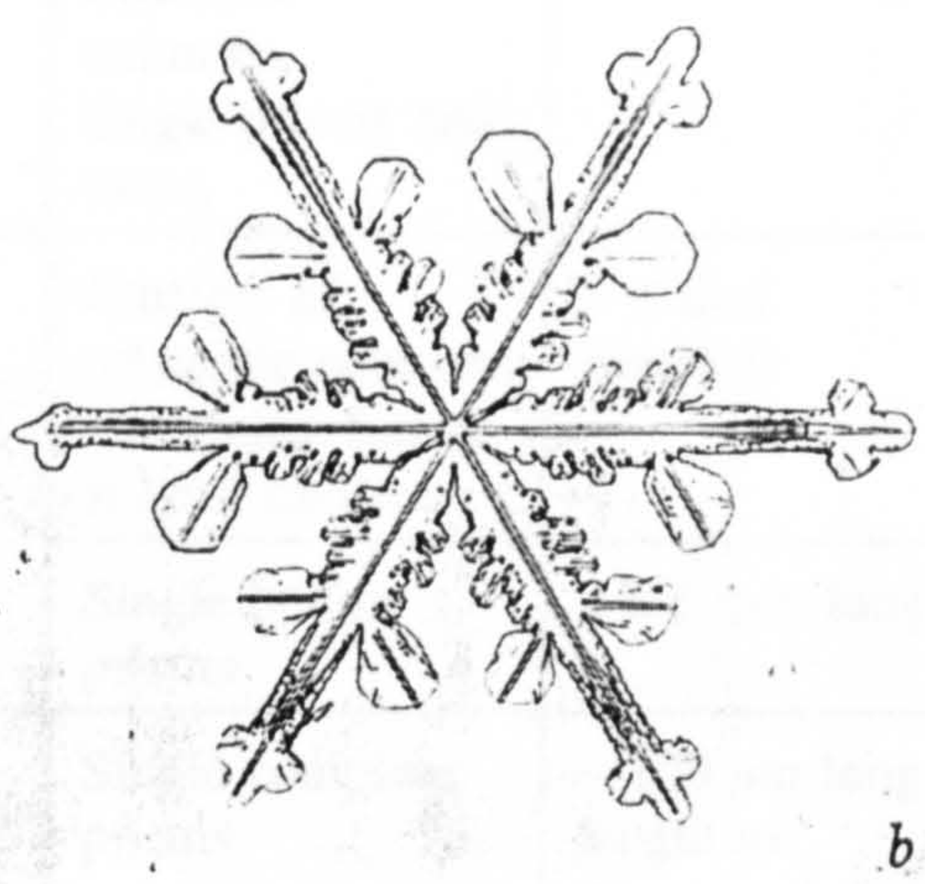

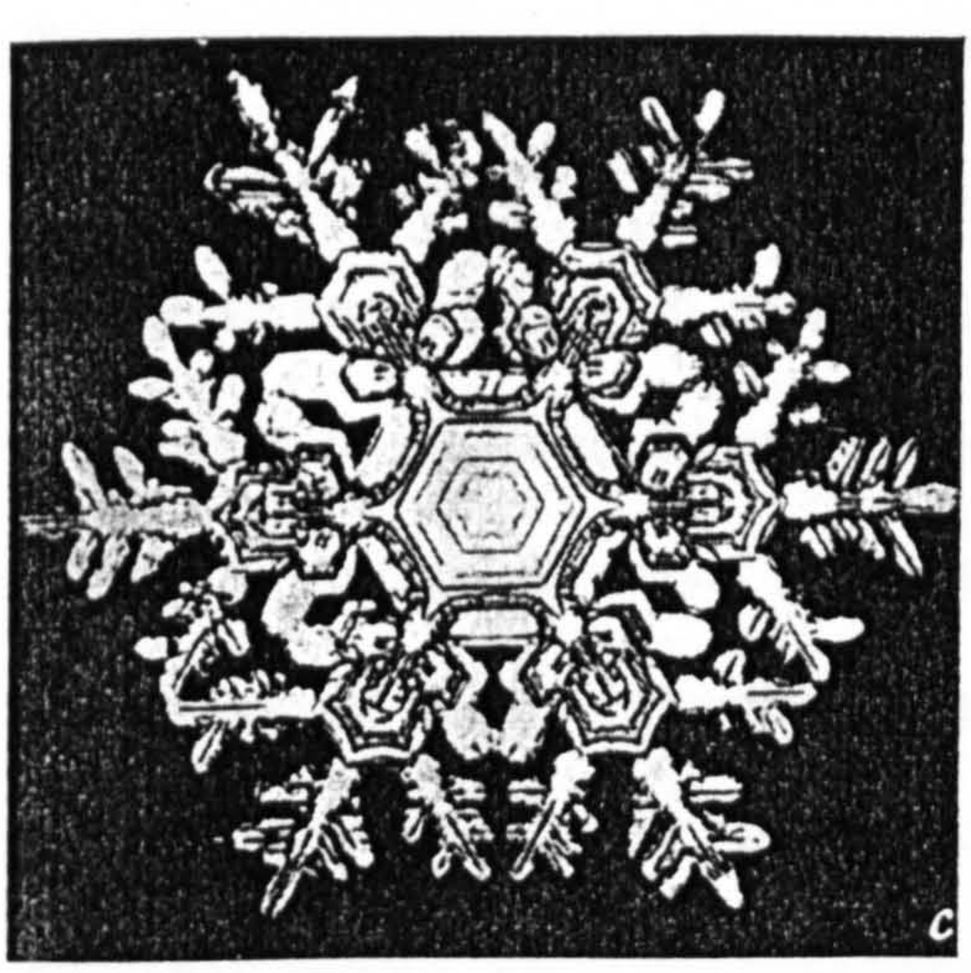

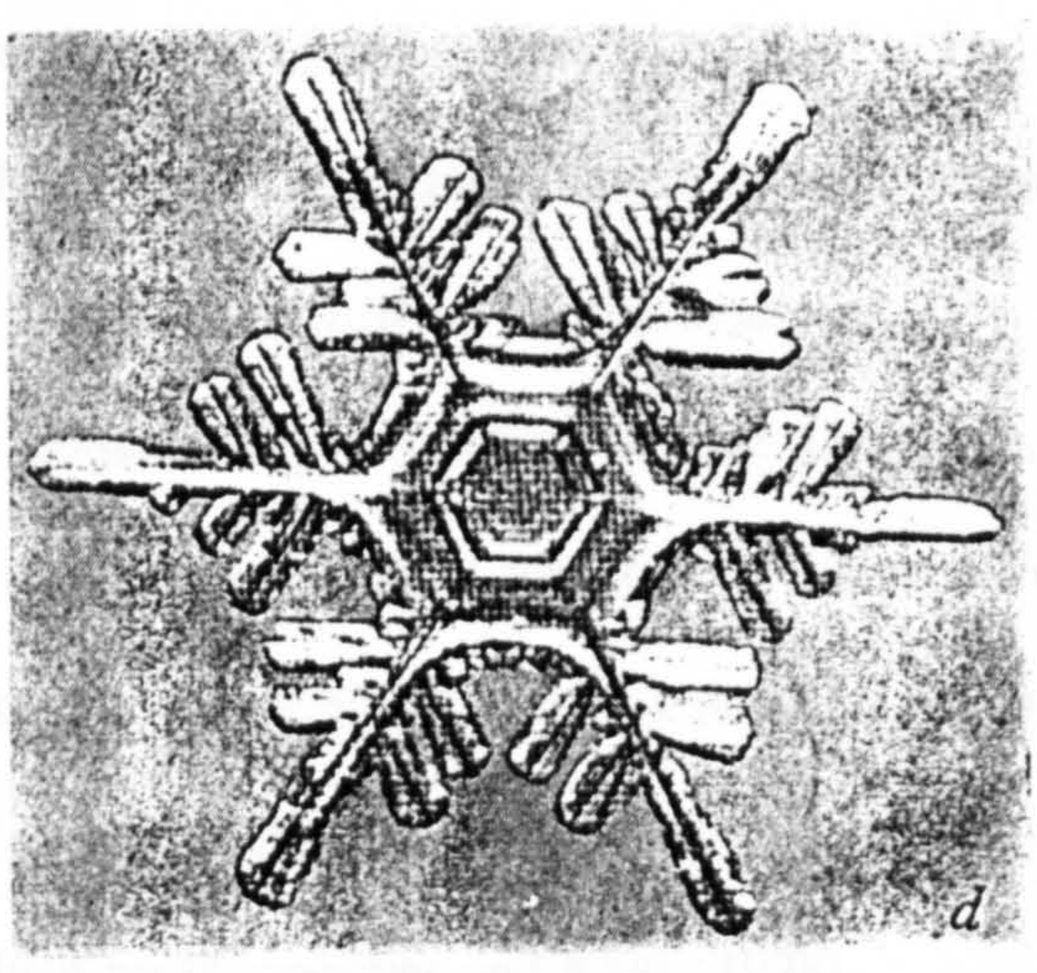

Table IX below, summarizes Weickman's observations of predominant crystal forms in different cloud types.

Table IX. Weickman's observations of predominant crystal forms in clouds.

Level of observation	Temperature range	Cloud types	Crystal forms	Crystal sizes
Lower troposphere	0° to -15° C	Nimbostratus Stratocumulus Stratus	Thin hexagonal plates Star-shaped crystals showing dendritic structure	50 µm to 0.5 mm diameter 10 to 20 µm thick
Middle troposphere	-15° to -30° C	Altostratus Altocumulus	Thick hexagonal plates Prismatic columns, single prisms and twins	~ 200 µm diameter
Upper troposphere	< -30° C	Isolated Cirrus	Clusters of prismatic columns containing funnel-shaped cavities	~ 1 mm diameter
			Single hollow prisms	~ 0.5 mm long
		Cirrostratus	Single complete prisms	~ 100 µm long, length to diameter = 1-5

4.3.4.2 Crystal mass and concentrations.

The 'ice content' (iwc), that is the mass of ice in the clouds, ranges from 0.001 g/m^3 in high altitude clouds (except Ci) to 0.1 g/m^3 in St and Ns. The concentration ranges from some units of tens per litre in high level clouds, to tens or hundreds per litre in Ns, As systems.

The density of the ice in the crystals can vary considerably depending on size and shape. Generally, we may say that as ice crystals increase in size from a few tens of microns to millimetres, the relative proportion of air inclusion increases and the density decreases from 0.9 to 0.5 g/m^3 [Feigelson 1984]. An excellent survey of the ice densities corresponding to crystals of various shapes and sizes has been given by Pruppacher and Klett [1978].

4.3.4.3 Cirrus clouds.

In Ci clouds the ice content varies from 0.01 to 0.4 g/m^3 depending upon season and geographical location. Thin cirrus usually bear ice contents between 0.01 and 0.05 g/m^3. In thick cirrus however, the ice content is typically greater than 0.1 g/m^3 and may reach up to 0.40 g/m^3, while the concentration of ice crystals ranges from 10 to 50 particles per litre [Pruppacher and Klett 1978].

Data for cirrus clouds appears to be somewhat sparse, compared to that available for other clouds, presumably owing to the difficulties in collection and lesser importance attached to these clouds in the past. However, recently the U.K. Meteorological Office collected and analyzed a series of airborne measurements from cirrus clouds (FIRE/ICE studies). The results

Fig. 15. Ice crystal spectra from the U.K. Met. Office FIRE/ICE studies.

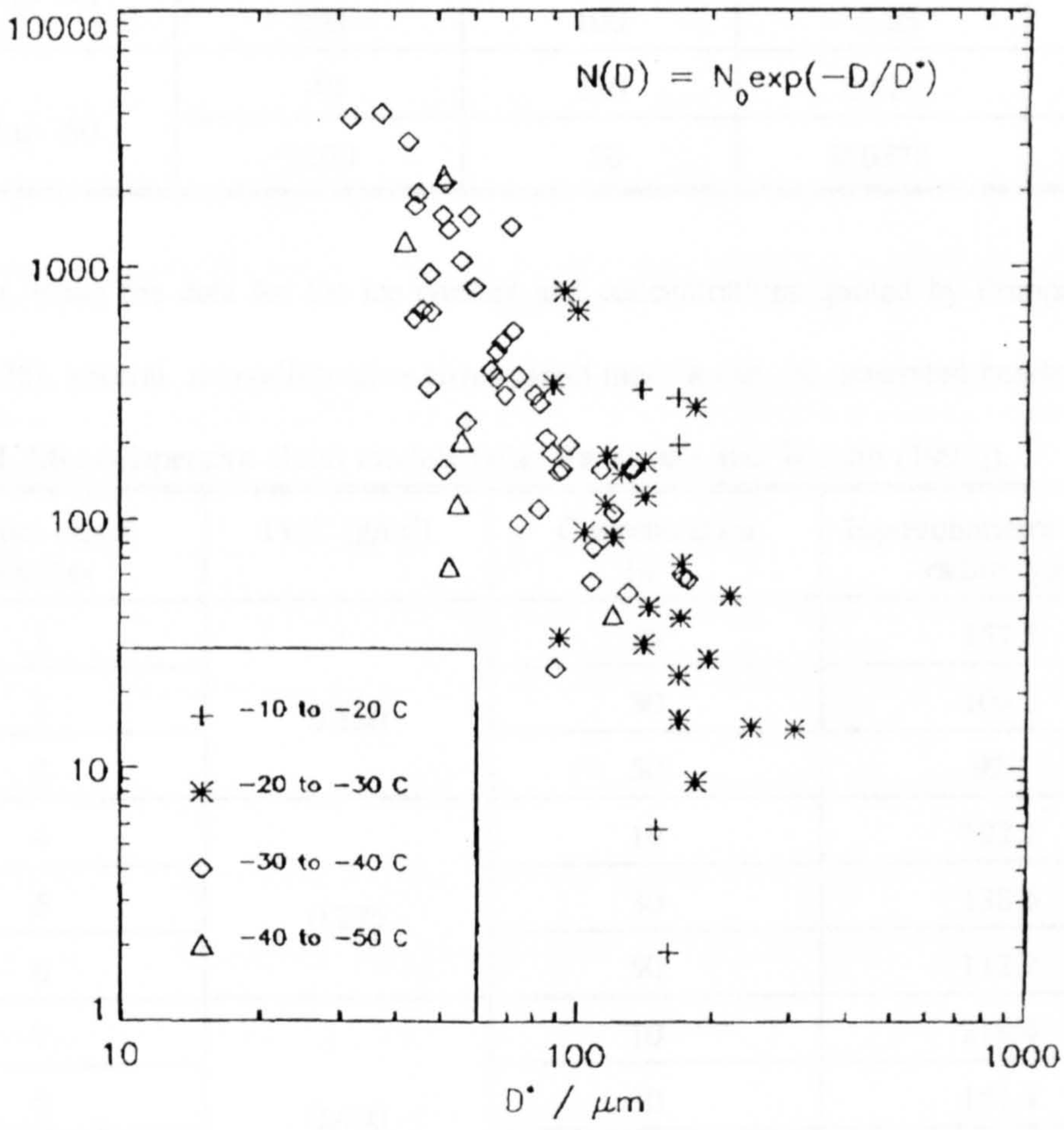

are summarized in figure 15. These data have been fitted with exponential distributions of the form $N(D)=N_0e^{-D/D^*}$ from which nine particle size distributions have been chosen as the most representative (see table X).

Table X. Ice particle size distribution parameters for Ci clouds, as deduced from the FIRE/ICE data.

Temperature [°C]	N_0[m^{-3} μm^{-1}]	D* [μm]	Ice Water Content [g/m^3]	Model No
-10 to -20	310	130	0.255	1
	200	160	0.377	2
-20 to -30	65	160	0.123	3
	160	130	0.1316	4
	25	200	0.1152	5
-30 to -40	1300	52	0.0274	6
	200	100	0.05	7
-40 to -50	40	120	0.024	8
	2100	50	0.0378	9

Moreover, using the data for the ice content and concentrations quoted by Pruppacher and Klett [1978], several monodispersive cirrus cloud models can be generated bearing various

Table XI. Monodispersive cloud models (after Papatsoris and Watson [1991]).

Model cloud number	IWC [g/m^3]	Concentration [lt^{-1}]	Equivolumetric sphere radius [μm]
1	0.150	10	157.5
2		30	109.2
3		50	92.1
4	0.275	10	192.7
5		30	133.6
6		50	112.7
7	0.400	10	218.4
8		30	151.4
9		50	127.7

combinations between the suggested concentration of crystals and ice content of the cloud [Papatsoris and Watson 1990]. The characteristics of each generated model can be seen in table XI, where the correspondent equivolumetric sphere radius is also given. Ice density has been assumed 0.917 g/m^3.

4.4 Modelling radio wave propagation in clouds at millimetre wavelengths.

So far, we have discussed the spatial structure and the physical characteristics of clouds. What we need next, is a proper electromagnetic theory to calculate the absorption and scattering cross sections of water droplets and ice crystals. Mie theory provides an excellent approach to modelling the extinction and back scattering of water droplets of any size in water clouds. When the condition $mx<<1$, is satisfied (m is the index of refraction and x is the size parameter), the Rayleigh approximation becomes valid and the calculations greatly simplify. Both attenuation and equivalent reflectivity are then proportional to the total mass content of the cloud. In order to assess the applicability range of the Rayleigh approximation, the product mx has been calculated for water at various wavelengths, assuming r=35μm (see table XII).

Table XII. Assessment of the applicability of the Rayleigh approximation for water clouds.

f [GHz]	30	60	100	150	300
λ [mm]	10	5	3	2	1
m (10°C)	5.73	4.24	3.44	2.98	2.61
mx, r=35μm	0.13	0.19	0.25	0.33	0.57

Since the maximum radius of the small portion of drops is for the overwhelming majority of clouds less than 35 μm, we can safely say that the Rayleigh approximation is applicable when large drops are not considered. For droplets with radii greater than 40μm, the Rayleigh approximation breaks down. One, must then use the exact Mie solution to calculate the absorption and scattering cross sections of water drops.

For ice m is 1.78 over the entire millimetre wave spectrum, and the Rayleigh approximation

breaks down for equivolumetric ice spheres with radii greater than 60μm. However, the sizes of the equivolumetric spheres in ice clouds exceed well the 60μm limit. Consequently, for ice the exact Mie solution must be used for the calculation of the extinction and back scattering cross sections of equivolumetric spheres.

4.4.1 Multiple scattering in clouds at millimetre wavelengths.

For the calculation of the extinction and back scattering properties of clouds, multiple scattering effects have been neglected. It is likely though that multiple scattering effects may occur in clouds. The problem of finding the intensity of the millimetre wave radiation inside and outside the cloud requires considerable effort and involves complex mathematical formulations. However, a much simpler qualitative method often proves useful in determining the significance of multiple scattering. The occurrence of multiple scattering is dependent on two conditions both being fulfilled:

(i) the scattering coefficient should be high compared to the absorption coefficient,

(ii) the medium under consideration should be sufficiently dense.

Ishimaru (private communication) and Guissard [1980], observe that if the scattering albedo $\omega_o=C_{sca}/(C_{sca}+C_{abs})$ is close to unity then multiple scattering can be significant. If $\omega_o<0.5$ then multiple scattering is probably negligible.

4.4.1.1 Water clouds.

Water clouds are generally considered dense media as the concentration of droplets in such clouds typically range from 100 to 1000 per cm^3. However, the scattering albedo of water droplets in the size range 0.1 to 100 μm is much smaller than unity (see figure 16). Even at 300 GHz the scattering albedo is $\omega_o\approx0.05$ for a droplet 50 μm in radius. Multiple scattering should thus not be significant in water clouds.

Fig. 16. Scattering albedo for spherical water droplets at various frequencies for a size range 0.1 to 100 μm.

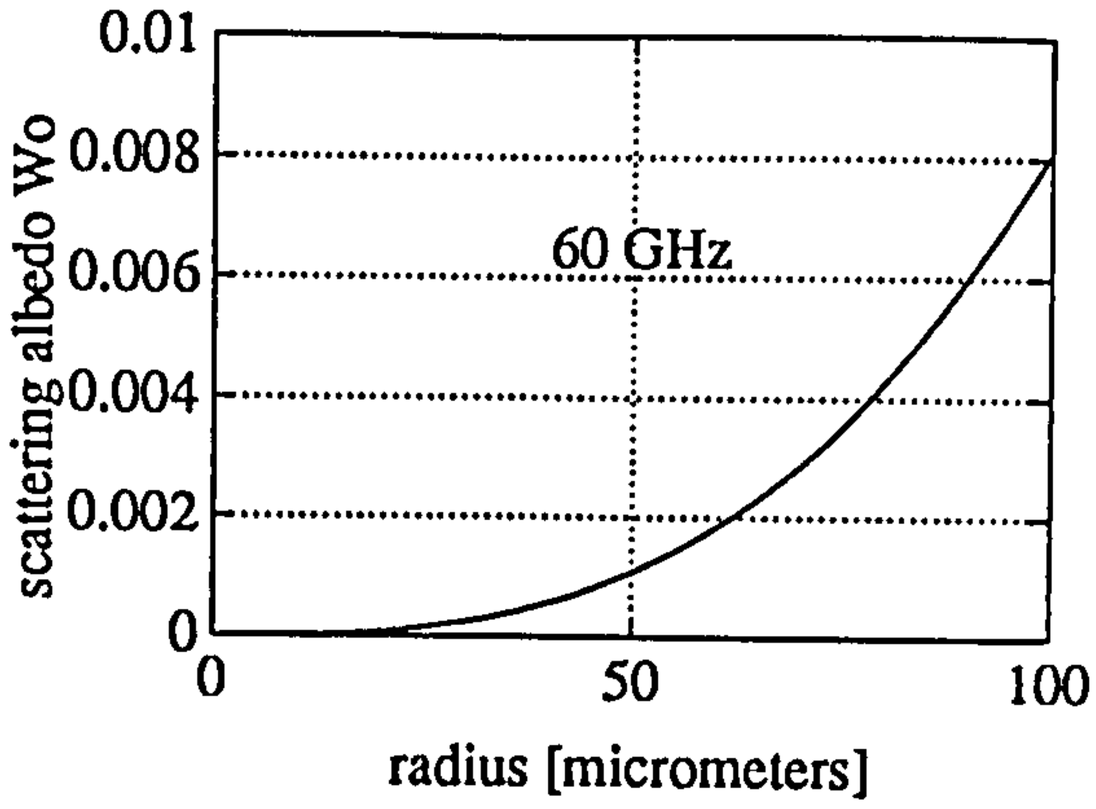

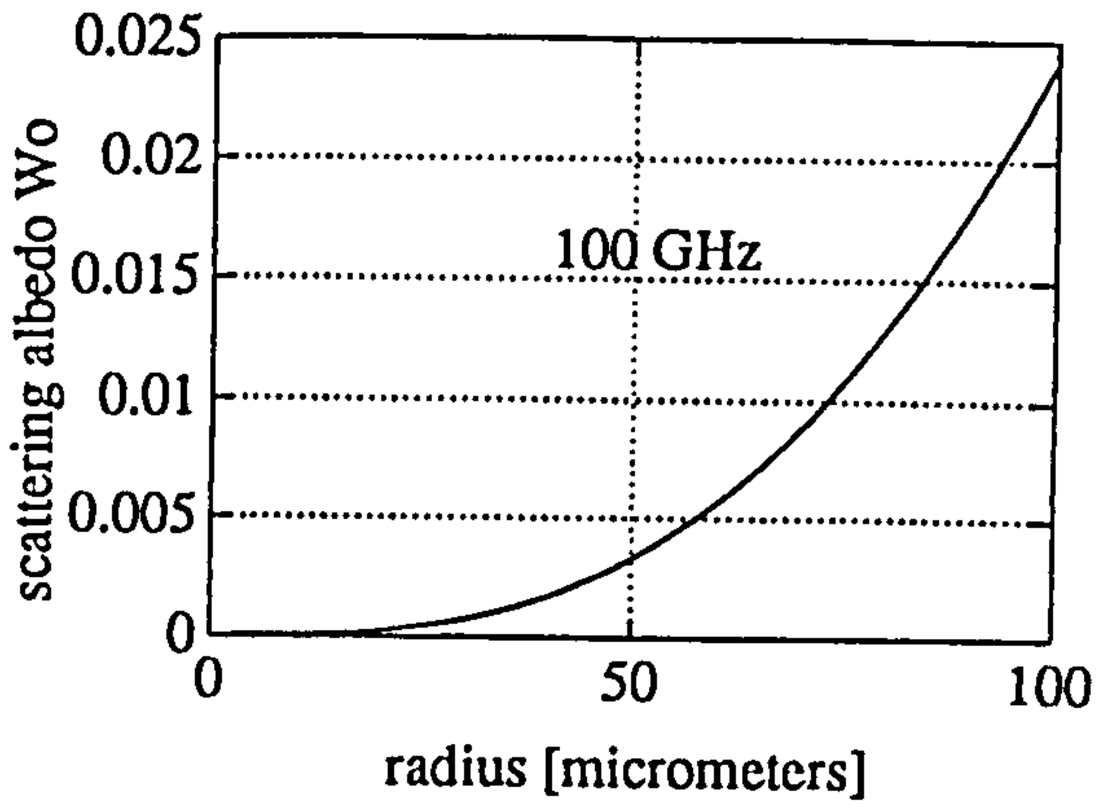

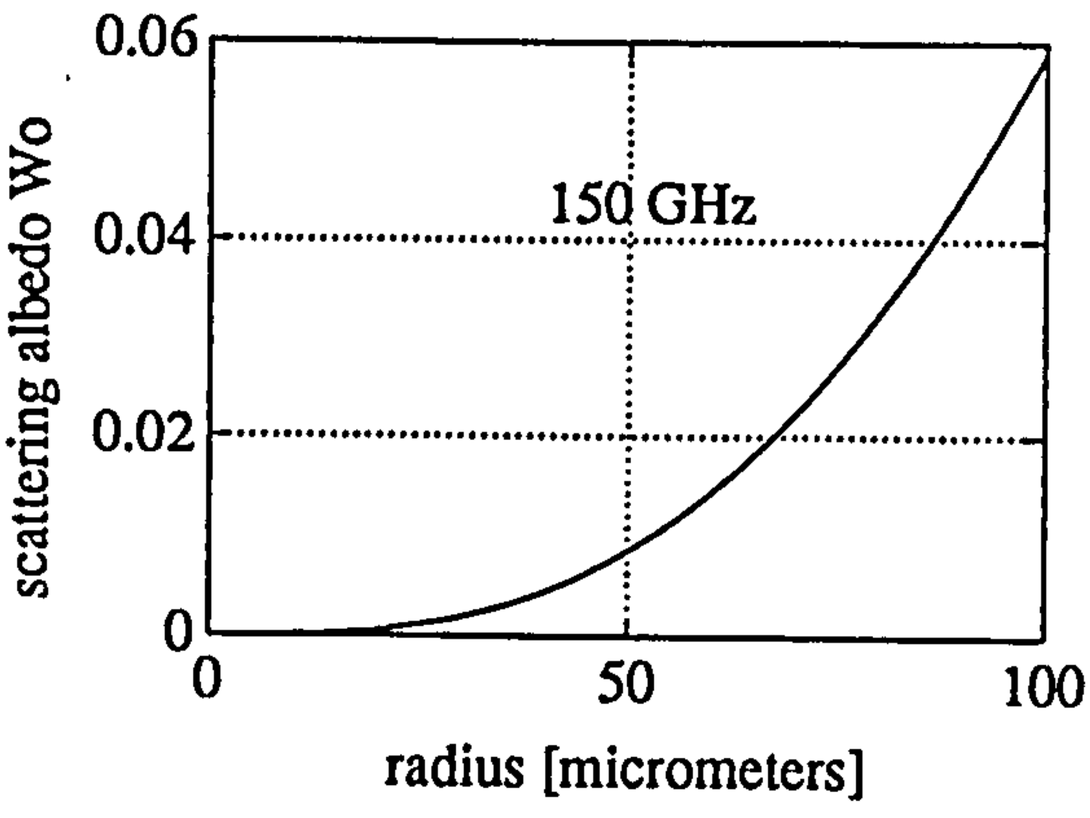

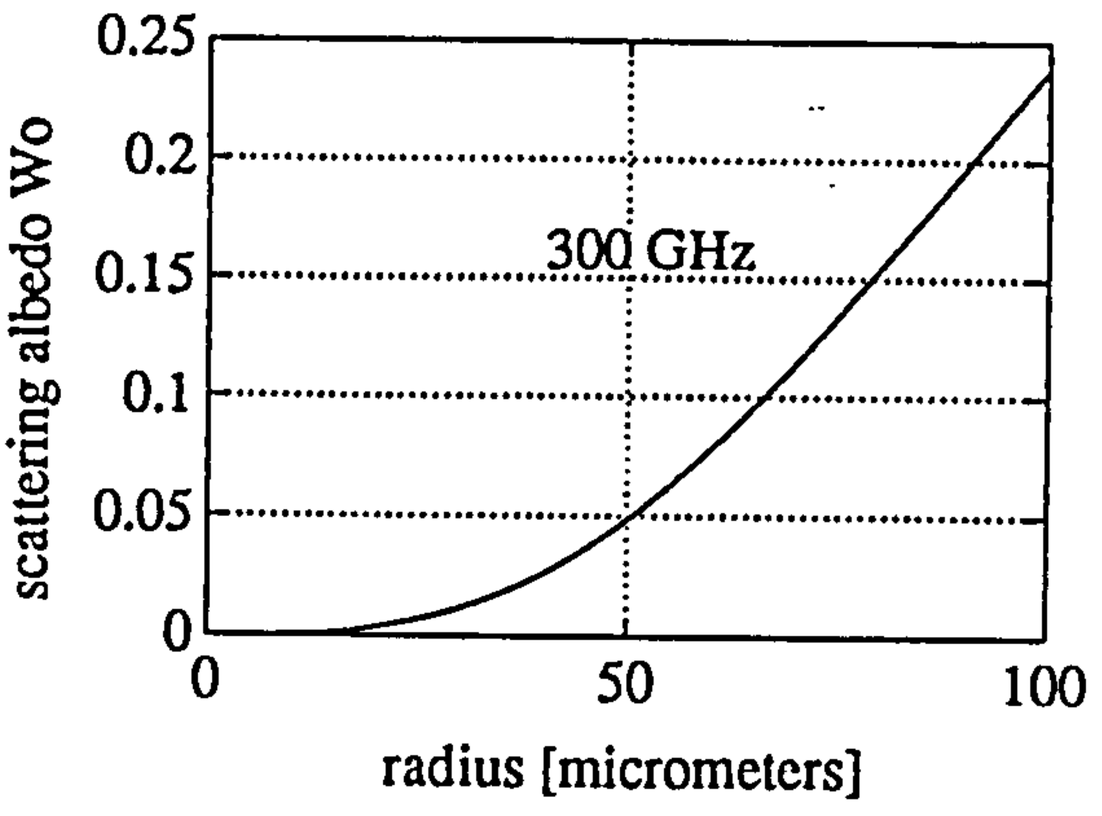

4.4.1.2 Ice clouds.

Figure 17 shows the scattering albedo ω_o for ice spheres in the size range 0.1 to 100 μm at various frequencies. Since ice is primarily a scattering medium, the albedo is expected to exceed the 0.5 margin. In table XIII the critical radii above which the albedo becomes greater than 0.5 for the above selected frequencies are tabulated. For ice forms of stratiform clouds

Table XIII. Critical radii above which the scattering albedo becomes greater than 0.5.

frequency [GHz]	60	100	150	300
critical radius [μm] ω_o=0.5	70	37	22	9.5

without significant growth, multiple scattering should not be significant for frequencies lower than 60 GHz. For frequencies greater than 100 GHz, the critical radius becomes small and the

importance of multiple scattering is expected to increase. On the other hand, the concentrations

Fig. 17. Scattering albedo for spherical ice particles at various frequencies for a size range 0.1 to 100 μm.

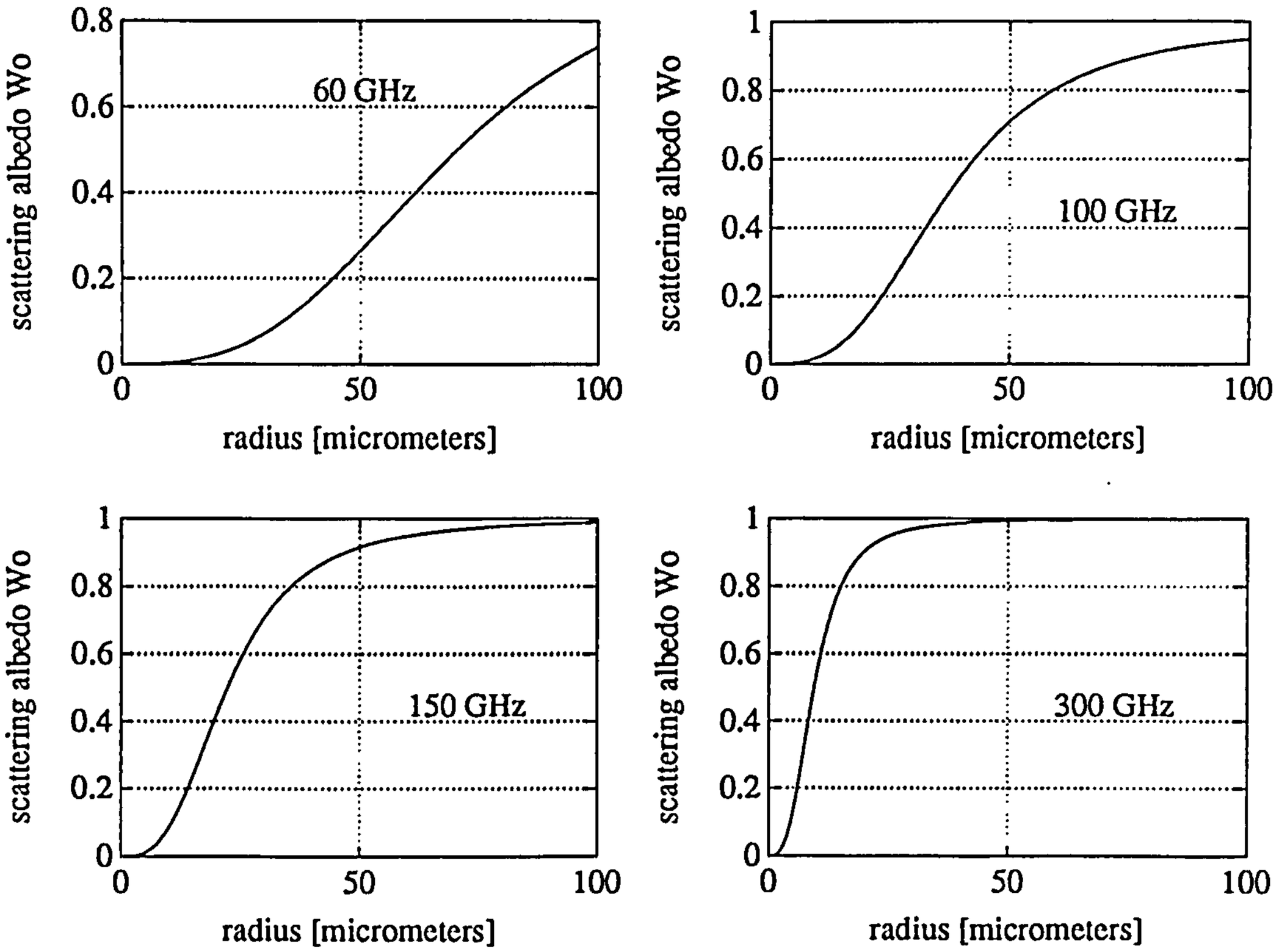

hand, the concentrations observed in ice clouds, including cirrus clouds, are fairly small (typically less than 1 cm^{-3}) and therefore do not give rise to multiple scattering effects. So, we can not give a clear answer about the significance and the extent of multiple scattering in ice clouds. Only rigorous quantitative approaches such that suggested by Takano and Liou [1989] should be able to answer this question definitely.

4.5 Extinction and back scattering properties of clouds.

In the following sections we have used Mie theory, to calculate the specific attenuation

$$\alpha = \int_{r_{min}}^{r_{max}} n(r) C_{ext}(m,x) dr \quad dB/hm$$

and the back scattering function (or radar reflection coefficient or simply reflectivity)

$$\beta = \int_{r_{min}}^{r_{max}} n(r)\sigma_b(m,x)dr \quad hm^{-1}$$

for the wide collection of cloud models given in the preceding sections. Here C_{ext} and σ_b are the extinction and back scattering cross sections, respectively. The contribution of large drops has been taken into account for the cloud models of Ajvazyan. For the remaining cloud models, that is the cloud models of Silverman and Carrier, the effects of large drops have been neglected. So it becomes possible to compare the results and assess the impact of large drops on the resultant attenuation and reflectivity. Calculations have also been done for the Cirrus models of the Met. Office and the generated monodispersive models. The temperature for water droplets has been assumed 0° C and for ice crystals -20° C, throughout.

4.5.1 Fog.

Fog clouds are distinguished from other clouds in their distance from the earth's surface. Fog clouds are generally classified according to the thermodynamic process that generates them. Advective fog is produced by the transport of moist air over a cooler surface resulting in the cooling of the surface layers below the dew points, with condensation taking place in the form of fog. Most sea fogs are advective. Both the size range of particles and the liquid water contents are large for this type of fog. Radiative fog is produced when stagnant moist air is in contact with ground that has become progressively cooler during the night due to radiating cooling. The cooling from below produces an temperature inversion in the layers next to the ground. This type of fog has both small size of particles and a small liquid water content. Calculations for the fog models of Silverman and Sprague are shown in figures 18 and 19. The attenuation resulting from the radiative fog is kept at low levels over the entire millimetre wave spectrum. In fact it never exceeds 0.1 dB/hm even at 300 GHz. A similar behaviour follows the radar reflection coefficient which does not exceed $5x10^{-6}$ hm^{-1} at 300 GHz.

Fig. 18. Specific attenuation for Silverman's fog models 1,2,3, and 4.

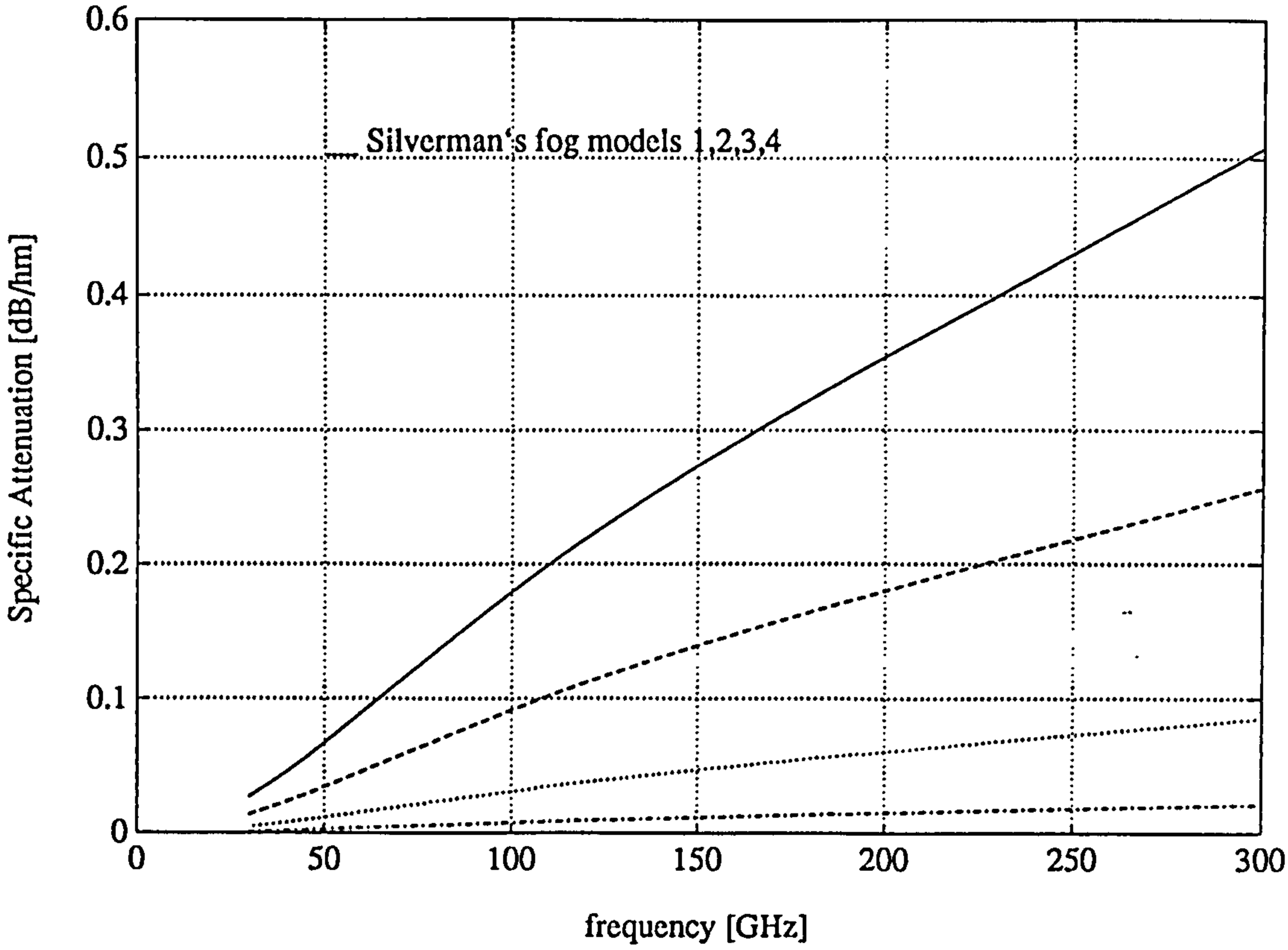

Fig. 19. Radar reflection coefficient for Silverman's fog models 1,2,3 and 4.

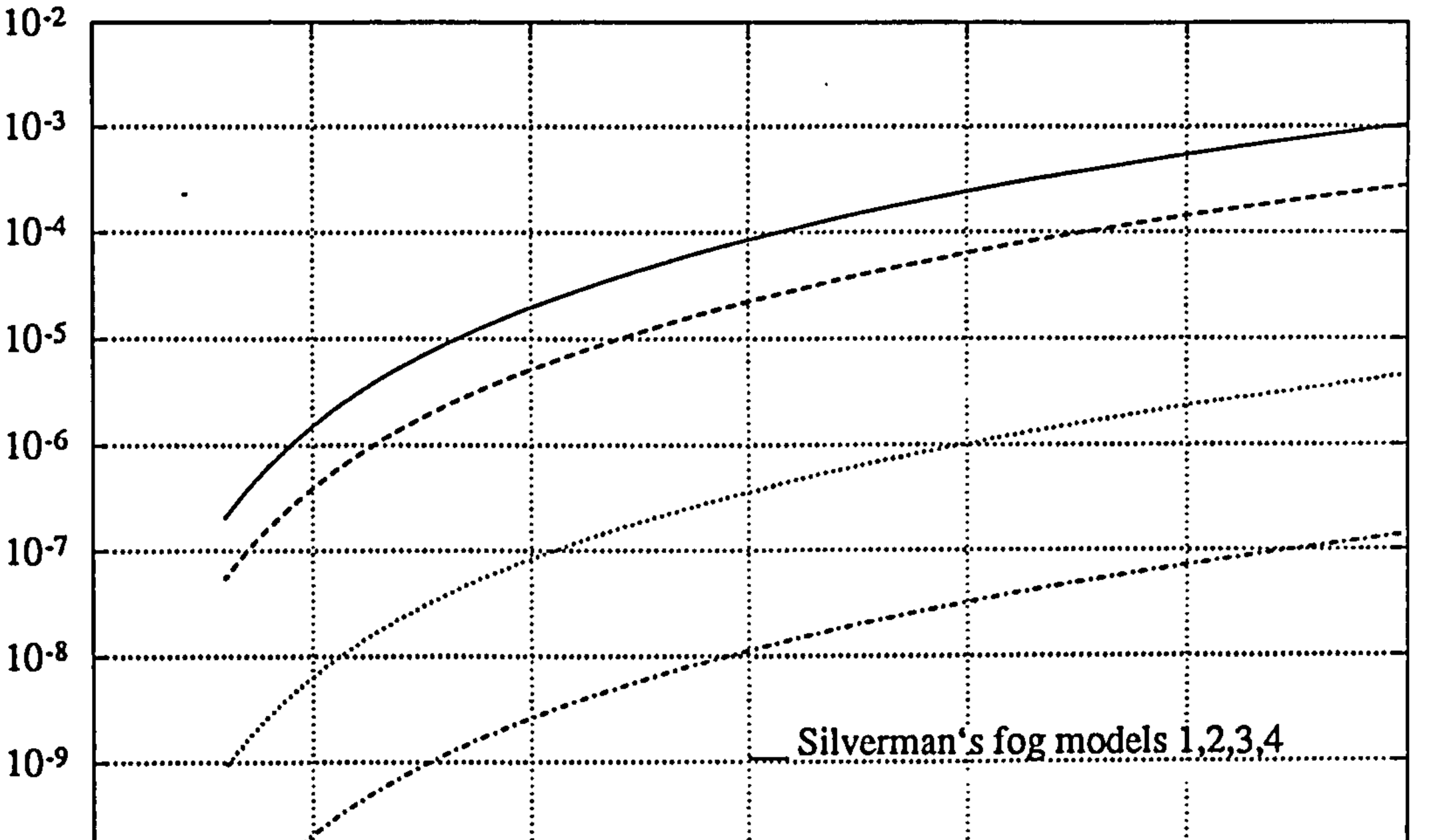

On the contrary, the attenuation and reflectivity resulting from advective fog are very significant (ie. α=0.1 dB/hm, $\beta=3\times10^{-6}$ hm^{-1} at 65 GHz) and compare well with those resulting from other non-precipitable clouds. Therefore, advective fog can not be distinguished from other non-precipitable clouds, unless the height of occurrence is known.

4.5.2 Stratiform clouds.

4.5.2.1 Stratus and Stratocumulus (St/Sc).

Calculations for stratus clouds can be seen in figures 20 and 21. Here Silverman's cloud models 9,10 and 11, Carrier's 6 and 1 and Ajvazyan's cloud model 2 have been considered. Table XIV summarizes the variation of the specific attenuation and reflectivity resulting from stratus clouds over the millimetre wave spectrum. The last row of the table gives the radar reflection coefficients resulting from Ajvazyan's cloud models for which the contribution of super-large drops has been taken into account.

Fig. 20. Specific attenuation for various stratus (St) models.

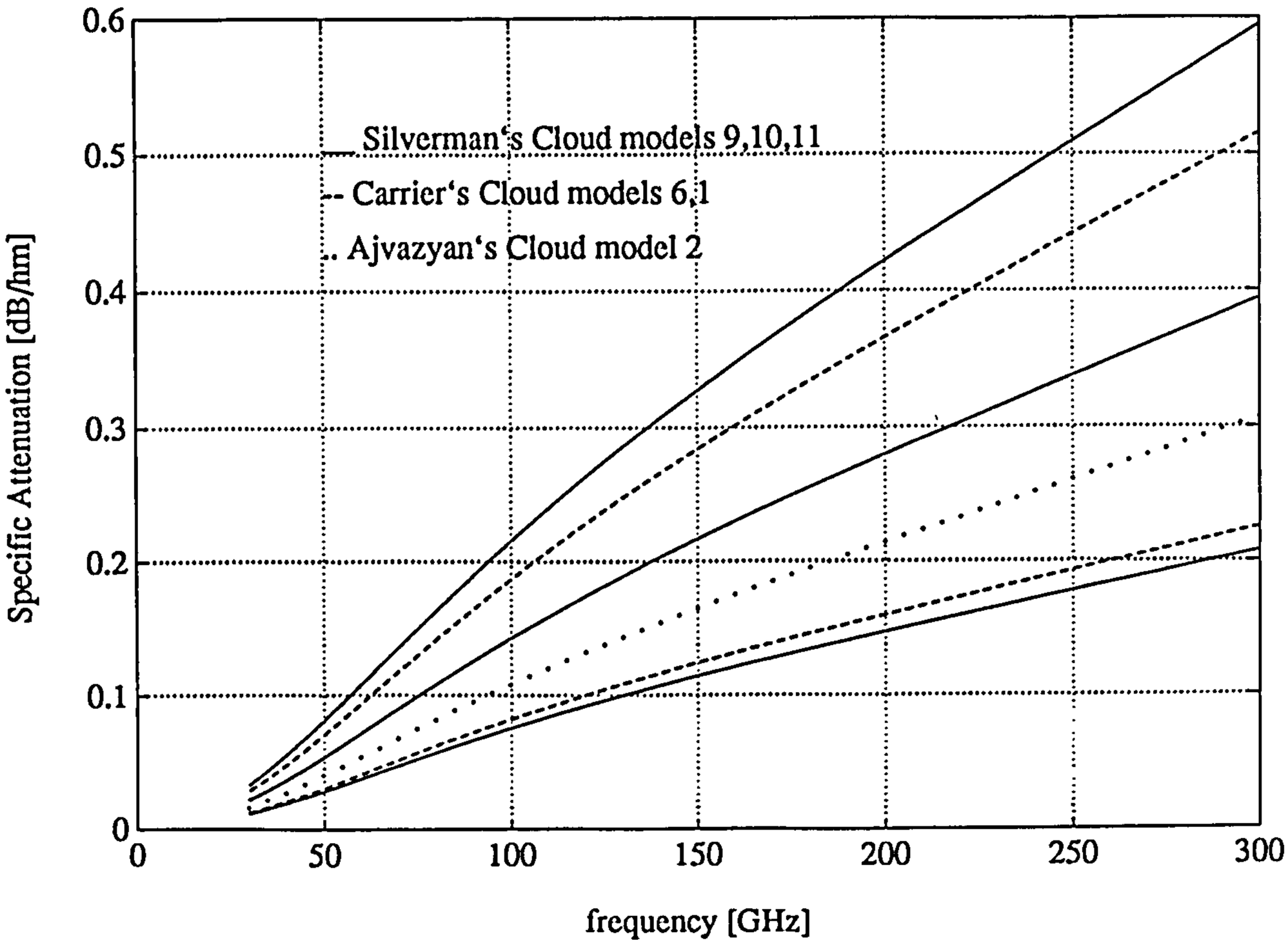

Fig. 21. Radar reflection coefficient for various stratus (St) clouds.

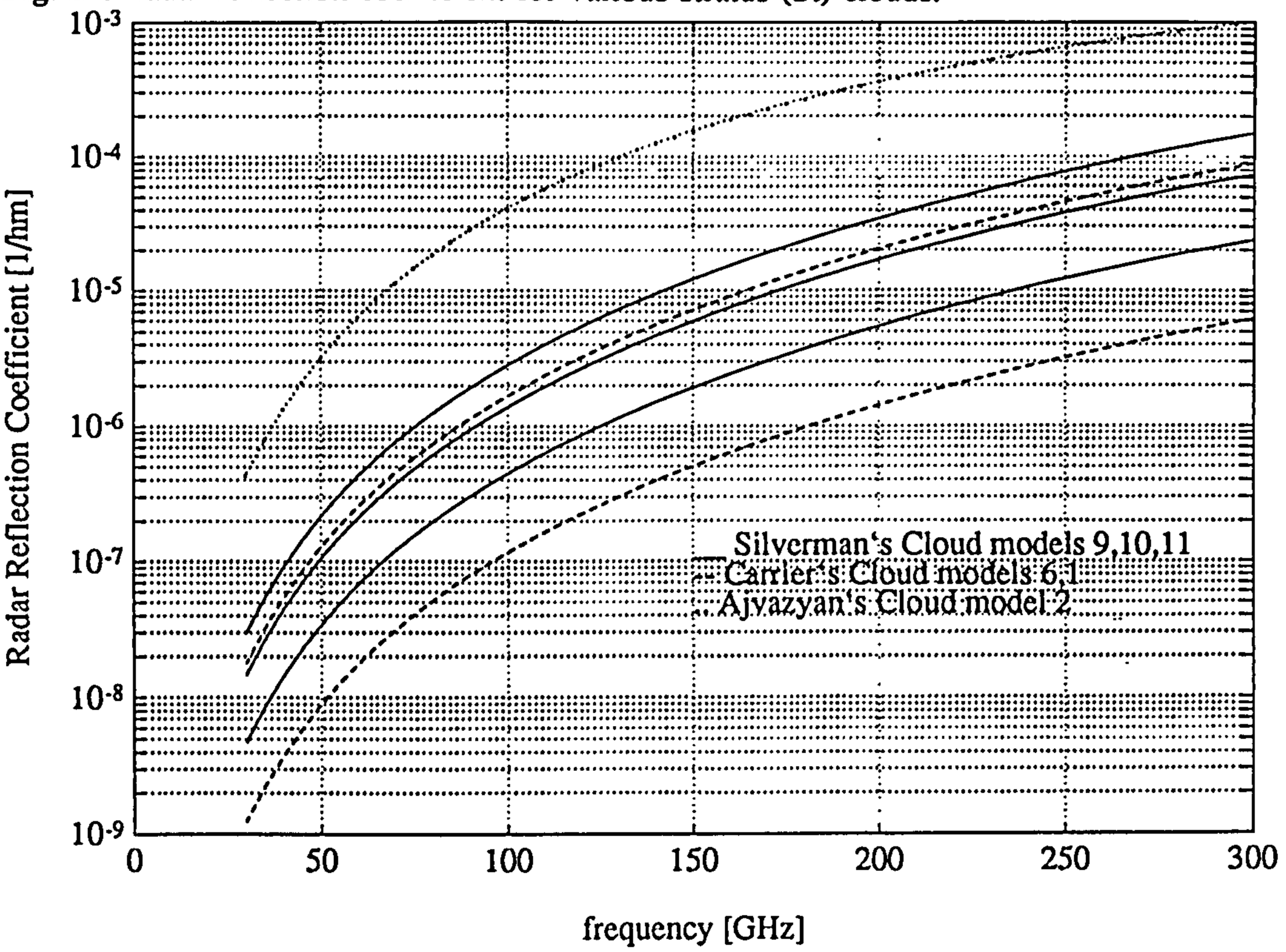

Table XIV. Specific attenuation and radar reflection coefficient values for St clouds.

f [GHz]	30		60		100		150		300	
	min	max	min	max	min	max	min	max	min	max
α [dB/hm]	0.01	0.03	0.03	0.1	0.07	0.22	0.12	0.33	0.21	0.60
β [hm^{-1}]	1e-9	3e-8	2e-8	5e-6	1e-7	3e-6	5e-7	1e-5	6e-6	2e-4
large drops		4e-7		6e-6		4e-5		1e-4		1e-3

Table XV. Specific attenuation and radar reflection coefficient values for Sc clouds.

f [GHz]	30		60		100		150		300	
	min	max	min	max	min	max	min	max	min	max
α [dB/hm]	0.02	0.05	0.04	0.12	0.10	0.27	0.15	0.43	0.30	0.77
β [hm^{-1}]	1e-8	5e-7	1e-7	1e-6	6e-7	4e-6	2e-6	1e-5	3e-5	2e-4
large drops		2e-6		3e-5		2e-4		6e-4		3e-3

Results for stratocumulus clouds may be found in figures 22 and 23. The calculations refer to Silverman's cloud models 7 and 12, Carrier's 3 and Ajvazyan's cloud model 1. Table XIV

Fig. 22. Specific attenuation for various stratocumulus (Sc) cloud models.

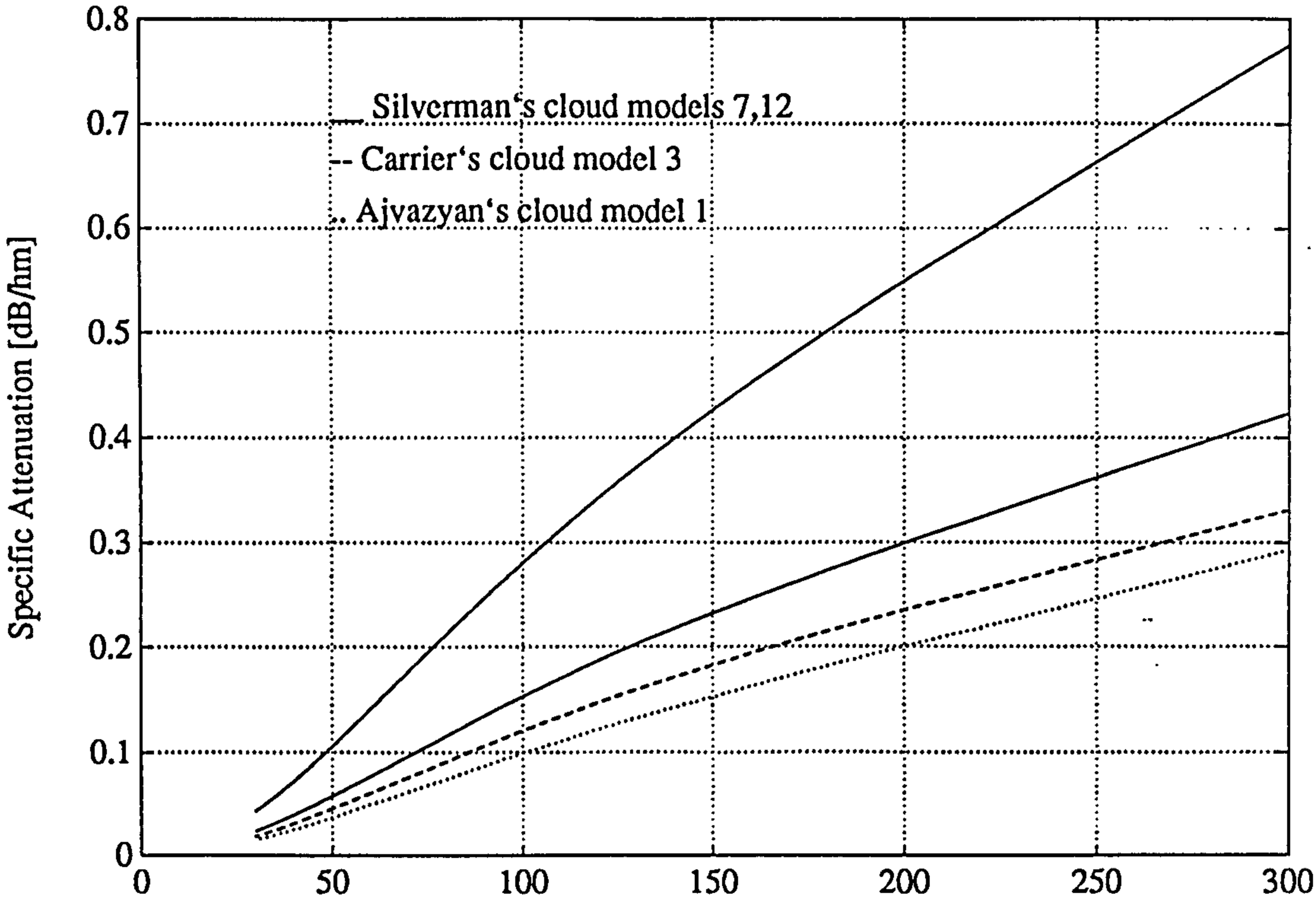

Fig. 23. Radar reflection coefficient for various stratocumulus (Sc) cloud models.

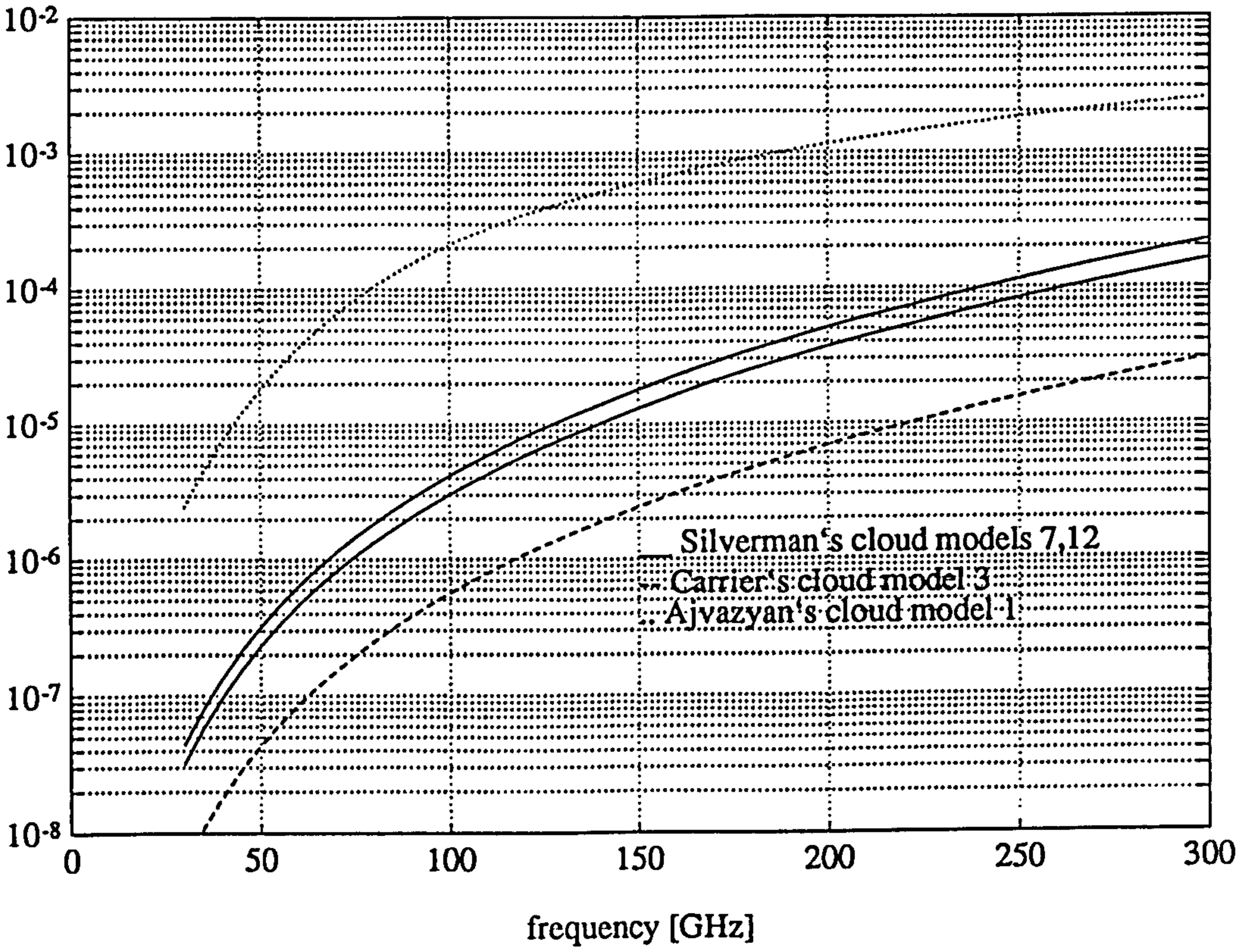

gives the variation of the specific attenuation and radar reflection coefficient of Sc clouds along the millimetre wave spectrum.

Generally, St and Sc clouds demonstrate the same extinction and backscattering properties. The presence of super-large drops does not affect the resultant attenuation but it certainly enhances the radar reflection coefficient by approximately one order of magnitude.

4.5.2.2 Altostratus and Nimbostratus (As/Ns).

Calculations for altostratus clouds may be seen in figures 24 and 25. Here, Silverman's cloud model 6, Carrier's 2 and Ajvazyan's cloud models 4 and 5 have been considered. Table XVI gives the variation of the specific attenuation and radar reflection coefficient of As clouds along the millimetre wave spectrum.

Fig. 24. Specific attenuation for various altostratus (As) cloud models.

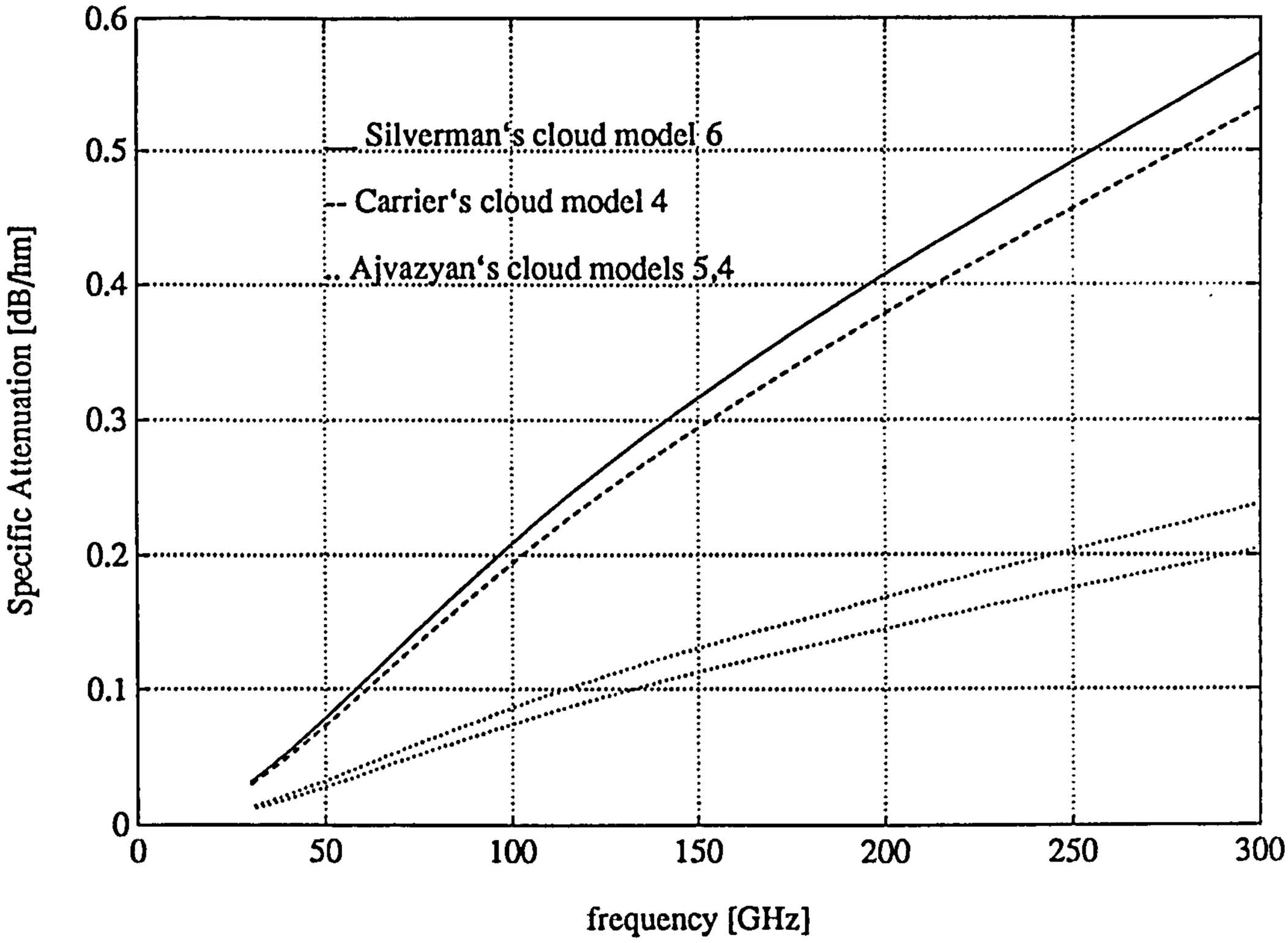

Fig. 25. Radar reflection coefficient for various altostratus (As) clouds.

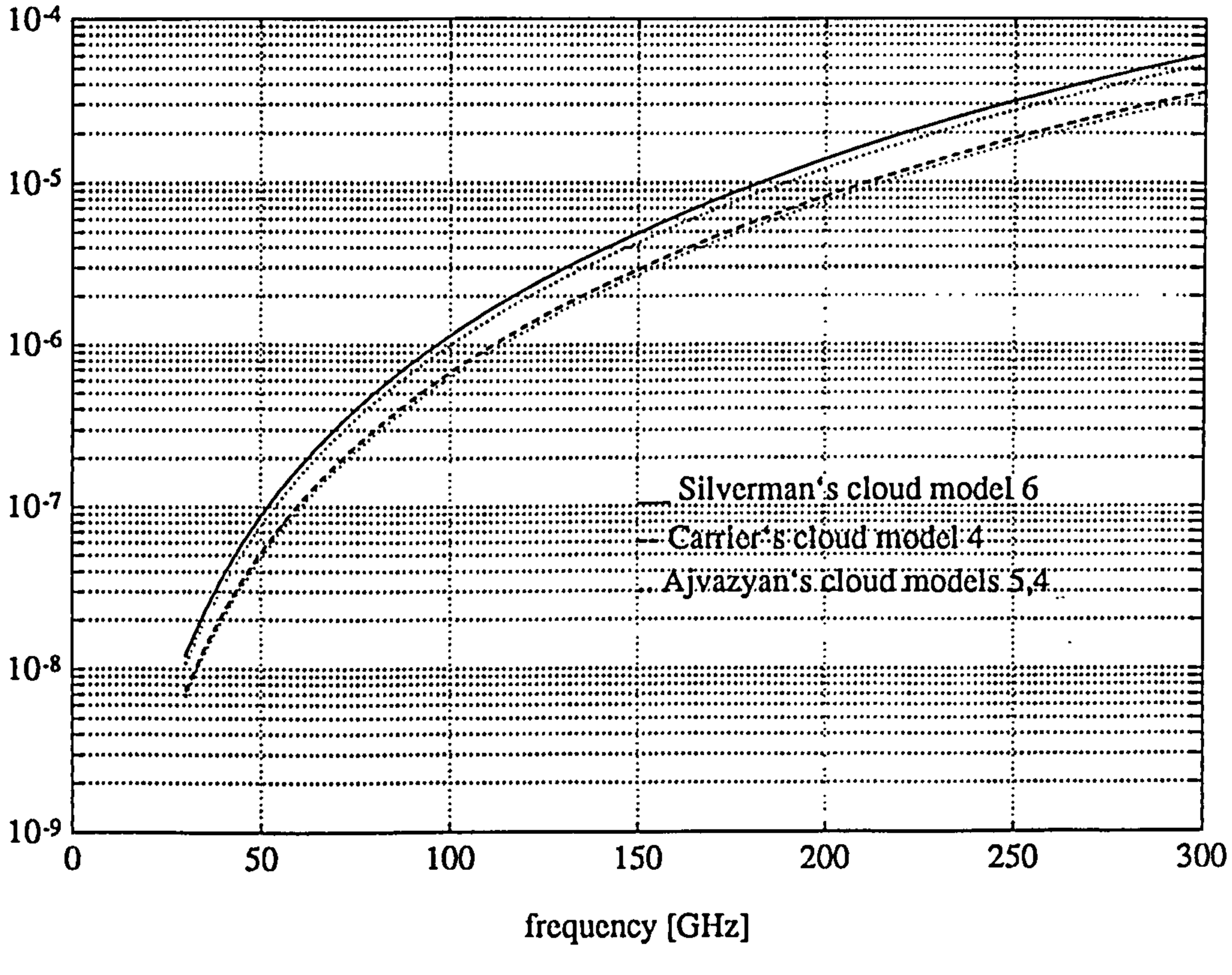

Table XVI. Specific attenuation and radar reflection coefficient values for As clouds.

f [GHz]	30		60		100		150		300	
	min	max	min	max	min	max	min	max	min	max
α [dB/hm]	0.01	0.03	0.03	0.10	0.07	0.21	0.12	0.32	0.20	0.57
β [hm^{-1}]	6e-9	1e-8	1e-7	2e-7	6e-7	1e-6	3e-6	5e-6	3e-5	6e-5

Results for nimbostratus clouds may be seen in figures 26 and 27. Silverman's cloud models 8 and 13, Carrier's 4 and Ajvazyan's cloud model 3 have been considered. Table XVII gives the variation of the specific attenuation and radar reflection coefficient of As clouds along the

Table XVII. Specific attenuation and radar reflection coefficient values for Ns clouds.

f [GHz]	30		60		100		150		300	
	min	max	min	max	min	max	min	max	min	max
α [dB/hm]	0.02	0.10	0.06	0.23	0.14	0.47	0.20	0.70	0.40	1.30
β [hm^{-1}]	5e-8	1e-7	6e-7	1e-6	5e-6	1e-5	2e-5	4e-5	2e-4	4e-4
large drops		2e-5		2e-4		4e-4		8e-4		2e-3

Fig. 26. Specific attenuation for various nimbostratus (Ns) cloud models.

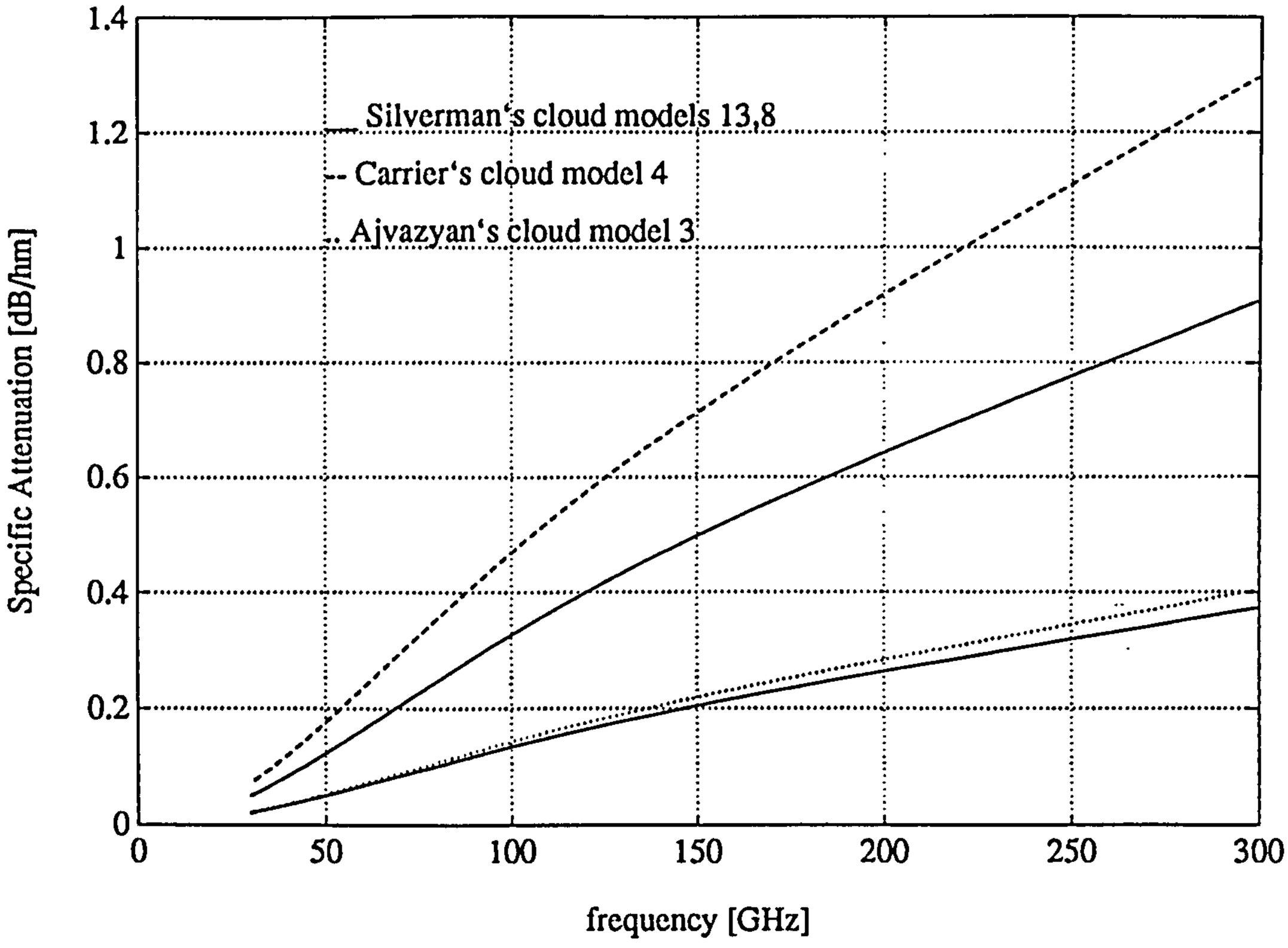

Fig. 27. Radar reflection coefficient for various nimbostratus (Ns) clouds.

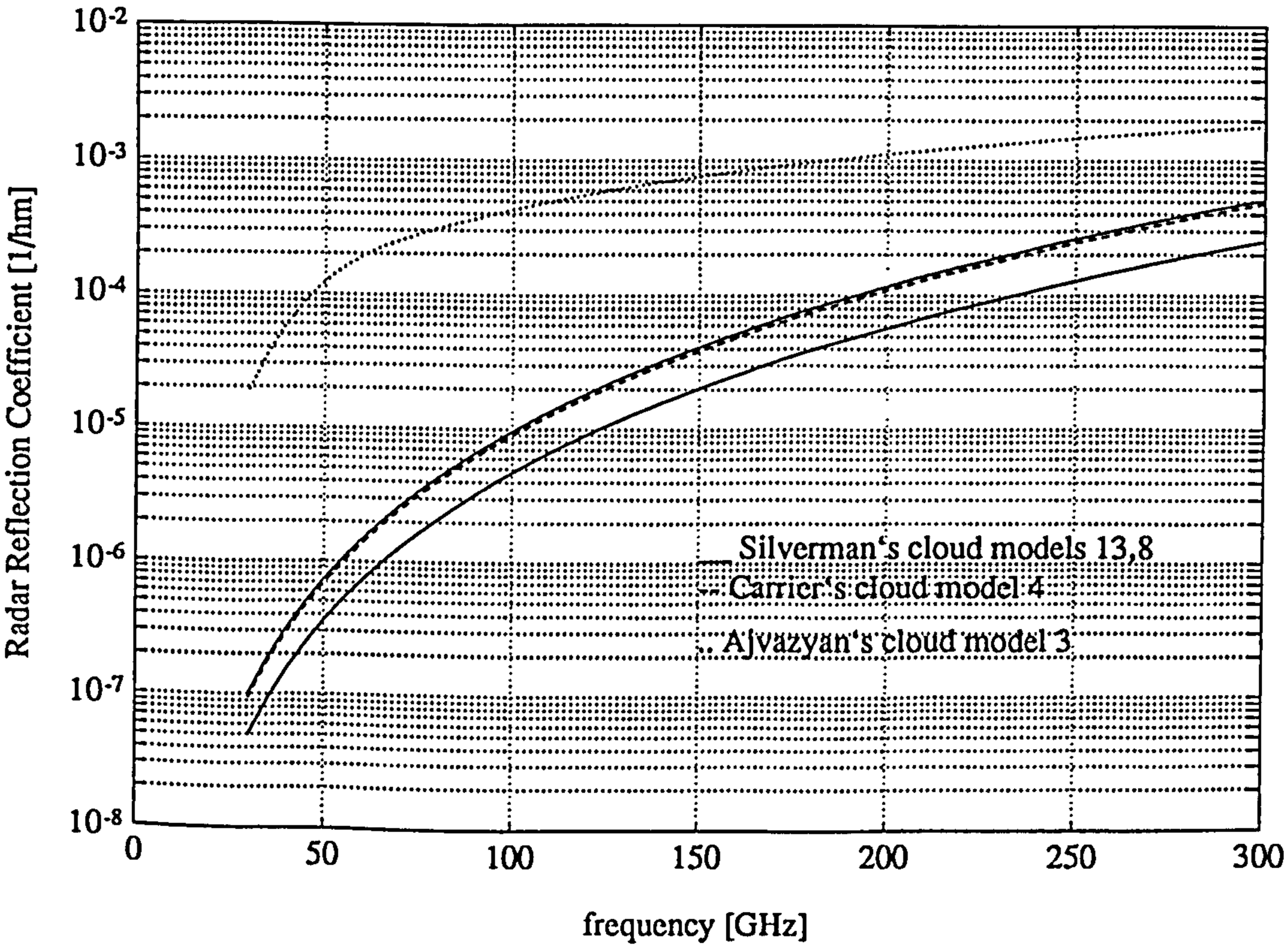

millimetre wave spectrum. Generally the resultant attenuation in Ns clouds is twice as much as in As and the radar reflection coefficient of Ns is one order of magnitude greater than the radar reflection coefficient of As, throughout the millimetre spectrum. Large drops enhance the reflection coefficient by somewhat less than two orders of magnitude for frequencies below 100 GHz, and by approximately one order of magnitude for frequencies above 100 GHz. Attenuation is insensitive to the presence of super-large drops.

4.5.3 Convective clouds.

4.5.3.1 Cumulus (Cu, Cu-hum, Cu-med, Cu-cong).

Results for cumulus clouds of various types may be seen in figures 28 and 29. Silverman's cloud models 5 and 14, Carrier's 7 and 5 and Ajvazyan's cloud models 10, 9 and 8 have been considered. Table XVIII gives the variation of the specific attenuation and radar reflection

Fig. 28. Specific attenuation for various cumulus (Cu) cloud models.

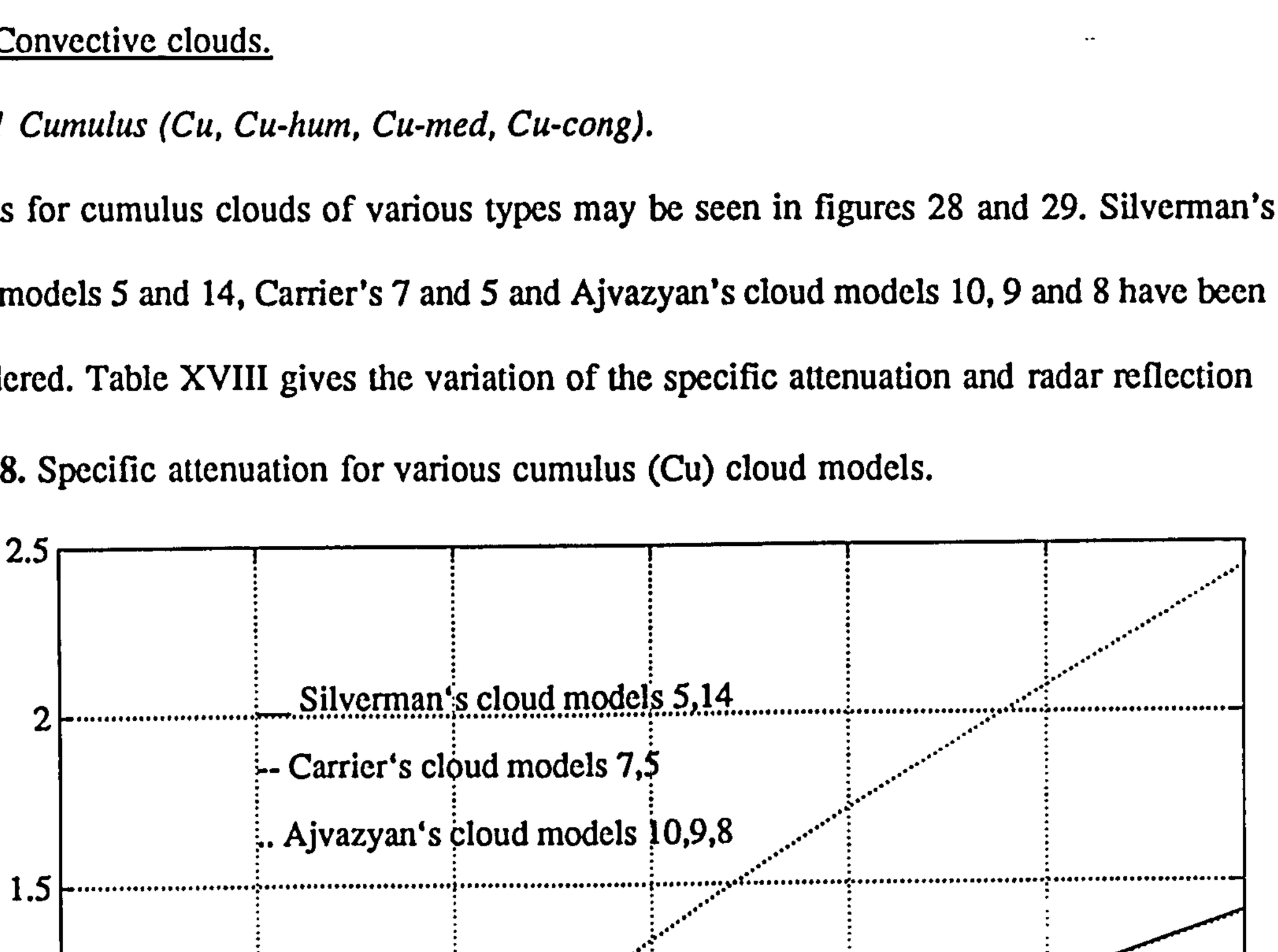

Fig. 29. Radar reflection coefficient for various (Cu) cumulus clouds.

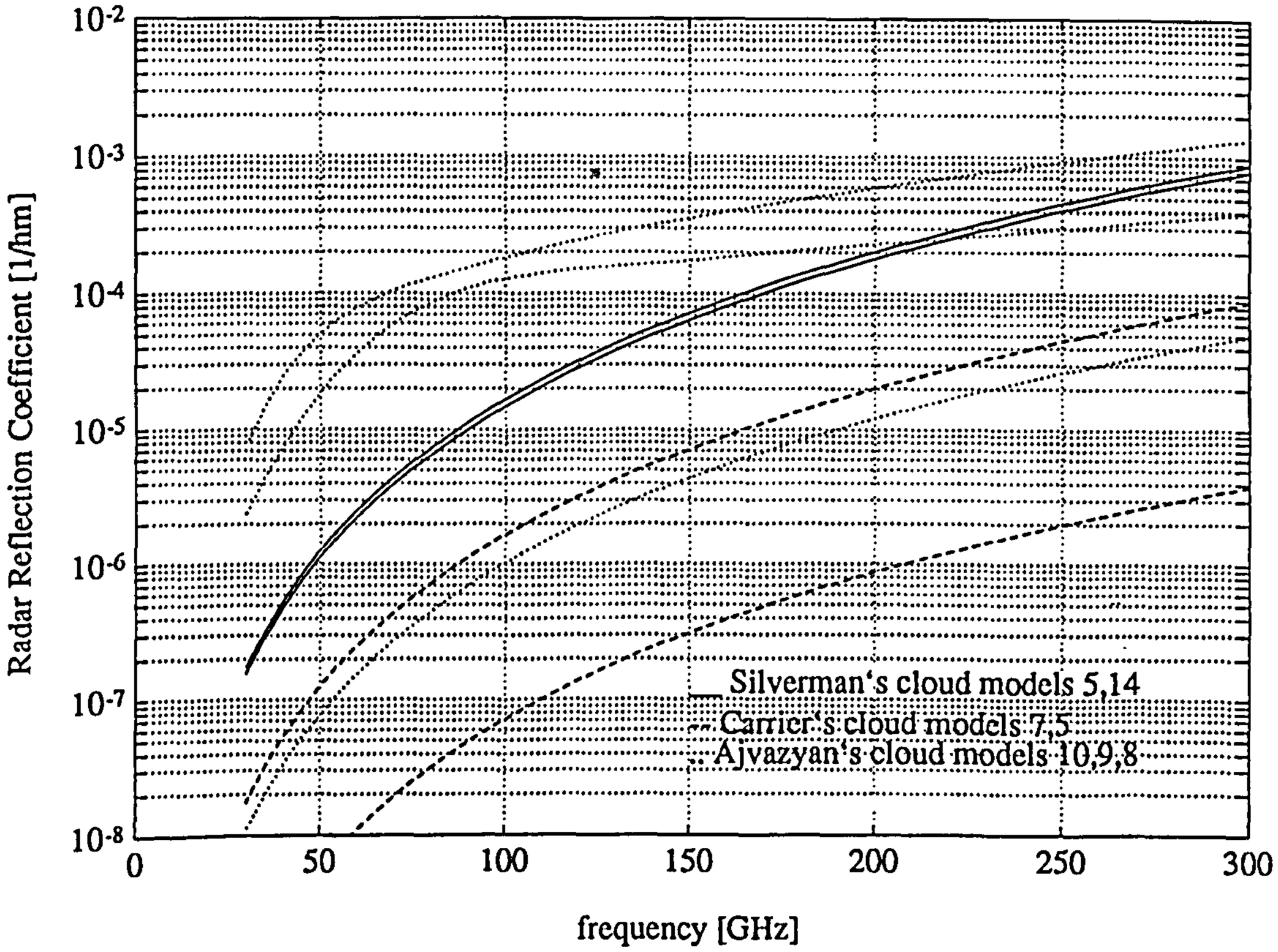

coefficient of As clouds along the millimetre wave spectrum. These clouds which are usually associated with high liquid water contents and large concentrations of super-large drops are heavily attenuating. Even at 100 GHz the attenuation resulting from a 2 km deep Cu-cong cloud is 17 dB (maximum). Super-large drops do not affect attenuation, but the radar reflection coefficient is enhanced by about somewhat less than one order of magnitude.

Table XVIII. Specific attenuation and radar reflection coefficient values for various Cu clouds.

f [GHz]	30		60		100		150		300	
	min	max	min	max	min	max	min	max	min	max
α [dB/hm]	0.02	0.20	0.04	0.40	0.06	0.85	0.08	1.33	0.15	2.40
β [hm^{-1}]	2e-9	2e-7	1e-8	2e-6	7e-8	2e-5	3e-7	7e-5	4e-6	9e-4
large drops	1e-8	8e-5	1e-7	7e-5	1e-6	2e-4	4e-6	4e-4	5e-5	1e-3

4.5.3.2 Cumulonimbus (Cb).

Calculations for cumulonimbus clouds may be seen in figures 30 and 31. Here, Carrier's

cloud model 8 and Ajvazyan's cloud models 13 and 14 have been considered. Table XIX gives the variation of the specific attenuation and radar reflection coefficient of Cb clouds along the millimetre wave spectrum. Carrier's model has not been taken into account in the compilation of table XIX, as not being representative for this particular type of cloud. Cb clouds which are usually associated with severe thunderstorms bear high lwc, typically greater than 2 g/m^3. Carrier quotes a lwc of 0.16 g/m^3 for his Cb cloud model, which is far from what is commonly accepted. There is a possibility though that Carrier's model refers to a very early stage of the cloud development where from the low lwc originates.

Table XIX. Specific attenuation and radar reflection coefficient values for Cb clouds.

f [GHz]	30		60		100		150		300	
	min	max	min	max	min	max	min	max	min	max
α [dB/hm]	0.25	0.45	0.70	1.40	1.60	3.10	2.50	4.50	4.65	7.25
β [hm^{-1}]	7e-5	6e-3	1e-3	7e-2	7e-3	1e-1	1e-2	1e-1	3e-2	1e-1

Fig. 30. Specific attenuation for various cumulonimbus (Cb) clouds.

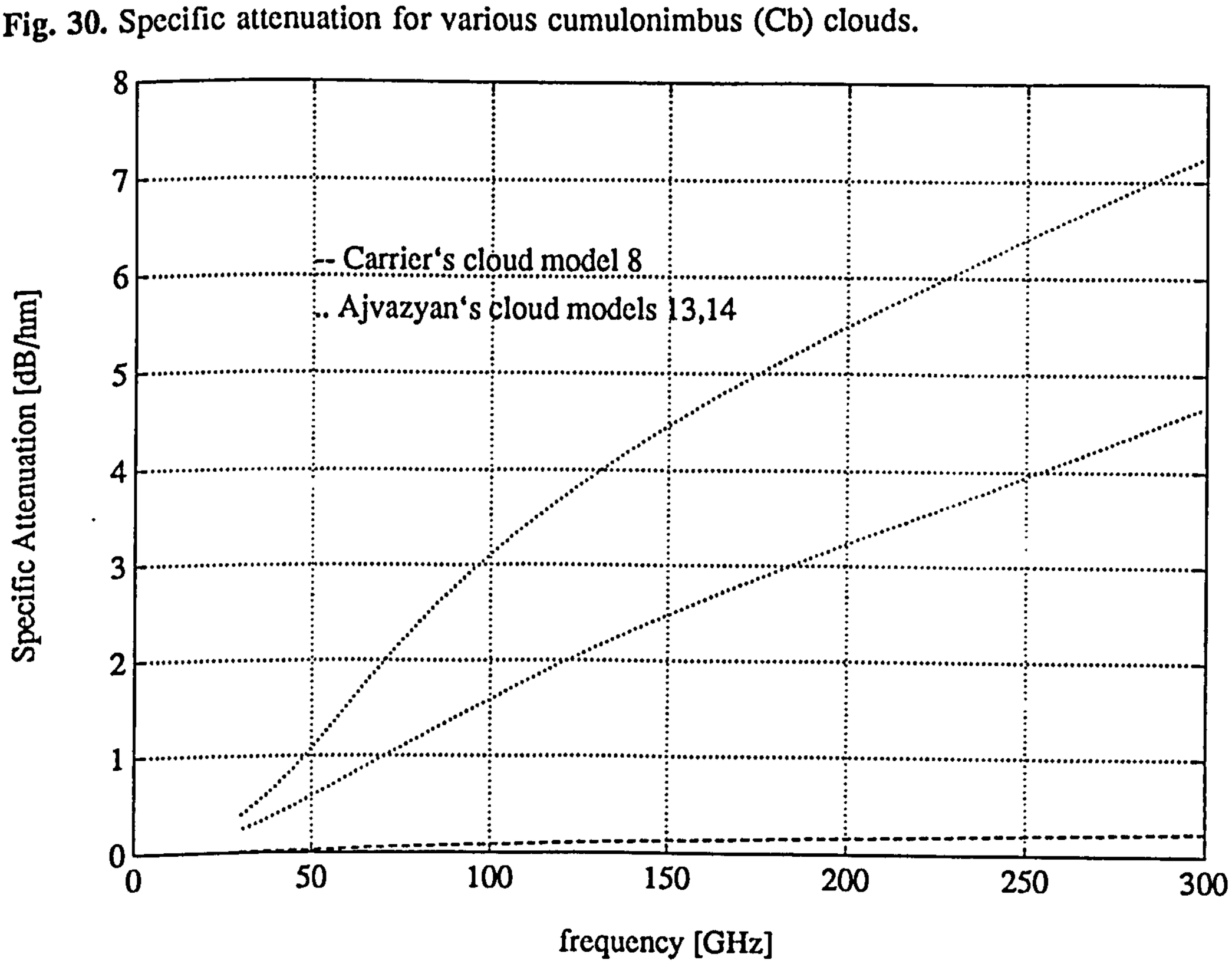

Fig. 31. Radar reflection coefficient for various cumulonimbus (Cb) clouds.

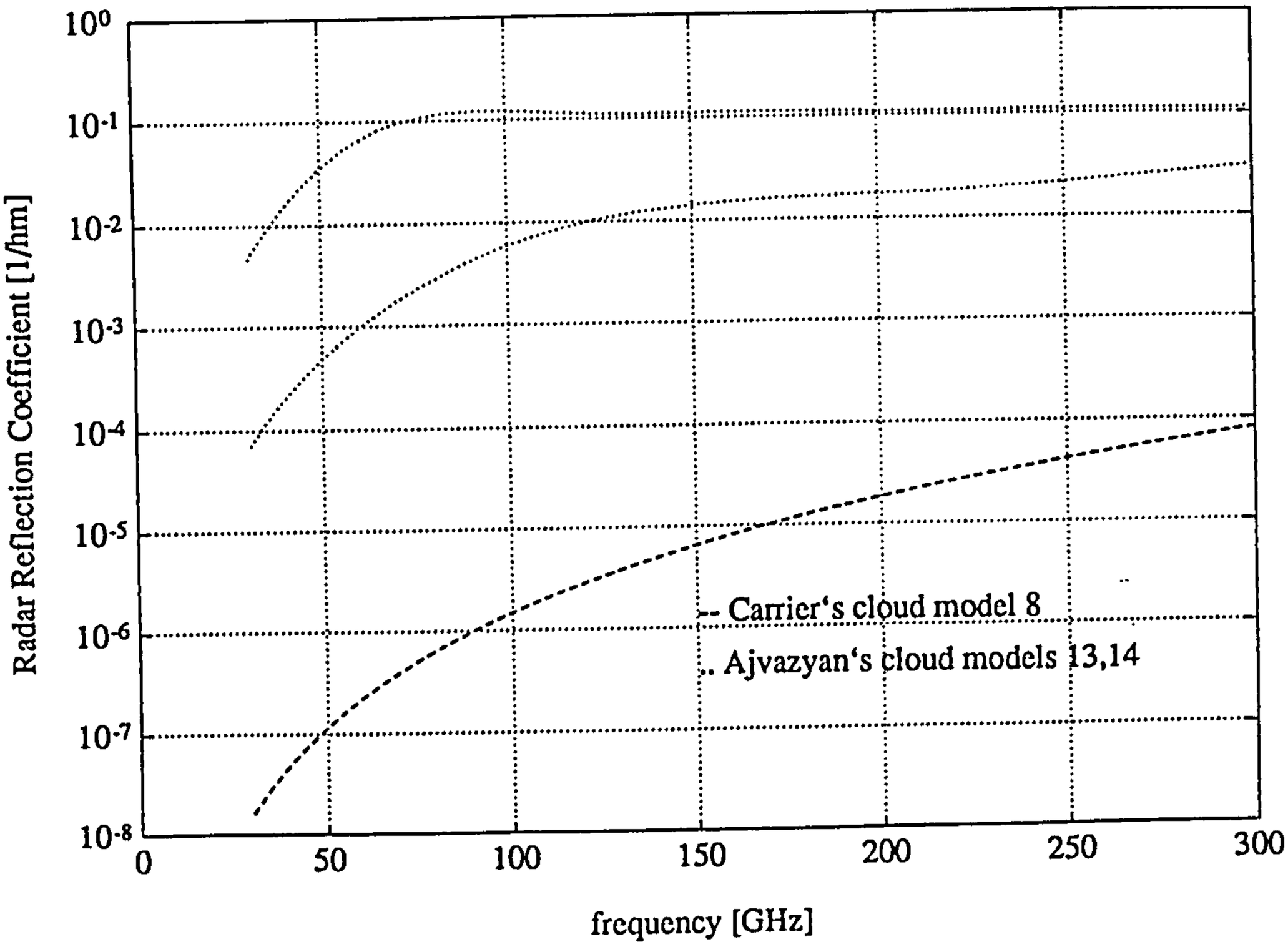

4.5.4 Cirrus (Ci).

Since the sampling instruments used in the FIRE/ICE experiments to sample particle sizes in Ci clouds were not able to pick up the largest particles, it is difficult to know exactly where the exponential size distribution should be truncated. For Ci clouds with high ice content, the contribution of larger particles is significant both to attenuation and reflection coefficient. Figures 32 and 33 illustrate this, showing the resultant attenuation and reflection coefficient at various frequencies for the Ci cloud models 1 and 7 of table X, truncated at r=150, 300 and 1000 μm. For Ci clouds with low ice content, the effect of truncation is not so pronounced. Based upon Weickman's observations (see table IX), ice particles with equivolumetric radius greater than 300 μm are unlikely to be found in such clouds. So, in the following calculations a truncation size limit of r=300 μm has been adopted.

Fig. 32. Effect of truncation of size spectra on attenuation and radar reflection coefficient for M.O. Ci cloud model 1.

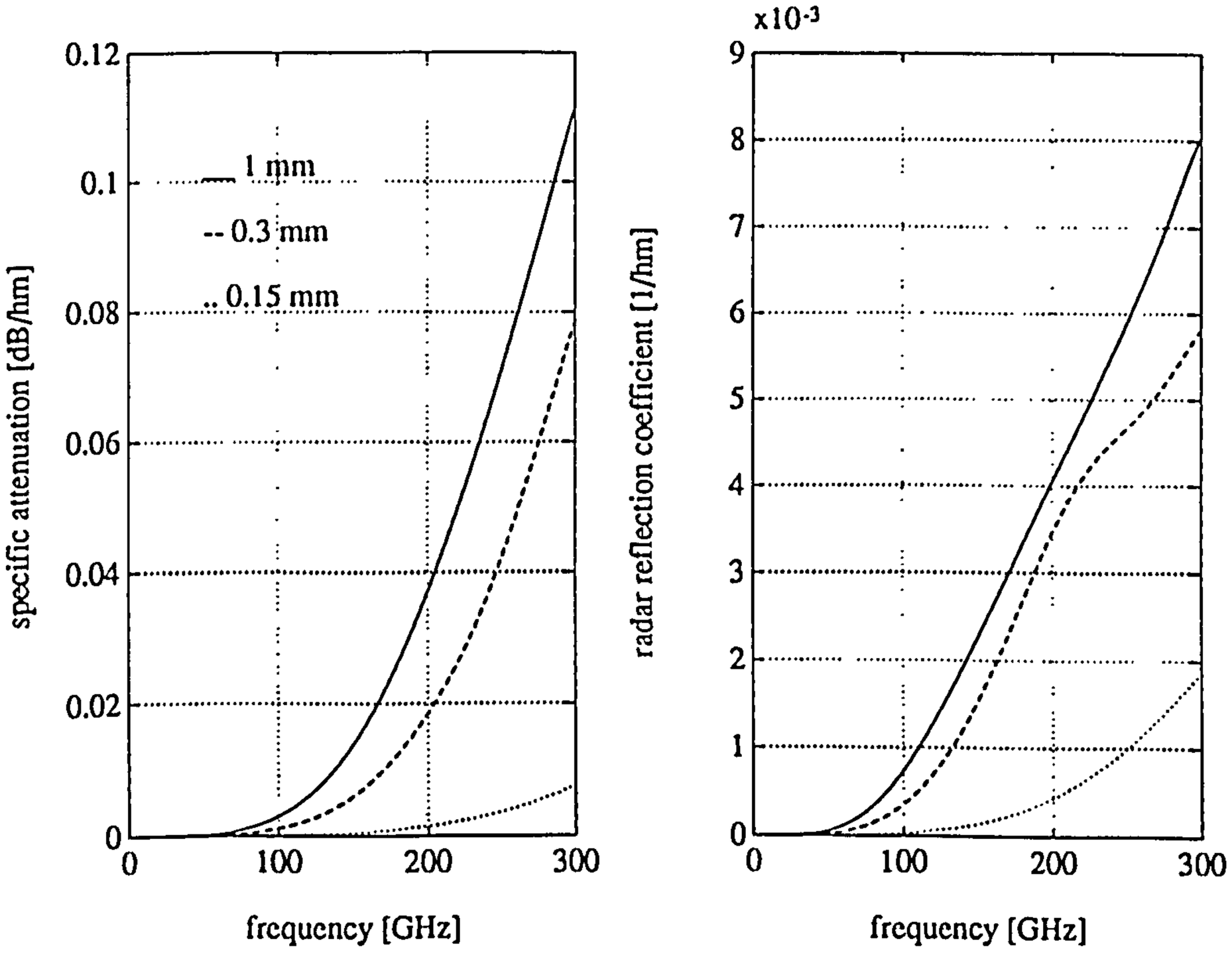

Fig. 33. Effect of truncation of size spectra on attenuation and radar reflection coefficient for M.O. Ci cloud model 7.

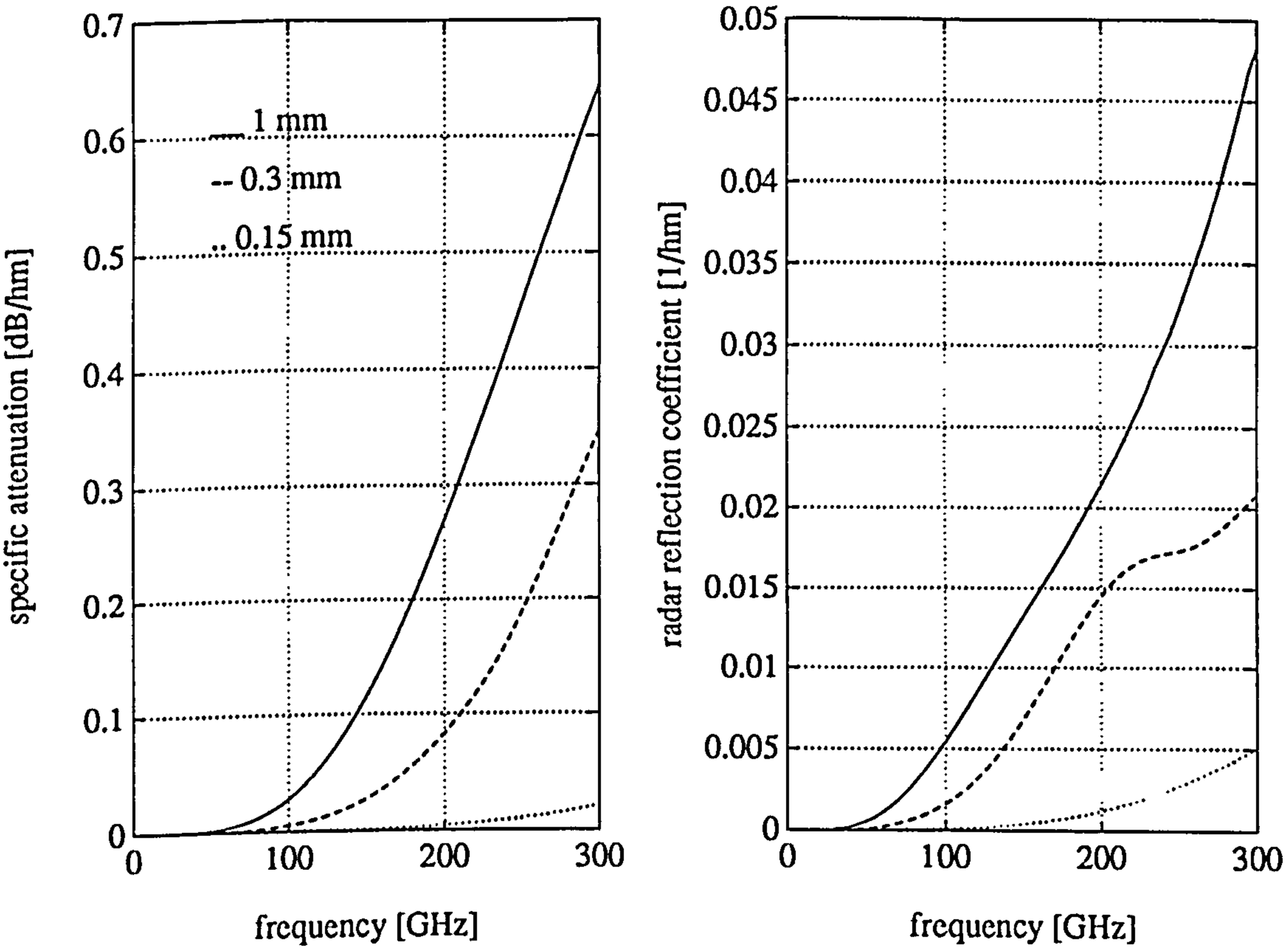

Fig. 34. Specific attenuation for the nine Ci cloud models of Met. Office.

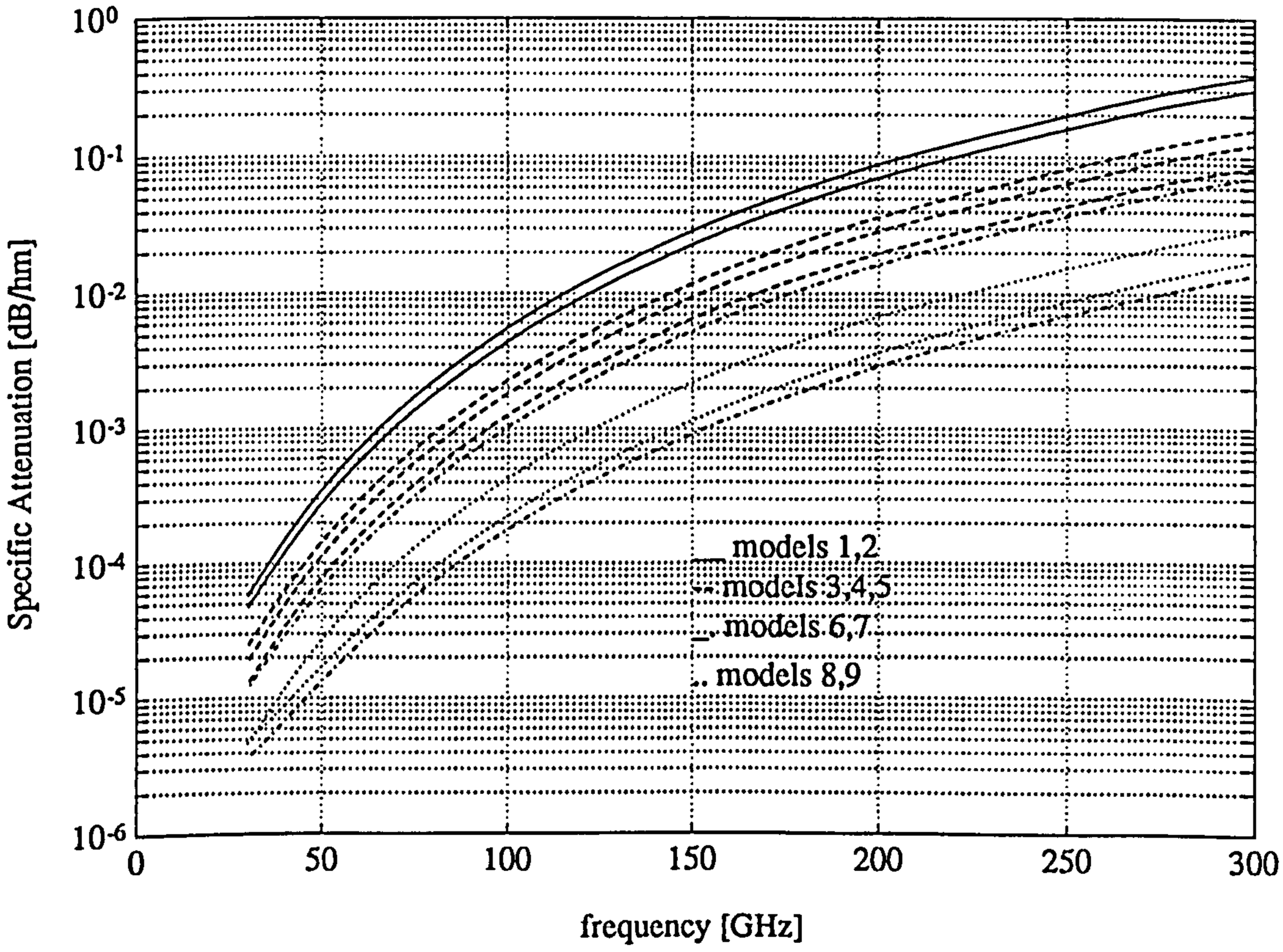

Fig. 35. Radar reflection coefficient for the nine Ci cloud models of the Met. Office.

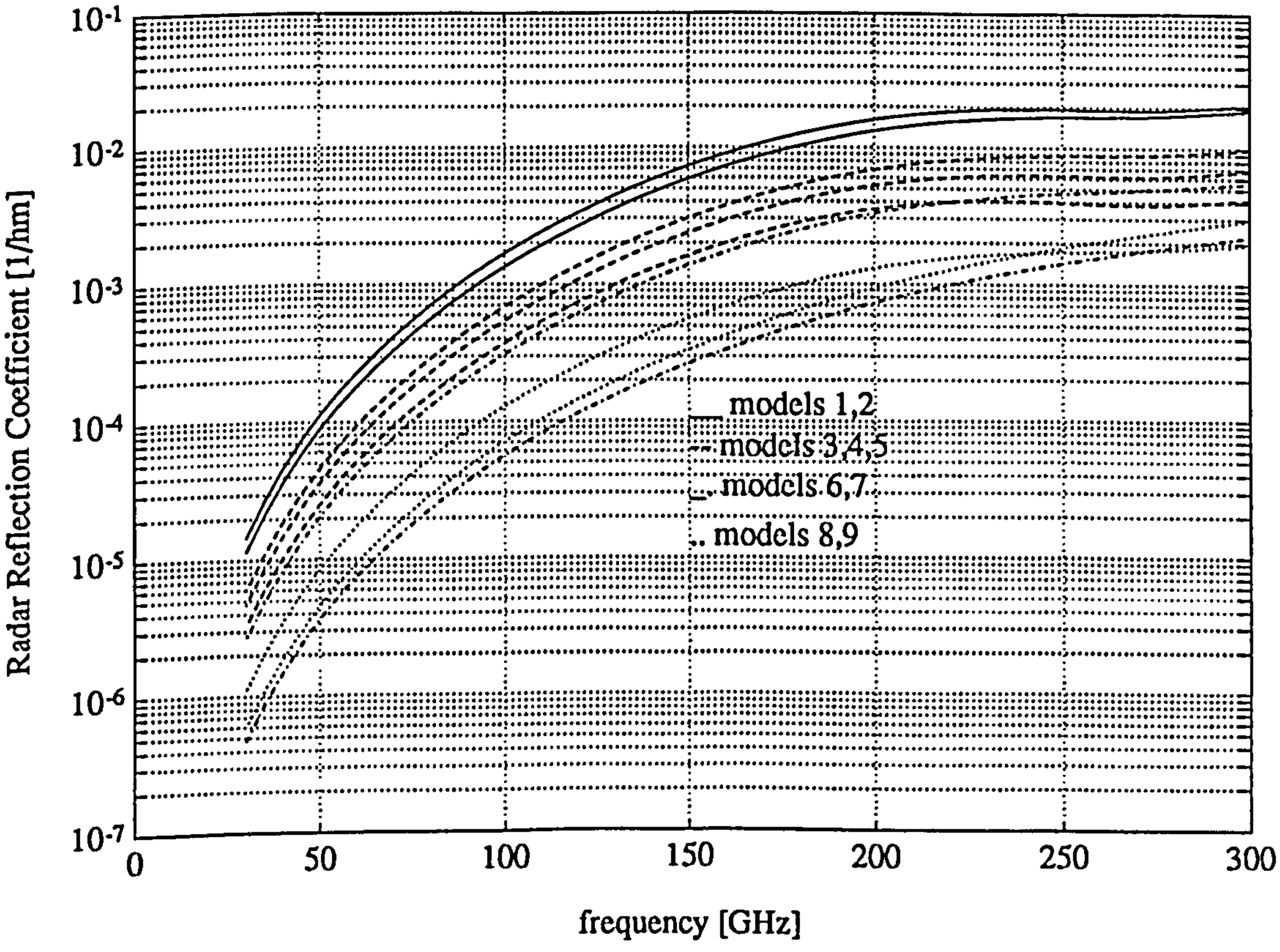

Calculations for the nine models of the Meteorological Office, may be seen in figures 34 and 35. The variation of the attenuation and radar reflection coefficient with frequency is given in table XX.

Table XX. Specific attenuation and radar reflection coefficient values for the Ci cloud models of the Meteorological Office.

f [GHz]	30		60		100		150		300	
	min	max	min	max	min	max	min	max	min	max
α [dB/hm]	1e-5	1e-4	5e-5	2e-3	4e-4	1e-2	2e-3	7e-2	3e-2	1e-2
β [hm^{-1}]	1e-6	4e-5	2e-5	5e-4	1e-4	4e-3	6e-4	2e-2	1e-2	8e-2

Table XXI. Specific attenuation and radar reflection coefficient values for the monodispersive Ci cloud models of table XI.

f [GHz]	30		60		100		150		300	
	min	max	min	max	min	max	min	max	min	max
α [dB/hm]	4e-6	6e-5	2e-5	6e-4	2e-4	6e-3	1e-3	3e-2	1e-2	4e-1
β [hm^{-1}]	5e-7	2e-5	6e-6	2e-4	6e-5	2e-3	3e-4	7e-3	2e-3	2e-2

Results for the monodispersive cirrus cloud models of table XI may be seen in figures 36 and 37. The lesser the concentration of the ice particles for a given ice content, the higher the resultant attenuation and radar reflection coefficient. For example, the specific attenuation resulting from cloud model 4 is five times higher than that resulting from cloud model 6, despite the fact that the two clouds have the same ice content. The variation of the attenuation and radar reflection coefficient with frequency is given in table XXI.

The calculations have been repeated for water, assuming the same mass content and concentration, so that a comparison between the resultant attenuation and reflection coefficient of ice crystals and water droplets is possible. Results for both ice and water can be seen in figure 38, where the minimum and maximum values of the resultant attenuation and reflection coefficient are shown.

Fig. 36. Specific attenuation for the monodispersive cirrus (Ci) clouds of table XI.

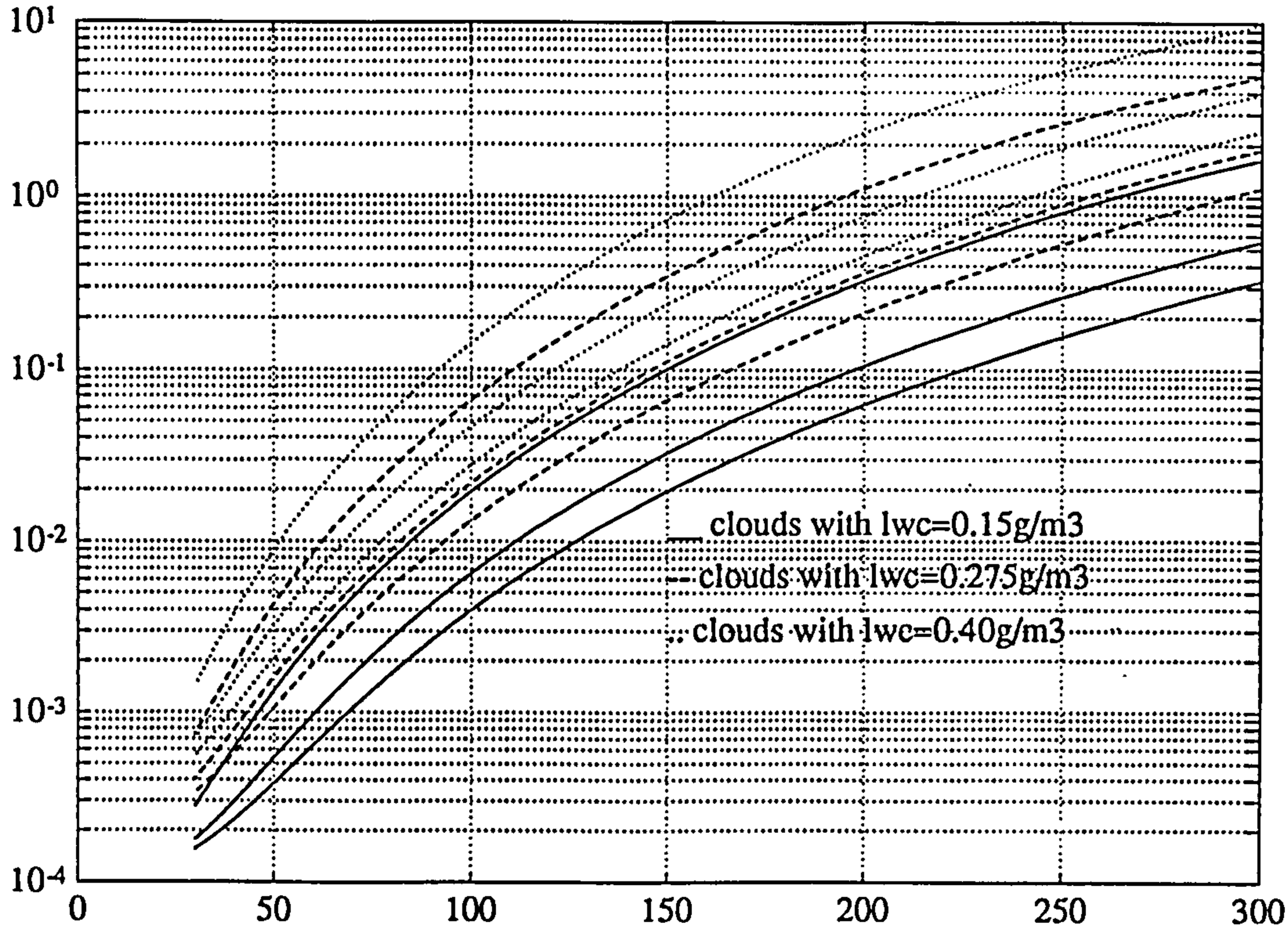

Fig. 37. Radar reflection coefficient for the monodispersive cirrus (Ci) models of table XI.

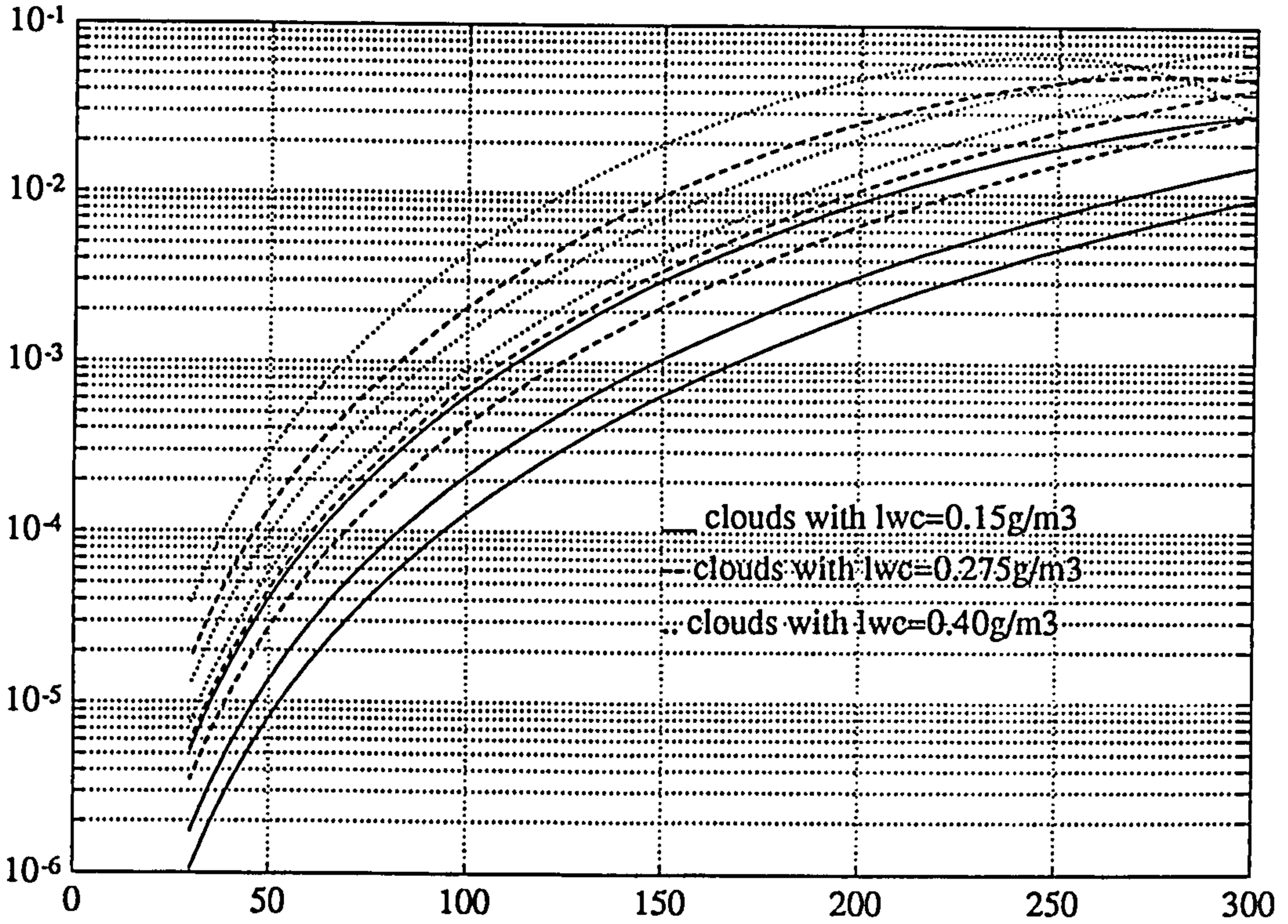

Fig. 38. Comparison between the ice and water attenuation and radar reflection coefficient resulting from the monodispersive cloud models of table XI.

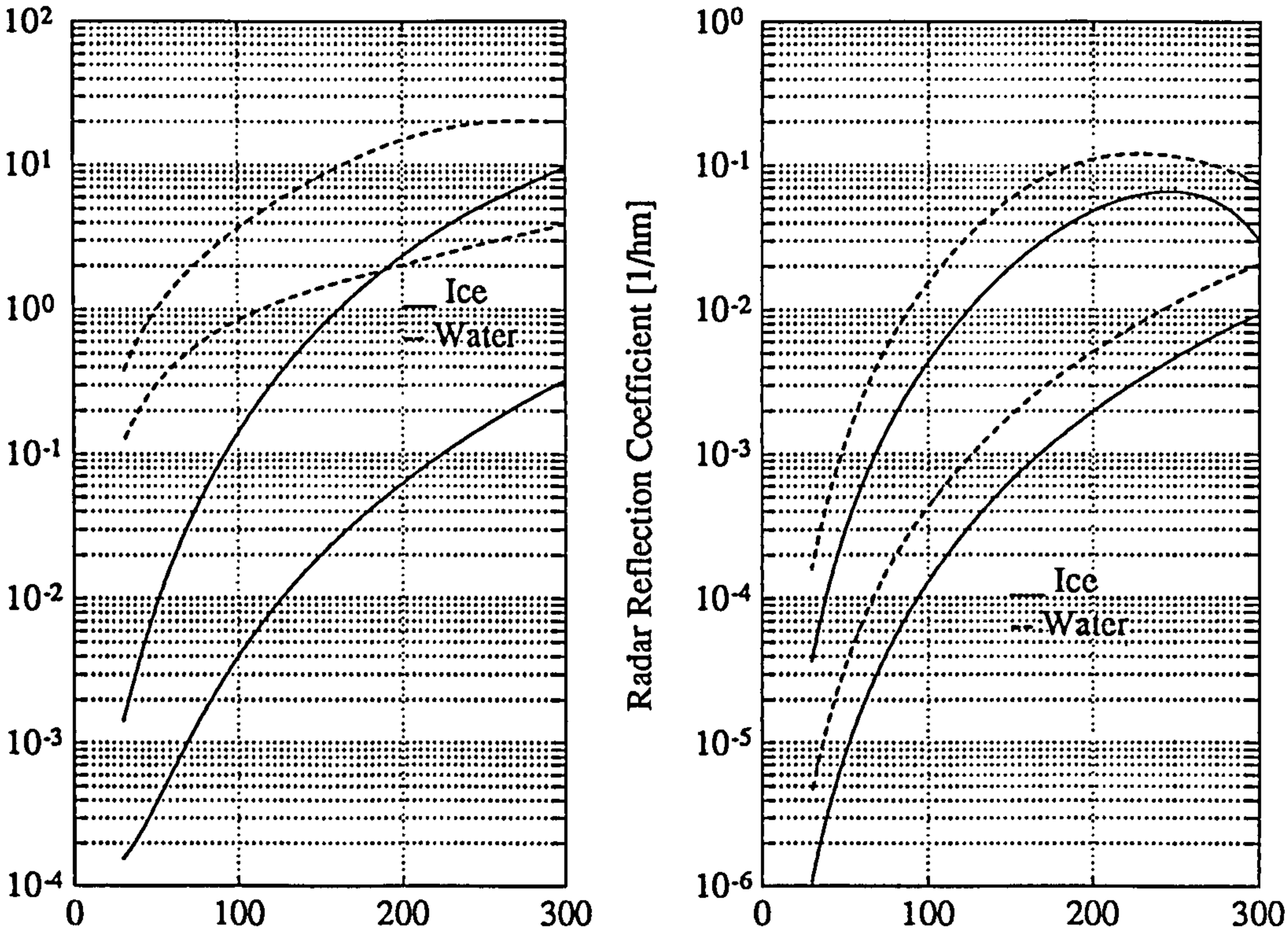

In conclusion for frequencies above 60 GHz the attenuation due to ice is not negligible, but below 100 GHz it is quite small. Attenuation due to cirrus clouds becomes important for frequencies above 150 GHz and comparable to that of water above 200 GHz. The radar reflection coefficient of cirrus clouds, is very high and comparable to that of water throughout the millimetre wave spectrum. Since in cirrus clouds attenuation is very small for frequencies below 100 GHz, these clouds can be easily identified by millimetre wave cloud radars. Values of the equivalent reflectivity are expected on the average to be around 0 dBZ.

4.6 The effect of super-large drops on the extinction and back scattering of clouds.

In the preceding sections specific attenuation and radar reflectivity calculations for the cloud models of Silverman, Carrier and Ajvazyan were presented. In these calculations the spectra of large drops were taken into account only for Ajvazyan's cloud models so that a comparison

with the results from the models of Silverman and Carrier became possible. It was seen that super-large drops may enhance the resultant radar reflection coefficient even by two orders of magnitude. This observation proves to be quite critical if millimetre wave radars are to be employed for the identification of various cloud types. Therefore the effect of super large drops on the resultant attenuation and reflectivity ought to be assessed in further detail. Results which summarize the effect of super-large drops in clouds may be seen in figures 39 and 40, respectively. Here, the specific attenuation and radar reflection coefficient calculations for Ajvazyan's selected cloud models are illustrated. The results shown with the continuous line refer to calculations for which only the spectra of small drops have been considered. The results depicted with the dashed line include the spectra of super-large drops so that the comparison becomes possible. For stratiform clouds (Sc, Ns) or cumuliform clouds (Cu-cong) with low concentrations of super-large drops (typically less than 500 m^{-3}) the attenuation increases slightly, but the radar reflection coefficient may increase by two orders of magnitude.

Fig. 39. Effect of super-large drops on the resultant attenuation for various cloud types.

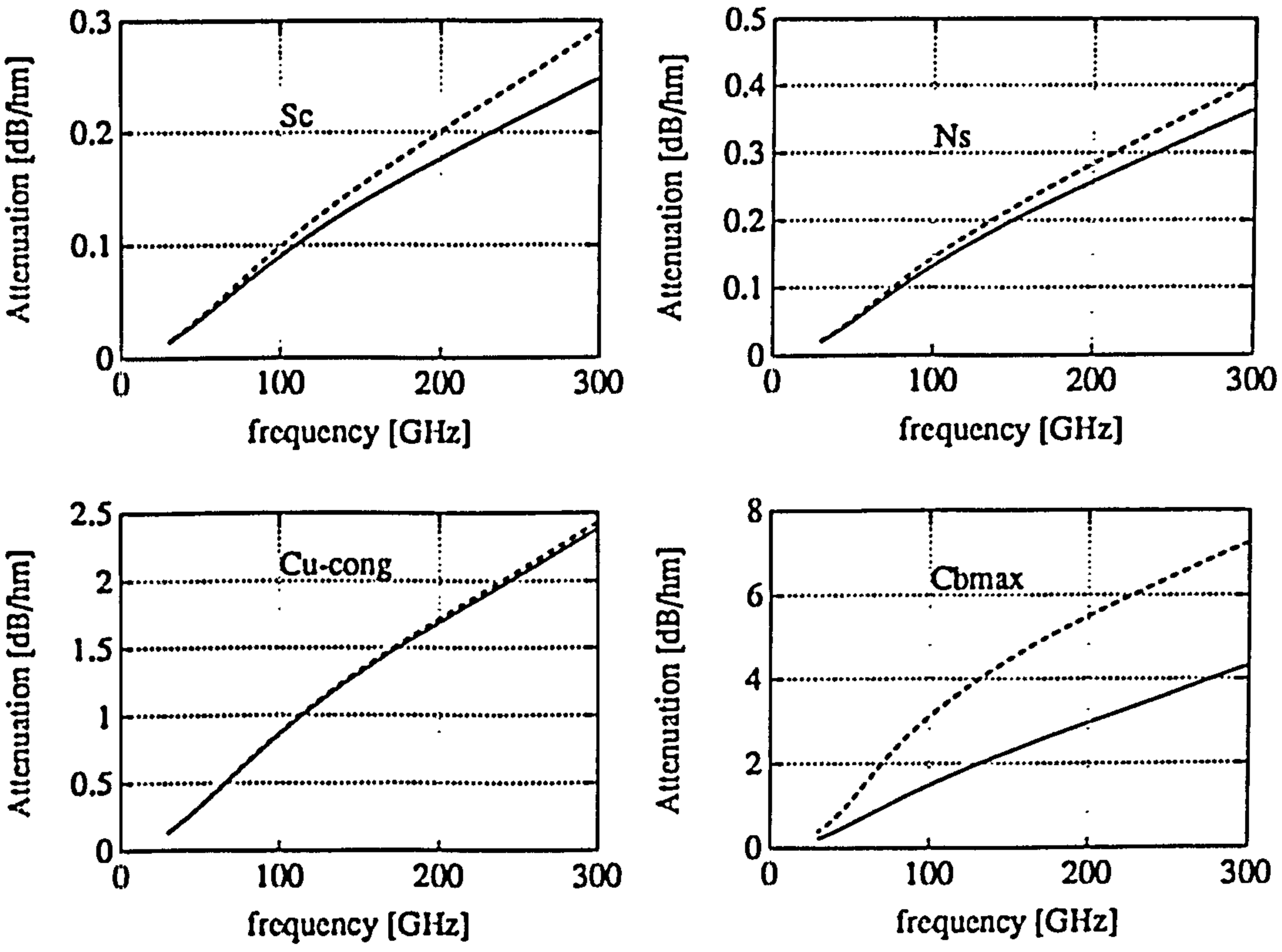

Fig. 40. Effect of super-large drops on the resultant radar reflection coefficient for various cloud types.

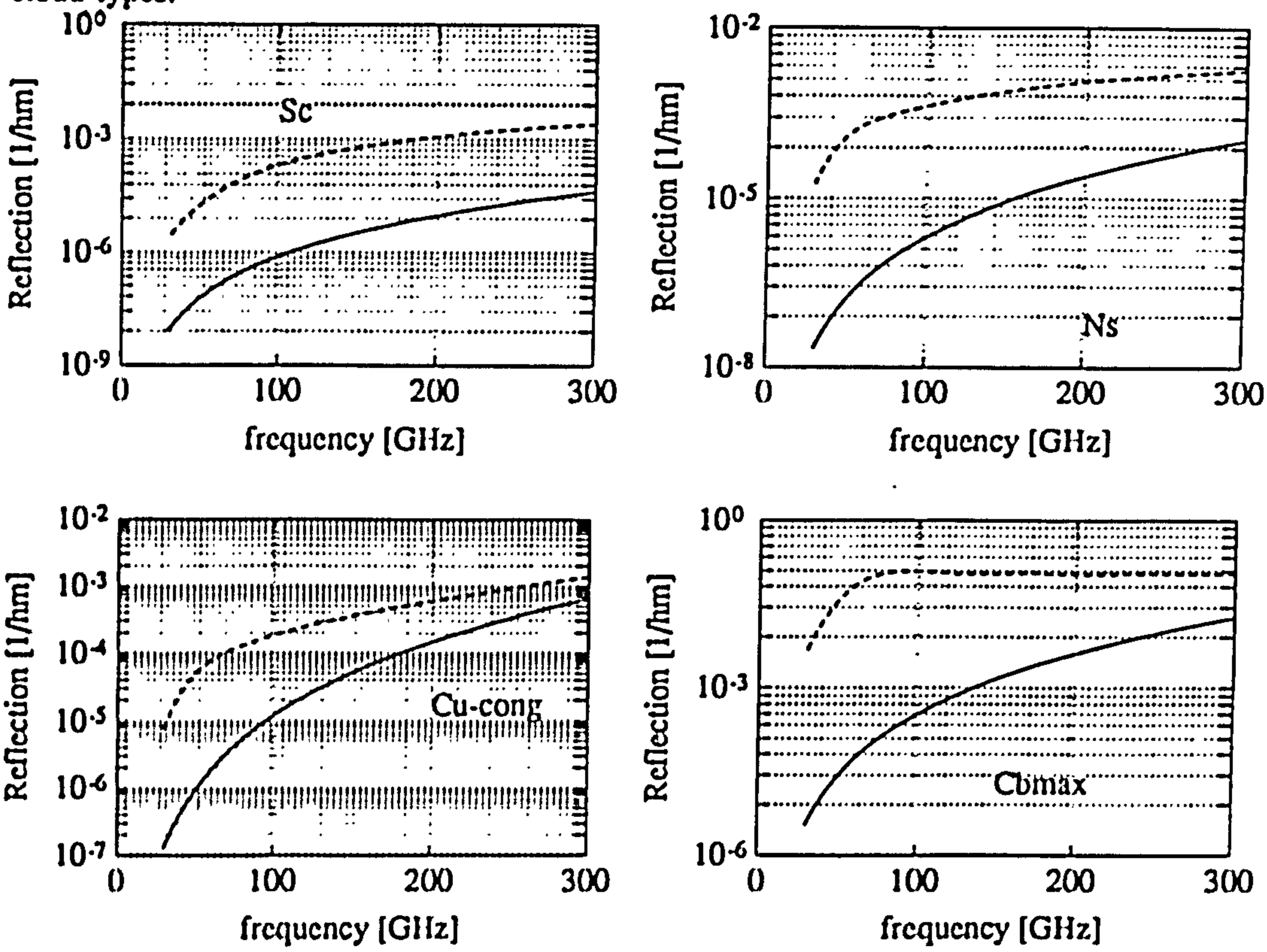

For vertically extended structures, such as the Cb (max) Ajvazyan's cloud model attenuation can be seriously affected, indeed it may increase even by 75% (extreme case) throughout the entire millimetre wave spectrum. For frequencies below 100 GHz the radar reflection coefficient is enhanced by about three orders of magnitude, but as we move to higher frequencies the difference gradually reduces and finally becomes one order of magnitude at 300 GHz. It is expected, however, that for much higher frequencies (ie infrared or optical) super-large drops would not significantly affect the radar reflection coefficient but the resultant attenuation.

4.7 Conclusions.

In this chapter extinction and back scattering tables and calculations for a wide variety of non-precipitable ice and water clouds over the entire millimetre wave spectrum have been given

for the first time. It was found that at millimetre wavelengths multiple scattering effects should not be a problem for water clouds, but for pure ice clouds and especially cirrus where large ice particles are often observed, a quantitative approach is necessary. The presence of super-large drops in water clouds is a major problem and although it does not particularly affect the resultant attenuation, it can seriously affect the resultant radar reflection coefficient to a worrying level. It is therefore concluded that modelling radiowave propagation through non-precipitable water clouds is a quite difficult task unless the distribution and liquid water content of the portion of super-large drops in the cloud are exactly known. Evidently, the employment of millimetre wave radars for the identification of certain cloud types should be problematic, unless other accompanying instruments (ie lidars and radiometers) support the measurements.

CHAPTER 5

REMOTE SENSING OF CLOUDS FROM SPACE.

5.1 Introduction.

The effect of clouds on the large scale circulation of the atmosphere is one of the major sources of uncertainty in predicting the climate change that would result from increased greenhouse gases. The vertical distribution of clouds, which is particularly poorly observed, affects the surface radiation balance and the profile of heat absorption and reradiation through the depth of the atmosphere. These have important impacts on the hydrological and carbon cycles and on the climate both globally and regionally. Better global observation of clouds, especially on their vertical distribution, are required to improve understanding of the climate system and to develop and validate the general circulation models used in the climate description. It is generally believed that there is cooling from low level clouds such as the extensive areas of stratocumulus over the oceans whereas high level clouds result in heating.

Fig. 1. Multi-layer cloud decks as seen by a ground based mmw radar (UK GEWEX Forum).

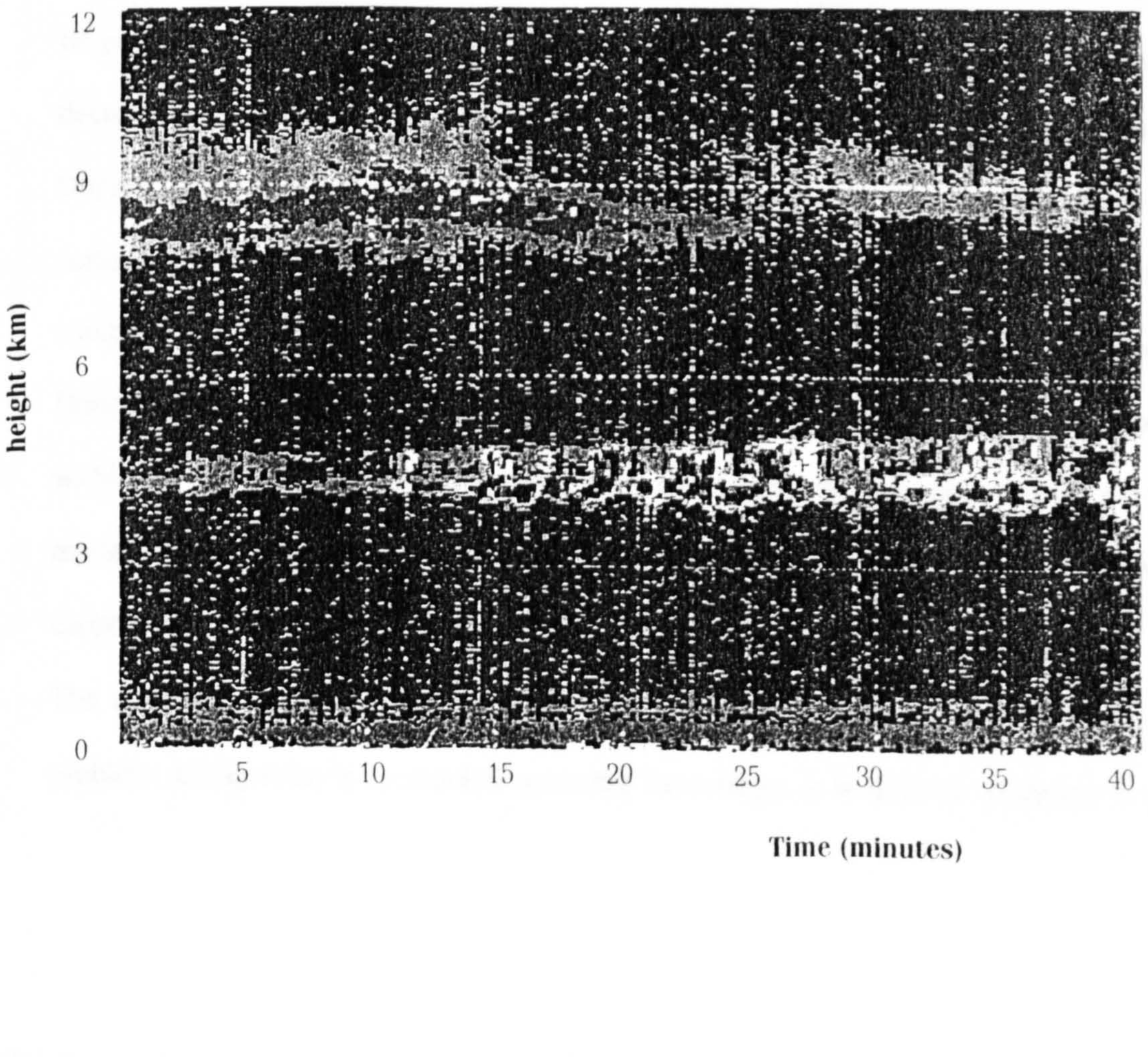

Millimetre wave radars can be designed to detect most clouds. Unlike the optical radiation generated by lidars, the millimetre radiation can penetrate most non-precipitating clouds to give estimates of vertical cloud profiles. An example of multi-layer cloud decks as seen by a ground based millimetre radar is shown in figure 1. Millimetre wave radar is thus the best available tool for measuring multiple cloud layers which are either not detected or identified ambiguously by other techniques.

5.1.1 Possible configurations for a spaceborne cloud radar.

The simplest configuration for a spaceborne cloud radar is that involving a nadir pointing fixed beam antenna. A first realistic approach would consider a radar designed to operate from an altitude of 500 km and requiring a mean instrument power of 300 Watts. This reduces complexity, data rate and costs, as well as permitting a degree of signal integration leading to improved sensitivity. Simple antenna design, and the use of a receiver and transmitter equipment that is fully or nearly fully developed, would avoid major technology developments. If a higher mean instrument power and lower orbit could be accepted, the fixed beam could be pointed between 30° and 40° ahead or behind the nadir direction. This would lead to a decrease of clutter returns from the earth's surface sufficient to allow pulse compression and Doppler processing techniques to be applied and a considerable increase in detection performance achieved. Receiver, processor and antenna design would be of course much more complex and the tilt of the sampling cell would cause a slight decrease in vertical resolution. Doppler processing would bring the capability to measure line of sight wind components within the clouds which may be valuable for a simulation into numerical weather prediction models. However, the added complexity of an off nadir pointing instrument with Doppler capabilities would lead to substantial extra cost and production effort.

The collection of data over a broad swath is another possibility, but a much more taxing problem. Using today's mechanical scanning technology, it is difficult to design a system

which allows sufficient integration time for measurement and provides a satisfactory scanning capability. Nevertheless, it is reasonable to envisage that, in the near future, the use of active array antenna technology will provide adaptive across-track scanning and the capability for much more enhanced cloud sampling.

5.1.2 Nadir pointing fixed beam millimetre wave cloud radar.

While a radar with Doppler and scanning capabilities could provide much more detailed cloud sampling, the resultant complexity and high costs limit our interest at least for the immediate future, to the much simpler nadir pointing fixed beam configuration. The characteristics in table I apply to a fixed beam nadir pointing millimetre wave radar which, on a satellite orbiting at 500 km altitude, would be capable of detecting with a vertical resolution of 500

Table I. Characteristics of a nadir pointing fixed beam millimetre wave radar.

Frequency	94 GHz
Peak transmitted power	1.5 kW
Antenna diameter	2 m
Pulse repetition frequency	5 kHz
Pulse length	3 μs
Integration time	1 s
Receiver noise level	3 dB
RF loss to antenna	4 dB
Nadir footprint	1 km
Mass	100 kg
Input power	300 W

m, clouds with a reflectivity of -30 dBZ at any level in the troposphere, in the presence of 5 dB of atmospheric attenuation [UK GEWEX Forum 1993]. A lower frequency radar (ie. 15 or 35 GHz) would not achieve the required sensitivity without resorting to a significantly larger antenna and/or more powerful transmitter, with consequent adverse impacts on overall

mass and power requirements. On the other hand, a higher frequency would suffer from unacceptably high atmospheric attenuation.

The assessment of the potential of this relatively simple radar to deduce information about the vertical structure of clouds is the subject of this chapter. First, information about the vertical structure for a wide selection of clouds is collated, and then the resultant attenuation and reflectivity profiles are calculated.

5.2 Cloud particle sizes and concentrations.

The following data have been identified and used for the calculation of attenuation and reflectivity profiles. In addition to the well established models, in each case where there are perceived weaknesses, more recent measurements have been sought.

5.2.1 Cirrus.

Data from Paltridge and Platt [1981], Foot [1988a] and the UK Meteorological office have been examined. Data for Cirrus appears to be somewhat sparse, compared to that available for other clouds, presumably owing to the difficulties in collection and the lesser importance attached in the past to these clouds. It is noted, in particular, that although variations in liquid

Table II. Cloud and flight information for five horizontally uniform and well-defined Cirrus decks and one isolated Cirrus patch over Sorocco, New Mexico, during March 1979. Symbol definition as follows: Z_o= cloud top; Z_b=cloud base; T_o=cloud top temperature; T_b=cloud base temperature; t_o=local time at cloud top; t_b=local time at cloud base; Θ=average solar zenith angle during profile; n=average number concentration, W=average ice water content.

Flight No.	Z_o [km]	Z_o-Z_b [km]	T_o [°C]	T_b [°C]	t_o [h]	t_b [h]	Θ [°]	n [cm^{-3}]	W [g/m^3]
1									
2	9.88	0.91	-49	-38	11.59	12.36	39.8	-	-
3	9.55	0.73	-56	-42	12.10	12.42	37.1	0.4	0.004
3a	9.70	0.15	-50	-49	11.40	11.52	36.8	-	-
4	10.1	1.03	-54	-46	12.00	11.50	36.2	0.4	0.006
5	10.3	2.43	-56	-36	12.45	13.40	39.5	0.9	0.023
6	9.42	1.46	-47	-34	13.45	14.12	42.2	0.8	0.024
7	9.73	1.82	-45	-32	11.55	12.47	33.3	0.9	0.026

water content and particle size with height are seen in the data examined, no general models for the height dependence of microphysical properties are available. Each cirrus deck is taken to be vertically and horizontally uniform in particle density and size distribution.

Paltridge and Platt reported aircraft measurements of the radiation and microphysical profiles of five horizontally uniform and well defined Cirrus decks and one isolated Cirrus cloud patch over Socorro, New Mexico during March 1979. A summary of the flight and cloud characteristics are given in table II.

Foot [1988a] gives a detailed description of a Cirrus formation which was observed over the south-west of England as part of a slow moving front oriented north-south over western Ireland. Two aircraft flying simultaneously collected information on the microphysical properties of the clouds, including size-spectra. A summary of the data collected from one of these flights is given in table III.

Table III. Microphysical and macrophysical description of a cirrus cloud, as observed by MRF H442 on 26 Feb 1981 over the SW of England. (Foot [1988a]).

Date and Flight No	Cloud Top [km]	Cloud Base [km]	Cloud Top Temp [°C]	Cloud Base Temp [°C]	Cloud Top IWC [g/m^3]	Cloud Base IWC [g/m^3]	Cloud Top r_{eff} [μm]	Cloud Base r_{eff} [μm]
26.2.81 H442	7.6	4.9	-45	-30	0.0134	0.0162	20	41

More comprehensive and better instrumented measurements of Cirrus are available from the UK Met Office FIRE/ICE studies [Illingworth 1992]. The results have been already summarized in table X of chapter 4.

5.2.2 Stratus and Stratocumulus.

Feigelson [1984] gives models for the spatial (and temporal) variation of liquid water content associated with St or Sc clouds (see figure 8 of chapter 4). Three temperature-dependent two layer models are derived from that figure, which are summarised in table IV.

Table IV. Feigelson's temperature dependent two layer St/Sc cloud models.

		Top [km]	Base [km]	Top lwc g/m^3	Base lwc g/m^3	Top r_1 [μm]	Base r_1 [μm]	Top temp [°C]	Base temp [°C]
Cloud Model 1	Upper layer	1.0	0.5	0.225	0.225	5.5	4.8	-10	-7
	Lower layer	0.5	0.0	0.225	0.07	4.8	4.0	-7	-3.5
Cloud Model 2	Upper layer	1.0	0.5	0.275	0.275	5.5	4.8	-5	-2
	Lower layer	0.5	0.0	0.275	0.100	4.8	4.0	-2	2
Cloud Model 3	Upper layer	1.0	0.5	0.375	0.375	5.5	4.8	5	8
	Lower layer	0.5	0.0	0.375	0.150	4.8	4.0	8	11

Since the concentration and sizes of cloud droplets can vary greatly from the average distributions, we have also used a number of samples of data and a number of models from other sources for the purposes of comparison. The Stratus and Stratocumulus cloud models also used in addition to Feigelson include Silverman and Sprague [1970] (included later in the AFGL models) and Carrier et al [1967], already given in tables IV and VI of chapter 4, respectively. Particular case studies examined include Foot [1988b] and Nicholls [1984]. Data from their studies are summarized in tables V and VI respectively. Foot's data were taken on a day with persistent Stratocumulus over the south-west of the UK. Nicholl gives data for typical marine Stratocumulus off the Yorkshire coast.

Table V. Cloud structure and microphysical description of a Sc sheet over the south-west of England (after Foot [1988b]).

Cloud top [km]	Cloud base [km]	Temp top [° C]	Temp base [° C]	r_{eff} top [μm]	r_{eff} base [μm]	LWC top $[g/m^3]$	LWC base $[g/m^3]$
2.2	1.25	-10	-3	7.7	5.8	0.44	0.10

Table VI. Cloud microphysical parameters and other characteristics of a marine Sc cloud off the Yorkshire coast (after Nicholls [1984]).

Cloud top [km]	Cloud base [km]	Temp top [°C]	Temp base [°C]	r_{eff} top [μm]	r_{eff} base [μm]	LWC top [g/m^3]	LWC base [g/m^3]
0.8	0.35	8.5	10.5	10.0	5.25	0.362	0.044

The spectra of precipitating Stratus or Stratocumulus, have been represented in our calculations by the relevant exponential size relation given in chapter 4, (also applicable to super-large populations in clouds) but with N_L increased by a factor of 100 for drizzle and by a factor of 1000 for light rain.

5.2.3 Altostratus and Nimbostratus.

Feigelson [1984] reporting on the studies of Borovikov and Mazin [1975], shows that in Ns and Ns-As cloud, although liquid water content first increases with height, at approximately 200-300 m above the cloud base, it then remains practically independent of height. Thus, the cloud models of Silverman and Sprague [1970] and Carrier et al [1967] in which the lwc is height independent have been selected to represent typical As, and Ns liquid water clouds. Nevertheless, it is noted that these clouds can also be mixed ice and water or contain purely ice crystals.

In view of the occurrence of mixed-phase As and Ns clouds, a two-layer ice/water model in addition to homogeneous liquid water clouds has been considered in the following calculations.

5.2.4 Convective clouds.

The variation of the liquid water content of a typical convective structure was given in figure 9 of chapter 4. From that figure and assuming that the maximum lwc occurs at 80% of the total cloud depth (=2 km), the following two-layer model for clouds with significant vertical

development has been deduced.

Table VII. Two-layer cloud model for a typical convective structure. (from figure 9 of chapter 4.)

	top [km]	base [km]	lwc top [g/m^3]	lwc base [g/m^3]
layer 1	2.0	1.6	0.01	1.0
layer 2	1.6	0.0	1.0	0.01

The convective cloud models of Silverman [1970], and Carrier et al [1967] have also been included in this analysis.

5.2.5 Special cloud case studies.

Two detailed case studies of convective clouds with large vertical structure have been examined in order to help to give an insight to the attenuation and reflectivity profiles appropriate to this type of cloud. These are, the study by Bennetts and Ouldridge [1985] of an anvil of winter maritime cumulonimbus and the studies of Magono and Lee [1973].

5.2.5.1 Winter maritime cumulonimbus anvil.

Bennetts and Ouldridge [1985] reported microphysical and dynamical measurements in the anvil of a winter Cb cloud that grew in maritime air near the United Kingdom. The anvil had a well-organised structure, with ice content in the central region exceeding 1 g/m^3. The ice appeared to be distributed uniformly over the size range of crystals with half the total mass contained in particles larger than 1 mm. The total particle concentration in certain places exceeded 0.15 per cm^3. Figure 2 depicts the shape of the anvil traced from a photograph, with the position of the MRF C-130 aircraft passes superimposed. The bars in the graph indicate uncertainty in position relative to the cloud reference frame. Information on the microscale characteristics of the anvil are given in figure 3, where the averaged differential distributions over the passes 3, 4, 5 and 6 are plotted. All the ice particle distributions are well represented

Fig. 2. Shape of the maritime Cb anvil traced from a photograph taken on 18 December 1980 at the north-west of the UK (from Bennetts [1984]).

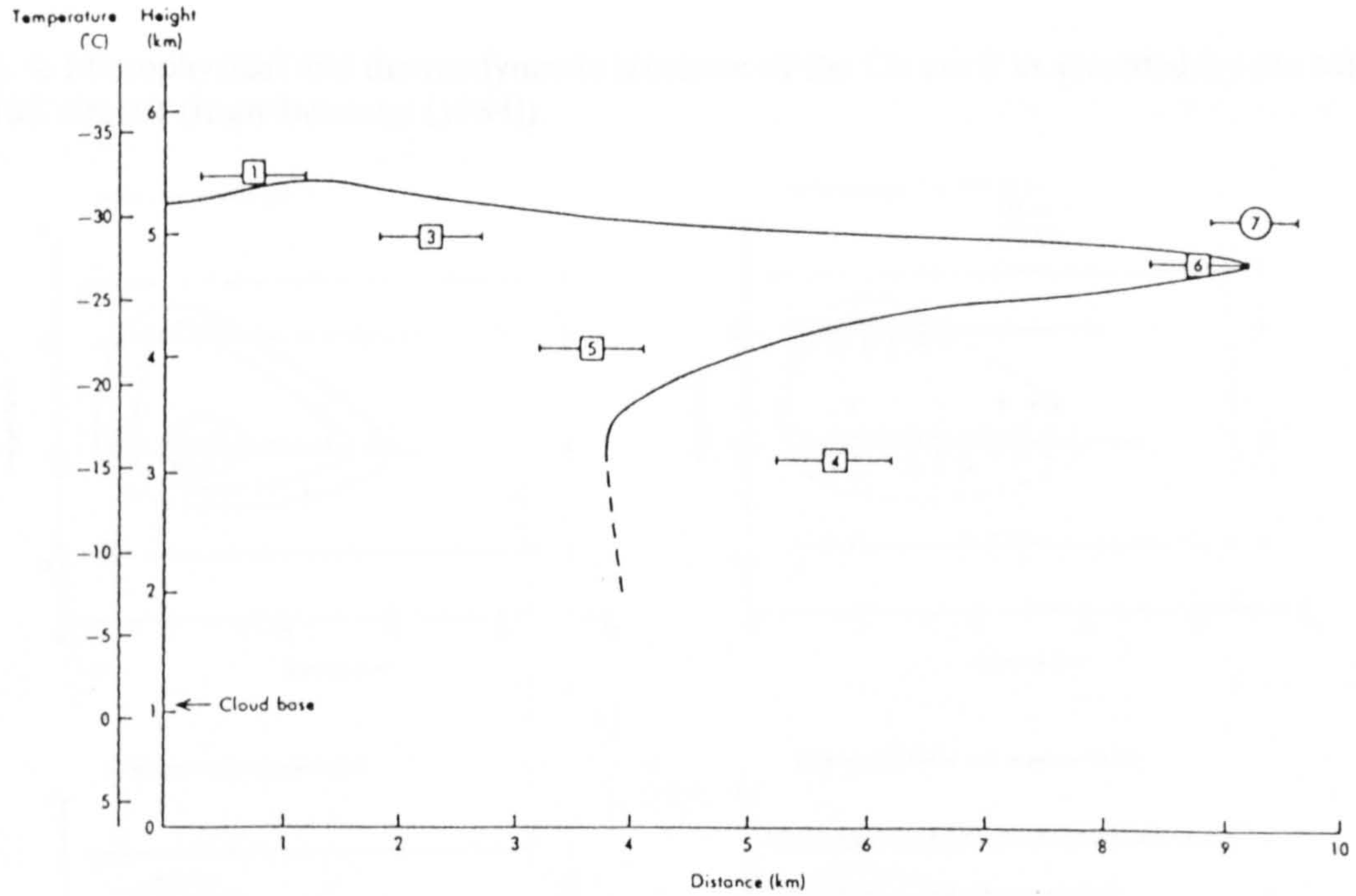

Fig. 3. Differential size distributions over passes 3, 6, 4 and 5 for a maritime Cb anvil (from Bennetts [1984]).

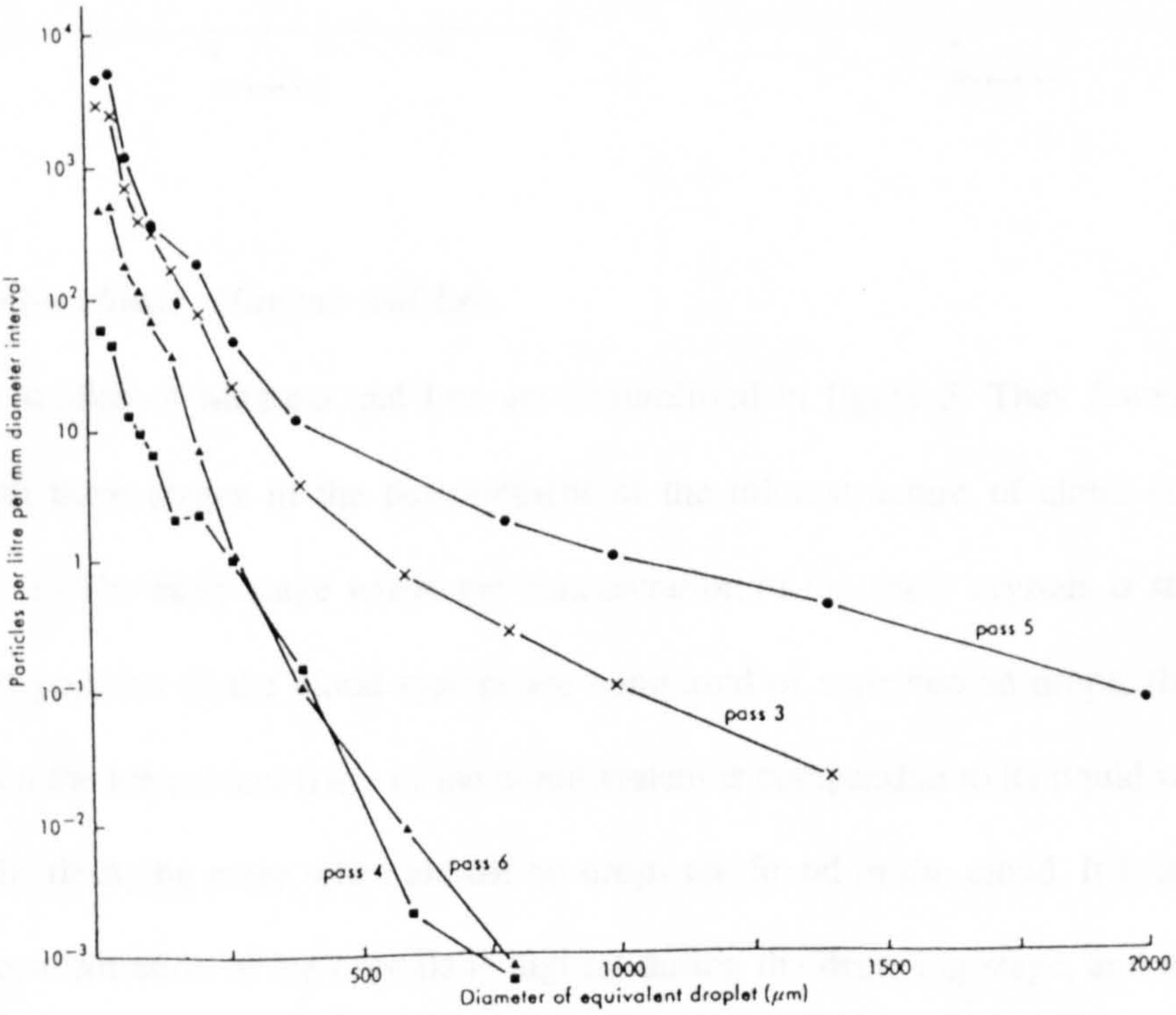

by an exponential distribution of the form $N(D)=N_0\exp(-D/D_0)$. The microphysical and thermodynamic structure of the anvil through passes 1, 3, 5 and 4 is given in figure 4.

Fig. 4. Microphysical and thermodynamic structure of the Cb anvil as recorded by the MRF C-130 aircraft (from Bennetts [1984]).

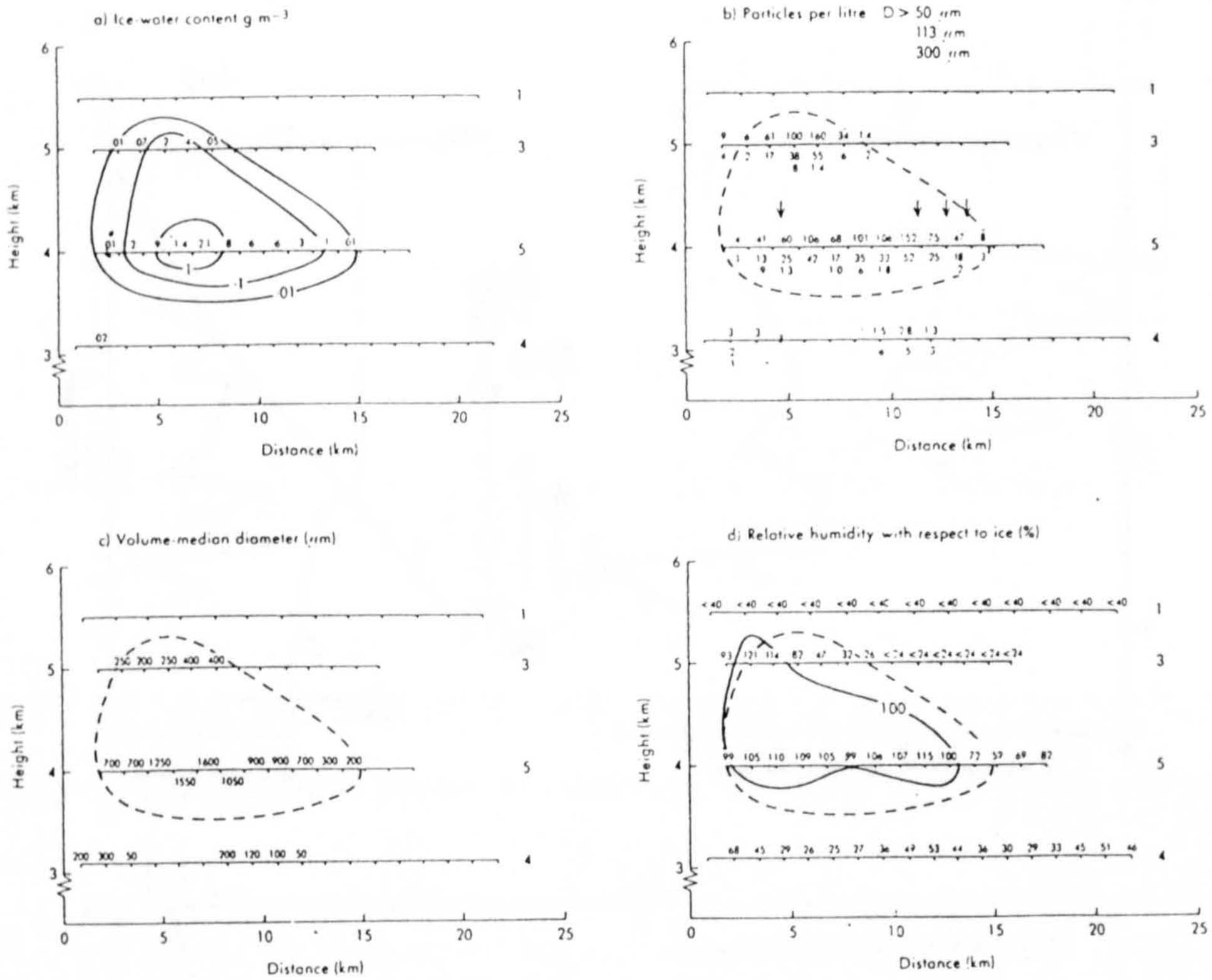

5.2.5.2 Snow clouds: Magono and Lee.

The case studies of Magono and Lee are exemplified in figure 5. They found it useful to distinguish three stages in the development of the microstructure of cloud containing ice particles: (a) The early stage where the concentration of the snow crystals is still small and almost all portions of the cloud system are composed of supercooled drops, (b) the mature stage when the ice content (iwc) of the cloud system is comparable to its liquid water content, and (c) the decaying stage when almost no drops are found in the cloud. It is noted that the number concentration of ice crystals is highest during the decaying stage, and that the cloud

ice content varies considerably with height, depending not only on the number concentration of the ice crystals but also on their shapes.

Fig. 5. Vertical structure of snow clouds during a storm in January, 1970, over Hokkaido, Japan: (a) early stage on January 22; (b) mature stage on January 24; (c) decaying stage on January 25 (from Magono and Lee, [1973]).

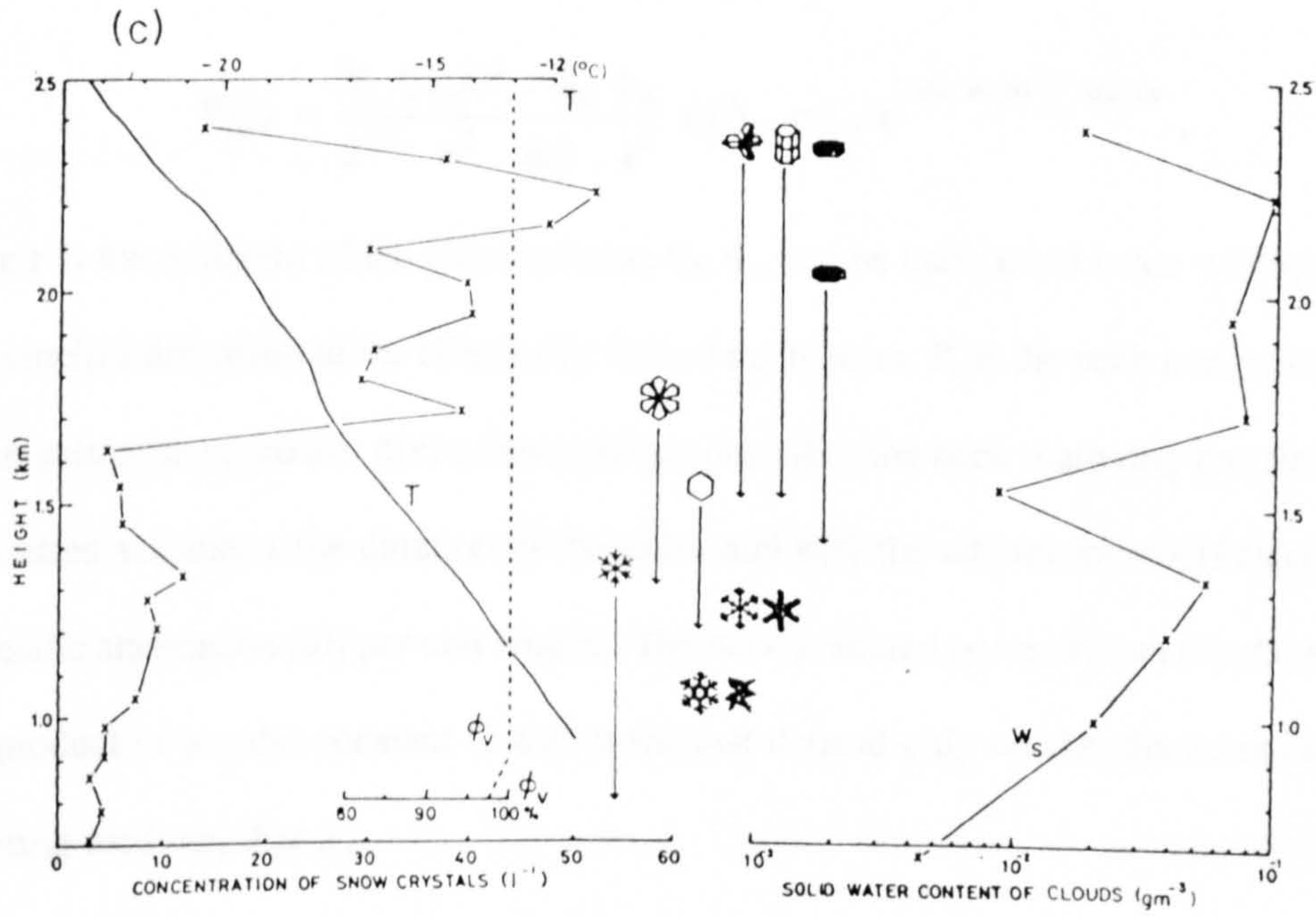

A multi-layer model for snow clouds in the decaying stage has been abstracted from the data of Magono and Lee for the purpose of calculation. The model is described in table VIII, below.

Table VIII. Microphysical parameters and macrophysical structure of a snow cloud in the decaying stage, as abstracted from the studies of Magono and Lee [1973].

Cloud layer	Altitude [km]	Concentration $N_T[lt^{-1}]$	IWC [g/m^3]	Temp [°C]
1	2.4	13	0.016	-23.4
2	2.2	52	0.1	-21.0
3	1.7	25	0.074	-18.2
4	1.5	5	0.01	-16.0
5	1.3	12.5	0.055	-14.0
6	0.0	3.5	0.0055	-10.0

5.3 Approach to calculation of cloud reflectivity and attenuation.

The conventional radar equation for volume scattering has been applied, modified to include

attenuation where the back scattered $\mathbf{P_r}$ is given by:

$$\mathbf{P_r(r)} = \frac{\mathbf{P_o}\,(\mathbf{G_o}\lambda)^2 \,.\, \theta_B\, \phi_B}{2^{10} \,.\, \pi^2 \,.\, \ell n 2 \,.\, \mathbf{r}^2}\, \eta(\mathbf{r}) \,.\, c\tau \,.\, \mathbf{e}^{-0.2\,\ell n\,10 \int_o^r \mathbf{k(s)}\,\mathbf{ds}}\,,$$

where **r** is the midpoint of the pulse volume, θ_B, ϕ_B are the half-power beam widths along the two principal directions of the elliptically shaped main beam, $\mathbf{P_o}$ is the peak transmitted power, $\mathbf{G_o}$ the gain of the antenna, $\eta(\mathbf{r})$ a function that describes the back scattering properties of the illuminated volume, τ the duration of the pulse and $\mathbf{k(s)}$ the attenuation coefficient in terms of specific attenuation (dB per unit length). The back scattered power $\mathbf{P_r}$ can also be expressed as a product of a radar constant **C** and terms that depend only on the characteristics of the scattering medium, that is,

$$\mathbf{P_r(r)} = \frac{\mathbf{C} \,.\, |\mathbf{K}|^2\, \mathbf{Z_e}}{\mathbf{r}^2} \,.\, \mathbf{e}^{0.2\ell n\,10 \int_o^r \mathbf{k(s)}\,\mathbf{ds}}\,,$$

where the radar constant is

$$\mathbf{C} = \frac{\pi^3\, \ell n\, 2}{2^{10} \,.\, \lambda^2} \,.\, \mathbf{P_o} \,.\, \mathbf{G_o^2} \,.\, \theta_B \,.\, \phi_B \,.\, c\tau\,,$$

and $\mathbf{Z_e}$ is defined as the equivalent radar reflectivity

$$\mathbf{Z_e} = \frac{\lambda^4}{\pi^5\, |\mathbf{K}|^2} \int_D \sigma_b(\mathbf{D}) \,.\, \mathbf{N(D)}\, \mathbf{dD}\,,$$

where $\sigma_b(\mathbf{D})$ is the radar cross section of a polydispersive medium described by a particle size distribution **N(D)**. **K** describes the dielectric properties of the medium and is given by:

$$\mathbf{K} = \frac{\mathbf{m}^2 - 1}{\mathbf{m}^2 + 2}\,,$$

where **m** is the complex index of refraction of the medium. The calculations presented in this chapter refer to the equivalent radar reflectivity $\mathbf{Z_e}$ (in dBZ) and include attenuation (in dB), given by the integral:

Furthermore, the radar beam is considered to be uniformly filled while the range of

$$A = \int_o^r k(s)\, ds.$$

incrementation is 25 m.

5.4 Particle scattering calculations.

Mie scattering calculations have been used throughout. Cloud particles, either water droplets or ice crystals, have thus been modelled as spheres. For the prediction of attenuation and reflectivity for water clouds, Mie scattering is an excellent approximation. For ice clouds, where very irregular shapes are encountered, the Mie scattering approach using equi-volume spheres should normally provide a first order estimate of attenuation and reflectivity. However, as Hardaker and Holt [1993] demonstrated, the model of the equi-volume sphere gives for the reflectivity results which are in surprisingly good agreement with results calculated from Fredholm Integral Method for prolates (ice needles) and oblates (plates) with axial ratios 1:5. The temperature for water droplets has been assumed 5° C and for ice crystals -15° C, througout. For a cloud of particles multiple scattering has been neglected. This should not be a problem for all water clouds and for most of ice clouds when observed at 94 GHz. A qualitative assessment of multiple scattering effects follows immediately.

5.5 Multiple scattering at 94 GHz.

Using the qualitative approach we adopted in the previous chapter, the scattering and absorption coefficients at 94 GHz for water drops in the size range 0.1 to 100 μm have been plotted (see figure 6). Clearly $\omega_o \ll 1$. Even at 300 GHz, ω_o is typically ~0.05. Multiple scattering should thus not be significant.

Figure 7 shows the scattering and absorption coefficients at 94 GHz for ice spheres in the size range 0.1 to 100 μm.

Fig. 6. Absorption and scattering cross sections of spherical water droplets at 94 GHz for a size range 0.1 to 100 μm. Also shown is the albedo, ω_o.

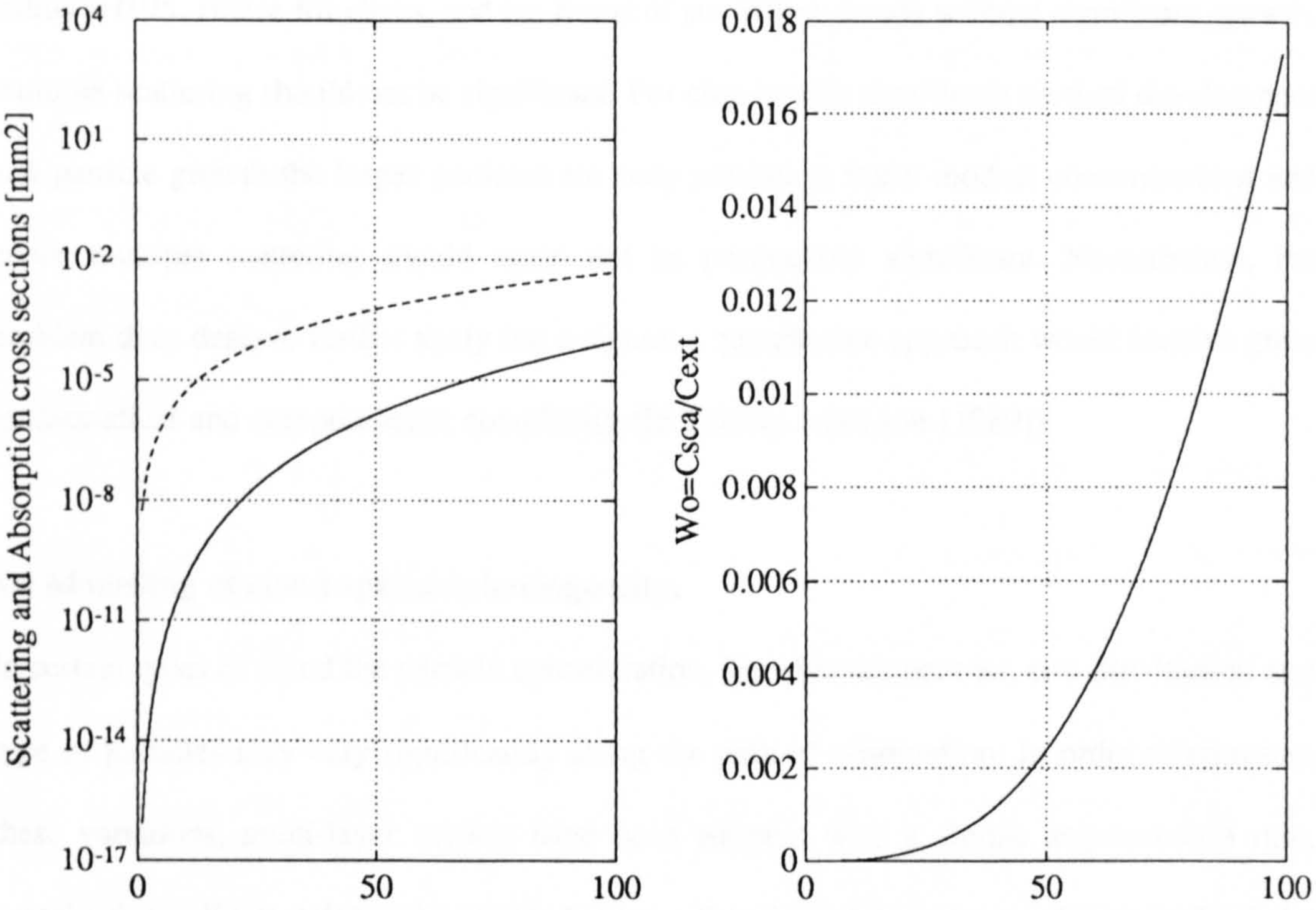

Fig. 7. Absorption and scattering cross sections of spherical ice crystals at 94 GHz for a size range 0.1 to 100 μm. Also shown is the albedo, ω_o.

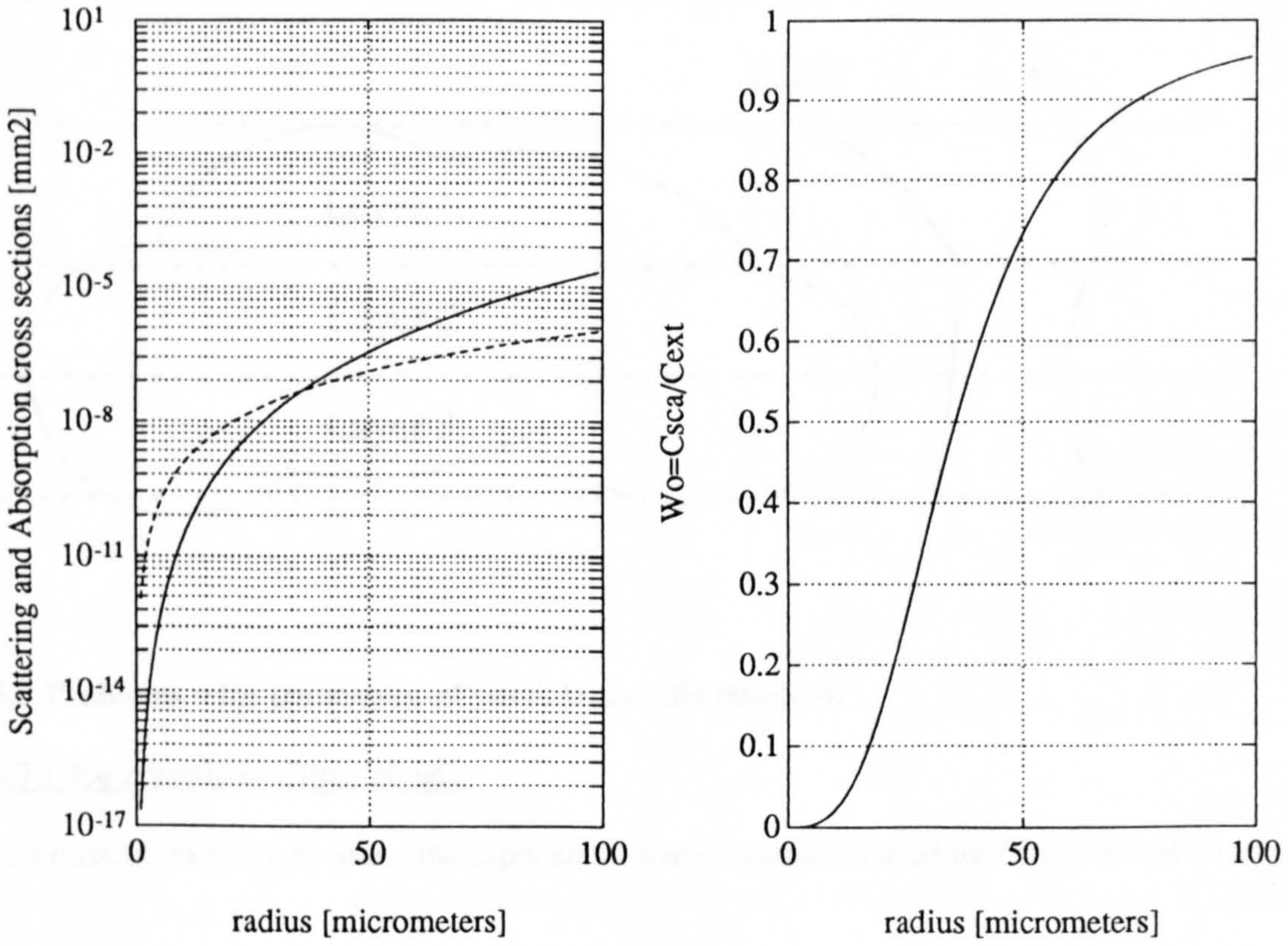

The critical radius is 40 μm above which the albedo exceeds 0.5. The albedo for a 100 μm radius is 0.95. Hence for cirrus, and ice forms of stratiform clouds without significant growth, multiple scattering should not be significant. For clouds with significant vertical development and particle growth the larger particles are only present at fairly modest concentrations and hence multiple scattering should again not be particularly significant. Nevertheless, the problem does deserve further study but a rigorous quantitative approach would involve great mathematical and computational complexity (ie Takano and Liou [1989]).

5.6 Modelling of cloud spatial inhomogeneity.

In certain types of cloud the particle concentration, liquid water content, size distribution and type of particles may vary significantly along the path of observation. In order to represent these variations, multi-layer models have been adopted with a simple segmentation rule, namely that a linear relationship holds between the cloud parameters and the depth of the cloud. Figure 8, demonstrates the utility of the approach.

Fig. 8. Segmentation of cloud volume into multi-layers for the elimination of inhomogeneity.

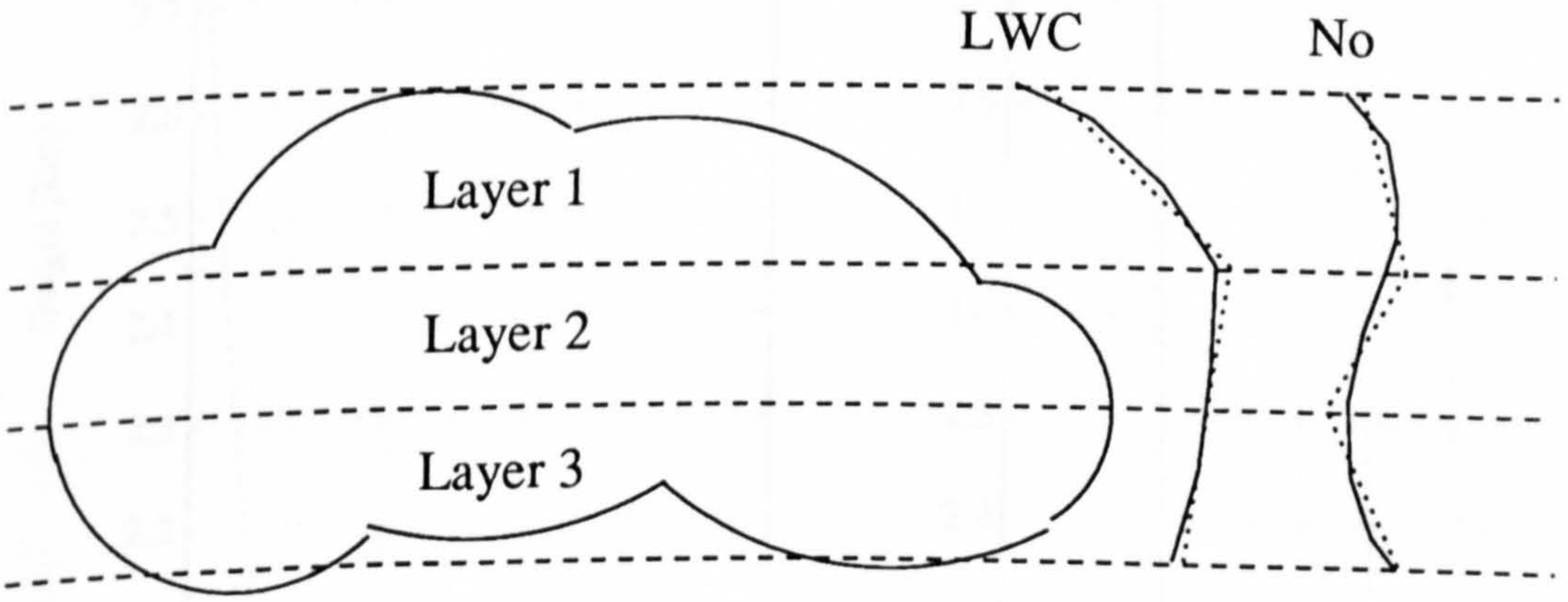

5.7 Problems with truncation of particle size distribution.

5.7.1 Ice crystals in Cirrus clouds.

It is difficult to estimate where the exponential size distributions used for Cirrus clouds should

be truncated, since it is understood that the instruments used to sample particle size will not pick up the largest particles. For high iwc, the contribution of larger particles is significant both to attenuation and reflectivity. Figure 9 illustrate this, showing attenuation and reflectivity profiles for the FIRE/ICE cloud model 1 (iwc=0.255 g/m^3) truncated at 300, 600 and 6000 μm. It is seen that if D_{max}=300 μm, the reflectivity is near 0 dBZ, but increases to near 15 dBZ for D_{max}=600 μm.

For Cirrus, a critical aspect is the visibility of other clouds beneath. Even with an extremely high limit on the size distribution (D_{max}=6000 μm), attenuation is reassuringly low (specific attenuation=1.0 dB/km/g). In these calculations, a maximun equivolumetric diameter D_{max}=600 μm has been taken for all ice cloud models.

Fig. 9. Effect of truncation of size spectra on attenuation and reflectivity for Met. Office Cirrus cloud model 1.

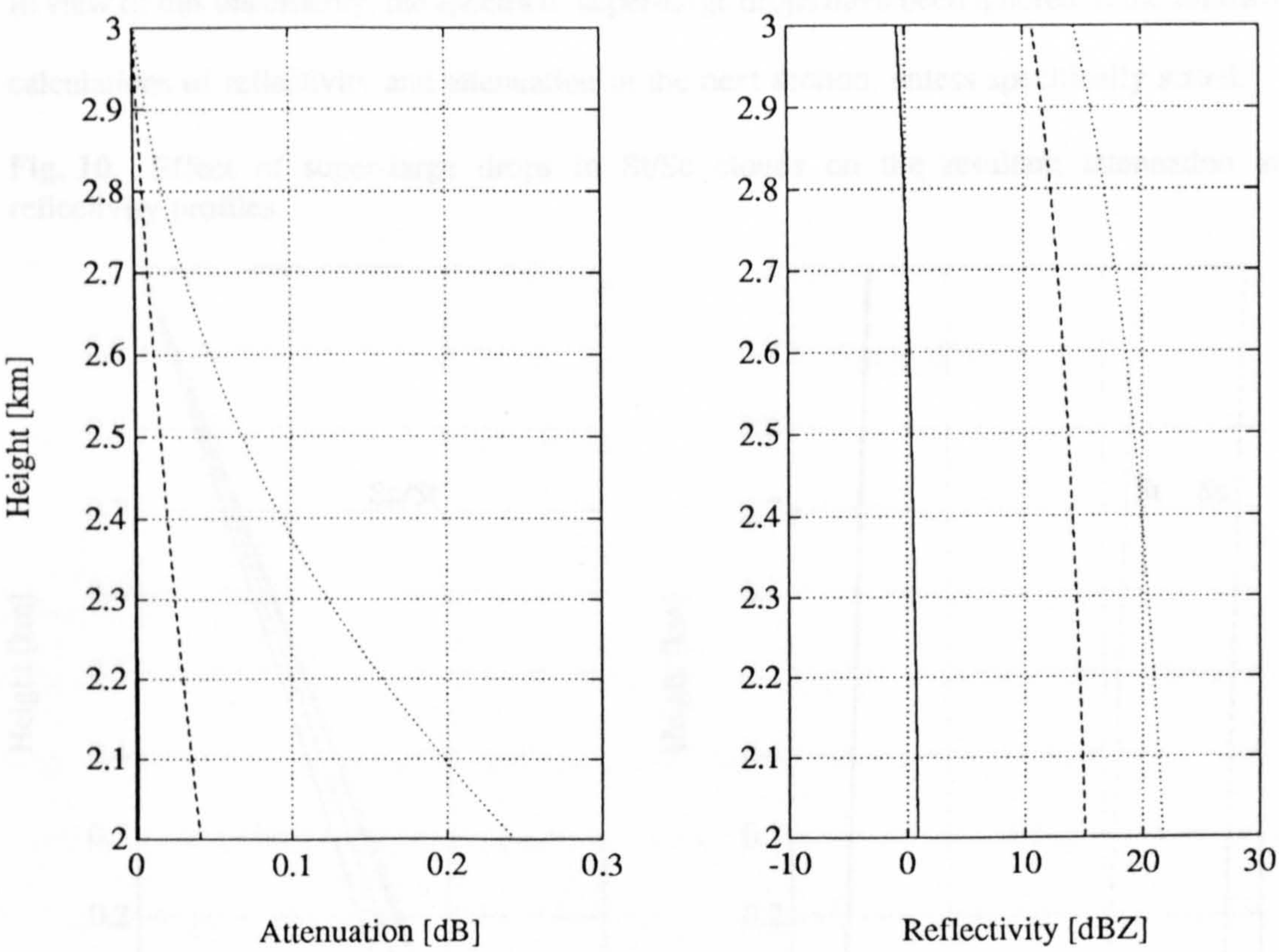

5.7.2 Super-large water drops in clouds.

The effects of the occurrence of super-large water drops in clouds have been dealt with in

chapter 4. Therefore, the same conclusions we derived there should here apply. Figures 10 and 11 demonstrate the effect of super-large drops on the resultant attenuation and reflectivity profiles for selected cloud types. For St or Sc clouds where r_{max} is less than 500 μm and the concentration of super-large drops is relatively low, the attenuation is hardly affected, but reflectivity is enhanced by 15-20 dBZ. In very thick Cb clouds where r_{max}=700 and the concentration of super-large drops is very high, the attenuation is dramatically affected (increases by 40%), as is the reflectivity (increases by 20 dBZ). Evidently, when the mass density of the super-large drops is near or above 0.03 g/m^3, both attenuation and reflectivity are affected. For lower mass densities only the resultant reflectivity is notably affected. However, the spectrum of large drops is very difficult to be precisely modelled for a particular type of cloud and it may greatly differ from observation to observation of the same cloud type. In view of this uncertainty, the spectra of super-large drops have been ignored in the following calculations of reflectivity and attenuation in the next section, unless specifically stated.

Fig. 10. Effect of super-large drops in St/Sc clouds on the resultant attenuation and reflectivity profiles.

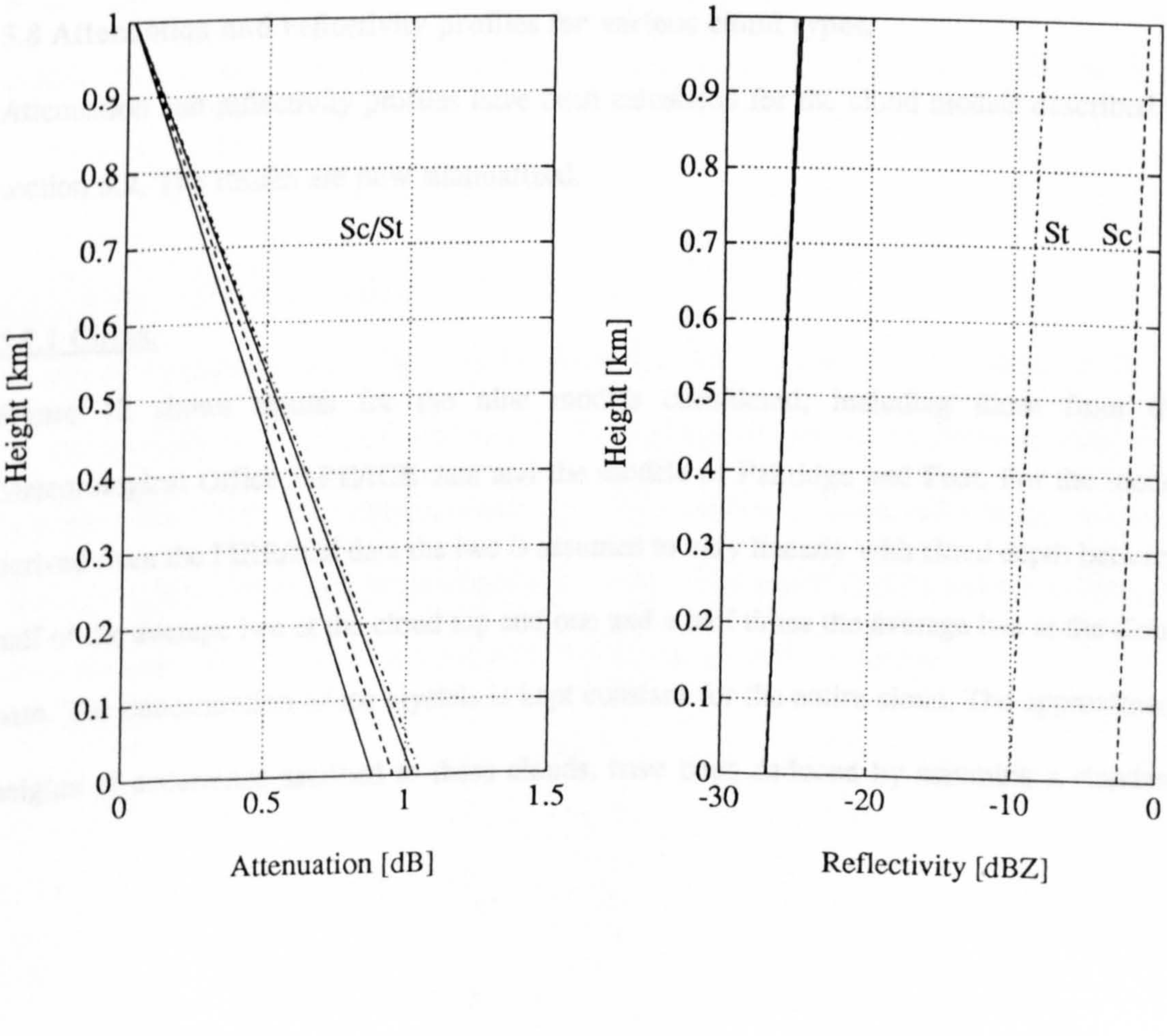

Fig. 11. Effect of super-large drops in Cb clouds on the resultant attenuation and reflectivity profiles.

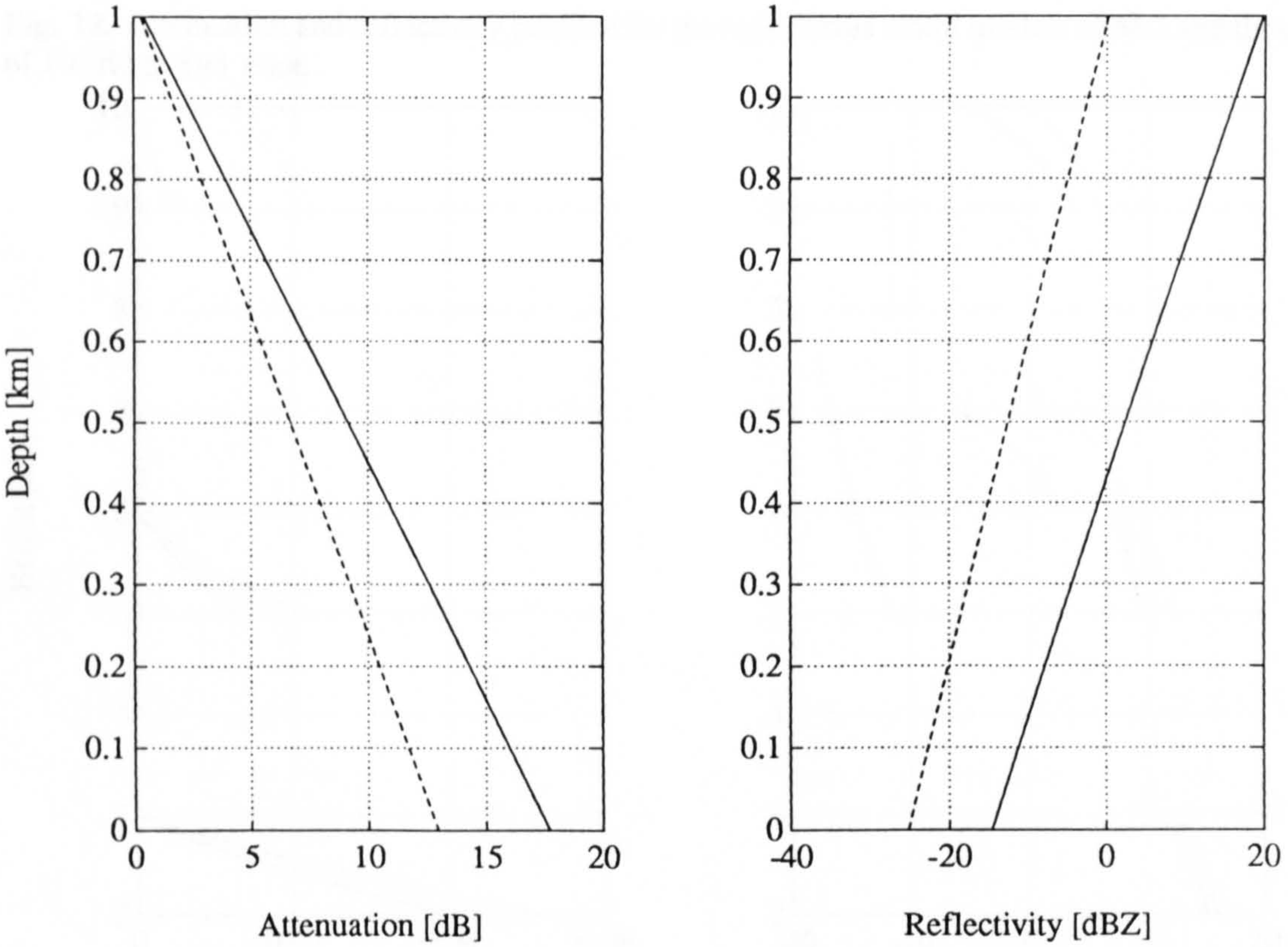

5.8 Attenuation and reflectivity profiles for various cloud types.

Attenuation and reflectivity profiles have been calculated for the cloud models described in section 5.2. The results are now summarized.

5.8.1 Cirrus.

Figure 12 shows results for the nine models considered, including those from the Meteorological Office FIRE/ICE data and the models of Paltridge and Foot. For the model derived from the FIRE/ICE data the iwc is assumed to vary linearly with cloud depth between half of the average iwc at the cloud top and one and a half times the average iwc at the cloud base. The concentration of ice crystals is kept constant for the entire cloud. The approximate heights of occurrence ascribed to these clouds, have been deduced by assuming a standard

adiabatic lapse rate of temperature with height (-6.5° C/km).

Fig. 12. Attenuation and reflectivity profiles for the nine Cirrus cloud models of MO and those of Paltridge and Foot.

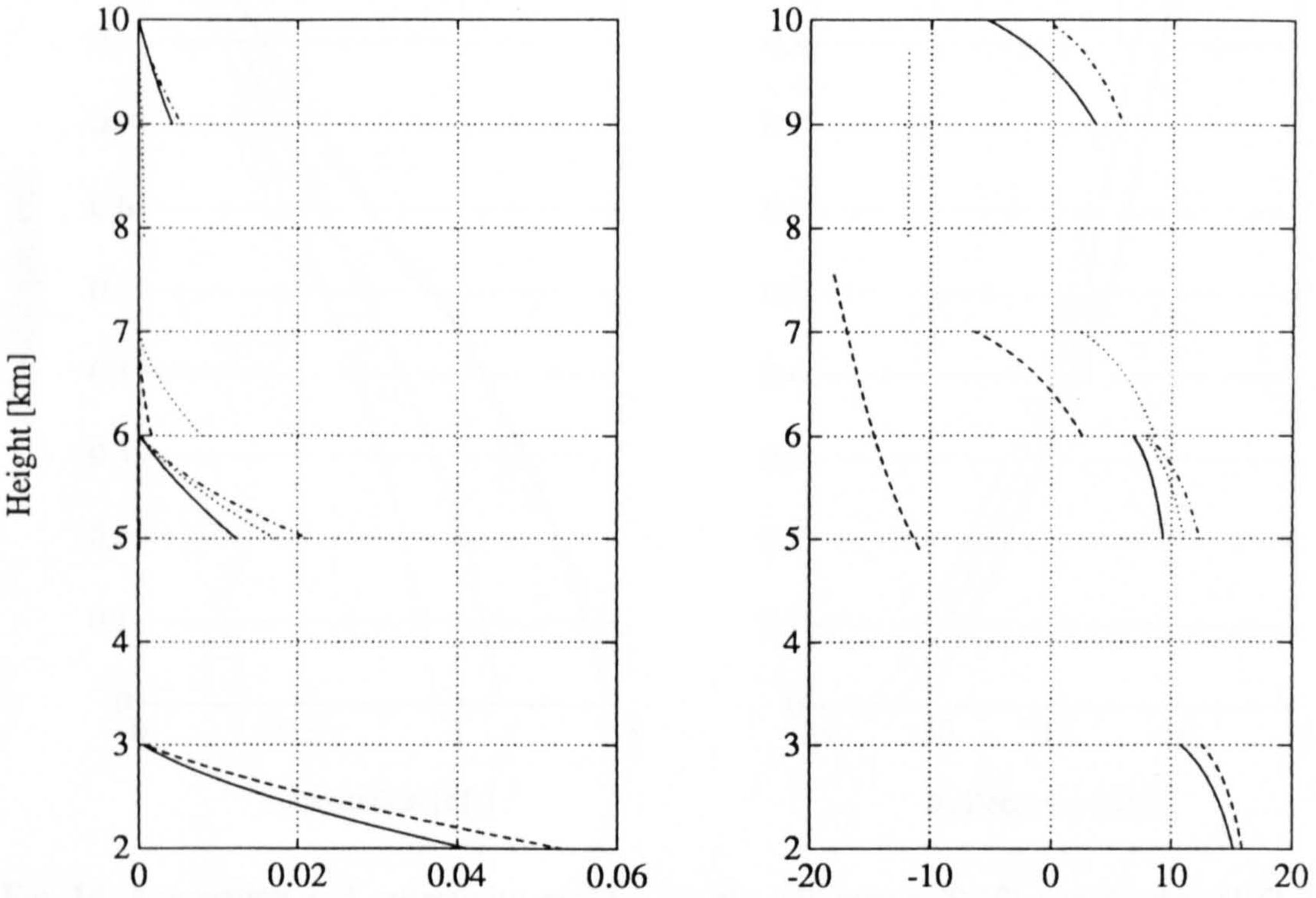

It is noted that in all cases the attenuation is negligible but the reflectivity may vary considerably (from -15 dBZ for thin clouds with iwc less than 0.02 gm^{-3} to 15 dBZ for thick Cirrus with iwc as high as 0.3 gm^{-3}).

5.8.2 Stratus and Stratocumulus.

Results for attenuation and reflectivity for cloud models 1-3 in table IV are plotted in figure 13. Each model is associated with a specific temperature range and corresponding lwc. Increasing lwc within the range taken does not very significantly affect reflectivity, though of course, attenuation increases proportionally to the lwc. (There is a 2.5 dBZ difference between cloud models 1 and 3 which bear lwc of 0.375 and 0.225 gm^{-3} respectively).

Fig. 13. Attenuation and reflectivity profiles for the St/Sc cloud models of Feigelson.

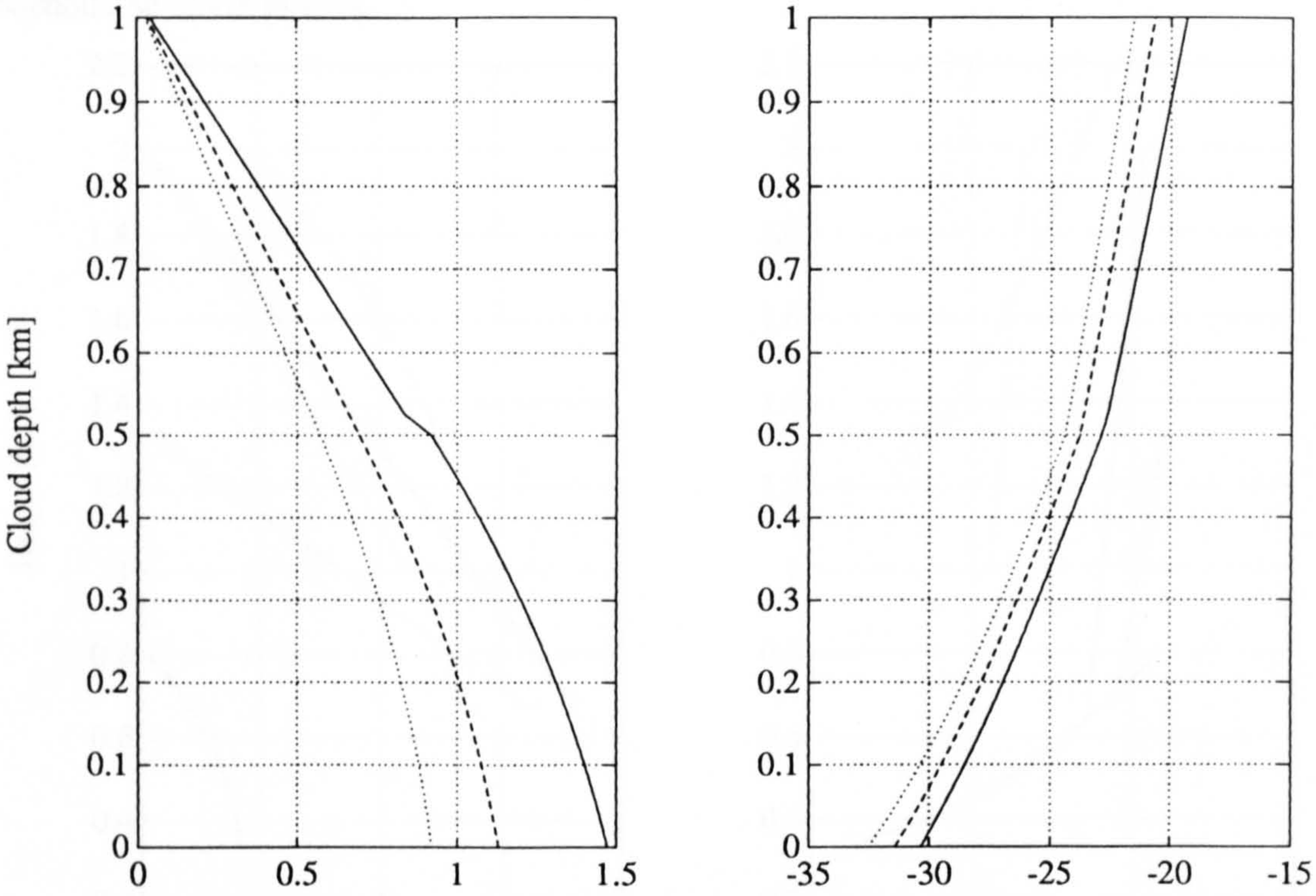

Fig. 14. Attenuation and reflectivity profiles for the Silverman (9,10) and Carrier (1,6) St cloud models.

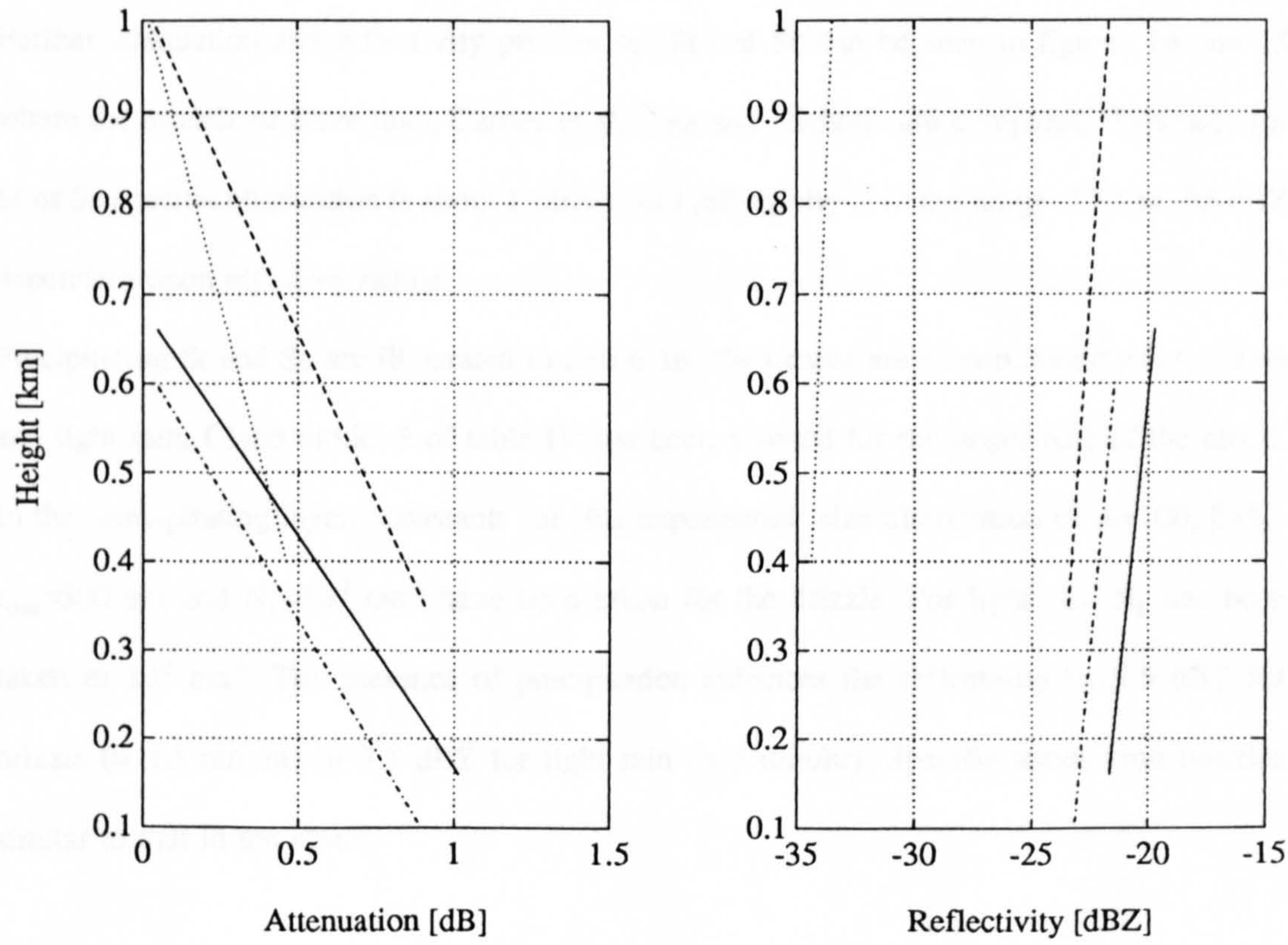

Fig. 15. Attenuation and reflectivity profiles for the Silverman (7,12), Carrier (3) and Foot and Nicholls Sc cloud models.

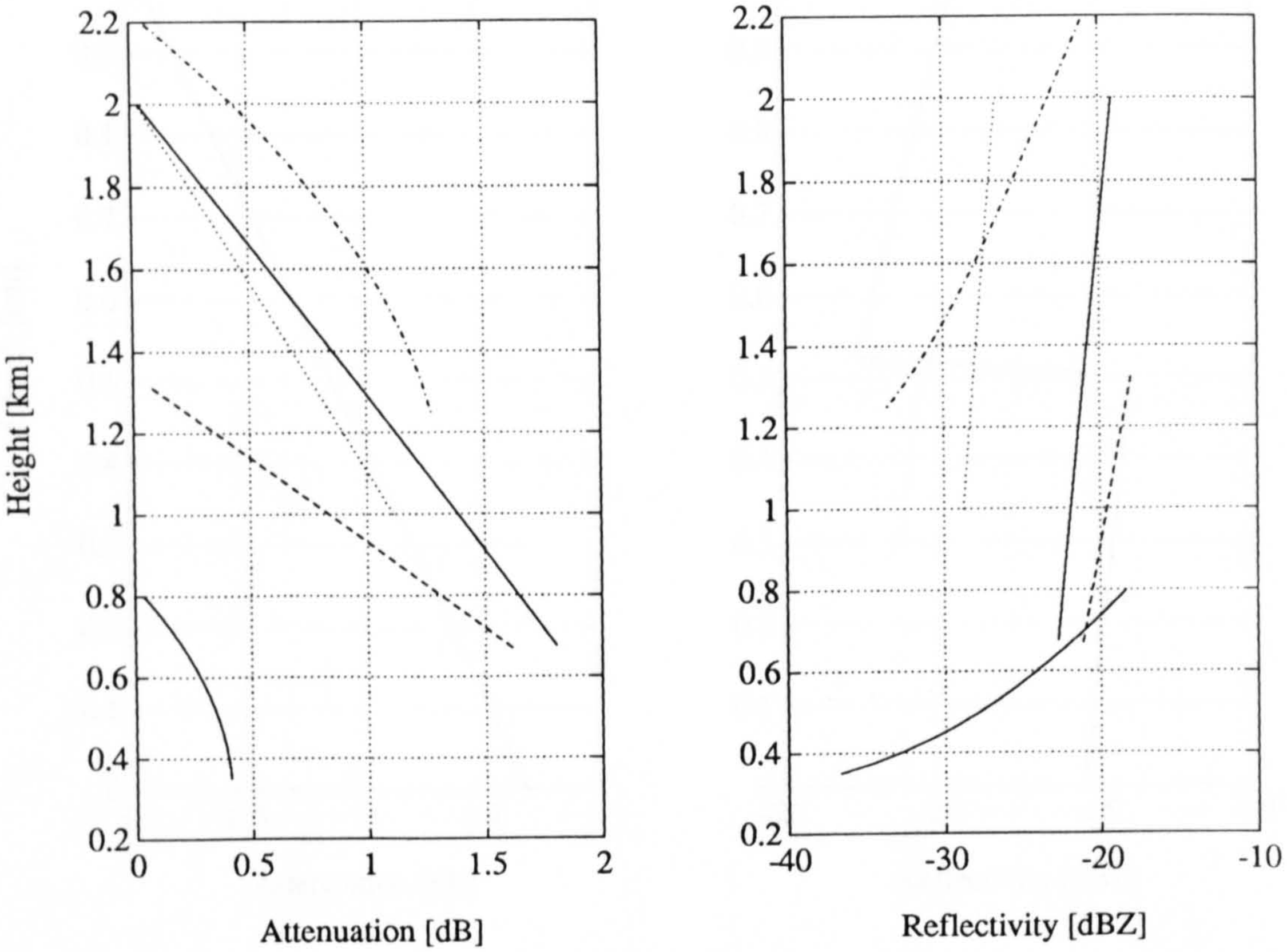

Further attenuation and reflectivity profiles for St and Sc can be seen in figures 14 and 15 where the models of Silverman, Carrier et al, Foot and Nicholls are compared. Typically for St or Sc specific attenuation is about 1 dB/km and reflectivity is in the range -17.5 to -35 dBZ dependent upon effective radius.

Precipitating St and Sc are illustrated in figure 16. Two cases are shown, namely for drizzle and light rain. Cloud model 3 of table IV has been adopted for the upper part of the cloud.

In the precipitating layer, constants for the exponential size distribution of A=100, β=6, r_{max}=500 μm and $N_L=10^{-2}$ cm^{-3} have been taken for the drizzle. For light rain N_L has been taken as 10^{-1} cm^{-3}. The presence of precipitation enhances the reflectivity by 2.5 dBZ for drizzle ($\equiv$ 2.5 mm/hr) or 7.5 dBZ for light rain ($\equiv$ 5 mm/hr). Specific attenuation remains similar to that in the cloud.

Fig. 16. Attenuation and reflectivity profiles for a precipitating St/Sc cloud model.

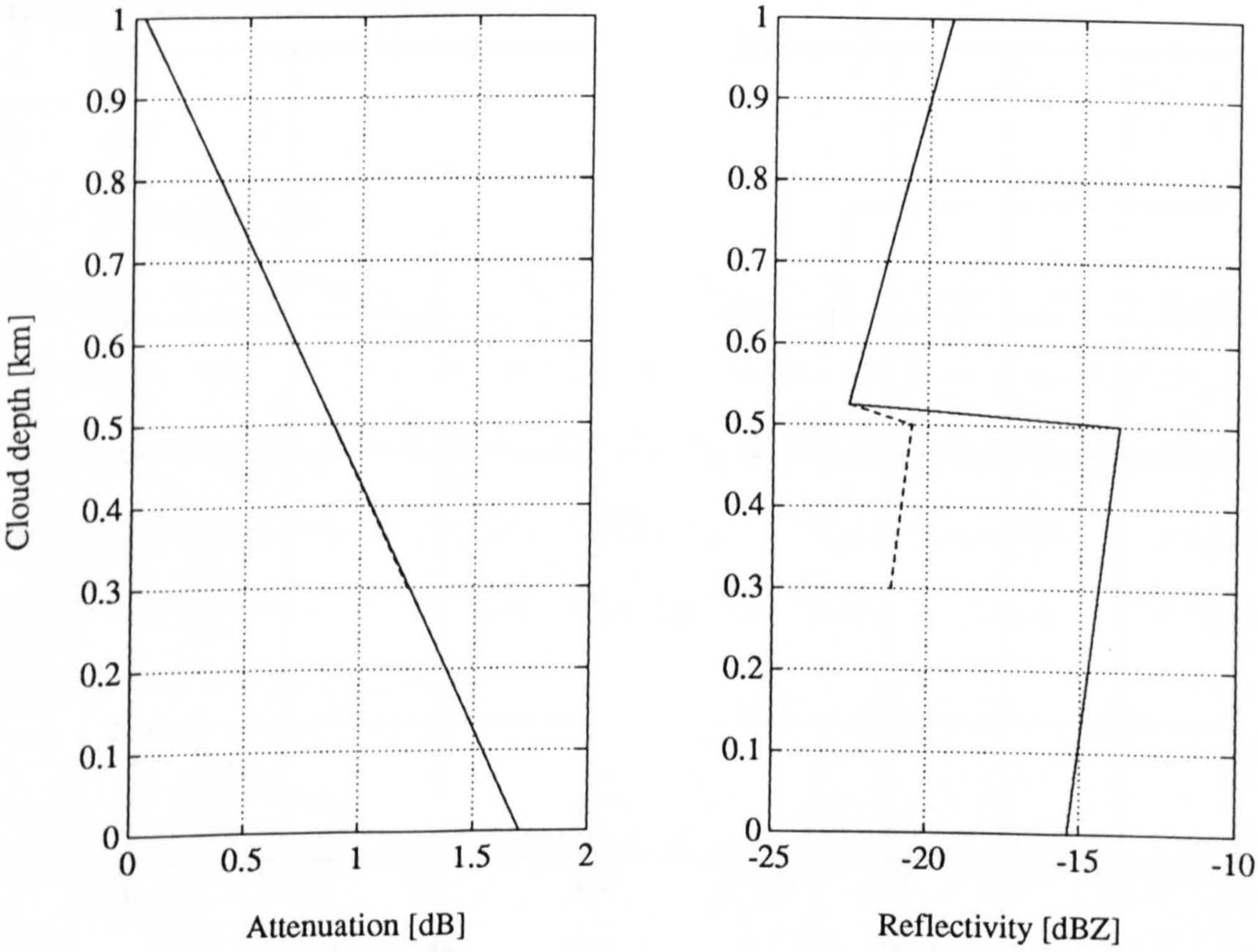

5.8.3 Altostratus and Nimbostratus.

Figure 17 shows the attenuation and reflectivity profiles for Silverman's As cloud model 6 and model 2 of Carrier et al. A two-layer ice/water cloud model has also been considered and illustrated in figure 17. For the upper part an iwc of 0.1 gm^{-3} has been taken with a concentration of 0.1 cm^{-3}, throughout the layer. In the lower part the cloud characteristics are the same as for Silverman's As cloud model. For the liquid water As cloud models attenuation is approximately 2dB/km and reflectivity is typically over -25 dBZ. The presence of ice in the upper part of the cloud would result in a significant enhancement of reflectivity but negligible attenuation. Therefore, multi-layer As structures can be easily recognized.

Results for Ns cloud models are shown in figure 18. Here Silverman's models 8 and 13 are taken along with model 4 from Carrier et al. Nimbostratus clouds seem to give values of reflectivity consistently higher by 10 dBZ than St or Sc. They are also heavily attenuating

Fig. 17. Attenuation and reflectivity profiles for the Silverman (6) and Carrier (2) As and the two layer model considered here.

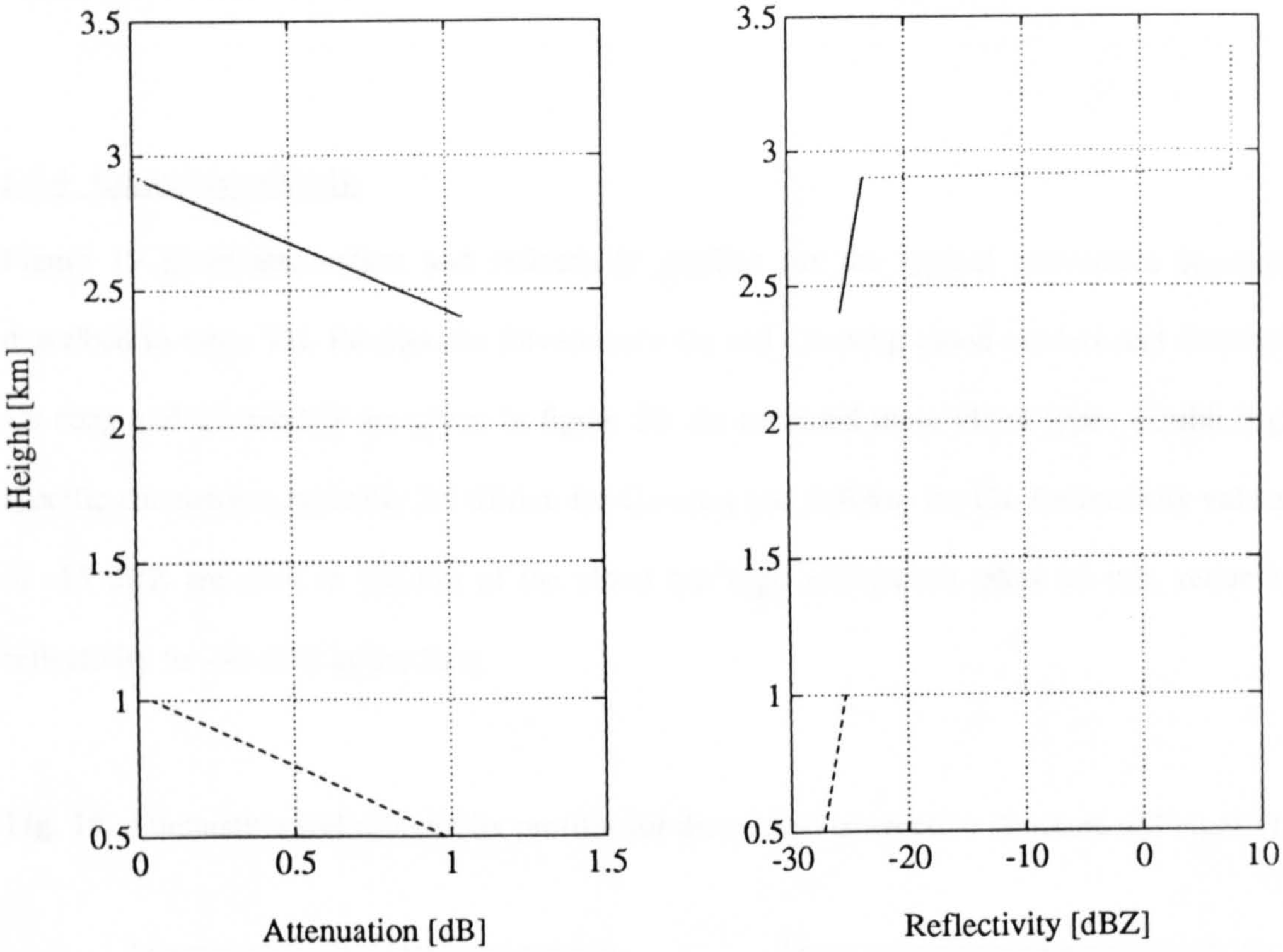

Fig. 18. Attenuation and reflectivity profiles for the Silverman (8,13) and Carrier (4) Ns cloud models.

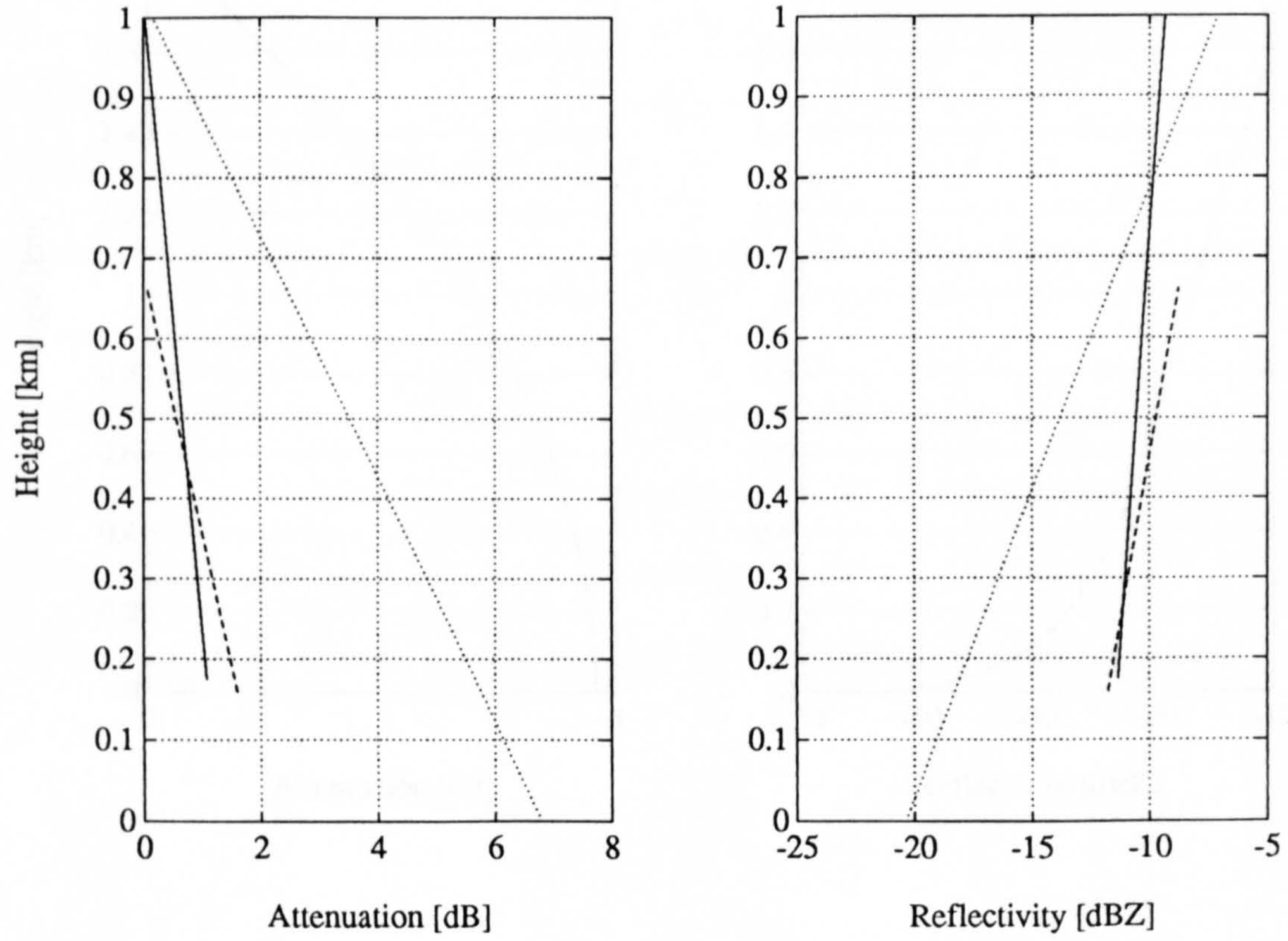

(~ 6 dB/km for Carrier's cloud model 4).

5.8.4 Convective clouds.

Figure 19 gives attenuation and reflectivity profiles for the typical convective structure described in table VII. Profiles for Silverman's Cu and Cu-cong cloud models and Carrier's Cu-cong and Cb models are given in figure 20. As expected these cloud types exhibit high specific attenuation, typically 2.5 dB/km for Cu-cong and 5dB/km for Cu. Reflectivity values of -15 dBZ are seen at the top of the cloud but high attenuation takes its toll, reducing reflectivity to -30 dBZ at the base.

Fig. 19. Attenuation and reflectivity profiles for the typical convective structure of Feigelson.

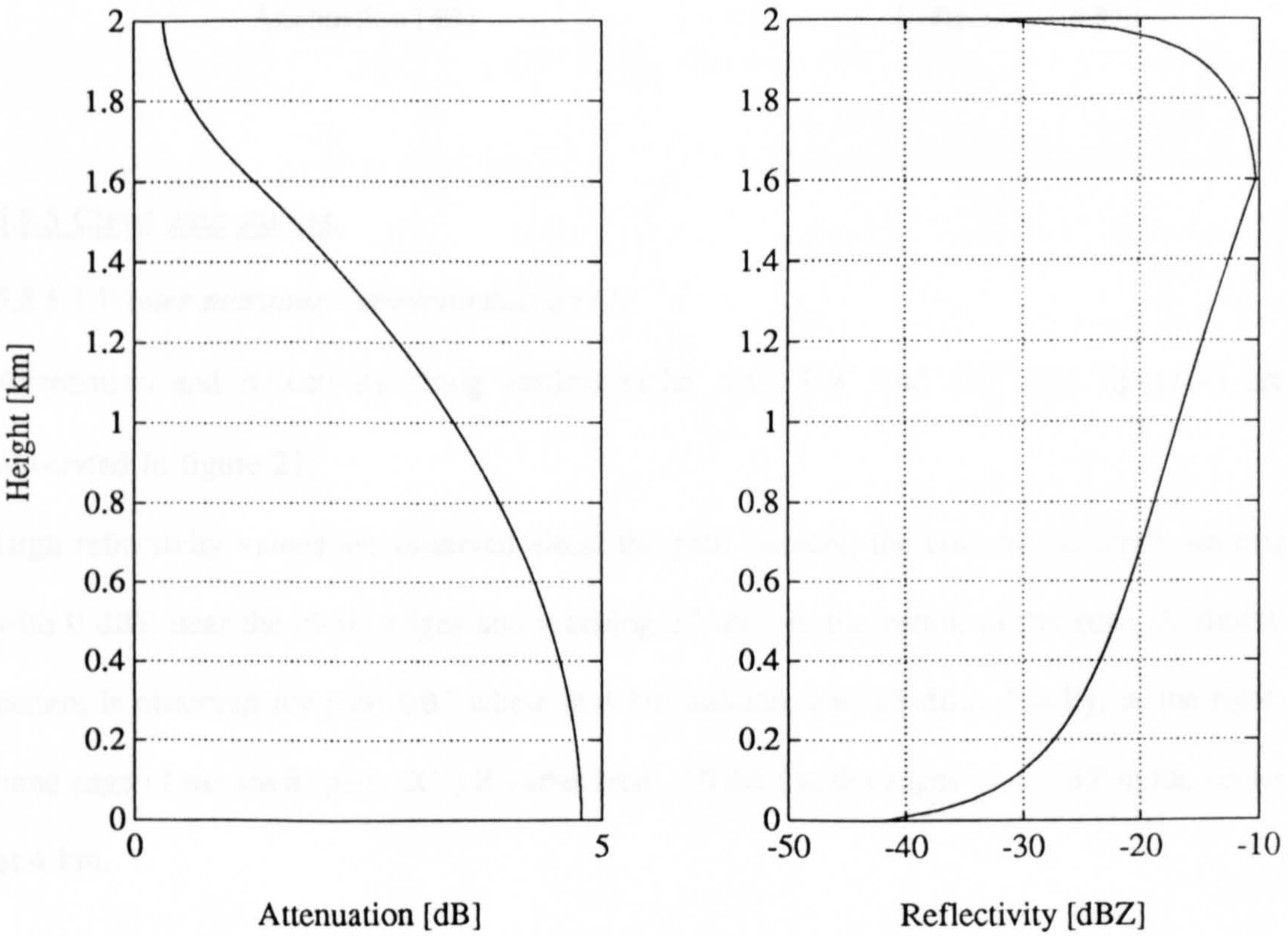

Fig. 20. Attenuation and reflectivity profiles for the AFGL Cu, (5) Cu-cong (14) and Carrier Cu-cong (7) cloud models.

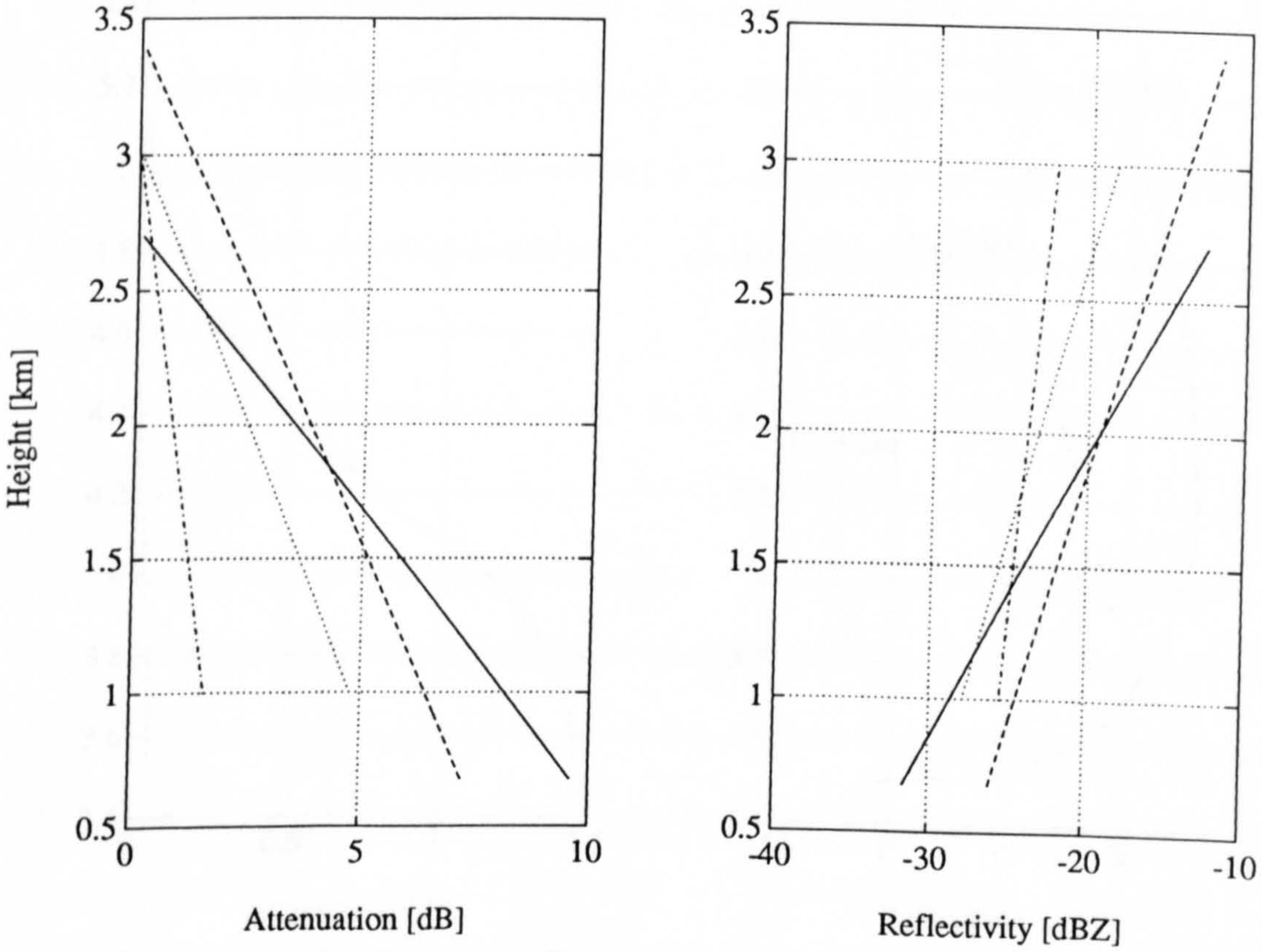

5.8.5 Cloud case studies.

5.8.5.1 Winter maritime cumulonimbus anvil.

Attenuation and reflectivity along vertical paths AA', BB' and CC' (see figure 4) are illustrated in figure 21.

High reflectivity values are observed along the path crossing the core of the anvil, starting with 0 dBZ near the cloud edges and reaching 25 dBZ in the centre of the core. A similar pattern is observed for path BB' where at 4 km altitude, Z=16.5 dBZ. Finally, at the right-hand edge of the anvil (path CC') Z varies from -10 dBZ at the edges to -5 dBZ in the centre at 4 km.

Fig. 21. Attenuation and reflectivity profiles for the maritime Cb anvil of Bennetts along vertical paths AA' (core), BB' (off the core) and CC' (right hand edge of the anvil).

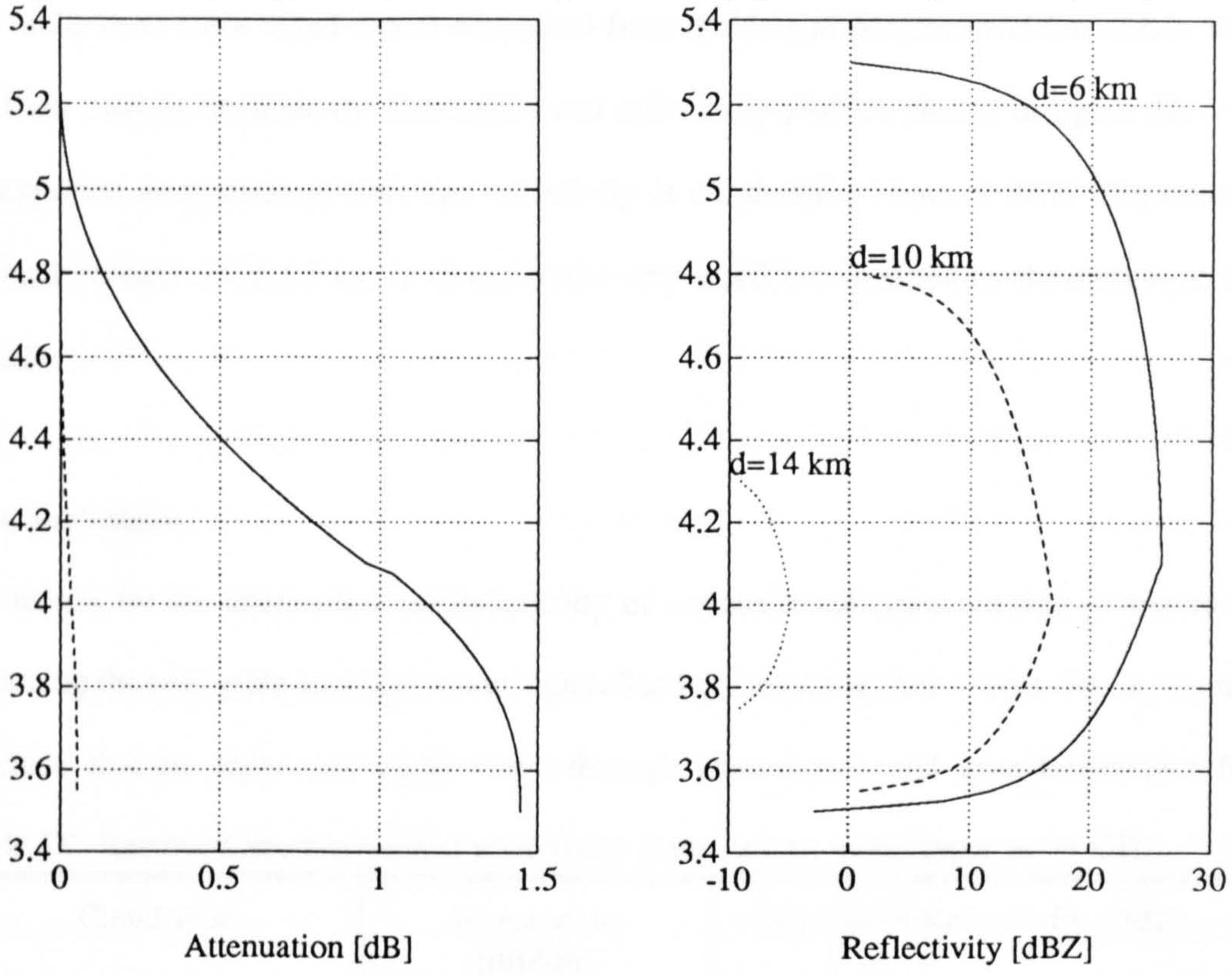

Fig. 22. Attenuation and reflectivity profiles for the snow cloud of Magono and Lee during the decaying phase (c).

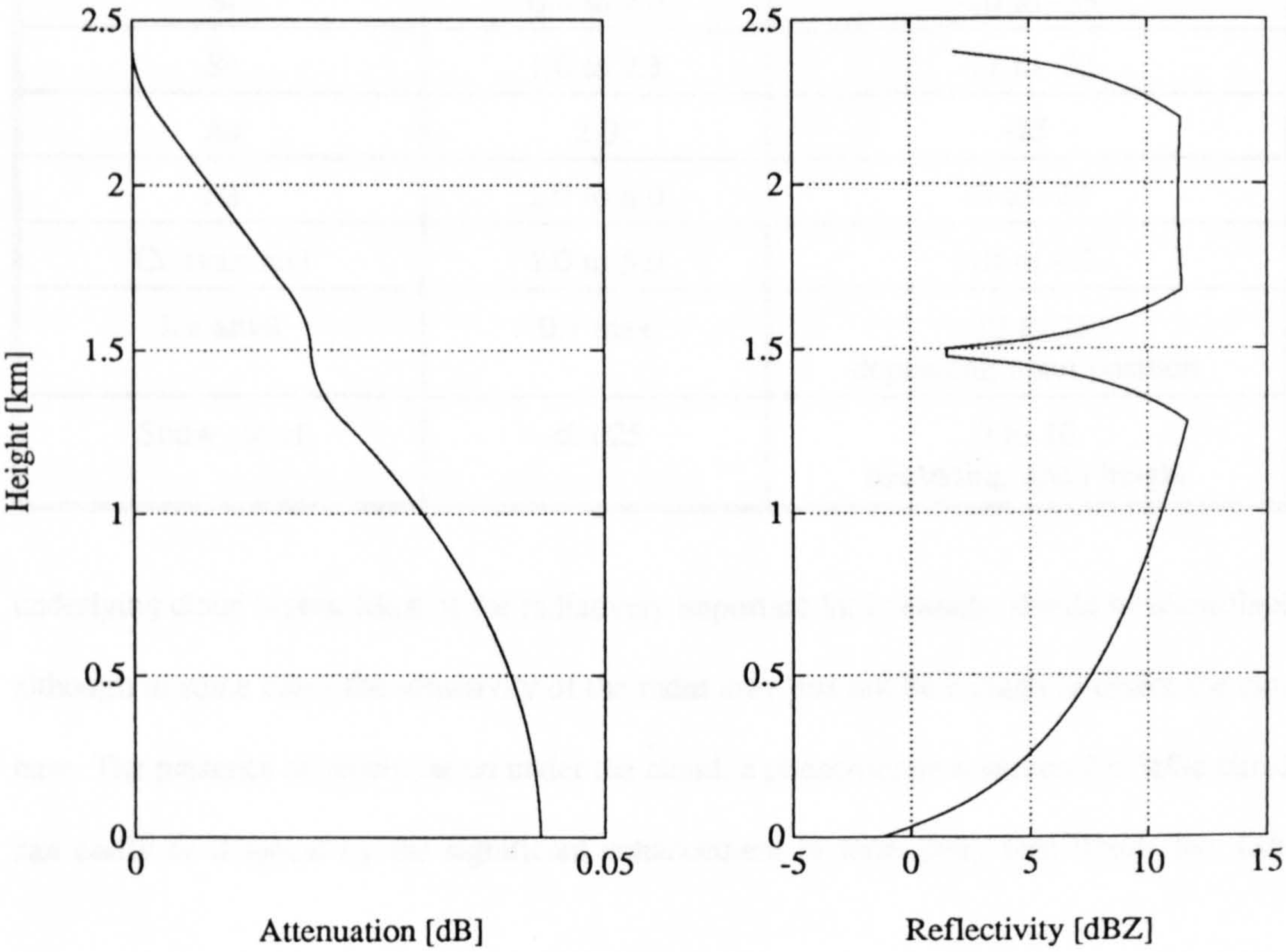

5.8.5.2 Snow clouds: Magono and Lee.

The multi-layer snow cloud model abstracted from the data of Magono and Lee (table VIII) has been used to calculate the attenuation and reflectivity profiles plotted in figure 22. As expected attenuation is low, but reflectivity is consistently above 5 dBZ. The unusual fluctuation observed at 1.5 km is related to the very small iwc reported by the authors at this altitude.

5.9 Conclusions.

The results for the attenuation and reflectivity of various cloud types are now summarized. Regarding the negligible attenuation and high reflectivity resulting from Cirrus clouds, we may conclude that the radar can easily "see" through these clouds and give information for underlying cloud layers. Most of the radiatively important St/Sc clouds, should be identifiable, although in some cases the sensitivity of the radar may just not be enough to detect the cloud base. The presence of precipitation under the cloud, a phenomenon common for St/Sc clouds, can easily be detected by the significant enhancement in reflectivity (see figure 16). Other

Table IX. Resultant attenuation and reflectivity from various cloud types at 94 GHz.

Cloud type	Attenuation [dB/km]	Equivalent Reflectivity [dBZ]
Ci	<0.3	-15 to 15
St	0.8 to 2.0	-20 to -35
Sc	1.0 to 2.5	-17 to -35
As	2.0	-25
Ns	2.0 to 6.0	-7 to -20
Cu (various)	1.0 to 5.0	-10 to -32
Ice anvil	0.7 max	-10 to 25 depending upon position
Snow cloud	<0.025	0 to 10 depending upon height

stratiform clouds such as As and Ns can be more easily mapped in their vertical extent, since the associated reflectivity clearly lies above the sensitivity limit. Mapping of clouds with significant vertical extent can be problematic. The high attenuation usually associated with these clouds, reduces dramatically the observed reflectivity and will not allow the base of the cloud to be observed. Typically, reflectivity is -30 dBZ for a 2 km deep cumuliform cloud. Ice anvils can be very well mapped in the horizontal as well as in their vertical extent. Furthermore, the resultant low attenuation (less than 0.75 dB/km), guarantees that information for the underlying cloud layers (ie the portion of the cloud that contains water droplets) can be obtained. Snow clouds should not be a problem. High reflectivity and negligible attenuation in combination with the height of occurrence should normally be the decisive factors for the identification and mapping of snow clouds.

In conclusion, the analysis presented in this chapter, favours the concept of a nadir pointing fixed beam spaceborne cloud radar. The -30 dBZ sensitivity limit implied by the preliminary specification considered in section 5.2, appears to be just adequate for the mapping of the vertical distribution of the most important cloud structures. The former analysis clearly indicates that a further 5 dBZ increase in the sensitivity is critically necessary to reduce uncertainties related to the detection of cloud bases. However, although the millimetre wave radar could successfully map the vertical distribution of various cloud types, it would not be necessarily able to definitely identify a certain cloud type if super-large drops are present in the cloud. Nevertheless, the presence and the description of the spectra of super-large drops in clouds is a subject that deserves further study.

CHAPTER 6

THE EQUATION OF RADIATIVE TRANSFER AT MM-WAVELENGTHS.

6.1 Introduction

Modelling the propagation of electromagnetic radiation in a medium which absorbs, emits and scatters radiation, is the subject of the theory of radiative transfer. In this chapter the fundamental quantities which the subject of radiative transfer deals with will be defined, and the equation that describes all the above physical mechanisms will be derived.

6.2 Definitions

6.2.1 The specific intensity.

The analysis of a radiation field often requires us to consider the amount of radiant energy, dE_ν, in a specified frequency interval $(\nu,\nu+d\nu)$ which is transported across an element of area $d\sigma$ and in directions confined to an element of solid angle $d\omega_s$, during a time dt (see fig. 1).

Fig. 1. Geometry of the radiation field.

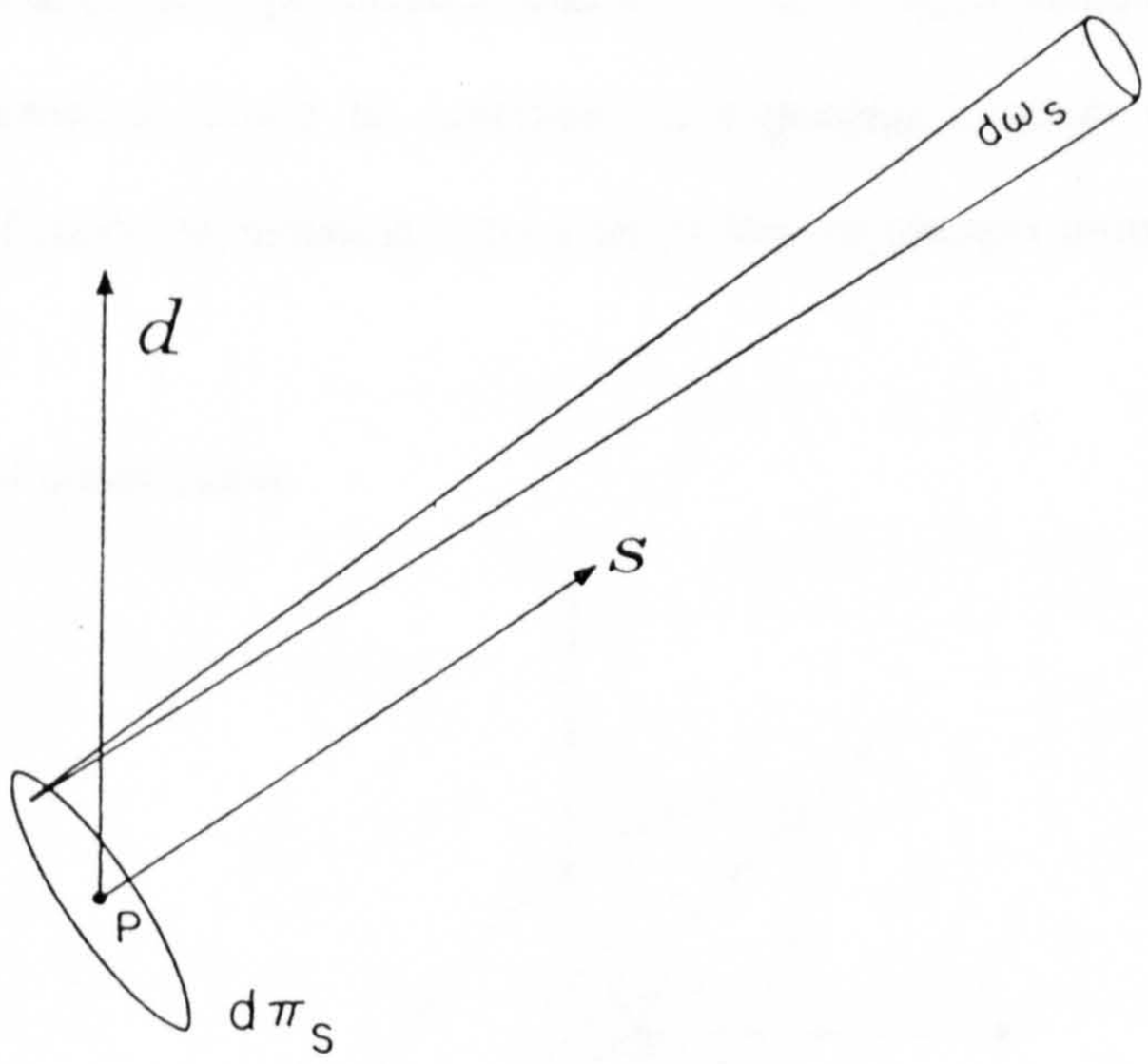

This energy, dE_ν, is expressed in terms of the specific intensity (or, more simply, the

intensity), I_ν, by:

$$dE_\nu = I_\nu(P,\bar{s})\, d\nu d\sigma d\omega_s dt \ .$$

If I_ν is not a function of direction the intensity field is said to be isotropic; if I_ν is not a function of position the field is said to be homogenous. And if the intensity is the same at all points and in all directions the field is said to be homogenous and isotropic. The intensity I_ν integrated over all the frequencies is denoted by I and is called the integrated intensity; thus

$$I = \int I_\nu d\nu \ .$$

While for most purposes the intensity I_ν sufficiently characterizes a radiation field, it is important to note that further parameters describing the state of polarization of the radiation field must be specified before we can regard the description of the field as really complete.

6.2.2 The Stokes parameters.

In order to describe a general radiation field, four parameters namely the intensity, the degree of polarization, the plane of polarization and the elipticity of the radiation at each point and in any given direction should be specified. In a gaseous medium the most convenient representation of polarized radiation is by a set of four parameters introduced by Sir George Stokes [1901].

Fig. 2. Ellipse of polarization.

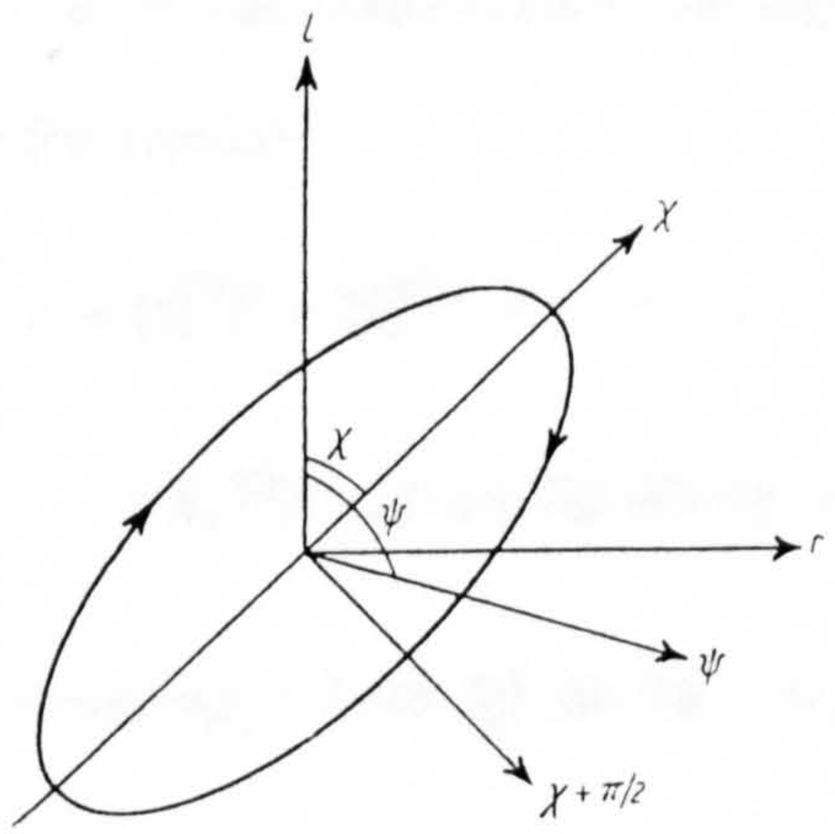

It is well known that in an elliptically polarized radiowave the vibrations of the electric (and the magnetic) vector in the plane transverse to the direction of propagation are such that the ratio of the amplitudes and the difference in phases of the components in any two directions at right angles to each other are absolute constants. A regular vibration of this character (either the electric or the magnetic field) can be represented by:

$$\xi_l = \xi_l^{(0)} \sin(\omega t - \epsilon_l) , \qquad \xi_r = \xi_r^{(0)} \sin(\omega t - \epsilon_r) ,$$

where ξ_l and ξ_r are the components of the vibration along two directions **l** and **r** at right angles to each other, ω the circular frequency of vibration, and $\xi_l^{(0)}$, $\xi_r^{(0)}$, ϵ_l, and ϵ_r are constants.

If the principal axes of the ellipse described by (ξ_l, ξ_r) are in directions making angles χ and $\chi + \frac{1}{2}\pi$ to the direction **l**, the equations representing the vibration take the simplified forms

$$(\xi_\chi = \xi^{(0)} \cos\beta \sin\omega t , \qquad \xi_{\chi+\frac{1}{2}\pi} = \xi^{(0)} \sin\beta \cos\omega t ,$$

where β denotes an angle whose tangent is the ratio of the axes of the ellipse traced by the end point of the electric vector. We shall suppose that the numerical value of β lies between 0 and $\frac{1}{2}\pi$ and that the sign of β is positive or negative according to as the polarization is right-handed or left-handed. Further, $\xi^{(0)}$ denotes a quantity proportional to the mean amplitude of the electric vector and whose square is equal to the intensity of the beam

$$I = [\xi^{(0)}]^2 = [\xi_l^{(0)}]^2 + [\xi_r^{(0)}]^2 = I_l + I_r ,$$

After some algebraic manipulation we can finally write for the regular vibrations representing an elliptically polarized beam the relations

$$I = [\xi_l^{(0)}]^2 + [\xi_r^{(0)}]^2 = I_l + I_r ,$$

$$Q = [\xi_{lu}^{(0)}]^2 - [\xi_r^{(0)}]^2 = I \cos 2\beta \sin 2\chi = (I_l - I_r) ,$$

$$U = 2\xi_l^{(0)} \xi_r^{(0)} \cos(\epsilon_l - \epsilon_r) = I \cos 2\beta \sin 2\chi = (I_l - I_r) \tan 2\chi ,$$

$$V = 2\xi_l^{(0)}\,\xi_r^{(0)}\sin(\epsilon_l-\epsilon_r) = I\sin 2\beta = (I_l-I_r)\tan 2\beta\sec 2\chi\ .$$

These are the Stokes parameters representing an elliptically polarized beam. We observe that among the quantities I,Q,U and V defined previously there exists the relation $I^2=Q^2+U^2+V^2$. Further, the plane of polarization and the elipticity follow from the equations $\tan2\chi=U/Q$ and $\sin2\beta=V/(Q^2+U^2+V^2)^{½}$. In some cases (ie when applying linear transformations to the Stokes parameters), it is more convenient to use a slightly different set of Stokes parameters, that is $\mathbf{I}=[I_l,I_r,U,V]$. The two sets are absolutely equivalent and as we have seen, $I=I_l+I_r$, $Q=I_l-I_r$. In representing the vibration by the former set of equations we have assumed the amplitudes and the phases to be constants. But in reality this is not attainable and the amplitudes or phases although may be constant for millions of vibrations, yet they may change irregularly millions of times a second. However, in an elliptically polarized beam these irregular vibrations must be such that the ratio of the amplitudes and the difference of phases $\delta=\epsilon_l-\epsilon_r$, should be absolute constants. Thus, the apparent intensity vector **I** is given by the mean values

$$I_l=\overline{[\xi_l^{(0)}]^2},\quad I_r=\overline{[\xi_r^{(0)}]^2},\quad U=2\overline{[\xi_l^{(0)}\ \xi_r^{(0)}]}\cos\delta,\quad V=2\overline{[\xi_l^{(0)}\ \xi_r^{(0)}]}\sin\delta\ ,$$

provided the shape and the orientation of the polarization ellipse remain constant through all vibrations.

6.2.3 Energy flux.

The component of flux in the **d**-direction, $F_{v,d}(P)$, is defined as the total energy flowing across unit area perpendicular to **d**, per unit frequency interval. An infinitesimal area $d\pi_d$ has a projected area in the **s**-direction

$$d\pi_s = d\pi_d\cos(d,\ s)\ ,$$

where (**d**,**s**) denotes the angle between the two vectors. The energy flux across $d\pi_d$, integrated over all **s**-directions is, from the definitions of $I_v(P,\mathbf{s})$ and $F_{v,d}(P)$,

$$F_{\nu,d}(P)d\nu d\pi_d = \int I_\nu(P, \bar{s})\cos(\bar{d}, \bar{s})\, d\pi_d d\omega_s d\nu ,$$

or

$$F_{\nu,d}(P) = \int I_\nu(P, \bar{s})\cos(\bar{d}, \bar{s})\, d\omega_s ,$$

where the integral extends over all solid angles.

6.2.4 Energy density.

Let us consider a cylinder, parallel to the s-direction, of length ds and cross-section $d\pi_s$. A quantum of radiation travelling in the s-direction will spend a time dt=ds/c in the cylinder, where c is the velocity of light.The total amount of energy in the cylinder made up of quanta

Fig. 3. Radiative heating.

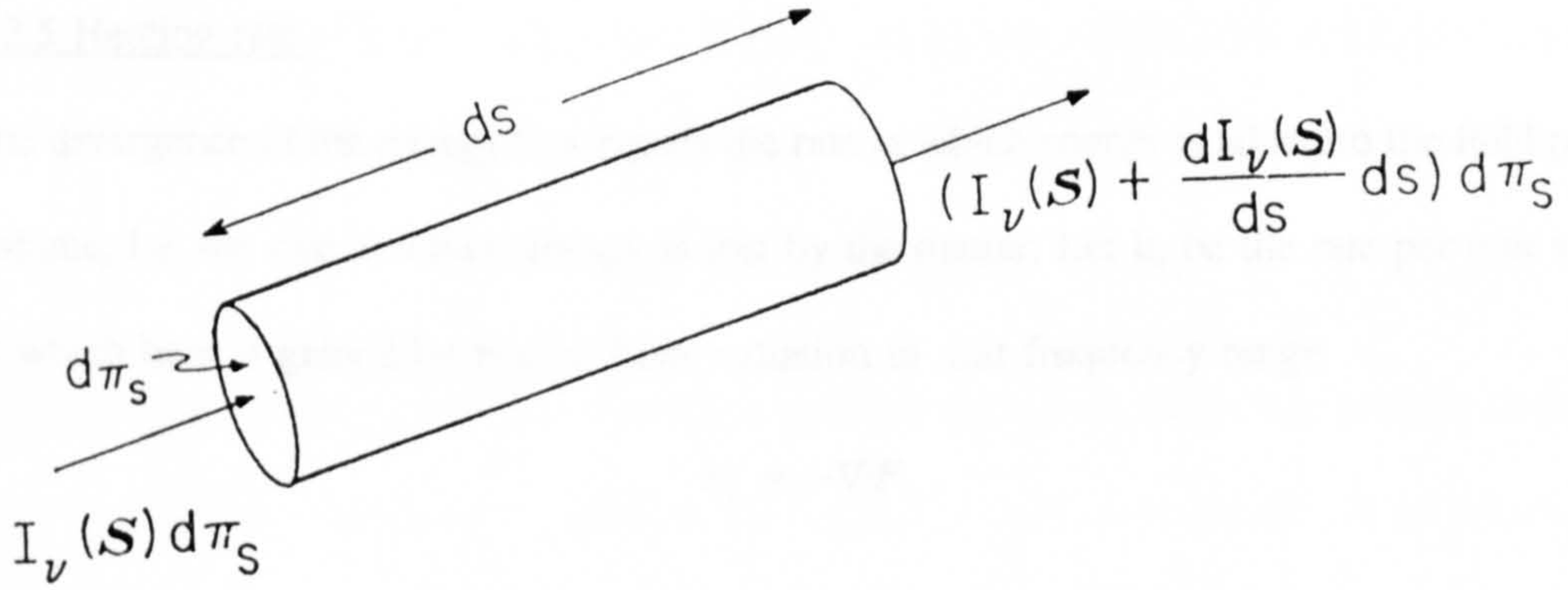

travelling in the s-direction within the solid angle $d\omega_s$ is that which crosses $d\pi_s$ in time dt

$$I_\nu(P, \bar{s})d\pi_s d\nu d\omega_s dt = \frac{I_\nu(P, s)}{c} d\pi_s d\nu d\omega_s ds .$$

The volume of the cylinder is $ds d\pi_s$ and these quanta contribute to the energy density an amount

$$\frac{I_\nu(P, \bar{s})}{c} d\nu d\omega_s .$$

Integrating over all directions we find for the energy density in the frequency range ν to ν+dν

$$u_\nu(P)d\nu = \frac{d\nu}{c}\int I_\nu(P, \bar{s})d\omega_s ,$$

Hence,

$$u_\nu(P) = \frac{4\pi}{c}\overline{I_\nu(P)} ,$$

where

$$\overline{I_\nu(P)} = \frac{1}{4\pi}\int I_\nu(P, \bar{s})d\omega_s$$

is the average intensity of the radiation field.

6.2.5 Heating rate

The divergence of the energy flux equals the rate at which energy is added to the field per unit volume, i.e. the rate at which energy is lost by the matter. Let h_ν be the rate per unit volume at which heat is gained by matter from radiation in unit frequency range

$$h_\nu = -\nabla\cdot F_\nu .$$

Expanding the right side of former equation and using the definition of flux we find

$$\nabla\cdot F_\nu = \int d\omega_s \frac{dI_\nu}{ds} .$$

The meaning of this equation is now made clear regarding figure 3. The energy lost by matter in the small cylinder is $\{dI_\nu(\mathbf{s})/ds\}ds d\pi_s d\omega_s$ per second per unit frequency range. Since $ds d\pi_s$ is the volume of the cylinder the heat loss per unit volume from radiation travelling in the **s** direction is $\{dI_\nu(\mathbf{s})/ds\}d\omega_s$, and the last equation follows by integrating over all ω_s.

It is now useful to introduce the concept of radiative equilibrium, whereby there is no net energy exchange between matter and the radiation field

$$h = \int h_\nu d\nu = 0 \ .$$

A special case of radiative equilibrium is monochromatic radiative equilibrium where

$$h_\nu = 0 \ .$$

In defining radiative equilibrium and in other problems concerning atmospheric thermodynamics the relevant quantities are those which are integrated over the entire spectrum.

In this case,

$$I = \int I_\nu d\nu \ , \qquad F = \int F_\nu d\nu \ , \qquad u = \int u_\nu d\nu \ , \quad etc.$$

6.3 The absorption coefficient.

A pencil of radiation traversing a medium will be weakened by its interaction with matter. If the specific intensity I_ν therefore becomes $I_\nu + dI_\nu$ after traversing a thickness d_s in the direction of its propagation, we write

$$dI_\nu = - \kappa_\nu \rho \ I_\nu \ ds \ ,$$

where ρ is the density of the material. The quantity κ_ν introduced in this manner defines the mass absorption coefficient for radiation of frequency ν. Now it should not be assumed that this reduction in intensity, which a pencil of radiation in passing through matter experiences, is necessarily lost to the radiation field. For it can very well happen that the energy lost from the incident pencil may all reappear in other directions as scattered radiation. In general we may, however, expect that only a part of the energy lost from an incident pencil will reappear as scattered radiation in other directions and that it represents the transformation of radiation into other forms of energy (or even of radiation of other frequencies). We shall therefore have to distinguish between the absorption and scattering. Considering first the case of scattering, we say that a material is characterized by a mass scattering coefficient κ_ν if from a pencil of radiation incident on an element of mass of cross-section $d\sigma$ and height d_s, energy is scattered

from it at the rate

$$\kappa_\nu \rho d_s \times I_\nu \cos\theta \, d\nu \, d\sigma \, d\omega$$

in all directions. Since the mass of the element is

$$dm = \rho \cos\theta \, d\sigma \, ds ,$$

we can also write

$$\kappa_\nu I_\nu \, dm \, d\nu \, d\omega .$$

It is now evident that to formulate quantitatively the concept of scattering we must specify in addition the angular distribution of the scattered radiation. We shall therefore introduce a phase function $p(\cos\Theta)$ such that

$$\kappa_\nu I_\nu \, p(\cos\Theta) \frac{d\omega'}{4\pi} \, dm \, d\nu \, d\omega ,$$

gives the rate at which energy is being scattered into an element of solid angle $d\omega'$ and in a direction inclined at an angle Θ to the direction of incidence of a pencil of radiation on an element of mass dm. The rate of loss of energy from the incident pencil due to scattering in all directions is

$$\kappa_\nu I_\nu \, dm \, d\nu \, d\omega \int p(\cos\Theta) \frac{d\omega'}{4\pi}$$

assuming that the phase function is normalized to unity, that is

$$\int p(\cos\Theta) \frac{d\omega'}{4\pi} = 1 .$$

When both scattering and true absorption are present, the scattered intensity is given again by the same expression, but the integral of the phase function over all directions is naturally less than unity, that is

$$\int p(\cos\Theta) \frac{d\omega'}{4\pi} = \overline{\omega_0} \leq 1 .$$

Thus the general case differs from the case of pure scattering only by the fact that the phase function is not normalised to unity.

It is evident from our definitions that ω_0 represents the fraction of the light lost from incident pencil due to scattering, while $(1-\omega_0)$ represents the remaining fraction which has been transformed into other forms of energy (or of radiation of other wavelengths). We shall refer to ω_0 as the albedo for single scattering. Moreover, when $\omega_0=1$ we shall say that we have a conservative case of perfect scattering.

The simplest example of a phase function is

$$p(\cos\Theta) = constant = \overline{\omega_0} \ .$$

In this case the radiation scattered by each element of mass is isotropic. Next to this isotropic case greatest interest is attached to Rayleigh's [1899] phase function,

$$p(\cos\Theta) = \frac{3}{4}(1 + \cos^2\Theta) \ .$$

This phase function is normalised to unity so that is an example of a conservative case of perfect scattering. Another phase function which is of particular interest in problems relating to planetary illumination is

$$p(\cos\Theta) = \overline{\omega_0}\,(1 + x\cos\Theta) \quad (-1 \le x \le +1) \ .$$

In general we may suppose that the phase function can be expanded as a series in Legendre polynomials of the form

$$p(\cos\Theta) = \sum_{l=0}^{\infty} \overline{\omega_l}\, P_l(\cos\Theta) \ ,$$

where the ω_l's are constants [Chandrasekhar 1950]. In practise the series on the right hand-side is a terminating one with only a finite number of terms.

6.4 The emission coefficient.

The emission coefficient j_ν is defined in such a way that an element of mass dm emits in directions confined to an element of solid angle $d\omega_s$, in the frequency interval $(\nu,\nu+d\nu)$ and in time dt, an amount of radiant energy given by:

$$j_\nu \, dm \, d\omega_s \, d\nu \, dt \ .$$

In the case of a medium which scatters radiation (not necessarily with an albedo $\omega_o=1$) there will be a contribution to the emission coefficient from the scattering of radiation from all other directions into the pencil of directions considered. Thus, the scattering of a pencil of radiation from a direction (θ',ϕ') contributes to a pencil in the direction (θ,ϕ), energy at the rate

$$\kappa_\nu dm d\nu d\omega_s \, p(\vartheta,\varphi;\vartheta',\varphi') \, I_\nu(\vartheta',\varphi') \, \frac{\sin\vartheta' d\vartheta' d\varphi'}{4\pi} \ ,$$

where we have written $p(\theta,\phi;\theta',\phi')$to denote the phase function for the angle between the directions specified by (θ,ϕ) and (θ',ϕ'). Hence the contribution, $j_\nu^{(s)}$, to the emission coefficient by scattering alone is

$$j_\nu^s \, (\vartheta,\varphi) = \kappa_\nu \, \frac{1}{4\pi} \int_0^\pi \int_0^{2\pi} p \, (\vartheta,\varphi;\vartheta',\varphi') \, I_\nu \, (\vartheta',\varphi') \, \sin\vartheta' \, d\vartheta' d\varphi' \ .$$

We may expect that in general there will be contributions to the emission coefficient from causes other than scattering (ie thermal emission which is a common case in planetary atmospheres). In this latter case, the emission coefficient is given by:

$$j_\nu = j_\nu^s + j_\nu^e \ ,$$

where j_ν^e refers to contributions resulting from causes other than scattering.

When $j_\nu^e=0$ we have a purely scattering atmosphere and

$$j_\nu \equiv j_\nu^s \ .$$

It must be noted however, that a scattering atmosphere does not imply that we have a case of

perfect scattering.

6.5 The source function.

The ratio of the emission to the absorption coefficient is called the source function and is denoted by J_ν. Thus,

$$J_\nu = \frac{j_\nu}{\kappa_\nu} .$$

Particularly for a scattering atmosphere the source function is written

$$J_\nu(\vartheta,\varphi) = \frac{1}{4\pi} \int_0^{\pi} \int_o^{2\pi} p(\vartheta,\varphi;\vartheta',\varphi') \, I_\nu(\vartheta',\varphi') \sin\vartheta' d\vartheta' d\varphi' .$$

The source function is greatly simplified when the gaseous medium is in local thermodynamic equilibrium (LTE). An atmosphere is said to be in local thermodynamic equilibrium when it is possible to define at each point in the atmosphere a temperature T such that the coefficients of absorption κ_ν and emission j_ν are related according to the Kirchhoff-Planck equation

$$j_\nu = \kappa_\nu B_\nu (T)$$

and

$$B_\nu(T) = \frac{2h\nu^3}{c^2} \frac{1}{e^{h\nu/kT}-1} ,$$

where B_ν is the Planck function (k and h are the Boltzmann and Planck constants, respectively). In this latter case the source function takes a particularly simple form,

$$J_\nu = B_\nu(T) .$$

6.6 The equation of transfer.

We shall now derive the fundamental equation which governs the variation of intensity in a medium characterized by an absorption coefficient κ_ν and an emission coefficient j_ν. (it should

be noted that the emission coefficient can itself depend on the radiation field as will be the case, for example, in a scattering atmosphere.) For this purpose consider a small cylindrical element of cross-section $d\sigma$ and height ds in the medium. From the definition of intensity, it now follows that the difference in the radiant energy in the frequency interval $(\nu,\nu+d\nu)$ crossing the two faces normally, in a time dt and confined to an element of solid angle, is given by:

$$\frac{dI_\nu}{ds} ds d\nu d\sigma d\omega dt \ .$$

This difference in energy must arise from the excess of emission over absorption in the frequency interval and element of solid angle considered. Now the amount absorbed is

$$\kappa_\nu \rho \ ds \times d\nu \ d\sigma \ d\omega \ dt \ ,$$

while the amount emitted is

$$j_\nu \rho \ d\sigma \ ds \ d\nu \ d\omega \ dt \ .$$

Counting up the gains and losses in the pencil of radiation during its traversal of the cylinder, we have

$$\frac{dI_\nu}{ds} = -\kappa_\nu \rho I_\nu + j_\nu \rho \ .$$

In terms of the source function J_ν we can rewrite this equation in the form

$$-\frac{dI_\nu}{\kappa_\nu \rho ds} = I_\nu - J_\nu \ .$$

This is the equation of transfer. In its more general form the equation transfer must take into account the polarization properties of the intensity. Chandrasekhar [1947], following the Stokes formalization wrote first the equation of transfer in vector form

$$-\frac{d\bar{I}(\vartheta,\varphi)}{\kappa\rho ds} = \bar{I}(\vartheta,\varphi) - \bar{J}(\vartheta,\varphi) \ ,$$

where $\mathbf{J}(\theta,\phi)$ denotes the vector source function for $\mathbf{I}(\theta,\phi)$. Generally, $\mathbf{J}=\mathbf{J}_s+\mathbf{J}_e$, where $\mathbf{J}_s$ is the contribution due to scattering and $\mathbf{J}_e$ is the contribution due to all other causes. To evaluate $\mathbf{J}_s(\theta,\phi)$, we must consider the elementary contribution $d\mathbf{J}_s(\theta,\phi;\theta',\phi')$ to the source function arising from the scattering of a pencil of radiation of solid angle $d\omega'$ in the direction (θ',ϕ').

This is given by:

$$d\bar{J}(\vartheta,\varphi;\vartheta',\varphi') = \bar{L}(\pi-\iota_2)\,\bar{R}(\cos\Theta)\,\bar{L}(-\iota_1)\,\bar{I}(\vartheta',\varphi')\,\frac{d\omega'}{4\pi}\,,$$

where $\mathbf{I}(\theta',\phi')$ refers to the directions parallel and perpendicular to the plane of scattering OP_1Z, and $\mathbf{R}(\cos\Theta)$ is a phase matrix which expresses the angular distribution of the scattered radiation (see figure 4).

Fig. 4. Geometry for the illustration of the equation of transfer in vector form (after Chandrasekhar [1950]).

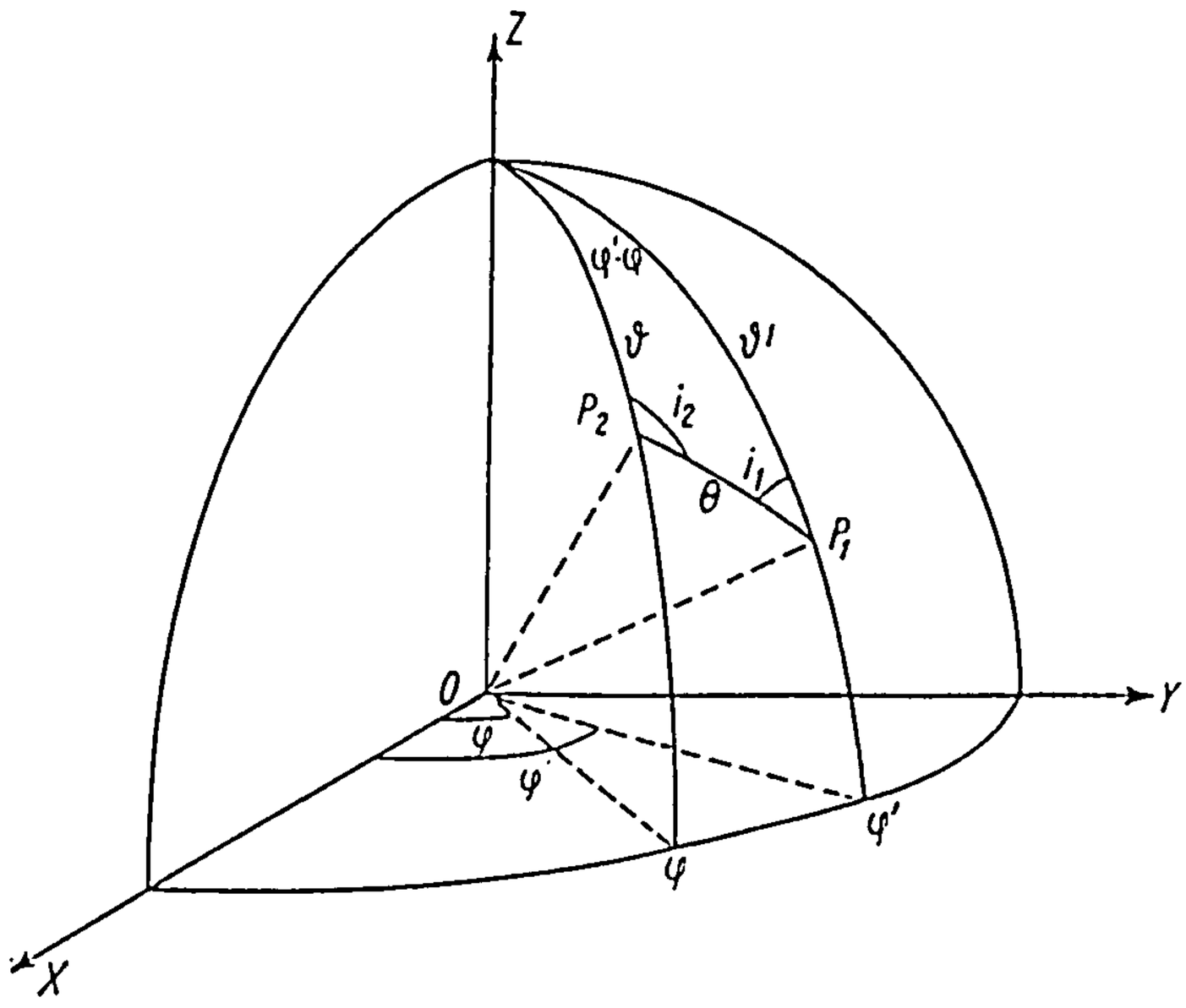

$L(i_1)$ and $L(\pi-i_2)$ are linear transformations that have been applied to the intensity vector to account for the effect of rotation of the axes of reference. i_1 is the angle between the meridian plane OP_1Z and the plane OP_1P_2, and i_2 is the angle between the planes OP_2Z and OP_1P_2.

The source function $\mathbf{J}_s(\theta,\phi)$ is now obtained by integrating the contribution $d\mathbf{J}_s(\theta,\phi;\theta',\phi')$ over all directions (θ',ϕ'). Thus,

$$\overline{J}_s(\vartheta,\varphi)=\frac{1}{4\pi}\int_o^{\pi}\int_o^{2\pi}\overline{L}(\pi-\iota_2)\,\overline{R}(\cos\Theta)\,\overline{L}(-\iota_1)\,\overline{I}(\vartheta',\varphi')\,\sin\vartheta' d\vartheta' d\phi' \ ,$$

or

$$\overline{J}_s(\vartheta,\varphi)-\frac{1}{4\pi}\int_o^{\pi}\int_o^{2\pi}\overline{P}(\vartheta,\varphi;\vartheta'\varphi')\,\overline{I}(\vartheta'\varphi')\,\sin\vartheta' d\vartheta' d\varphi' \ ,$$

where the phase-matrix $P(\theta,\phi;\theta',\phi')$ is given by:

$$\overline{P}(\vartheta,\varphi;\vartheta',\varphi') = \overline{L}(\pi-\iota_2)\,\overline{R}(\cos\Theta)\,\overline{L}(-\iota_1) \ .$$

Thus, the source function J can be calculated and the equation of radiative transfer in vector form is now fully defined.

6.7 The solution of the equation of transfer.

The general solution of the equation of transfer was given by Chandrasekhar [1950]

$$I(s) = I(0)\,e^{-\tau(s,0)} + \int_0^s J(s')e^{-\tau(s,s')}\,\kappa\rho\,ds' \ ,$$

where $\tau(s,s')$ is the optical thickness of the material between the points s and s'; thus

$$\tau(s,s') = \int_{s'}^{s}\kappa\rho\,ds \ .$$

The physical meaning of the solution is clear. It express the fact that the intensity at any point and in a given direction results from the emission at all anterior points, s', reduced by the factor $e^{-\tau(s,s')}$ to allow for the absorption by the intervening matter.

6.7.1 The solution of the equation of transfer at mm-wavelengths.

A typical nadir viewing problem in satellite remote sensing is the calculation of radiance at some altitude z_s above the earth, due to the combined effect of radiating surface at z_s, such as the land, sea or cloud top, and the thermal emission of the atmosphere (see figure 5). At

Fig. 5. A typical nadir viewing application in remote sensing.

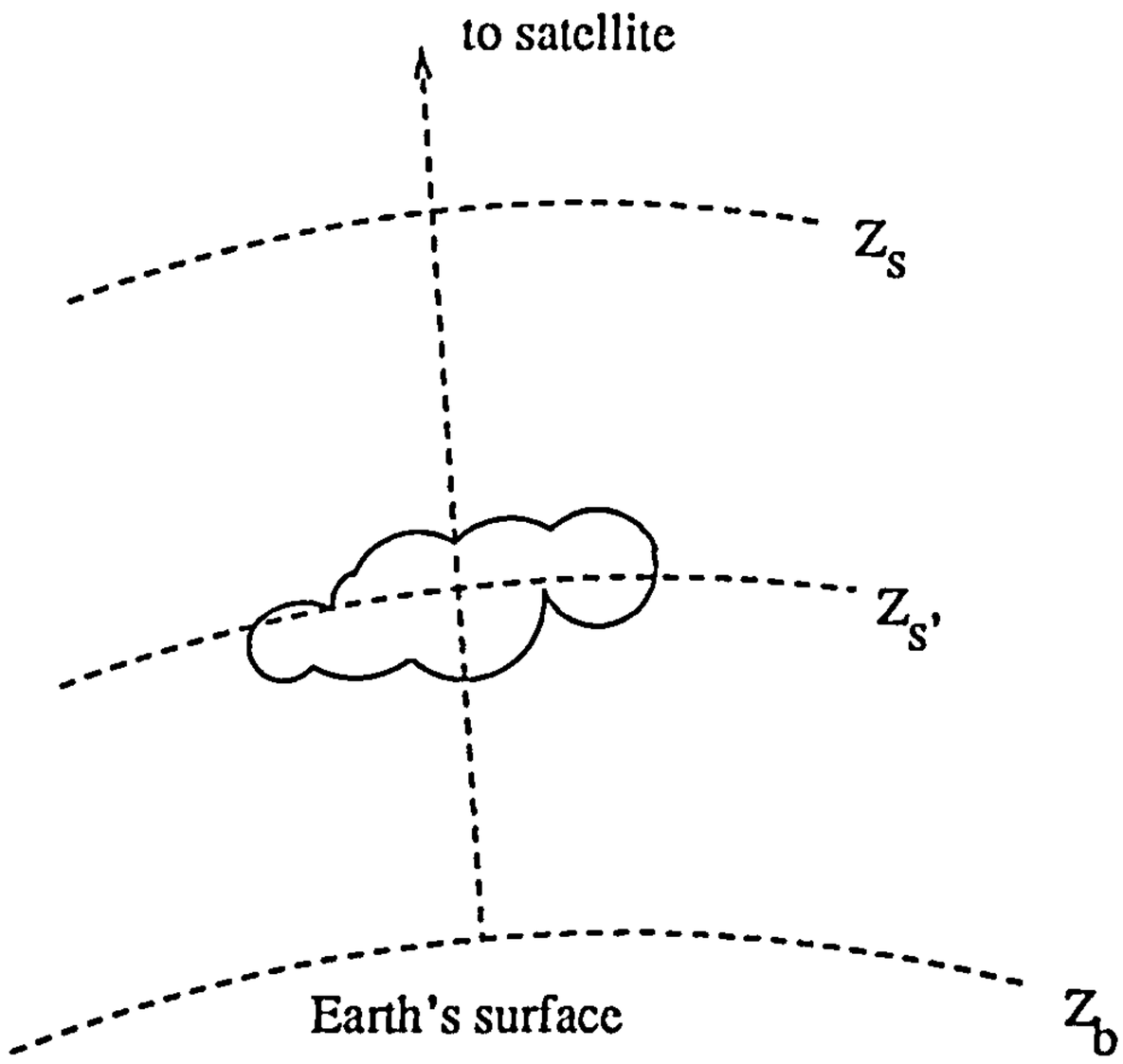

millimetre wavelengths where scattering by gases or suspended particles is negligible, the equation of radiative transfer takes a particularly simple form

$$I_\nu(z_s)=I_\nu(z_{s'})\ e^{-\tau_\nu(z_{s'},z_s)} + \int_{z_{s'}}^{z_s} B_\nu(z,T(z))\ k_\nu(z)\ \rho(z)\ e^{-\tau(z,z_s)}dz\ ,$$

where $I_\nu(z_{s'})$ is the intensity of radiation leaving the surface, ρ is the density of the absorbing gas, k_ν is the volume absorption coefficient, τ_ν is the optical depth and B_ν the Planck function. Generally, the intensity $I_\nu(z_{s'})$ is given by:

$$I_\nu(z_s')=\epsilon B_\nu(z_s') + (1-\epsilon)[B_\nu(z_b)e^{-\tau_\nu(z_b,z_{s'})} + \int_{z_b}^{z_s} B_\nu(z)\ k_\nu(z)\rho(z)\ e^{-\tau(z,z_s)}dz]\ ,$$

where ϵ is the emittance and T_s the temperature of the surface. The effective edge of the earth's atmosphere is z_b and T_b is the temperature at its boundary. The first term of the former equation represents the thermal emission of the surface. The second term represents the total radiation reaching the surface from the atmosphere, multiplied by the reflectance 1-ϵ, if we assume specular reflection. If the surface is a black body, then ϵ=1 and the second term

disappears. For a limb viewing case looking into deep space, the observed radiance will be due to atmospheric thermal emission alone and will be given by:

$$I_\nu(z_s') = \int_{z_s'}^{z_s} B_\nu(z,T(z))\ k_\nu(z)\ \rho(z)\ e^{-\tau(z,z_s)} dz\ .$$

6.8 Breakdown of thermodynamic equilibrium.

In strict thermodynamic equilibrium the source function depends upon the temperature, frequency and the velocity of light only. As we have already seen, this assumption greatly reduces the problems involved in the solution of the equation of transfer. It is therefore important to make an objective assessment of the applicability of this idealization under atmospheric conditions.

As Einstein demonstrated, an element of matter placed in a constant temperature enclosure may not absorb or emit energy according to Planck's and Kirchhoff's laws because of the existence of stimulated emission. A molecule may be stimulated by the impact of a photon and the resultant emission depends upon the intensity of the radiation environment. This phenomenon can not be described by classical thermodynamics. Instead, methods of quantum mechanical statistics have to be employed to explain the net energy transfer resulting from the interactions between molecules and the radiation field. The description of the physical processes involved in conditions where no LTE prevails is rather complicated and as such it will be omitted. Nevertheless, it should be mentioned that in the middle and higher atmosphere (altitudes > 80 km) the conditions for the existence of LTE begin to break down. In the following chapters we will ignore this fact, since at millimetre wavelengths the absorption and emission properties of the atmospheric gases are not seriously affected by the non-existence of LTE conditions.

CHAPTER 7

CALCULATION OF ABSORPTION AND DISPERSION SPECTRA OF ATMOSPHERIC GASES AT MM-WAVELENGTHS AND THE EFFECT OF TRACE GASES ON RADIOWAVE PROPAGATION.

7.1 Introduction.

At millimetre wavelengths absorption and dispersion by atmospheric gases can have significant effect on the propagation of electromagnetic radiation. Close to the earth's surface, absorption by atmospheric gases is dominated by water vapour and oxygen. Nevertheless, other atmospheric gases, including trace constituents, put their spectral signatures in the millimetre frequency spectrum (see figure 1). Although such contributions to attenuation are negligible for communication systems operating close to the earth's surface, they may become important for applications in remote sensing, navigation and communications operating at high altitudes. For the characterisation of the absorption and dispersion along slant paths at high altitudes, the spectra of various trace gases, refraction effects and relative air mass calculations must be evaluated. Computer programs are already available to calculate absorption spectra. FASCOD from Clough et al [1981], performs radiance and transmittance calculations, but it is very complicated and difficult to use particularly from the point of view of the radio engineer. In this chapter a simpler yet rigorous approach to modelling -the Atmospheric Propagation Model (APM) is described. The model addresses the needs of the radio engineer but may also be used for remote sensing applications. A line-by-line summation technique is used but interaction mechanisms are included and also provision is made for the water vapour continuum. Radiometric data and measurements verify the validity of the modelling approach. The effects of trace gases on radiowave propagation at wavelengths shorter than 3 mm are for the first time presented. Calculations for communication systems operating at high altitudes are given. The spectra of the two principal contributors, H_2O and O_2 are compared with the spectra of various trace gases. It is found that the contributions of trace gases are important.

Fig. 1. Spectral lines of various atmospheric gases from AFGL's HITRAN 1986 compilation.

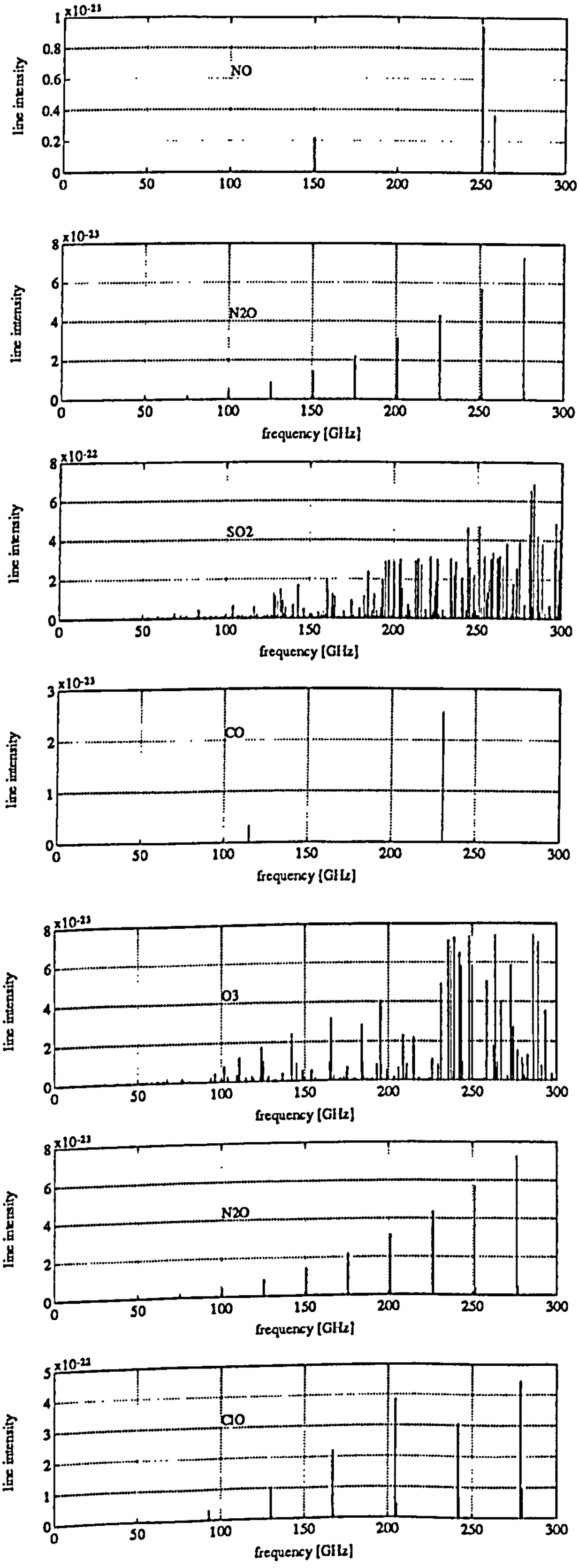

7.2 Theory of gaseous absorption.

Neglecting the interaction between modes of energy it can be written for the energy of an isolated molecule

$$E = E_r + E_v + E_e + E_t ,$$

where E_e, E_v, E_r are the electronic, vibrational and rotational energies, respectively and E_t is the translational energy. The first three terms in equation are quantized, and take discrete values only, these values being specified by one or more quantum numbers. Any combination of quantum numbers defines an energy state or quantum state, or term.

For absorption or emission to take place matter must interact with the incident field of electromagnetic radiation which in practice must involve an electric or magnetic dipole or quadrupole moment. In other words, for a molecule to be able to interact with an electromagnetic field and absorb or create a photon of frequency ν, it must possess at least transiently, a dipole oscillating at that frequency. For emission or absorption spectra this transient dipole is expressed in terms of quantum mechanics by the transition dipole moment. For a transition between states with eigenfunctions ψ_i and ψ_j is defined as

$$\mu_{ij} = -e\int \psi_j^* r \psi_i d\tau$$

where r is the location of the electron. The coefficient of stimulated absorption (and emission) and therefore the intensity of the transition is proportional to the square of the transition dipole moment and a detailed analysis gives

$$S_{ij} \sim \frac{|\mu_{ij}|^2}{6\epsilon_0 h^2}$$

and only if the transition dipole moment is non-zero does the transition contribute to the spectrum.

Interactions resulting in transitions of the dipole moment can differ widely in strength. Electric dipole interactions are greater by a factor of order 10^5 than magnetic dipole interactions;

electric dipole interactions are of the order of 10^8 times stronger than electric quadrupole interactions. Electric dipole transitions are therefore responsible for the strongest spectral lines, and are called permitted transitions. Other transitions are loosely named forbidden. The nature of a transition can be specified in terms of the quantum numbers of the upper and lower states (see Herzberg [1945],[1950]). Such a relationship is known as a selection rule. When a transition takes place from one energy state to another, the frequency ν of the absorbed or emitted quantum being given by 's relation,

$$\Delta E = h\nu \ ,$$

where h is 's constant and ΔE the energy gap between the energy states involved in the transition.

The most general transition involves simultaneous changes of electronic, vibrational, and rotational energy. The minimum energy jumps commonly observed vary considerably between the three forms, and provide a convenient preliminary method of distinguishing between them. Minimum changes in rotational energy are typically of the order of 1 cm^{-1}. Rotation lines, that is lines due to rotational energy changes only, therefore form part of the microwave or the far infrared spectrums. Vibrational energy changes are rarely less than 600 cm^{-1}. This is so much larger than the minimum for rotational energy change that vibrational transitions never occur alone, but with many simultaneous rotational changes giving a group of lines which constitute a vibration-rotation band, usually in the intermediate infrared spectrum. An electronic transition typically involves a few electron volts of energy, and the resulting absorption or emission usually occurs in the visible or ultraviolet spectrum. Atoms can exhibit electronic line spectra, but molecules have complex band systems, with simultaneous changes of all three forms of quantized energy.

In reality a transition from one energy level to another is very complicated and usually involves simultaneous changes of all three quantized forms of energy. To a first approximation the three forms of internal energy are additive. A typical term scheme is shown in figure 2.

If the energies were strictly independent the selection rules for a combined transition could be regarded as a combination of the three separate selection rules, (that is the selection rules for a rotational, vibrational or an electronic transition to occur) except that where symmetry properties are involved the symmetry of the complete wave function must be considered. In practice bands resulting from combined transitions differ markedly from expectation on a non-interacting model. This is partly because of the need to consider the total wave function where symmetry rules are involved, e.g the total angular momentum includes all types of angular momentum, and it is to this that the selection rule must be applied. There are, however, also energy interactions between electronic, vibrational, and rotational states which strongly influence the resulting spectra. Any further attempt to give insight to the mechanism that the interacting internal energies undergo, goes beyond the scope of this thesis and the interested reader is advised to consult the excellent works of Herzberg [1945],[1950].

Fig. 2. Typical term scheme for the ν_3 fundamental mode of H_2O (after Herzberg [1945]).

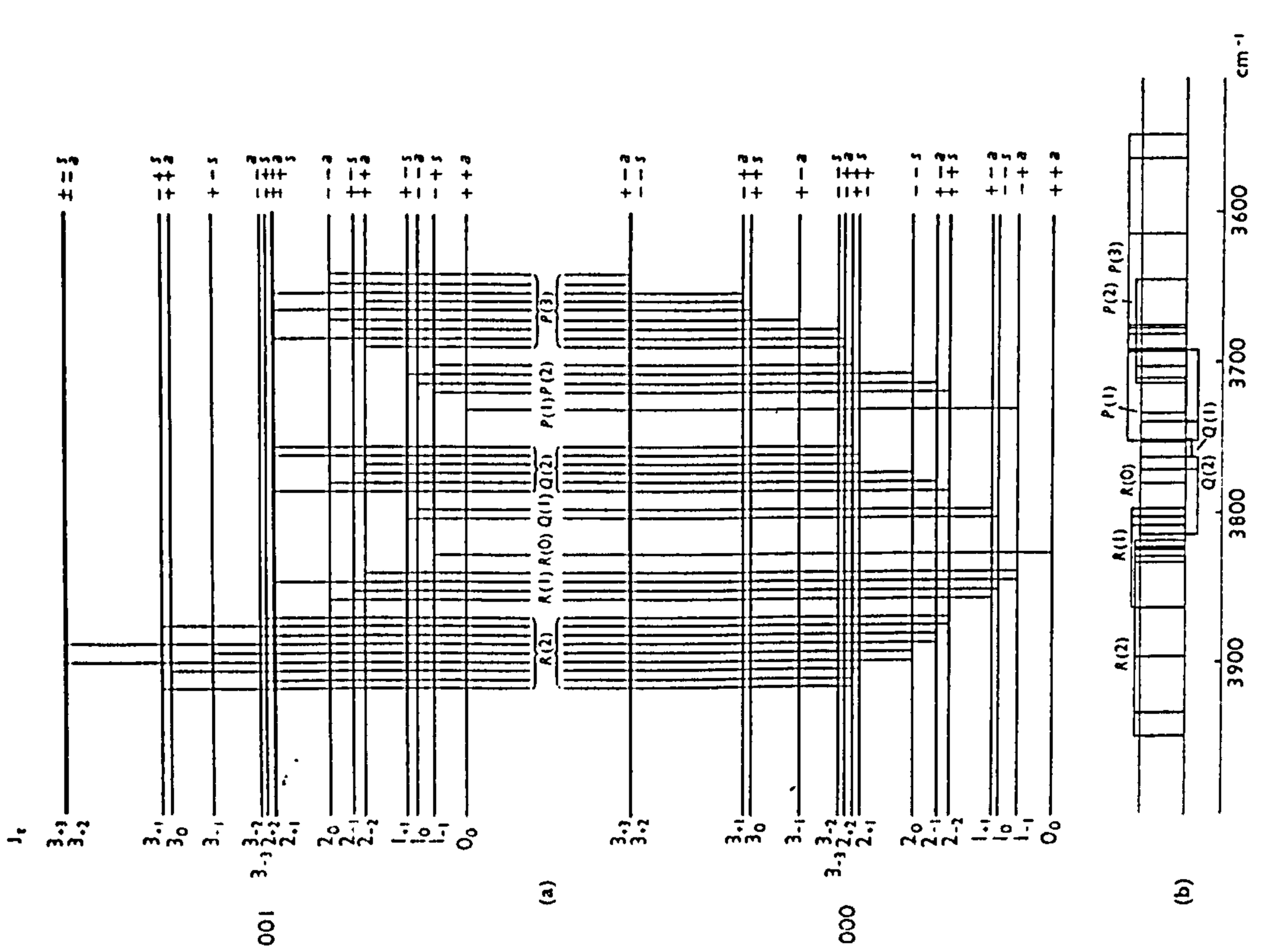

The energy states of gaseous molecules are well defined and discrete and therefore the positions of the resultant spectral lines can be calculated. The U.S. Air Force Geophysics Laboratory (AFGL) high-resolution transmission molecular absorption database (known under the acronym HITRAN [Rothman et al 1987]), gives the exact positions and other characteristics of the spectral lines of gaseous molecules between 0 and 17900 cm^{-1}. The 1986 edition of the HITRAN database was used to derive all the necessary spectroscopic information. The database was selectively accessed to provide suitable line files for the atmospheric gases of interest. The interaction of electromagnetic radiation with the absorbing matter within the vicinity of a single spectral line is described by the volume absorption coefficient k_v

$$k_v(x)=S(x)\ f(\nu-\nu_0,x)\ \rho(x),$$

where x denotes position, $f(\nu-\nu_0,x)$ is the line shape factor, S(x) is the line strength, ν_0 is the centre of the absorption line and $\rho(x)$ the density of the absorbing gas. Generally, the volume absorption coefficient k_v is a function of the density of the absorbing substance, and the pressure and temperature of the atmosphere, all of which can vary along the path of observation. The transmittance or optical depth, $\tau(\nu)$, between two points x_1 and x_2 along a path of observation resulting from a single spectral line is given by:

$$\tau(\nu)=\exp\left[-\int_{x_1}^{x_2} S(x)\ f(\nu-\nu_0,x)\ \rho(x)\ dx\right],$$

and for a band of spectral lines by:

$$T(\nu)=\exp\left[-\sum_{ij}\int_{x_1}^{x_2} S_{ij}(x)\ f_{ij}(\nu-\nu_{ij},x)\ \rho_j(x)\ dx\right],$$

where $S_{ij}(x)$ is the strength of the i'th line of the j'th absorbing gas in the path from position x_1 to x_2, $f_{ij}(\nu-\nu_{ij},x)$ is the line shape factor, ν_{ij} is the position of the line centre, and $\rho_j(x)$ the

density of the absorbing gas. Here we assume that when lines overlap their individual contributions to the optical depth simply add together. This is an essential simplification, adequately justified in terms of the relatively sparsely spaced spectral lines of various gases in the mm to sub-mm frequency spectrum, and the values of pressure and temperature in the atmosphere. Line strengths and positions may be calculated using quantum mechanics and are dependent on temperature, geometrical configuration of the molecule and the population of the lower energy state of the transition. The line strength of a spectral line involving a transition from state i to state j is given by:

$$S_{ij} = \frac{8\pi^3}{3hc}\,\nu_{ij}\left[1-\exp\left(\frac{-c_2\nu_{ij}}{T}\right)\right]\frac{g_i I_a}{Q(T)}\exp\left(\frac{-c_2 E_i}{T}\right) R_{ij}\,10^{-36}\,,$$

where h is Plank's constant, ν_{if} is the resonant frequency of the line, E_i is the energy of the lower energy state of the transition, g_i is the nuclear spin degeneracy of the lower level, Q(T) is the total partition function, I_a is the natural isotopic abundance, c_2 is the second radiation constant and R_{if} the Einstein transition probability. The total partition function Q for temperatures encountered in the atmosphere is given by the following approximate expressions

$$Q = \frac{kG}{\sigma hB}\,T \quad \textit{for linear,} \qquad Q = \frac{G}{\sigma}\left[\frac{\pi}{ABC}\left(\frac{kT}{h}\right)^3\right]^{1/2} \quad \textit{for non-linear molecules,}$$

where σ is the symmetry number depending on the group of which the molecule is a member, h is Plank's constant, k is Boltzmann's constant, G is the common factor of the molecule and A,B and C are its rotational constants. Line shapes depend upon the mechanisms of molecular collisions and motions, and are, therefore temperature and pressure dependent.

7.3 The line shape function.

The physical mechanism that dominates spectral line broadening close to the earth's surface is collisional interactions between molecules. This is also known as pressure broadening and is successfully interpreted by the Van Vleck-Weisskopf (VVW) line shape function

$$f(\nu,\nu_0) = \frac{1}{\pi}\left[\frac{1-i\delta}{(\nu-\nu_0)-i\gamma_L} + \frac{1+i\delta}{(\nu+\nu_0)+i\gamma_L}\right] \quad [cm] \ ,$$

where δ is the interference coefficient suggested by Rosenkranz [1975] to describe pressure induced line interference for the oxygen 60 GHz band (δ=0 for all other gases), and γ_L is the collisional line width parameter. The collisional line width parameter is a function of both pressure p and temperature T and is given by:

$$\gamma_L=\gamma_{L_0}\left(\frac{p}{p_0}\right)\left(\frac{T}{T_0}\right)^{-x} \quad [cm^{-1}] \ ,$$

where x varies usually 0.5 and 1.0 and γ_{L0} is the value of the line width parameter at normal atmospheric conditions, $p=p_0$ and $T=T_0$.

At sufficiently low pressures, collisional broadening is negligible compared to thermal broadening (also known as Doppler broadening). Because molecular velocities have a Gaussian distribution, the Doppler line shape is also a Gaussian

$$f(\nu,\nu_0) = \frac{1}{\sqrt{\pi}\ \gamma_D}\exp\left[-\left(\frac{\nu-\nu_0}{\gamma_D}\right)^2\right] \quad [cm] \ ,$$

and the Doppler line width is given by:

$$\gamma_D = 3.58\times10^{-7}\ \nu\sqrt{\frac{T}{M}} \quad [cm^{-1}] \ ,$$

where M is the molecular weight of the gas.

When collisional and thermal broadening become comparable, the resonance frequency in the collision shape expression should be convolved with the Gaussian shift probability distribution over all possible Doppler shifts. This convolution is called the Voight profile

$$f(\nu,\nu_0) = \frac{i}{\pi}\int_{-\infty}^{+\infty}\frac{e^{-t^2}}{z-t}dt \quad [cm] \ ,$$

where z is a complex argument related to the collisional γ_L and thermal γ_D line widths (Penner

[1959]) and $t=(\nu-\nu_0)/\gamma_D$.

7.3.1 Applicability of the Voight profile in the earth's atmosphere.

Several empirical fits and numerical methods have been proposed by various researchers in order to approximate the Voight convolution integral (Whiting [1968], Kielkopf [1973], Drayson [1976]). Adopting Kielkopf's empirical approximation which has been successfully used to fit experimental data, the applicability of the Voight profile can be investigated. In fig. 3 the line width ratios γ_V/γ_L and γ_V/γ_D as a function of the line width ratio γ_L/γ_D are plotted.

Fig. 3. Applicability region of the Voight function.

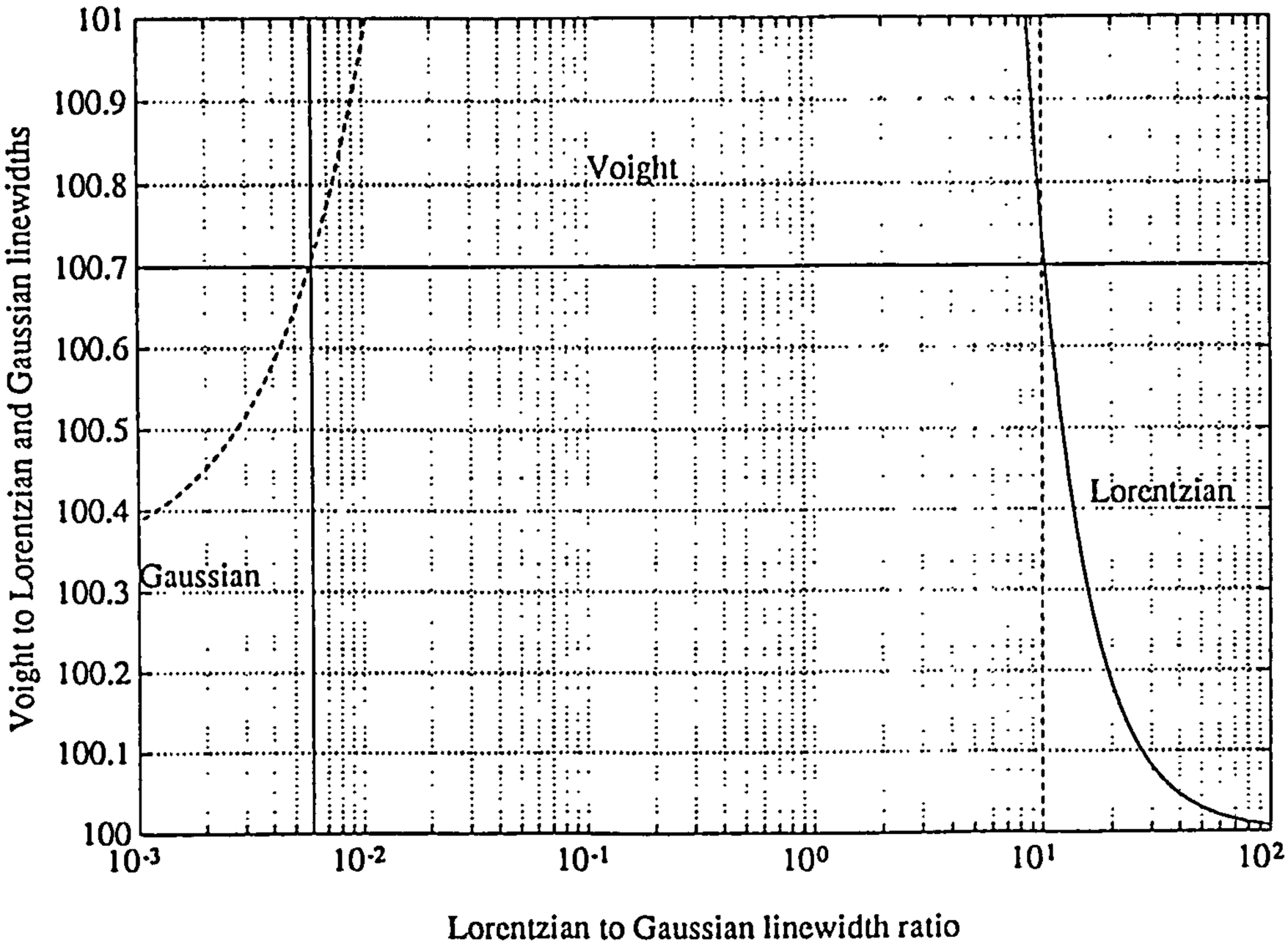

For values of the ratio $\gamma_L/\gamma_D>>1$ the Voight line width tends asymptotically towards the Lorentzian, while for $\gamma_L/\gamma_D<<1$ the Voight line width tends asymptotically towards the Gaussian line width. For intermediate values of the line width ratio, the convolution integral has to be numerically evaluated. The numerical evaluation is usually a time consuming process, especially when line-by-line summation techniques are applied over a great number of spectral lines. In FASCOD (Clough et al [1980]), the Voight function is evaluated to an

accuracy of 3% for obvious computational advantages. However, in APM where only millimetre spectral lines are considered, a much better accuracy can be achieved with inherent advantages for millimetre remote sensing applications. The Voight function can be approximated by somewhat better than 0.7%, when the line width ratio γ_L/γ_D falls between 10 and 0.006 (see figure 3).

Applying the line width criterion, the altitude range within the Voight profile is applicable for various atmospheric gases can be determined. The line width ratio γ_L/γ_D is given by:

$$\frac{\gamma_L}{\gamma_G} = \frac{\gamma_{L0}\left(\frac{p}{p_0}\right)\left(\frac{T}{T_0}\right)^{-x}}{3.58\times10^{-7}\nu\sqrt{\left(\frac{T}{M}\right)}} .$$

What is really required, is to find where the function $f(\gamma_{L0},\nu,x,M,p,T) = C-\gamma_L/\gamma_D$ minimizes for the two extreme values C=10.0 and C=0.006. The atmospheric pressure follows an exponential distribution, while temperature is interpolated linearly between the boundary values given in the U.S. Standard Atmosphere (USSA) tables (NOAA [1976]). As far as the rest of the variables are concerned, the molecular weight M has a fixed value for each molecule but the temperature exponent x and the ratio γ_{L0}/ν have to be evaluated for each separate absorption line. Table I gives the minimum and maximum heights for which the Voight line shape becomes appropriate for various atmospheric gases when the line width criterion is applied.

Table I. Applicability range of altitudes for Voight profile considering various gases.

Gas	Altitude min [km]	Altitude max [km]
H_2O	39	112
O_2	50	104
O_3	46	108
CO	49	104
NO	46	100
NO_2, N_2O	49	108

The transition of the 184.5 GHz O_3 line shape function from a Lorentzian at low altitudes to a Gaussian at high altitudes can be seen in figure 4. Reference atmosphere is the USSA.

Fig. 4. Transition of the 184.5 GHz O_3 line from a Lorentzian at low altitudes to a Gaussian at high altitudes.

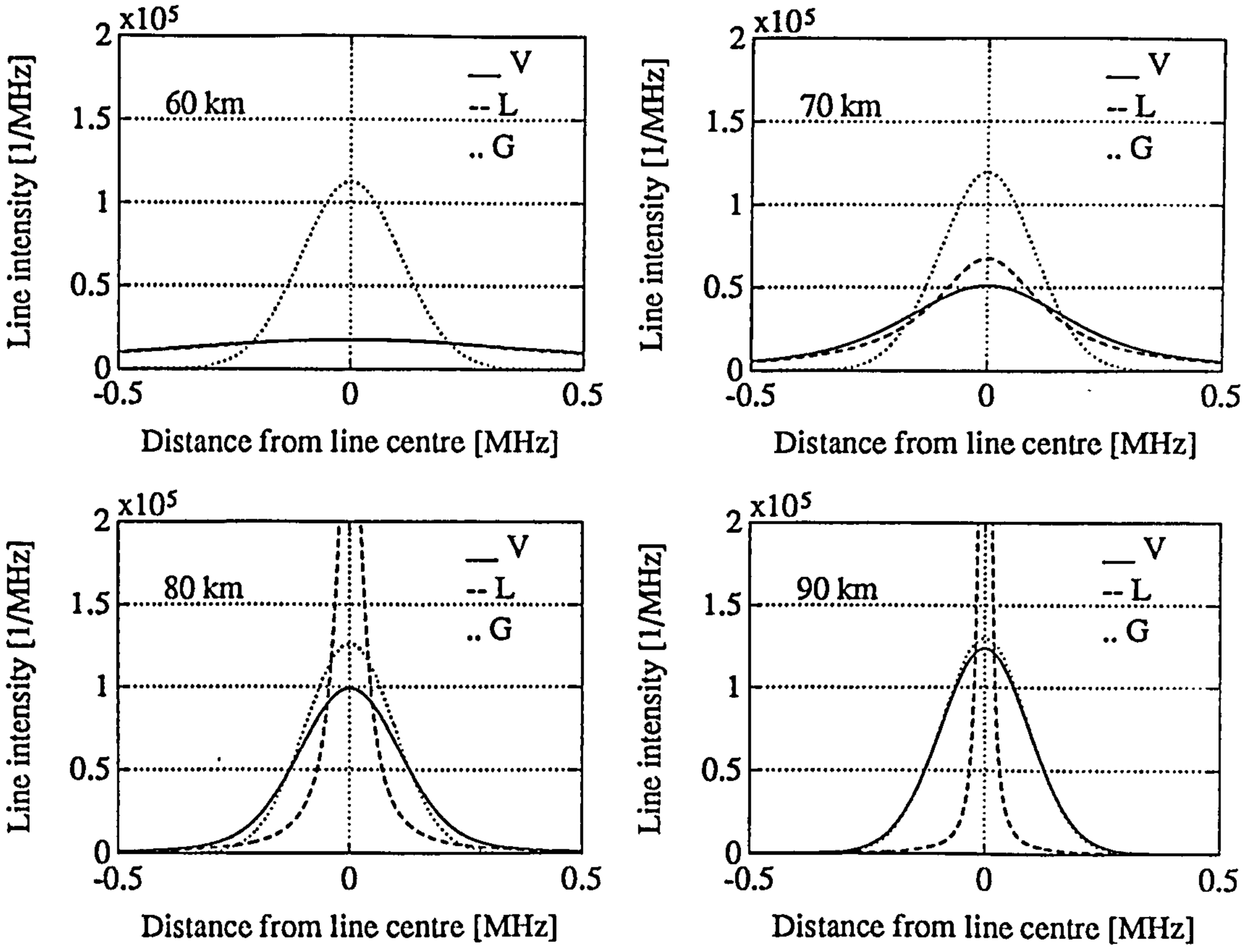

7.3.2 Voight profile evaluation.

A particularly fast and accurate numerical algorithm which was suggested by Hui et al [1978] has been adopted for our calculations. In this method the complex Voight function is approximated by a quotient of the form

$$V(z) = \frac{\sum_{i=0}^{p} a_i z^i}{z^{p+1} + \sum_{i=0}^{p} b_i z^i},$$

where V(z) is the Voight function of complex argument z, p=6, and a_i, b_i are appropriately determined coefficients given in table II.

Table II. Hui's [1978] coefficients for the approximation of the Voight function.

i	p=6	
	a_i	b_i
0	122.608	122.608
1	214.382	352.731
2	181.929	457.334
3	93.156	348.704
4	30.180	170.354
5	5.913	53.993
6	0.564	10.480

7.4 Method of calculating the spectra of atmospheric gases.

7.4.1 Line-by-line summation technique.

The calculation of the resonant spectra of all atmospheric gases is calculated by considering individual contributions from all the spectral lines across the millimetre frequency spectrum. At some frequency separation, which depends upon constituent density and line intensity, contributions from distant lines can be neglected. Of course, the suitable line shape function must be chosen according to the specific atmospheric conditions, pressure and temperature. The Van Vleck-Weisskopf, Voight and Gaussian line shape functions are exclusively used in APM for all atmospheric gases.

7.4.2 Oxygen.

A modified VVW line shape function is used in the special cases of oxygen, as suggested by Rosenkranz [1975] to describe pressure induced line interference between the closely spaced lines of the 60 GHz oxygen band. Line coupling occurs when collisions between a radiating molecule and broadening gas molecules cause the transfer of population between rotational-vibrational molecular states and result in a redistribution of spectral intensity within a band.

Rosenkranz [1975] presented a method in which weak coupling approximations and a first order expansion of the band's shape lead to an accurate description of the microwave spectrum of oxygen in the atmosphere. APM incorporates the latest interference coefficients as suggested by Rosenkranz [1988].

In addition to pressure induced line interference, Zeeman splitting of oxygen lines must be taken into account for altitudes above 30 km. Oxygen, being a paramagnetic molecule is subject to the earth's magnetic field, which although weak, is capable of introducing a line splitting. A reasonable approximation valid for all microwave absorption lines according to Liebe [1989], appears to be

$$\gamma_Z = \sqrt{\gamma_L^2 + 6.944\times10^{-13}\, B_0^2} \quad [cm^{-1}] \,,$$

where B_0 is the geomagnetic field strength from 25 to 65 μTesla depending on geographic location and altitude.

7.4.3 Water vapour.

Although the line by line approach predicts successfully the resulting absorption and dispersion from O_2 and other trace gases, it proves to be insufficient to explain the observed measurements for water vapour (Ulaby et al [1973a,1973b], Gibbins et al [1975, 1976], Gimmestad et al [1976], Emery et al [1978]) as well as laboratory measurements (Frenkel and Woods [1966], Bignell [1970], Burch et al [1971], Llewellyn-Jones et al [1978], Liebe [1975], [1987]). This seems not to be the case near the H_2O line centres, but in the window regions. This insufficiency has established the existence of excess water vapour absorption (EWA) to account for the discrepancy between theory and measurements (Gibbins et al [1973], Straiton and Tolbert [1959], Emery et al [1975], Gimmestad et al [1977]). As a result an empirically derived term, known as the H_2O continuum, has to be added to the contributions of local lines below 1 THz to complete the characterization of the water vapour spectra at millimetre

wavelengths.

The empirically derived H_2O continuum depends on the square of the water vapour density and shows a very strong negative temperature dependence. During the past two decades the explanation of the 'anomalous' absorption followed three schools of thought. The first is a molecular approach searching for water polymers $(H_2O)_n$ and their spectra in the atmosphere with sizes of n=2 or n=3 as possibilities (Harries et al [1969], Viktorova and Zhevakin [1967], [1971], Suck et al [1979], Carlon and Harden [1980]). The second assumes a liquid water uptake by submicron aerosol particles under conditions of high relative humidity (>85%) (Nilsson [1979], Hodges [1972]). The other (Clough et al [1980]) attributes the excess water vapour absorption to collision broadened far wings of allowed transitions (free-free transitions arising from the allowed dipole moments of isolated molecules). Each conjecture is supported by some experimental evidence, but appears to be contradicted by other results. Only recently Ma and Tipping [1990] have given a theoretical interpretation in which the far wings of allowed rotational transitions is shown to be the determinative mechanism that controls both the magnitude and the strong negative temperature dependence of the continuum absorption. Although for our calculations Liebe's [1989] temperature and density dependence for the continuum absorption have been adopted, the water vapour continuum formula differs from that of Liebe's because of the different number of resonant lines involved in this approach. For the dispersive continuum Hill's [1988] expression, which calculates the contribution of all lines above 1 THz using the 1982 AFGL line-parameters compilation, has been adopted. So the water vapour continuum is given by:

$$k_a(\nu) = 3.8\times10^{-6}\,\nu^2\left[31.6\left(\frac{300}{T}\right)^{7.5}e+p\right]e\left(\frac{300}{T}\right)^{3} \quad [cm^{-1}]\ ,$$

$$k_d(\nu) = 1.2566\times10^{-5}Q\sum_{j=1}^{4}A_j\left(\frac{296}{T}\right)^{a_j}\left(1-B_j\frac{296}{T}\right)(\nu/33)^{2j} \quad [rad\ cm^{-1}]\ ,$$

where p and e are the dry air and water vapour partial pressures in Atm, respectively, T is the

absolute temperature in K, ν is frequency in cm^{-1}, Q is absolute humidity in $g \cdot m^{-3}$ and the coefficients A_j, a_j and B_j are given in table III.

Table III. Hill's [1988] coefficients for a dispersive continuum.

j	A_j	a_j	B_j
1	1.382	1.650	0.199
2	-0.214	0.162	3.353
3	-0.149	0.178	3.101
4	-0.109	0.192	3.005

7.4.4 Trace gases.

The resonant spectra of trace gases are calculated employing the line by line summation technique. Each absorption line gives a contribution at the frequency of consideration depending upon the intensity of the line and the distance from the line centre. The line shape function is as usually appropriately evaluated according to the atmospheric conditions.

7.4.5 Other contributions.

In addition to the water vapour continuum, other contributions must be here discussed for the sake of completeness. Residuals from very strong CO_2 lines in the far-infrared and optical frequencies form a CO_2 continuum which, nevertheless, is too weak to add any contributions at millimetre wavelengths.

Pressure induced nitrogen absorption becomes important at high pressures and for frequencies above 100 GHz. According to Stone [1984], it can be expressed as

$$k_{N_2}(\nu) = 5.42\times10^{-10}\ \nu^2\ (1-1.9718\times10^{-3}\nu^{1.5})\ p^2\left(\frac{300}{T}\right)^{3.5} \quad [cm^{-1}] \ .$$

Finally the term $k_{N(0)}$ is used to describe the non-dispersive radio refractivity:

$$k_{N(0)} = 2\pi\nu 10^{-6}\ [\ N_{dry}(p,T) + N_{wet}(e,T)\ ] \quad [rad\ cm^{-1}] \ ,$$

with the dry and wet components of refractivity given by:

$$N_{dry} = 78.6687\times10^{3}\ \frac{p}{T}\ , \qquad N_{wet} = 3.8\times10^{8}\ \frac{e}{T^{2}} - 5.6742\times10^{3}\ \frac{e}{T}\ ,$$

where p and e are the barometric and water vapour partial pressures in Atm, respectively, and T the temperature in K.

7.5 Modelling the atmosphere.

7.5.1 The refractive atmosphere.

In order to calculate the attenuation and dispersion spectra of atmospheric gases, we need to know their concentration and distribution along the path of observation. Furthermore, since the line intensity and line shape function are sensitive to pressure and temperature variations, an efficient way of representing the propagation medium is needed. An excellent approach is to slice the atmosphere in many spherical concentric layers and assume exponential profiles

Fig. 5. Relative air mass geometry.

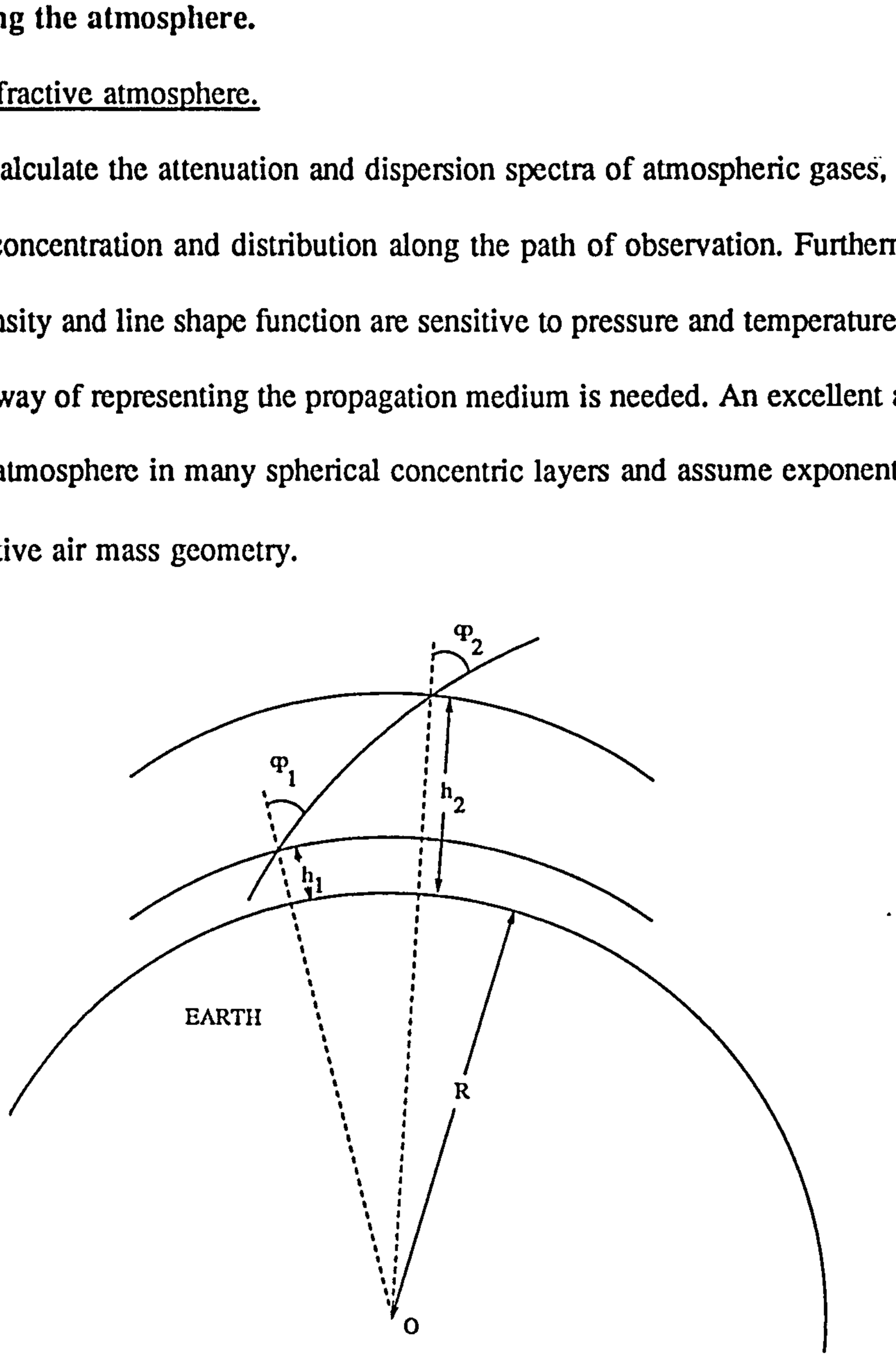

of density and pressure between layer boundaries. Each layer is taken to be in local

thermodynamic equilibrium (LTE). Figure 5 shows a spherically symmetric atmosphere for which refraction effects are taken into account. The relative air mass between height points h_1 and h_2 is given by:

$$M(h_2,\phi_2) = \frac{\int_{h_1}^{h_2} \frac{n(h)(R+h)\rho(h)dh}{\sqrt{n(h)^2(R+h)^2 - n(h_1)^2(R+h_1)^2\sin^2\phi_1}}}{\int_{h_1}^{h_2}\rho(h)dh},$$

where n is the index of refraction, dh is the height increment and ρ the gas density at point h along the ray path in the atmosphere. In our approach a simple closed form approximation, which includes the effects of refraction and the variation of atmospheric density with altitude was adopted for the calculations. Uplinger [1981] has represented the relative air mass integral between height points h_1 and h_2 by the following set of equations:

$$M(h_2,\phi_2) = \frac{\sqrt{\pi S}}{\cos\phi_1}\, e^{S}\, erfc(\sqrt{S}), \quad with \quad S=\frac{\cot^2\phi_1 X}{2(1-\Delta)}, \quad X=\frac{(R+h)}{H_{dry}},$$

where Δ is the refraction ratio and is given by:

$$\Delta = \frac{X\left[N_{dry}(h_1)+\frac{H_{dry}}{H_{wet}}N_{wet}(h_1)\right]\times 10^{-6}}{1+\left[N_{dry}(h_1)+N_{wet}(h_1)\right]\times 10^{-6}},$$

and H_{dry} and H_{wet} are the scale heights of the dry and moist air components of refractivity. Comparison with ray traces in the U.S. Standard Atmosphere shows Uplinger's approximation is accurate to within a few percent at an angle 90° to the zenith, with rapidly increasing accuracy for smaller to the zenith angles.

7.5.2 Elimination of inhomogeneity of atmospheric layers.

Providing that each layer is found in LTE and each gas is uniformly mixed within it, an effective pressure, temperature and absorber amount may be specified for each layer. The

effective values are those that make the absorption and/or emission of an equivalent homogeneous layer equal to that of the non-homogeneous layer. There is no single definition of the effective pressure or temperature because the effective values depend upon many factors and will in general be different for different absorbing gases. The most generally acceptable definition, however, is the density weighted average, also known as the Curtis-Godson approximation

$$\overline{P} = \frac{\int P(h)\rho(h)dh}{\int \rho(h)dh}, \quad \overline{T} = \frac{\int T(h)\rho(h)dh}{\int \rho(h)dh},$$

where P is the atmospheric pressure, T is the atmospheric temperature and ρ the total air density. The pressure and total air density are both assumed to follow an exponential profile with scale heights H_p and H_ρ respectively. At the layer boundaries the values of pressure, temperature and gas density are tabulated in various reference Atmospheres. Inside the layer, temperature is interpolated linearly while pressure and temperature follow an exponential distribution. That is,

$$P(h) = P_1 \, e^{\frac{-h}{H_p}}, \quad H_p = -(\Delta h) \,/\, \ln(P_2/P_1)$$

for pressure and

$$\rho(h) = \rho_1 \, e^{\frac{-h}{H_\rho}}, \quad H_\rho = -\Delta h \,/\, \ln(\rho_2/\rho_1)$$

for density.

7.6 APM implementation.

The APM model is able to perform calculations along arbitrarily specified paths within the earth's atmosphere. The calculations are applicable for a specific frequency or for a frequency band with appropriately specified frequency step. The line-by-line summation technique is

extended over an appropriately specified frequency interval, such that only the lines which lie in the interval are employed for the calculations. Several standard reference atmospheres may be selected or externally specified. The modelling approach is summarized in figure 6 below.

Fig. 6. The Atmospheric Propagation Model; modelling approach and internal structure.

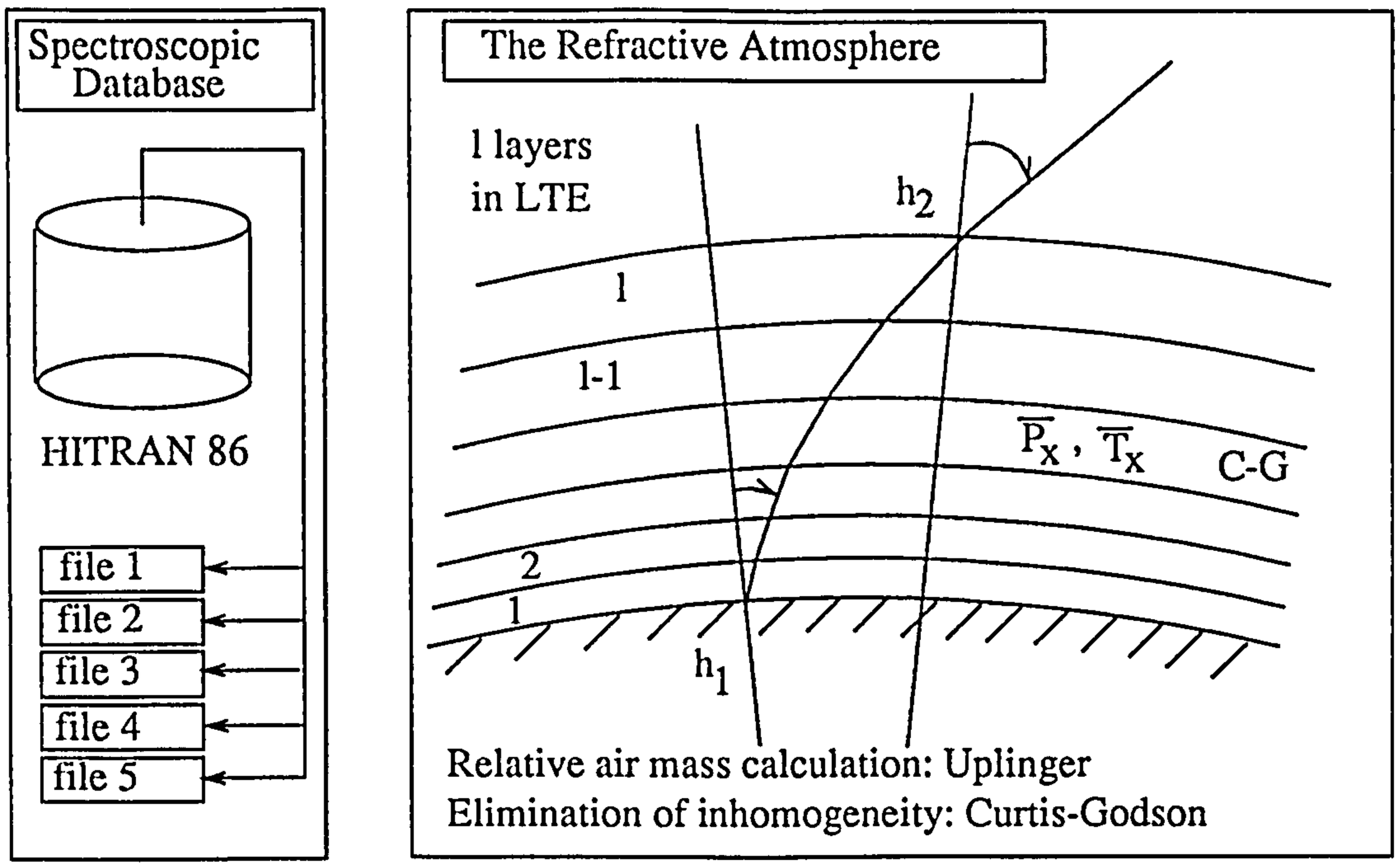

Model Atmospheres

U.S.S.A.
Summer Mid-Latitude
Winter Mid Latitude
Subarctic Summer Atmosphere
Subarctic Winter Atmosphere

User specified

The lineshape function

VVW profile (pressure broadening)
Doppler (thermal broadening)
Voight profile (combined pressure & thermal broadening)

It is numerically evaluated, Hui

Calculation of the resonant spectra of atmospheric gases.

Line-by-line summation tecnique

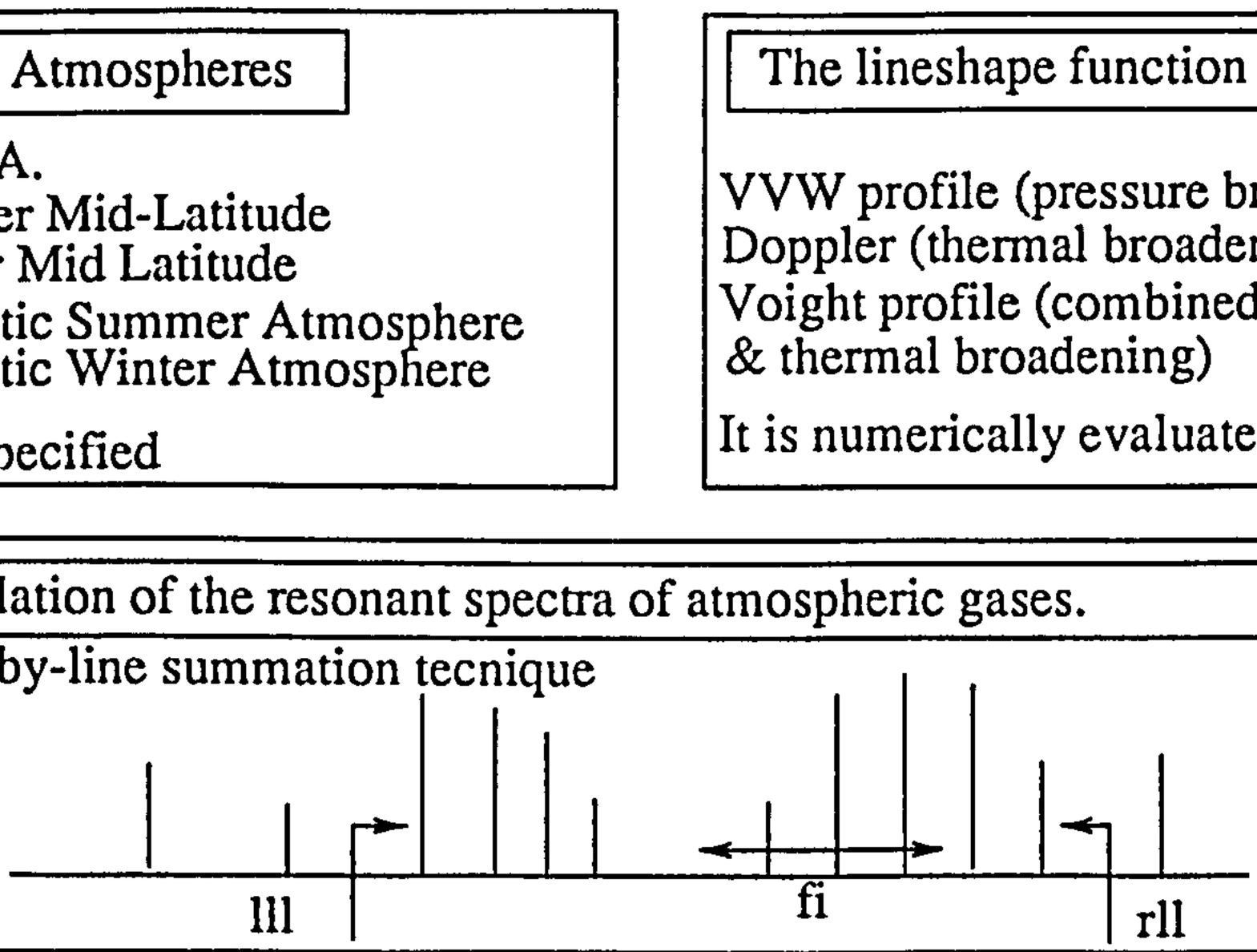

Other contibutions and special cases

O2: line interference, Zeeman effect
H2O continuum: empirically derived to correct the observed EWA.
N2: pressure induced absorption for frequencies above 100 GHz.

7.7 APM versus experiment.

In this section APM predictions are compared with experimentally collected data and measurements of clear and humid air attenuation at millimetre frequencies. The results are summarized in table IV.

Table IV. Comparison between measurements and APM predicted values.

References	Freq. [GHz]	Measured att. [dB]		APM predicted att. [dB]	Difference [%]
Westwater et al [1988]	20.60	0.497	summer	0.544	< 9
		0.159	winter	0.203	< 22
	31.65	0.278	summer	0.336	< 17
		0.158	winter	0.182	< 13
	90.00	1.190	summer	1.370	< 13
		0.411	winter	0.533	< 23
Hogg et al [1983]	31.65	0.163		0.182	< 10
Altshuler et al [1968]	15.00	0.0786		0.076	< 3
	35.00	0.2467		0.244	< 1
Reber [1972]	51.75	2.43±0.06		2.44	< 1
	68.14	2.60±0.05		2.48	< 5
Frenkel [1966]	150.0	1.50		1.54	< 3
Ulaby and Straiton [1973]	230.0	5.50		5.40	< 2
	300.0	10.0		11.10	< 10

During 1987 and 1988 Westwater et al [1988] measured atmospheric thermal emission at frequencies of 20.6, 31.65 and 90.0 GHz, using ground based zenith-viewing radiometers. The data were then converted to attenuation statistics by use of the mean radiating temperature approximation. Table IV summarises the zenith attenuation statistics and compares them with APM derived calculations. Unfortunately, temperature, pressure and humidity height profiles were not exactly known but in order to make the comparison feasible, APM was fed by the most relevant model atmospheres, that is the U.S. Winter and Summer Midlatitude Atmospheres. The agreement is generally within 16% and seems satisfactory, regarding the

displayed deviations and the era resulting from the arbitrary use of the model atmospheres. Hogg et al [1983] measured at a frequency of 31.65 GHz the zenith absorption by water vapour in the atmosphere. The data were obtained at three locations in the United States with total surface pressure of about 1010, 920 and 840 mbars and corresponding mean temperatures 276.3±6.0, 278.4±7.9 and 272.5±3.9 K, respectively. For weather conditions matching those of the U.S. Winter Midlatitude Atmosphere a 0.163 dB zenith attenuation is measured that differs 0.019 dB from the APM calculated (less than 10% difference).

Altshuler et al [1968], made also some measurements at 15 and 35 GHz. For a surface water vapour density of 5.9 g/m^3 -which corresponds to the surface water vapour density of the U.S. Standard Atmosphere- their best straight line fit gave 0.0786 and 0.2467 dB zenith attenuations at these frequencies. APM was run with the USSA as the input model atmosphere to give 0.0763 and 0.2441 dB for the zenith attenuations, at the same frequencies, respectively. In this case the measured and the calculated values lie very close to each other (within 2% average) indicating the utility of the approach when the atmospheric height profiles are known.

Ulaby and Straiton [1973] using radiometric techniques measured zenith attenuation in the 183 to 323 GHz region. The accuracy of the measurements was said to be within 20%. For a surface water vapour density of 9.0 g/m^3 measurements of 5.5 and 10 dB were reported at 230 and 300 GHz, respectively. APM gave for the same atmospheric conditions (interpolating between the results obtained from the U.S. Standard and Summer Atmospheres) values of 5.4 and 11.1 dB, respectively. The agreement is very good, in general better than 10%.

Frenkel and Woods [1966] measured at room temperatures in a laboratory environment specific attenuation values for H_2O and its mixtures with N_2, CO_2 and O_2. At 150 GHz a gas system with 7.5 mm H_2O and 750 mm N_2 partial pressures gave a value of 1.5 dB/km for the specific attenuation, while APM at the same conditions gave a value of 1.54 dB/km.

Also oxygen zenith attenuation measurements at the tails of the 60 GHz band are compared with APM calculated values. Reber [1972], measured 2.43±0.06 and 2.60±0.05 dB zenith

oxygen attenuation values at 51.75 and 68.14 GHz. The calculated values are 2.44 and 2.48 dB, respectively. The small difference of 0.12 dB at the right tail of the band is rather due to the coarse temperature approximation assumed for the interference coefficients in APM. It must be noted however, that this difference could be equally caused by the fact that the temperature profile of the atmosphere in which the measurements were made was different from that assumed in the U.S. Standard Atmosphere.

In conclusion, regarding the displayed measurement deviations and the error introduced by the arbitrary use of the model atmospheres when the surface water vapour densities were not exactly known, the agreement between measurements and predictions is very good, typically better than 10%.

7.8 Comparison with Liebe's MPM.

A comparison between APM-predicted specific attenuation and dispersion values and those

Fig. 7. Comparison between predictions from APM and MPM [Liebe 1989] for ground level conditions.

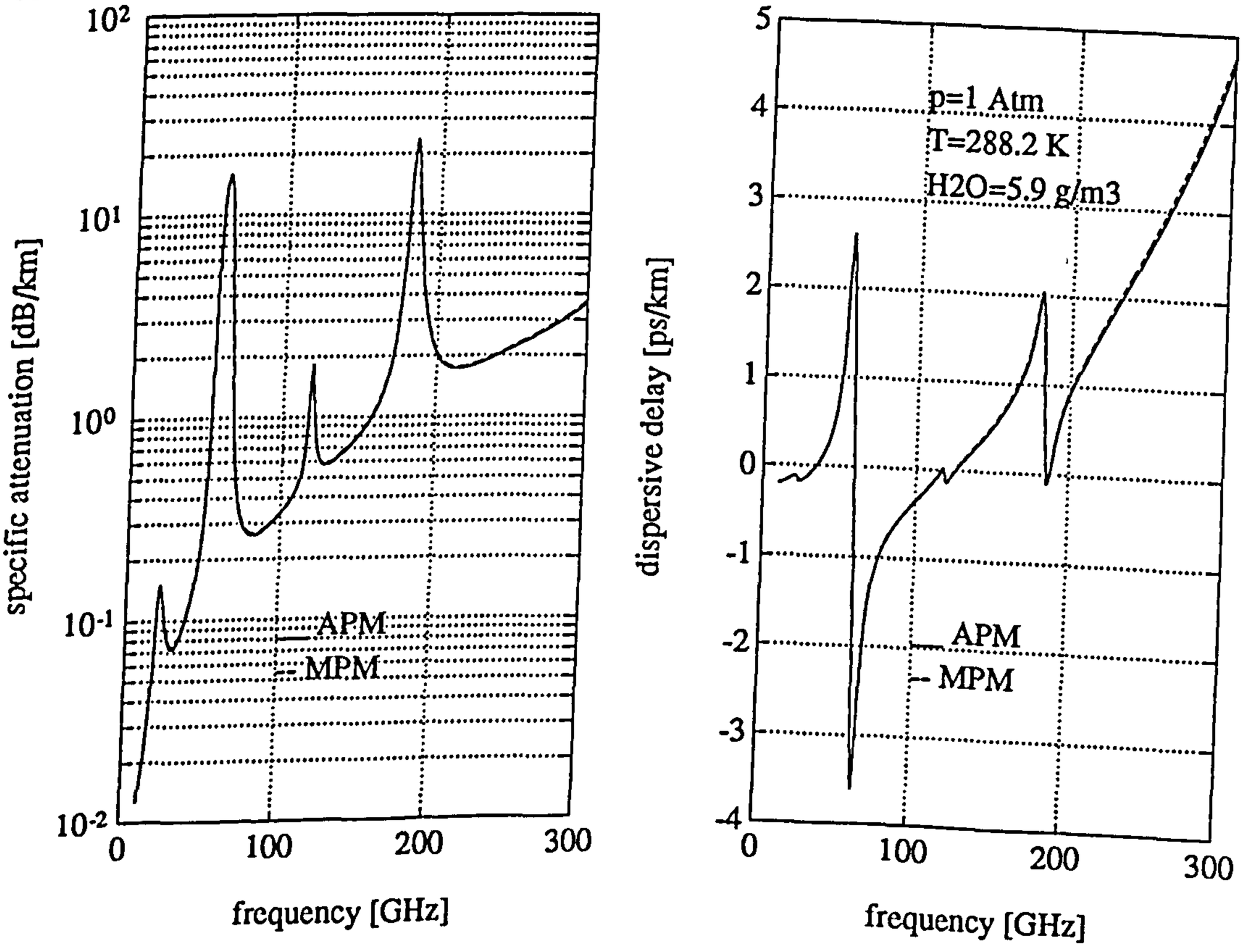

from Liebe's well established model for ground level conditions (the Millimetre-wave Propagation Model, MPM [1989]) are given in figure 7 for the frequency range 10 to 300 GHz. The difference (too coarse to be revealed in the graph) is always less than 5% and arises mainly due to the use of different sources of spectroscopic information and the different number of resonant lines included in each model.

7.9 The effect of trace gases on radiowave propagation at high altitudes.

Various example calculations demonstrate the utility of the approach. For all calculations the U.S. Standard Atmosphere [1976] has been adopted. Figure 8 shows the individual contributions of several atmospheric gases and the total resultant attenuation for a slant path which starts off at 20 km initial height and extends up to a 120 km height point. The angle to the zenith is 85 degrees and the frequency range of interest lies between 174 and 190 GHz.

Fig. 8. Calculations along a 20-120 km slant path at 85° to the zenith. (a) Individual contributions from various gases; (b) comparison of the total attenuation and attenuation predicted only from O_2 and H_2O.

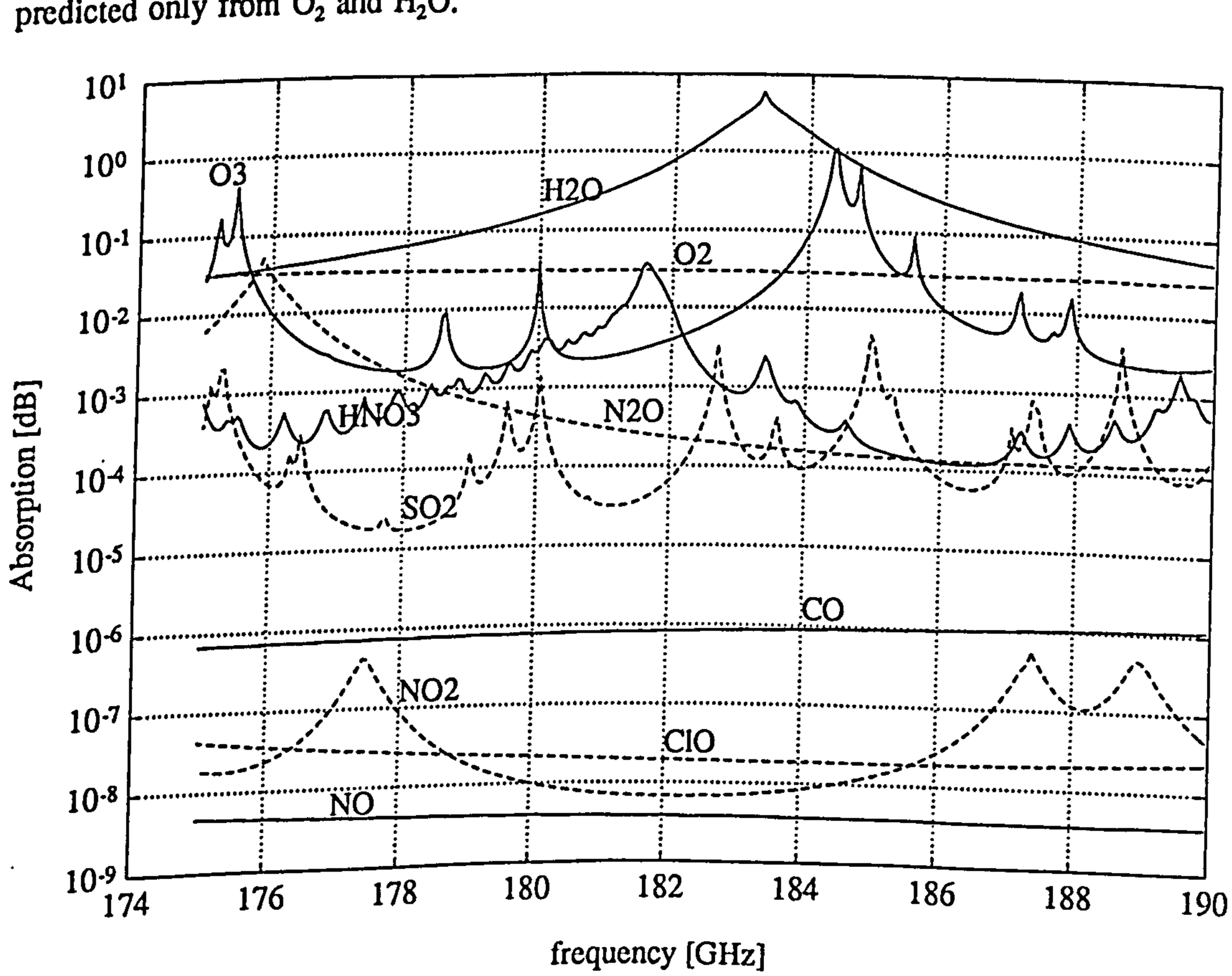

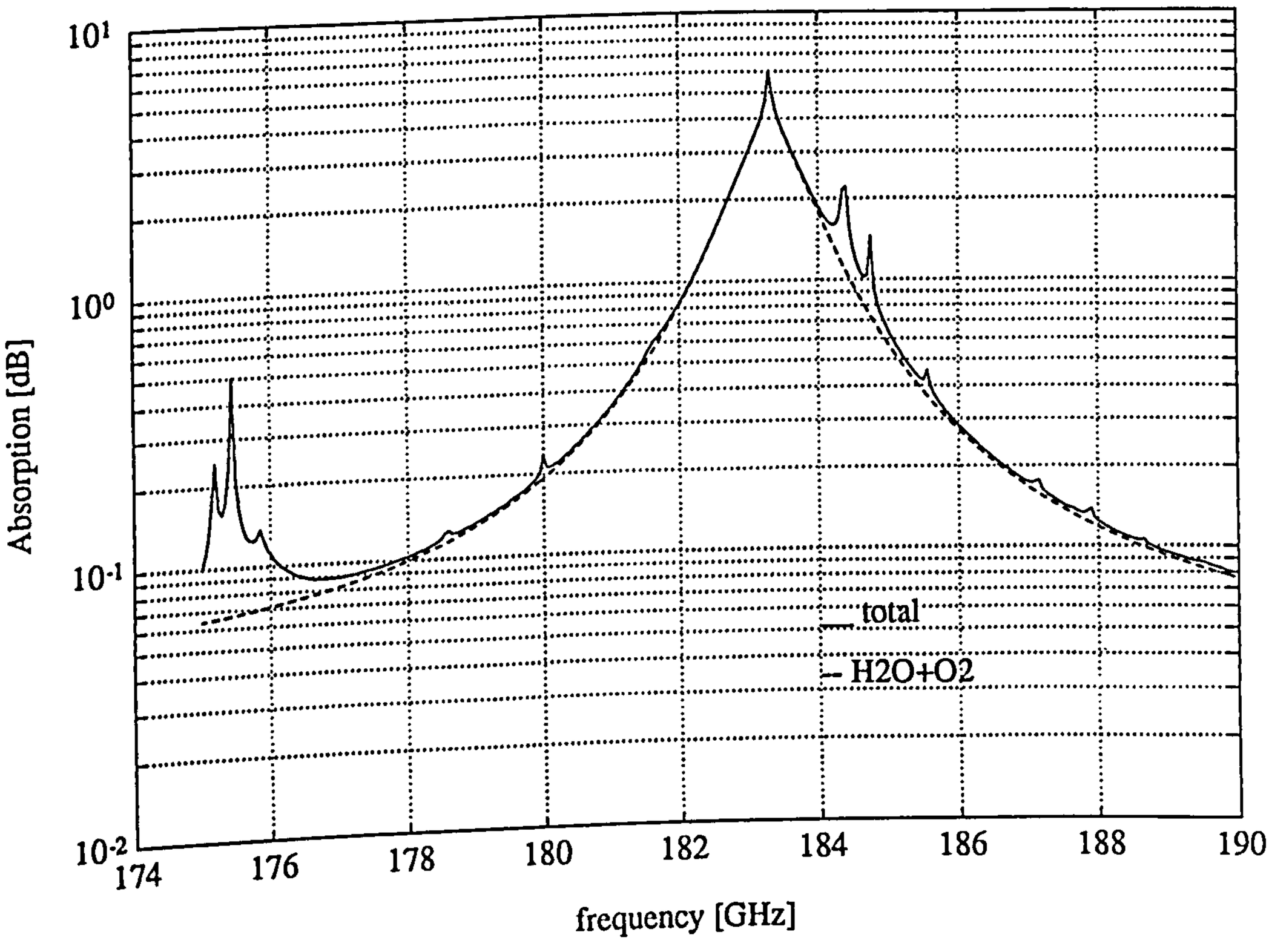

Fig. 9. Calculations along a 10-120 km slant path at 10° to the zenith. (a) Individual contributions from various gases; (b) comparison of the total attenuation and attenuation predicted only from O_2 and H_2O.

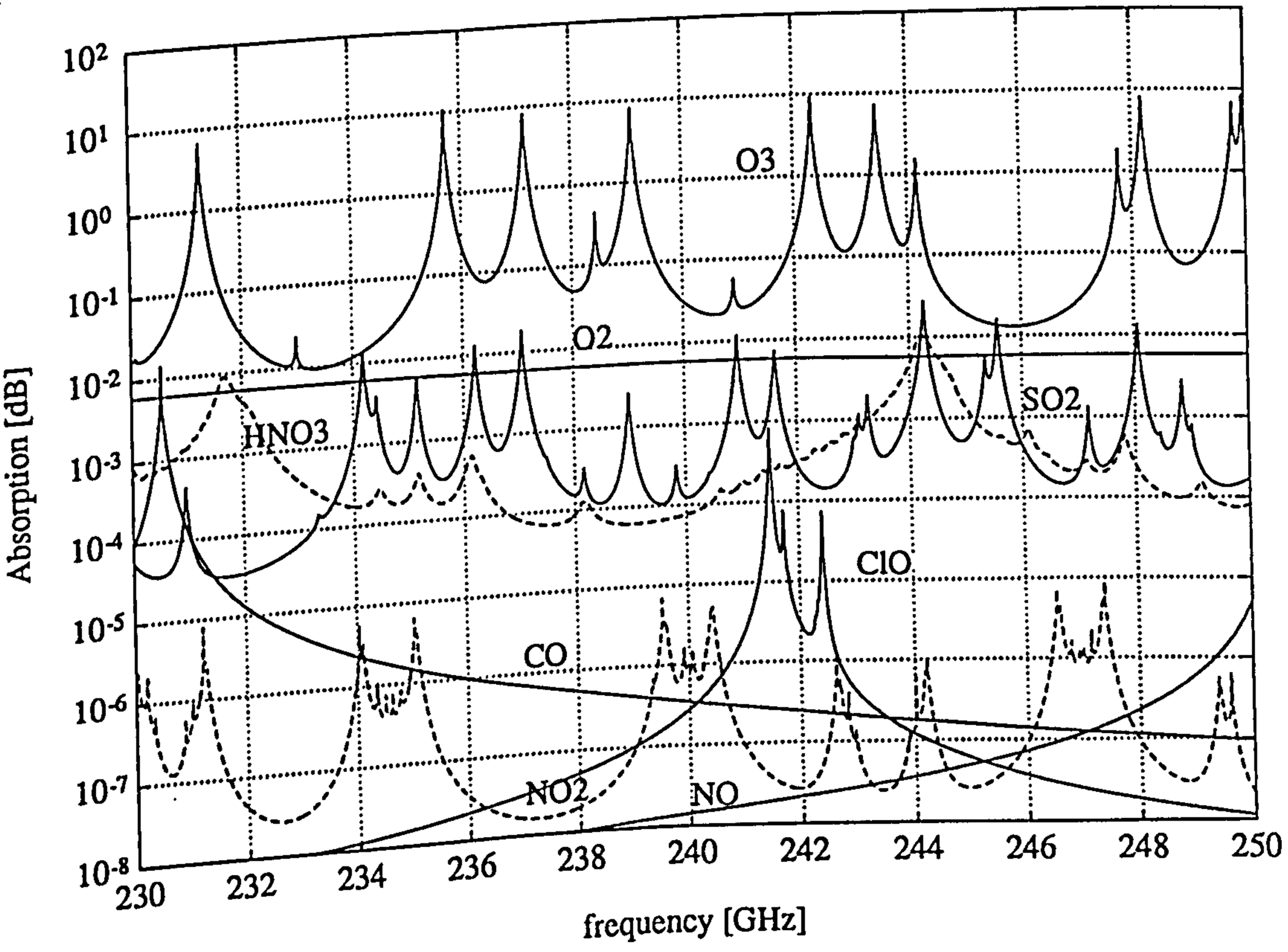

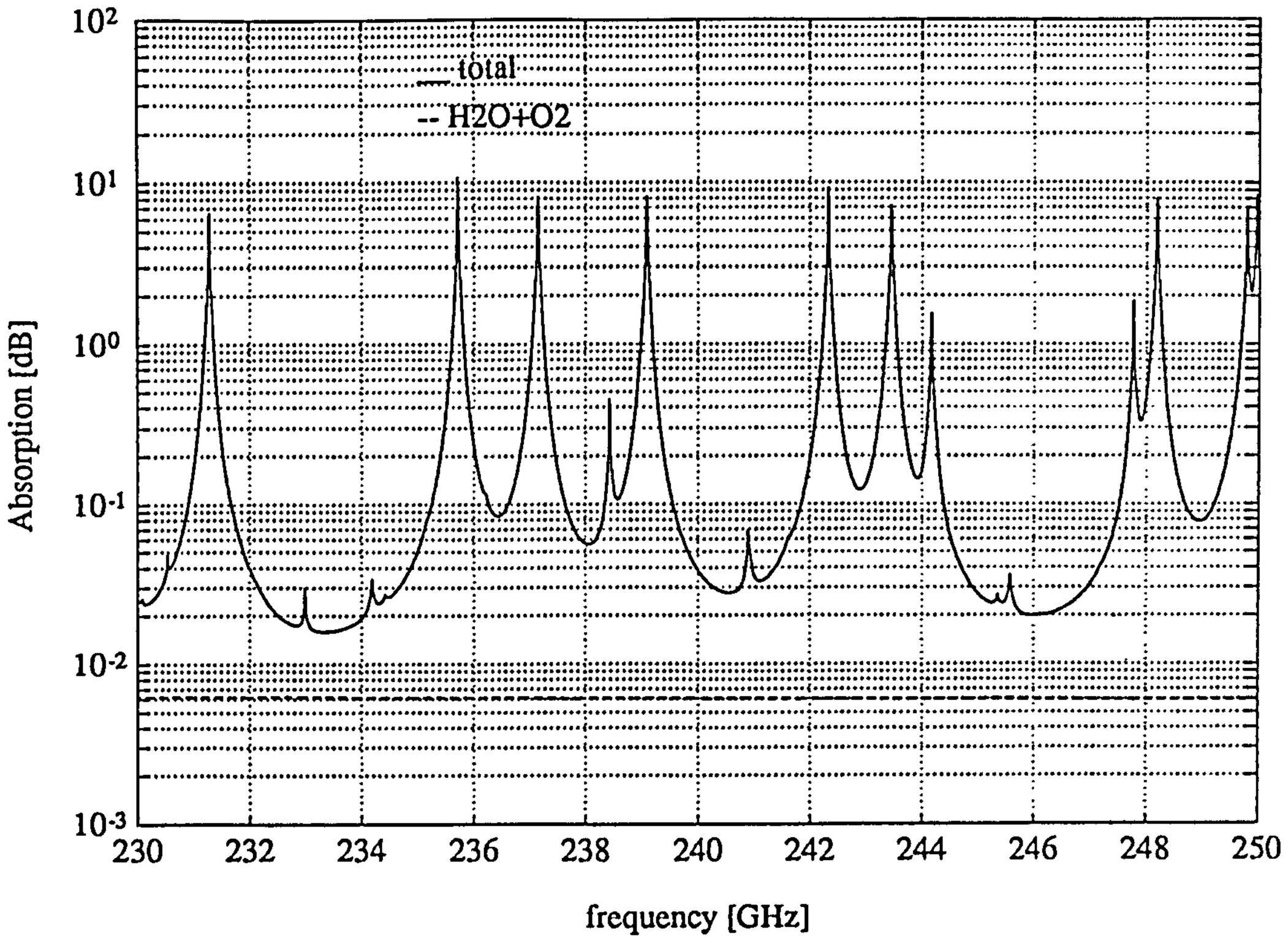

The frequency step is 1 MHz and the 30 atmospheric layers that have been considered here, give an excellent accuracy convergence. In a similar way figure 9 characterises radiowave propagation along a slant path which starts off at 10 km initial height and extends up to a 120 km height point. The angle to the zenith is only 10 degrees and the frequency range of interest lies between 230 and 250 GHz. The same frequency step has been used but now a total of 40 atmospheric layers have been employed to give an excellent accuracy convergence.

Looking carefully figures 8 and 9, we note that trace gases play a role in the characterisation of the radiowave propagation through the earth's atmosphere when slant paths at high altitudes are considered. Their contribution to attenuation may not be negligible as previously assumed, indeed for selected frequency intervals in the millimetre wave spectrum trace gas contributions may be dominant.

7.10 Conclusions.

A computer based prediction method for the calculation of the resultant absorption [dB] and dispersion [rad] by atmospheric gases in planetary atmospheres with particular applicability in the earth's atmosphere has been presented. The Atmospheric Propagation Model (APM) is useful to the radio engineer for characterisation of the clear air absorption and dispersion present in ground to satellite, ground to aircraft or aeronautical to satellite communication links. It could also be a useful aid for applications in remote sensing and navigation.

CHAPTER 8

USE THE 60 GHz OXYGEN BAND LEFT TAIL FOR AIR TRAFFIC CONTROL/ NAVIGATION AND BROADBAND TRANSMISSION PURPOSES.

8.1 Introduction.

With a significant part of the microwave and lower millimetre spectra already well used in both fixed and mobile services and on ever increasing demand for spectrum, especially for new mobile services, it is especially relevant to consider portions of the spectrum which give maximum re-use advantage. The 60 GHz absorption oxygen band is one such spectral region for which the physical properties ought to be assessed in some detail before choices are made for particular applications. Currently, civilian aeronautical mobile to satellite services occupy little spectrum and offer very modest services to the public. As broadband services become available on terrestrial systems, including HDTV broadcast and fast image-file retrieval from data bases, a demand for new high quality in flight services, including live TV services may be generated.

Despite the current relatively modest use of the radio spectrum, aeronautical-mobile services are already encountering difficulty in finding new spectrum for conventional in-flight services to the public and for traffic management and navigation [Lundberg 1992]. One of the problems of course with this type of service, is the inherent global coordination problem. Use of the tails of the 60 GHz band could very significantly alleviate that problem.

The scenario of interest is the use of part of the 60 GHz band for topside air traffic control and broadband transmission purposes. In this chapter the Atmospheric Propagation Model (A.P.M.) [Papatsoris and Watson 1992b] has been employed to estimate the absorption and dispersion present in slant path geometries. So, possible it becomes to take a close look at the left band tail of the oxygen absorption band in these novel applications.

8.2 General properties of the band.

It is well known that the pressure broadened lines evident at ground level from 50 to 70 GHz,

Fig. 1. Zenith absorption and phase dispersion for the left tail of the 60 GHz oxygen absorption band from 10 km initial height.

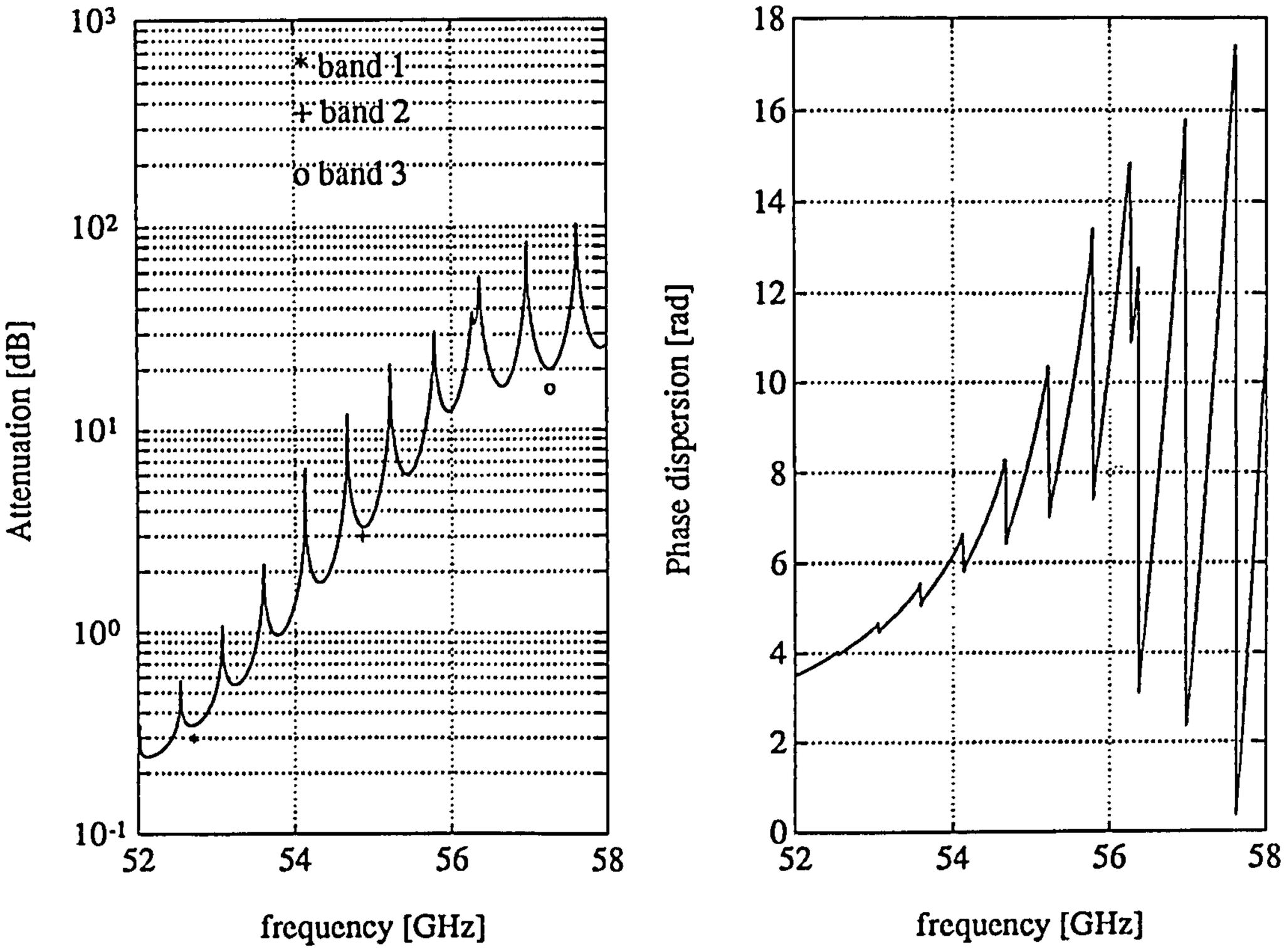

divide into a complex series of bands at high altitude (see figure 1). Line-by-line calculation of the absorption along a particular slant path is a computer intensive process and involves a number of different broadening mechanisms in addition to evaluation of the Voight convolution integral (see previous chapter). The contribution from the water vapour continuum must also be included.

8.3 Calculations for example flight paths.

In order to illustrate the typical losses encountered from aircraft to satellite and aircraft to ground, calculations have been made for example ascent and descent paths. A satellite is considered to be placed in a geostationary orbit at 50 degrees West (see figure 2). The aircraft takes off from New York airport at 40.40 deg North latitude and 73.50 deg West longitude,

flies over the Atlantic ocean and finally lands at London Heathrow airport at 51.28 deg North latitude and 0.27 deg West longitude. Along the flight path the elevation angle ranges from 15.5° and 37.5° and the angle to the zenith from 6.86° to 8.36°.

Fig. 2. Aircraft to satellite and aircraft to ground path geometry.

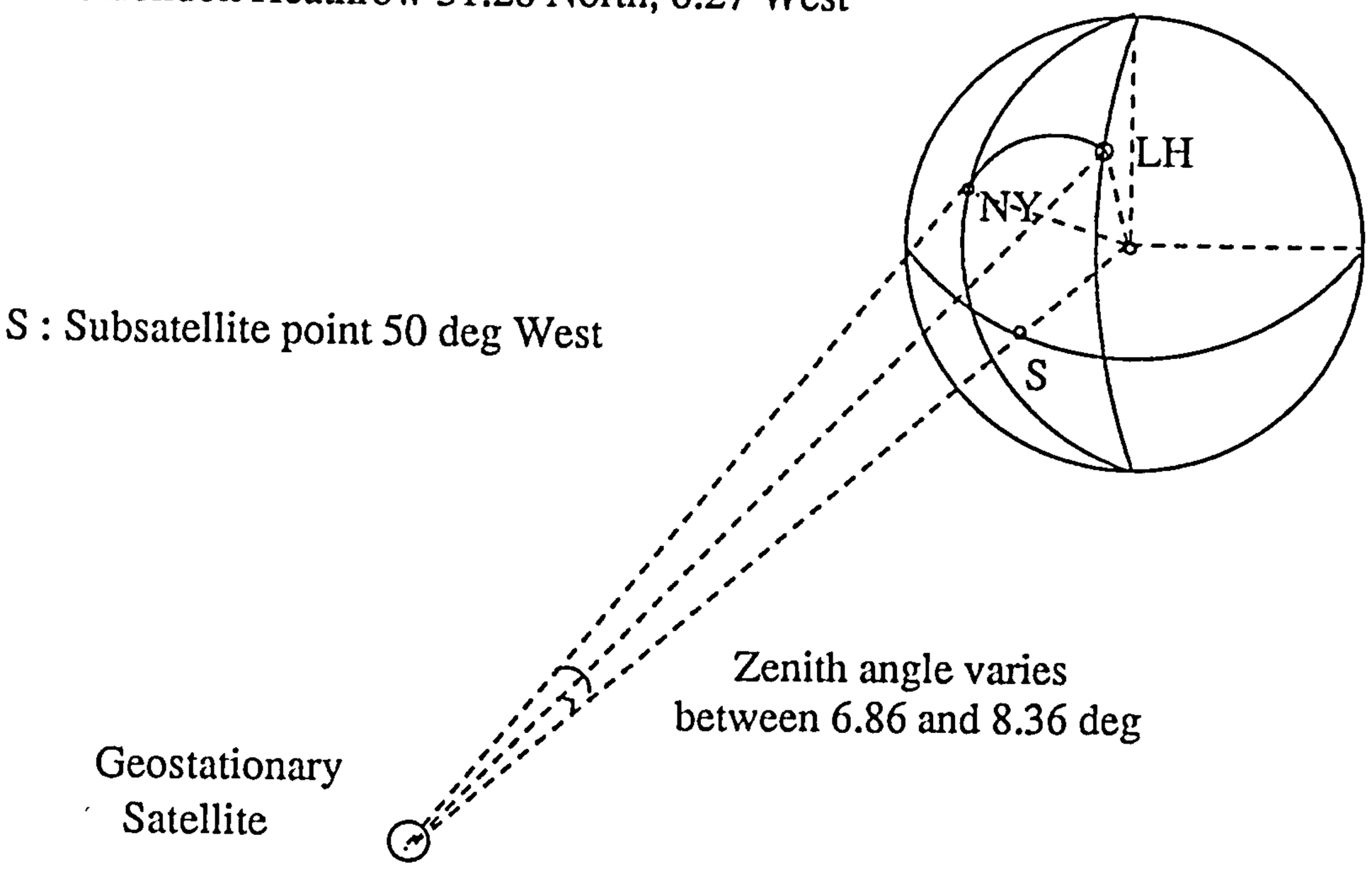

For the calculations, three groups of frequencies have been selected which can be seen in table I (also depicted in figure 1). The first frequency of each group corresponds to the frequency of an absorption line, and the other to a valley where minimum absorption occurs.

Table I. Selected frequencies in the left tail of the oxygen absorption band.

	Frequency [GHz]		
	group 1	group 2	group 3
Absorption lines	52.542	54.671	56.968
Windows	52.714	54.767	57.260

The position of the plane during the procedures of ascending and descending as a function of altitude or the horizontal distance from the points of departure/arrival is given in table II.

These data have been collected during the course of a real flight and are considered as representative in determining the position of an aircraft during a typical ascent or descent.

Table I. Position of aircraft during the procedures of ascending and descending.

Descent		Ascent	
Altitude [m]	Distance from landing point [km]	Altitude [m]	Distance from take off point [km]
10670	340	300	1
10670	288	424	3
10670	232	653	4
10518	227	771	6
8689	177	906	8
8536	175	1070	9
7588	150	1284	12
6555	128	1425	14
6402	126	1678	16
6150	124	2024	17
5300	107	2284	19
4426	87	2368	20
4347	84	2554	22
4293	83	2683	25
4267	81	2767	27
3427	52	2962	28
3396	50	3059	30
3350	49	3180	32
3317	47	3505	35
1724	20	3744	40
1631	18	3987	45
1533	16	4241	49
1231	10	4354	53
1164	7	5793	86
1082	5	5945	91
883	4	9299	226
565	2	9451	271
284	1	10670	365

Figures 3 and 4 show the attenuation and phase dispersion from sea level to the plane (zenith) and from the plane to the satellite during the ascent, as a function of the aircraft altitude. After the ascent has finished, the aircraft precedes over the ocean at a fixed altitude which usually ranges from 9 to 13 km, according to the relevant air control codes. In a similar way, figures 5 and 6 show the attenuation and phase dispersion from sea level to the plane (zenith) and from the plane to the satellite during the descent, as a function of the aircraft altitude. Finally, figures 7 and 8 summarize the results both for the aircraft to ground (AG) and aircraft to satellite (AS) paths, so that evaluation of the isolation is possible.

The most interesting observation emerges for the frequency of 54.862 GHz. At an altitude of 4 km the path loss from the aircraft to the satellite and the path loss from the aircraft to the ground are equal, that is AS = AG = 4 dB. At an altitude 2 km higher, AS = 8 dB, AG = 16 dB and the isolation becomes 8 dB. As the aircraft advances at higher altitudes the isolation

Fig. 3. Zenith attenuation and phase dispersion from aircraft to ground during the ascent.

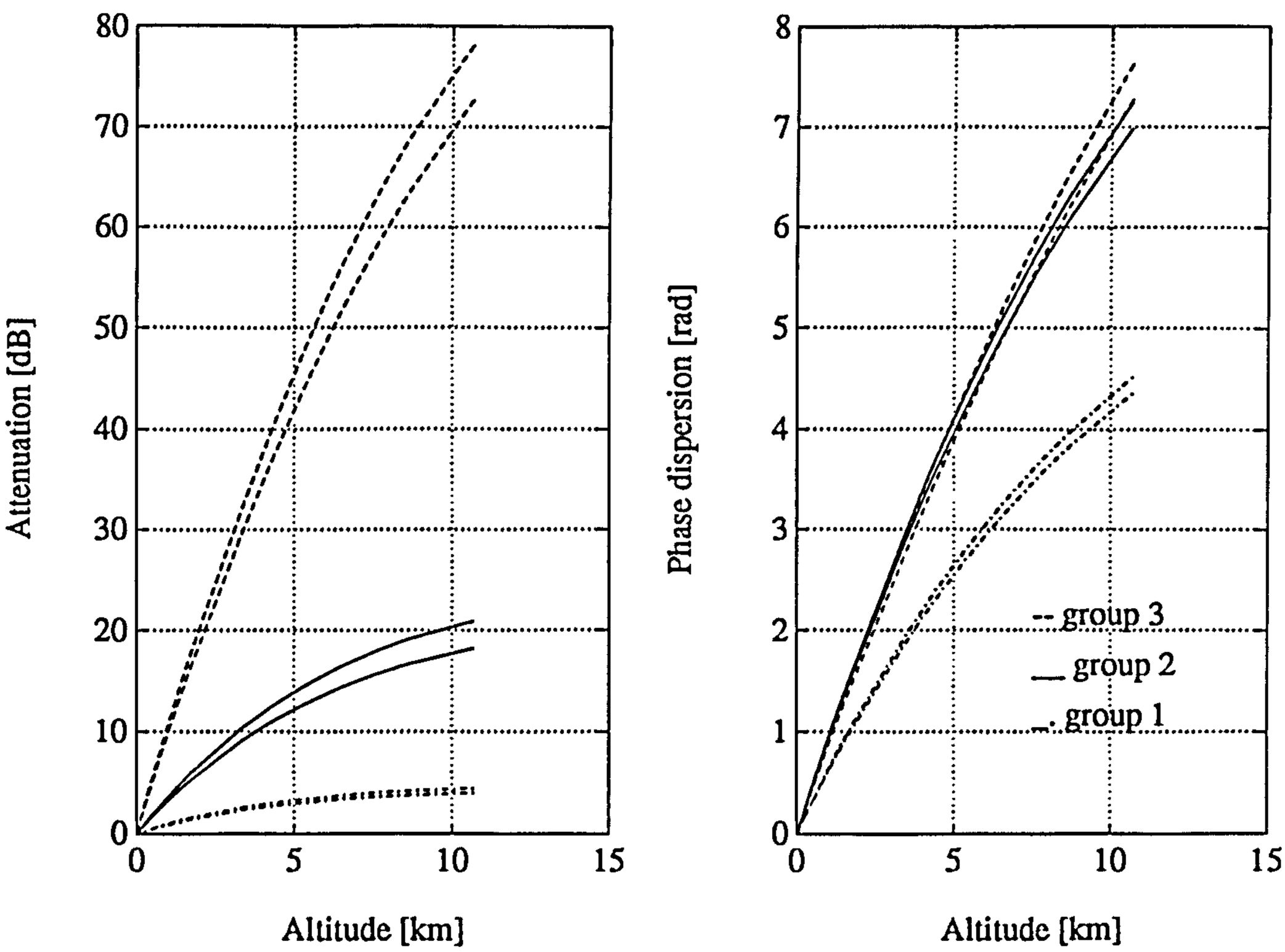

Fig. 4. Attenuation and phase dispersion from aircraft to satellite during the ascent.

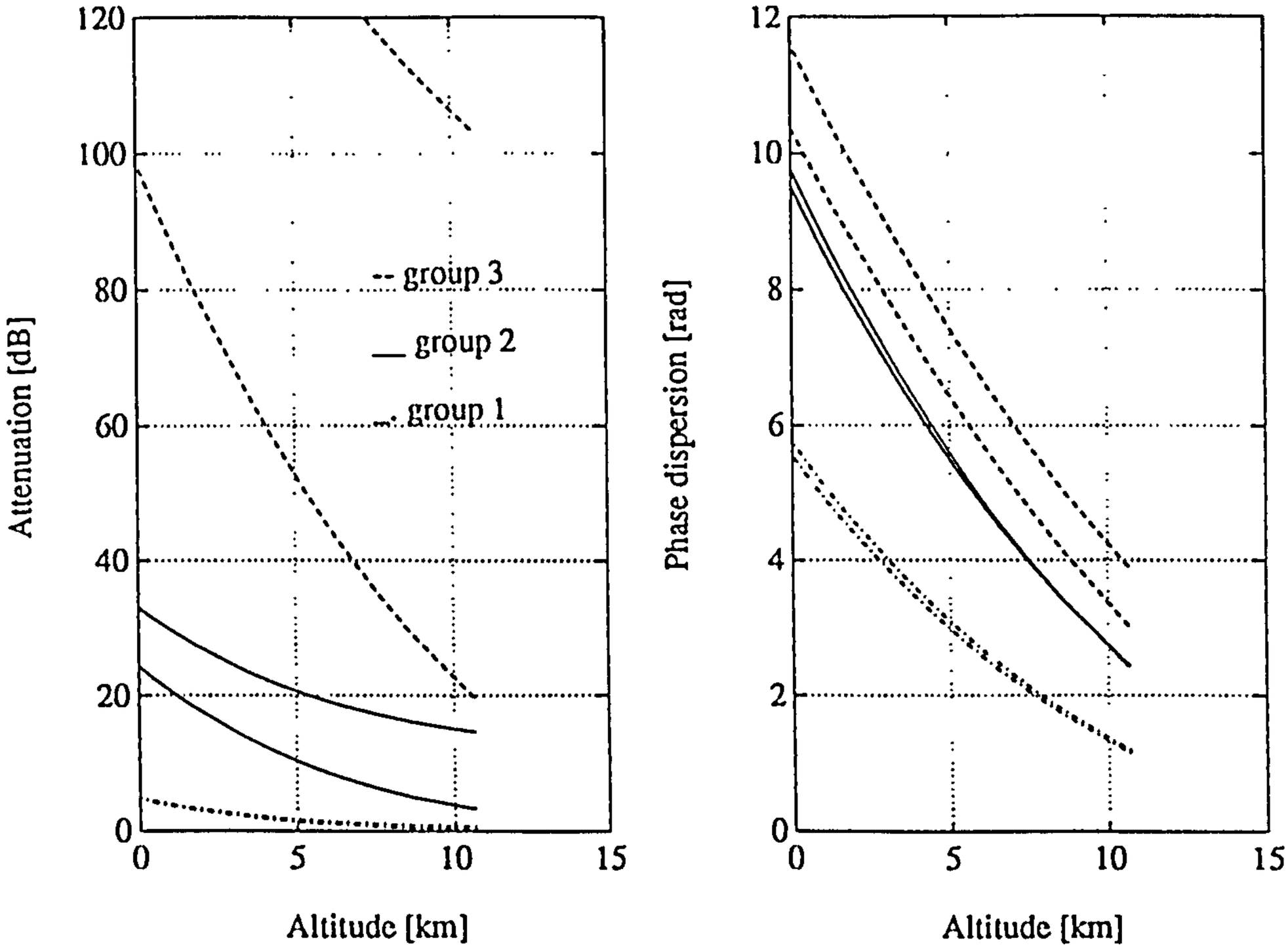

Fig. 5. Zenith attenuation and phase dispersion from aircraft to ground during the descent.

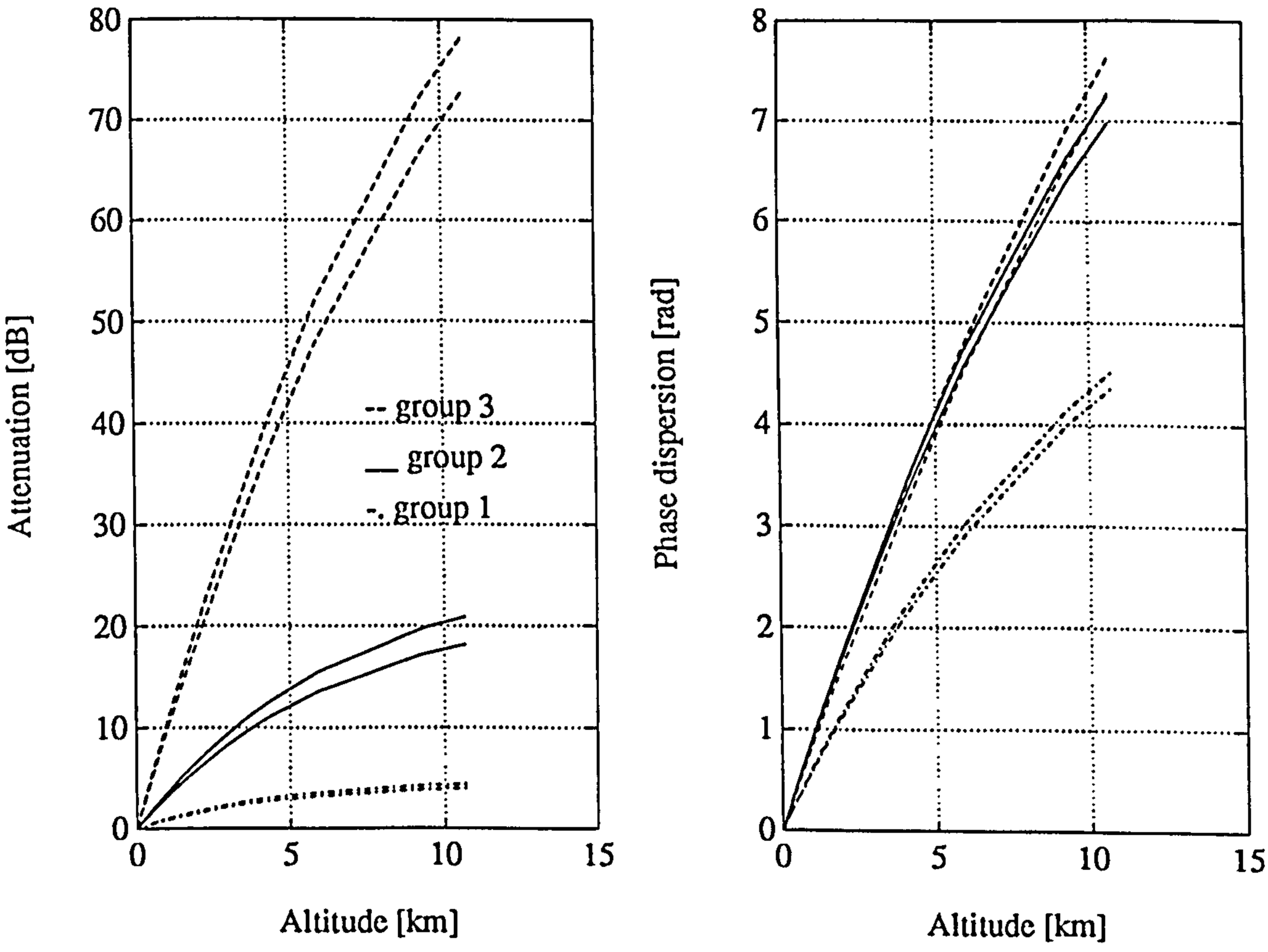

Fig. 6. Attenuation and phase dispersion from aircraft to satellite during the descent.

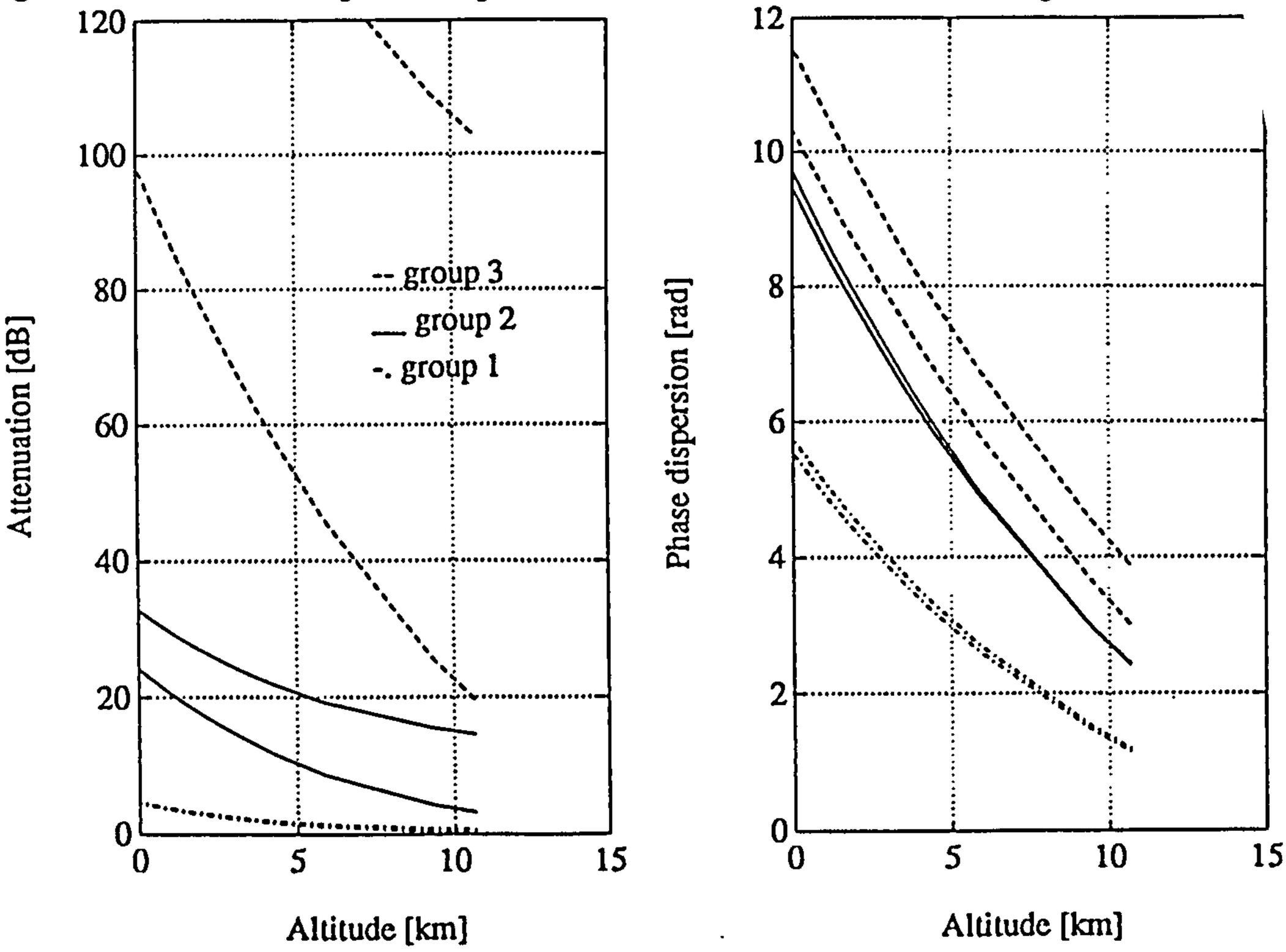

Fig. 7. Evaluation of the isolation between the aircraft to satellite (AS) and aircraft to ground (AG) paths during the ascent.

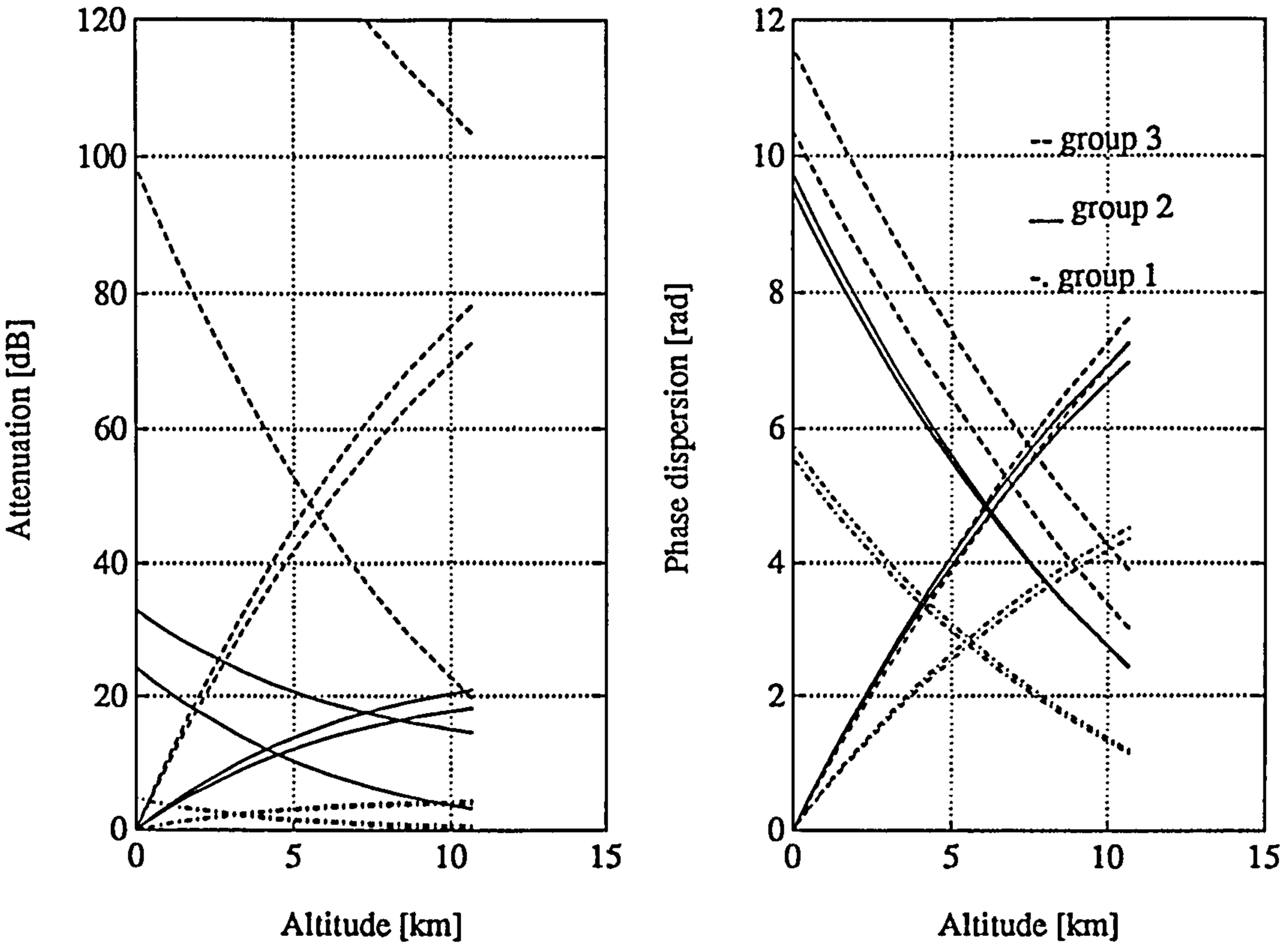

Fig. 8. Evaluation of the isolation between the aircraft to satellite (AS) and aircraft to ground (AG) paths during the descent.

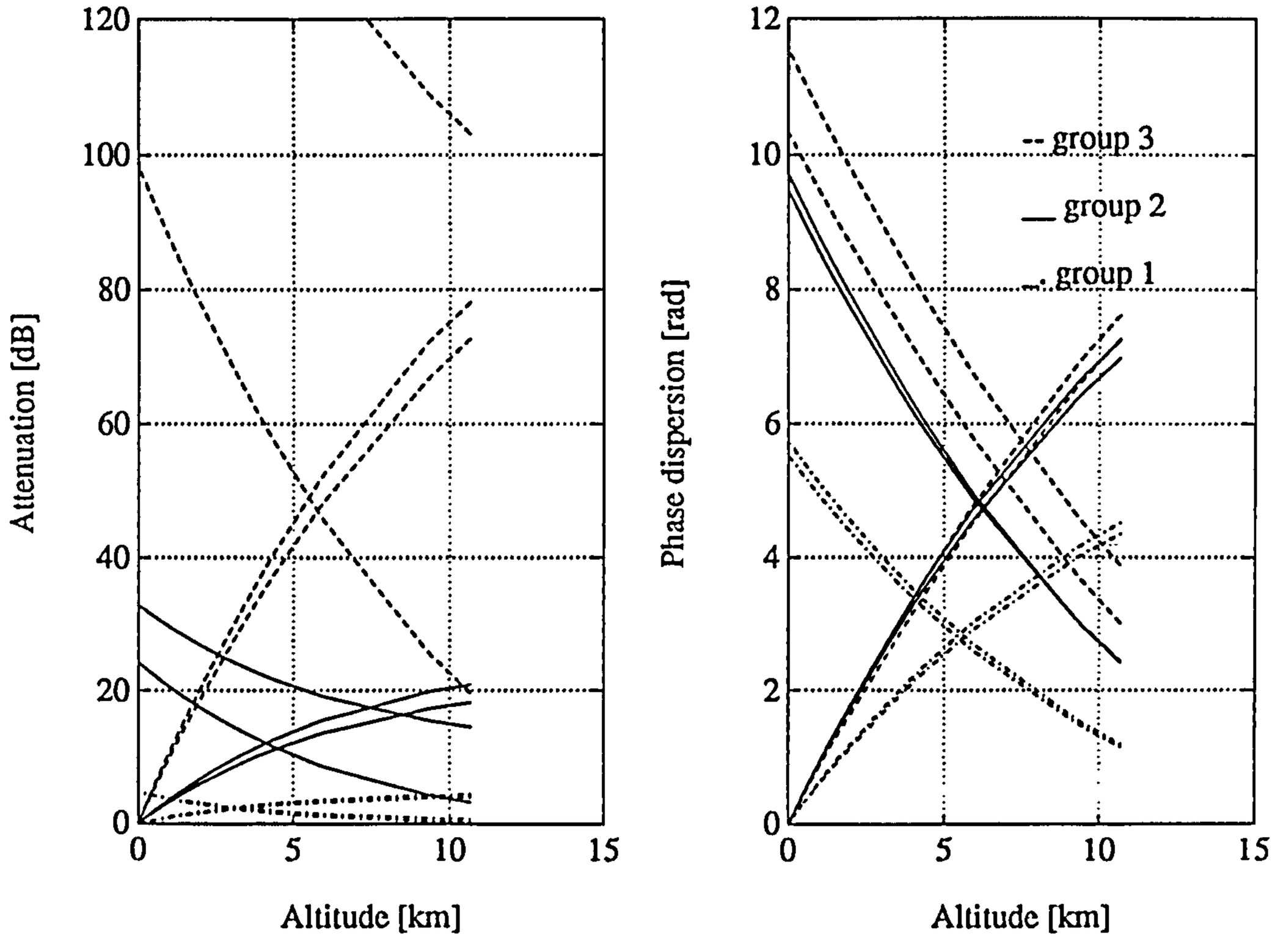

increases to 12 dB at 8 km and 17 dB at 10 km, while the aircraft to satellite path losses reduce attractively to 6.25 dB and 3.75 dB, respectively.

8.4 Conclusions.

It is concluded from this study that frequencies should be selectable within the band that provide good isolation to the ground and acceptable excess path loss to the aircraft. This conclusion seems to favour the concept of top-side air traffic control and navigation leading to improvement in safety and security. The plentiful spectrum available in these bands should also be able to sustain broadband links, though a correct choice of frequencies is necessary as may be the use of phase equalisation. Nevertheless, this theoretical treatment would benefit from a more rigorous and detailed evaluation of the Zeeman effect which affects the polarization state of the radiowave. Also, before any final decisions are taken the complexity

of the attenuation and phase properties of the band should be supported by detailed experimental studies.

REFERENCES

Aden, A.L., [1951], *Journal of Applied Physics*, Vol. 22, p. 601.

Agafonova, S.I., (ed), [1970], *Handbook of the climate of the USSR*, Part 5: Cloudiness and atmospheric phenomena, Nos. 1-34, Gidrometeoizdat, Leningrad.

Ajvazyan, H.M., [1991a], "Extreme values of extinction and radar reflection coefficients for mm and sub-mm waves in clouds", *International Journal of Infrared and Millimetre Waves*, Vol. 12, No 2, pp. 157-175.

Ajvazyan, H.M., [1991b], "Extinction and radar reflection coefficients of mm and sub-mm waves as a function of cloud drops temperature", *International Journal of Infrared and Millimetre Waves*, Vol. 12, No 2, pp. 177-190.

Aleksandrov, E.L., and Yudin, K.B., [1979], "The vertical profile of microstructure parameters of stratus clouds", *Meteorologiya i Gidrologiya*, No. 12, p. 57.

Altshuler, E.E, Falcone, Jr., Wulfsberg, K.N., [1968], "Atmospheric effects on propagation at millimeter wavelengths", *IEEE spectrum*, Vol. 5, pp. 83-90, July.

Atlas, D., Battan, L.J., Harper, W.G., Herman, B.M., Kerker, M., and Matijevic, E., [1963], "Back-scatter by dielectric spheres (Refractive index ~ 1.6)", *IEEE Transactions on Antennas and Propagation*, pp. 68-72, January.

Atlas, D., Eberman, J., Meneghini, R., and Moore, R.K., [1981], *The outlook for precipitation from space*, NASA TM-82172.

Baranov, A.M., [1960], High-level clouds and flying conditions in them, *LKVVIA*, Leningrad.

Bennetts, D.A., and Ouldridge, M., [1984], "An observational study of the anvil of a winter maritime cumulonimbus cloud", *Quart. Jou. Roy. Meteor. Soc.*, Vol 110, pp. 85-103.

Bignell, K.J., [1970], "The water vapour infrared continuum", *Quart. Jou. Roy. Meteor. Soc.*, Vol. 96, pp. 390-403.

Blake, R.G., [1989], "The role of radio for fixed local access", *British Telecom Technol. Journal*, Vol. 7, pp. 123-135.

Blau, H.H., Fowler, M.G., Chang, D.T., and Ryan, R.T., [1972], *Cloud microstructure studies*, ERT P-375 NASA Final Report, Contract NAS 5-21696.

Borovikov, A.M., [1963], *Cloud Physics*, Israel program for scientific translations, Jerusalem.

Borovikov, A.M., and Mazin, I.P., [1975], "Microphysical characteristics of clouds" In: *Aeroclimatological atlas-handbook of the USSR*, No 3, Vol 1, Part 2, p. 127. Gidrometeiozdat, Moscow.

Brussaard, G., Watson, P.A., Leyten, L., Papatsoris, A.D., Kamp van de, M.M.J.L., and Herben, M.H.A.J., [1991], *Atmospheric modelling and millimetre wave propagation*, Final

ESA Report, Contract 89/8600/NL/PB(SC).

Burch, D., Gryvnak, D., and Pembrook, J.Jr., [1971], *Continuous absorption in the 8-14 μm range by atmospheric gases*, Philco-Ford Report Fl9 628-69-C-0263.

Carlon, H.R., and Harden, C.S., [1980], "Mass spectrometry of ion-induced water clusters: an explanation of the infrared continuum absorption", *Applied Optics*, Vol. 19, No. 11, June.

Carrier, L.W., Cato, G.A., and von Essen, K.J., [1967], "The back-scattering and extinction of visible and infrared radiation by selected major cloud models", *Applied Optics*, Vol 6, No 7, July 1967, pp. 1209-1261.

Chandrasekhar, S., [1947], *Astrophysics Journal*, Vol. 105, p. 424.

Chandrasekhar, S., [1950], *Radiative Transfer*, Oxford University Press, reprinted by Dover Publications 1960, Inc., New York.

Clough, S.A., Kneizys, F.X., Davies, R., Gamache, R., and Tipping, R., [1980], "Theoretical line shape for H_2O; application to the continuum", in *Atmospheric Water Vapour*, Deepak, Wilkinson and Ruhnke (Editors), Academic Press.

Clough, S.A., Kneizys, F.K., Rothman, L.S., and Gallery, W.O., [1981], "Atmospheric spectral transmittance and radiance: FASCOD1B", 152 / *SPIE Vol. 277, Atmospheric Transmission.*

Damosso E., Stola, L., and Brussaard, G., [1983], "Characterization of the 50-70 GHz for space communications", *ESA Journal*, Vol. 7, pp. 25-43.

Drayson, S.R., [1976], "Rapid computation of the Voight profile", *Jou. Quant. Spectrosc. Radiat. Transfer*, Vol. 16, pp. 611-614, Pergamon Press.

Dubrovina, L.S., [1968], "Characteristics of the cloud cover over the USSR according to aircraft-sounding data", *Trudy NIIAK*, No. 27, p. 3.

Dubrovina, L.S., (ed.) [1975], *Aeroclimatological atlas-handbook of the USSR*, No. 3, "Statistical characteristics of the spatial and microphysical structure of clouds", Gidrometeoizdat, Moscow.

Durbin, W., [1956], *Droplet sampling in Cumulus Clouds*, Air Ministry Meteorol. Res. Comm. Publication 991, AD 147512.

Emery, R.J., Moffat, P., Bohlander, R., and Gebbie, H.G., [1975], "Measurement of anomalous atmospheric absorption in the 4 to 15 cm^{-1} range", *J. Atm. Terrestr. Phys.*, Vol. 37, pp. 587-594.

Emery, R.J., Zavody, A.M., and Gebbie, H.A., [1978], "Measurements of atmospheric absorption in the range 4-17 cm^{-1} and its temperature dependence", *J. Atm. Terr. Phys.*, Vol. 40.

Feigelson, E.M., (ed), [1981], *Radiation in a cloudy atmosphere*, Hydrometeoizdat.

Feigelson, E.M., [1984], *Radiation in a Cloudy Atmosphere*, Atmospheric Sciences Library,

D. Reidel Publishing Company.

Fletcher, N.H., [1962], *The physics of rain clouds*, Cambridge University Press, London.

Foot, J.S., [1988a], "Some observations of the optical properties of clouds. II: Cirrus", *QJR Meteorol. Soc.*, Vol. 114, pp. 145-164.

Foot, J.S., [1988b], "Some observations of the optical properties of clouds. I: Stratocumulus", *QJR Meteorol. Soc.*, Vol. 114, pp. 129-144.

Frenkel, L., and Woods, D., [1966], "The microwave absorption of H_2O vapor and its mixtures with other gases between 100 and 300 GHz", *Proc. IEEE*, Vol. 54, No. 4, pp. 498-505, April.

Fujita, M., Okamoto, K., Yoshikado, S., and Nakamura, K., [1984], "Inference of rain rate profile and path-integrated rain rate by an airborne microwave rain scatterometer/radiometer", *22nd Conference on Radar Meteorology*, Amer. Met. Soc.

Gasiewski, A.J., [1990a], "Satellite-based atmospheric sensing using passive millimetre and sub-millimetre wave observations", *URSI G A, Prague*, Abs, p. 585.

Gasiewski, A.J., Barret, J.W., Bannani, P.G., and Staelin, D.H., [1990b], "Aircraft based radiometric imaging of tropospheric temperature and precipitation using the 118.75 Ghz oxygen resonance", *Journal of Applied Meteorology*, Vol. 29, No 7, pp. 620-632.

Gastine, M., Courtois, L., and Dormann, J.L., [1967], "Electromagnetic resonances of free dielectric spheres", *IEEE Transactions on Microwave theory and Techniques*, Vol. MTT-15, No. 12, December.

Gibbins, C.J., Gordon-Smith, A.C., and Gebbie, H.A., [1973], "Anomalous absorption in the atmosphere for 2.7 mm radiation", *Nature*, Vol. 243, pp. 397-398.

Gibbins, C.J., Gordon-Smith, A.C., and Croom, D.L., [1975], "Atmospheric emission measurements at 85 to 118 GHz, *Planet. Space Sci.*, Vol. 23, pp. 61-73.

Gibbins, C.J., Wrench, C.L., and Croom, D.L., [1976], "Atmospheric emission measurements between 22 and 150 GHz, *Proceedings of the URSI Commission F Symposium, La Baule, France*, pp. 19-21.

Gimmestad, G.G., and Gebbie, H.A., [1976], "Atmospheric absorption in the range 12 to 31 cm^{-1} measurements in a horizontal path", *J. Atm. Terr. Phys.*, Vol. 38, pp. 325-328.

Gimmestad, G.G., Ware, R.H., Bohlander, R., and Gebbie, H.G., [1977], "Observations of anomalous sub-mm atmospheric spectra", *Astroph. J.*, Vol. 218, pp.331-333.

Goody, G.A., [1964], *Atmospheric radiation: I Theoretical basis*, Oxford University Press.

Gottwald, A., [1976], *Space Research XVI*, Berlin: Akademie-Verlag.

Guissard, A., [1980], *Study of the influence of the atmosphere on the performance of an imaging microwave radiometer*, Univerite Catholique de Louvain, Final Report ESA/ESTEC Contract No 4124/79/NL/DG(SC).

Haddock, F., [1956], *Report NRL Progress*, June 1956, p. 15.

Hardaker, P., and Holt, A.R., [1993], Interim report for the spaceborne cloud radar feasibility study in a meeting held at Rutherford Appletton Laboratories, February 11th.

Harries, J.E., Burroughs, W.J., and Gebbie, H.G., [1969], "MM wavelength spectroscopic observation of water dimer in the vapour phase", *Quart. J. Roy. Met. Soc.*, Vol. 95, pp. 799-807.

Herman, B.M., and Battan, L.J., [1961], "Calculations of Mie back-scattering of microwaves from ice spheres", *Quart. J. Roy. Met. Soc.*, Vol. 87, pp. 223-230.

Herzberg, G., [1945], *Molecular spectra and molecular structure I: Infrared and Raman spectra of polyatomic molecules*, published by Van Nostrand Reinhold Company.

Herzberg, G., [1950], *Molecular spectra and molecular structure II: Spectra of diatomic molecules*, published by Van Nostrand Reinhold Company.

Hill, R.J., [1988], "Dispersion by Atmospheric Water Vapor at Frequencies Less Than 1 THz", *IEEE Trans. Antennas and Propagation*, Vol. 36, No 3, March.

Hodges, J.A., [1972], "Aerosol extinction contribution to atmospheric attenuation in infrared wavelengths", *Applied Optics*, Vol. 11, No. 10, Oct.

Hogg, D.C., Guiraud, F.O., and Westwater, E.R., [1983], "Emission measurements of 31.6 GHz absorption by atmospheric water vapor", *Radio Science*, Vol. 18, pp. 1295-1300, December.

Holt, A.R., and Evans, B.J., [1977], "Some resonance effects in scattering of microwaves by hydrometeors", *Proc. IEE*, Vol. 124, pp. 1114-1116, December.

Hufford, G.A., [1989], "A model for the permittivity of ice from 0 to 1000 GHz", *URSI Nat. Radio Science Meeting*, Boulder CO, p. 14, January 4-6th.

Hui, A.K., Armstrong, B.H. and Wray, A.A., [1978], "Rapid computation of the Voight and complex error functions", *J. Quant. Spectrosc. Radiat. Transfer*, Vol. 19, pp. 509-516, Pergamon Press.

Hulst van de, H.C., [1957], *Light scattering by small particles*, published by John Wiley & Sons Inc., New York.

Illingworth, A. [1992], Ice spectra from the FIRE/ICE studies, Private Communication.

Inada, H., and Plonus, M.A, [1970a], "The geometric optics contribution to the scattering from a large dense dielectric sphere", *IEEE Transactions on Antennas and Propagation*, Vol. AP-18, No. 1, January.

Inada, H., and Plonus, M.A, [1970b], "The diffracted field contribution to the scattering from a large dense dielectric sphere", *IEEE Transactions on Antennas and Propagation*, Vol. AP-18, No. 5, September.

Ishimaru, A. [1993], Multiple scattering at millimetre wavelengths, Private Communication.

Kerker, M., [1969], *The scattering of light and other electromagnetic radiation*, Academic Press, New York.

Khrgian, A.Kh., [1977], "The structure of stratiform clouds", Izv. Akad. Nauk. USSR, *Fiz. Atmos. Okeana*, Vol. 13, No. 11, p. 1150.

Khrgian, A.Kh., and Mazin, I.P., [1956], "Analysis of methods of characterizing raindrop distribution spectra", *Tr. Tsents. Aerolog. Observ.*, Vol. 17, pp. 36-46, (translation), Moscow.

Kielkopf, J.F., [1973], "New approximation to the Voight function with applications to spectral line profile analysis", *Journal of the Optical Society of America*, Vol. 63, No. 8.

Kouyoumjian, R.G., Peters, L.Jr., and Thomas, D.T., [1963], "A modified geometrical optics method for scattering by dielectric bodies", *IEEE Transactions on Antennas and Propagation*, Vol. AP-11, No. 6, November.

Liebe, H.J., [1975], *Studies of oxygen and water vapor microwave spectra under simulated atmospheric conditions*, OT Report 75-65, June, (U.S. Government Printing Office).

Liebe, H.J. and Layton, D.H., [1987], *Millimeter-wave properties of the atmosphere: laboratory studies and propagation modelling*", NTIA Report 87-224, US Dept. of Commerce, October.

Liebe, H.J., [1989], "MPM - An Atmospheric Millimetre-wave propagation model", *International Journal of Infrared and Millimetre Waves*, Vol. 10, No. 6.

Liebe, H.J., and Hufford, G.A., [1989], "Modelling millimeter-wave propagation effects in the atmosphere", *AGARD Conference on Atmospheric propagation in the UV, visible, IR and mmw regions and related systems aspects*, CP-454 on Atmospheric propagation, Copenhagen, October.

Llewellyn-Jones, D.T., Knight, R.J., and Gebbie, H.A., [1978], "Absorption by water vapour at 7.1 cm^{-1} and its temperature dependence", *Nature*, No. 274, pp. 876-878.

Lobanova, V.Ya, [1968], "The structure of a climatic cloud field along a specified direction", *Trudy NIIAK*, No. 27, p. 21.

Lundberg, O., [1992], "Can aviation beat the spectrum squeeze?", *Aeronautical Satellite News*, No 25, Dec. 91-Jan. 92.

Ma Q., and Tipping R.H., [1990], "Water vapor continuum in the millimeter spectral region", *J. Chem. Phys.*, Vol. 93, No. 9, pp. 6127-6139, November.

Magono, C., and Lee, C.W., [1966], "Meteorological classification of natural snow-crystals", Hokkaido Univ., *J. Faculty Sci.*, Ser. 7 (Geophysics), Vol. 2, No. 4, pp. 321-335.

Magono, C., and Lee, C.W., [1973], *J. Meteor. Soc.*, Japan, 51, p. 176.

Manabe, T., Liebe, H.J., and Hufford, G.A., [1987], "Complex permittivity of water between

0 and 30 THz", in Conf. Dig. *12th Int. Conf. Infrared and Millimeter Waves*, Lake Buena Vista, FL, Dec. 14-18.

Mason, B.J., [1971], *The physics of clouds*, Oxford Clarendon Press, 2nd edition.

Mason, B.J., [1975], *Clouds, rain and rainmaking*, Cambridge University Press, 2nd edition.

Mazin, I.P., and Schmeter, S.M., [1983], *Clouds, their structure and formation physics*, Hydrometeoizdat.

Metz, Von H.J., und Dettmar, H.K., [1963], "Zur Berechung der Miescen Streukoeffizienten fur reele Brechungsindizes", *Kolloid-Zeitschrift und Zeitschrift fur Polymere*, Band 192, Heft 1-2.

Mie, G., [1908], "Beitrage zur Optik Truber Medien", *Ann. Physik*, Vol 25, p. 377.

Murphy, D.J., Moser, P.J., Nagl, A., and Uberall, H., [1980], "A surface wave interpretation for the resonances of a dielectric sphere", *IEEE Transactions on Antennas and Propagation*, Vol. AP-28, No. 6, November.

Numerical Algorithms Group Ltd., [1988], The NAG Fortran Library Manual.

Nicholls, S., [1984], "The dynamics of stratocumulus: aircraft observations and comparisons with a mixed layer model", *QJR Meteorol. Soc.*, Vol. 110, pp. 783-820.

Nilsson, B, [1979], "Meteorological on aerosol extinction in the 0.2-40 μm wavelength range", *Applied Optics*, Vol. 18, No. 20, Oct.

NOAA [1976], *US Standard Atmosphere*, NOAA-S/T 76-1562, US Government Printing Office, Washington DC.

Ott, H. Von, [1942], "Reflexion und Brechung von Kungelwellen", *Annalen der Physik*, 5 Folge, Band 441.

Papatsoris, A.D., [1990], *Tables of absorption and scattering cross sections of spherical ice and water particles*, Internal Report No 461, Bradford University, Dept. of Electrical and Electronic Engineering.

Papatsoris, A.D., and Watson, P.A., [1991], *Interim Report for ESA/ESTEC contract 8600/89/PB(SC)*, January.

Papatsoris, A.D., and Watson, P.A., [1992a], "A rigorous explanation of the resonances observed in the scattering from ice particles", *Open Symposium in Wave propagation and Remote sensing (URSI)*, Ravenscar North Yorkshire, United Kingdom, 8-12 June.

Papatsoris, A.D., and Watson, P.A., [1992b], "Calculation of absorption and dispersion spectra of atmospheric gases at millimetre wave frequencies", *Open Symposium in Wave propagation and Remote sensing (URSI)*, Ravenscar North Yorkshire, United Kingdom, 8-12 June.

Papatsoris, A.D., and Watson, P.A., [1992c], "Evaluation of the absorption and dispersion present on slant paths in the oxygen band left tail", *Open Symposium in Wave propagation and*

Remote sensing (URSI), Ravenscar North Yorkshire, United Kingdom, 8-12 June.

Paltridge, G.W., and Platt, C.M.R., [1981], "Aircraft measurements of solar and infrared radiation and the microphysics of cirrus cloud", *QJR Meteorol. Soc.*, Vol 107, pp. 367-380.

Pendorf, R., [1960], *Scattering coefficients for absorbing and non-absorbing aerosols*", Tech. Rept. RAD-TR-60-27, Air Force Cambridge Res. Lab., Bedford, Massachusetts.

Penner, S.S., [1959], *Quantitative Molecular Spectroscopy and Gas Emissivities*. Addison-Wesley, Reading, Mass., Chapter 3.

Peters, L.Jr., Kawano, T., and Swarner, W.G., [1965], "Approximations for dielectric or plasma scatterers", *Proceedings of the IEEE*, Vol. 53, pp. 882-892, August.

Pilgrim, M., Scott, R.P., Carver, R.D., and Ellis, B.J., [1989], "The M^3VDS Saxmundham demonstrator-multichannel TV distribution by mm-waves", *British Telecom Technol. Journal*, Vol. 7, pp. 5-19.

Plank, M., [1913], *Vorleungen uber die Theorie der Warmestrahlung*, Leipzig: Barth, English edition 1959 by Dover Publications, Inc.

Probert-Jones, J.R., [1963], In *Electromagnetic scattering*, (M. Kerker ed.), p. 237., Pergamon Press, Oxford.

Pruppacher, H.R., and Klett, J.D., [1978], *Microphysics of clouds and precipitation*, Boston D.Reidel Publishing Company.

Ray, P.S., [1972], "Broadband complex refractive indices of ice and water", *Applied Optics*, Vol 11, No 8, pp. 1836-1844, August.

Ray, P.S., and Stephens, J.J. [1974], "Far-field transient backscattering by ice spheres", *Radio Science*, Vol. 9, No. 1, pp. 43-55, January.

Rayleigh, L., [1899], *Scientific Papers*, Cambridge, England, paper i, pp. 87,104,518.

Reber, E.E., [1972], *Journal of Geophysical Research*, Vol 77, p. 3831.

Rheinstein, J., [1968], "Backscatter from spheres: A short pulse view", *IEEE Transactions on Antennas and Propagation*, Vol. AP-16, No. 1, January.

Richardson A.J., and Watson, P.A., [1990], "Use of the 55-65 GHz oxygen absorption band for short range broadband networks with minimal regulatory control", *Proc. IEE*, Vol. 137, Part 1, No 4, pp. 233-241.

Rothman, L.S., Gamache, R.R., Goldman, A., Brown, L.R., Toth, R.A., Pickett, H.M., Poynter, R.L., Flaud, J.M., Camy-Peyret, C., Barbe, A., Husson, N., Rinsland, C.P., and Smith, A.H., [1987], "The HITRAN database: 1986 edition", *Applied Optics*, Vol. 26, No. 19.

Rosenkranz, P.W., [1975], "Shape of the 5mm Oxygen Band in the Atmosphere", *IEEE Transactions on Antennas and Propagation*, Vol. AP-23, No. 4, July.

Rosenkranz, P.W., [1988], "Interference coefficients for overlapping oxygen lines in air", *J. Quant. Spectrosc. Radiat. Transfer*, Vol. 39, pp. 287-297.

Ruck, G.T., Barrick, D.E., Stuart. W.D., and Kirchbaum, C.K., [1970], *Radar Cross Section Handbook*, New York: Plenum.

Senior, T.B.A., and Goodrich, R.F., [1964], "Scattering by a sphere", *Proceedings of the IEE*, Vol 3, p. 907.

Shettle, E.P., [1990], "Models of aerosols, clouds and precipitation for atmospheric propagation studies," *AGARD Conference on Atmospheric propagation in the UV, visible, IR and mmw regions and related systems aspects*, CP-454, pp. 15.1-15.12.

Silverman, B.A., and Sprague, E.D., [1970], "Airborne measurements of In-Cloud visibility", *National Conference on Weather Modification*, American Meteorological Society, April 6-9, Santa Barbara, California.

Stokes, G.G., [1901], *Mathematical and physical papers of Sir George Stokes*, Cambridge, England, paper No 3, pp. 233-51.

Stone, N.W., Read, L.A., Anderson, A., Dagg, I.R., and Smith, W., [1984], "Temperature dependent collision-induced absorption in nitrogen", *Can. J. Phys.*, 62, pp. 338-347.

Straiton, A.W., and Tolbert, W., [1959], "Anomalies in the absorption of radiowaves by atmospheric gases", *Proceedings of the IRE*, pp. 898-903, May.

Stratton, J.A., [1941a], *Electromagnetic theory*, McGraw Hill Book Company Ltd., p. 394.

Stratton, J.A., [1941b], *Electromagnetic theory*, McGraw Hill Book Company Ltd., pp. 594-597.

Suck, S.H., Kassner, L.Jr., and Yamaguchi, Y., [1979], "Water cluster interpretation of IR absorption spectra in the 8-14 μm wavelength region", *Applied Optics*, Vol. 18, No. 15, August.

Takano, Y. and Liou, K.N., [1989], "Solar Radiative Transfer in Cirrus Clouds. Part: Theory and Computation of Multiple Scattering in an Anisotropic Medium", *J. Atmos. Sci.*, Vol 46, No 1.

Ulaby, F.T., [1973a], "Absorption in the 220 GHz atmospheric window", *IEEE Transactions on Antennas and Propagation*, AP-21, pp. 266-269.

Ulaby, F.T. and Straiton, A.W., [1973b], "Atmospheric attenuation studies in the 183-325 GHz region", *IEEE Transactions on Antennas and Propagation*, AP-17, No 3, pp. 337-342, May.

UK GEWEX Forum, [1993], *Concept for a spaceborne cloud radar system*, A contribution to the World Climate Research Program's Global Energy and Water Cycle Experiment - (GEWEX), prepared under the auspices of the UK GEWEX forum, January.

Uplinger, W.G., [1981], "A simple model for relative air mass", *Fourth Conference on Atmospheric Radiation*, Toronto, Canada (American Meteorological Society), June.

Valley, S.L., (ed), [1965], *Handbook of Geophysics and Space Environments*, AFCRL.

Viktorova, A.A., and Zhevakin S.A., [1967], "Absorption of microwaves in air by water-vapor dimers", *Soviet Physics - Doklady*, Vol. 11, No 12, June.

Viktorova, A.A., and Zhevakin S.A., [1971], "Band spectrum of a dimer of water vapor", *Soviet Physics - Doklady*, Vol. 15, No 9, pp. 836-855.

Visher, S.S., [1966], *Climatic Atlas of the United States*, Harvand University Press, Cambridge, Mass.

Warner, J., [1969], "The microstructure of cumulus clouds. Part 1: General features of the droplet spectrum", *J. Atm. Sci.*, Vol. 96, No. 5, pp. 1049-1059.

Weickman, H.K., [1947], *Die Eisphase in der Atmosphere*, Reports and translations No 716, Ministry of supply (A), Volkenrode pp. 244-247.

Westwater, E.R., Snider, J.B. and Falls, M., [1988], *Observations of atmospheric emission and attenuation at 20.6, 31.65 and 90 GHz by a ground-based radiometer*, NOAA Technical Memorandum ERL WPL-156.

Whiting, E.E., [1968], "An empirical approximation to the Voight profile", *J. Quant. Spectrosc. Radiat. Transfer*, Vol. 8, pp. 1379-1384, Pergamon Press.

Zak, E.G., [1962], "The vertical distribution of high-level clouds", *Trudy TsAO*, No. 39, p.13.

Van Vleck, J.H., and Weisskopf, V.F., [1945], "On the shape of collision broadened lines", *Rev. Mod. Phys.*, Vol. 17, pp. 227-236.

APPENDIX A

MIE SCATTERING PROGRAM FOR THE CALCULATION OF ABSORPTION AND SCATTERING CROSS SECTIONS OF SPHERICAL PARTICLES.

A.1 Main program.

```
c     MIE CALCULATIONS FOR SPHERICAL SCATTERERS
c     Program made by A.D.Papatsoris
c     July 1990
c     ------------

c     Declarations and Data
c     -------------------------
      parameter (n=101)
      complex*16 cyjx(n),cyjy(n),cyyx(n),cwx(n),cyhx(n)
      complex*16 tas1,tas2,tas3,tan(n),tbn(n)
      complex*16 s0,s180,m,m2,x,y,jx1,jy2,hx1,jy3
      real*8 a,la,ua,da,f,l,temp,pi,v,help1(n-1),help2(n-1),asca,j,xr
      real*8 dic(2),Cabs,Cext,Csca,sigma
      integer nz,ifail,not,lc
      character*1 woi,coe,scale
      character*20 filename
      data pi / 3.1415926535897 93d0 /
      data dic / -1.0d0, 1.0d0 /

c     Read the data
c     ----------------
      print*, 'Enter the frequency of the radiowave f [GHz] :'
      read(5,*) f

c     Calculation of the Index of Refraction
c     ------------------------------------------
      print*, 'Index of refraction calculated [c] or entered [e] ?'
      read(5,*) coe
      if(coe.eq.'e') then
         print*, 'Enter index of refraction (real,imag) :'
         read(5,1002) m
      else
         print*, 'Enter temperature [C] :'
         read(5,*) temp
         print*, 'Enter "w" for water, or "i" for ice :'
         read(5,*) woi
         if(woi.eq.'w') then
            call manabe_water(f,temp,m)
         else
            call ray_ice(f,temp,m)
```

```
   endif
endif
print*, 'Index of refraction=',m
print*, 'Enter lower limit radius [mm] :'
read(5,*) la
print*, 'Enter upper limit radius [mm] :'
read(5,*) ua
print*, 'Enter radius step [mm] :'
read(5,*) da
      print*, 'Enter filename :'
      read(5,*) filename
      open(1,file=filename)

c     Initialization
c     --------------
      l=300.0d0/f
      scale='u'
      nz=0
      ifail=0
      v=0.5
      m2=m*m

c     Calculations
c     ------------
      do 1,a=la,ua,da

         xr=2.0d0*pi*a/l
         if(xr.gt.91.0) then
            not=101
         else
            not=xr+10
         endif
         x=dcmplx(xr,0.0d0)
         y=m*x

         call s17def(v,x,not,scale,cyjx,nz,ifail)
         call s17dcf(v,x,not,scale,cyyx,nz,cwx,ifail)
         call s17def(v,y,not,scale,cyjy,nz,ifail)

         do 20,i=1,not-1
            help1(i)=dreal(cyjx(i+1))
            cyjx(i)=dcmplx(help1(i),0.0)
            cyjy(i)=cyjy(i+1)
            help2(i)=dreal(cyyx(i+1))
            cyyx(i)=dcmplx(help2(i),0.0)
            cyhx(i)=dcmplx(help1(i),-help2(i))
20       continue
```

```
c     Indermediate calculations
c     -------------------------------
        do 30,i=1,not-1
          tas1=y*cyjy(i)-i*cyjy(i-1)
          tas2=x*cyjx(i)-i*cyjx(i-1)
          tas3=x*cyhx(i)-i*cyhx(i-1)
          jx1=cyjx(i)*tas1
          jy2=cyjy(i)*tas2
          hx1=cyhx(i)*tas1
          jy3=cyjy(i)*tas3
          tan(i)=(jx1-m2*jy2)/(hx1-m2*jy3)
          tbn(i)=(jx1-jy2)/(hx1-jy3)
 30     continue

c     Calculation of amplitude function S(0), S(180)
c     ----------------------------------------------------
        s0=dcmplx(0.0d0,0.0d0)
        s180=dcmplx(0.0d0,0.0d0)
        asca=dcmplx(0.0d0,0.0d0)
        do 40,i=1,not-1
          j=2.0d0*i+1.0d0
          lc=mod(i,2)+1
          s0=s0+j*(tan(i)+tbn(i))
          asca=asca+j*(dconjg(tan(i))*tan(i)+dconjg(tbn(i))*tbn(i))
          s180=s180+j*dic(lc)*(tan(i)-tbn(i))
 40     continue
        s0=0.5d0*s0
        s180=s180*0.5d0

c     C cross sections are in [mm2]
c     ------------------------------------
        Cext=(l**2.0/pi)*dreal(s0)
        Csca=(l**2.0/(2.0d0*pi))*asca
        Cabs=Cext-Csca
        sigma=(4.0d0/xr**2.0d0)*
     $          ((dreal(s180)**2.0d0)+(dimag(s180)**2.0d0))

c     Storing the results
c     ---------------------
        write(1,1005) a,Cabs,Csca,Cext,sigma

c     End Loop
c     ------------
 1     continue
       close(1)
 1002 format(2(d16.10))
 1005 format(4(e16.10,1x),e16.10)
       end
```

A.2 Subroutine for the calculation of the refractive index of water.

```
c     Program made by A.D.Papatsoris
c     Adapted from Manabe et al [1987]
c     Valid for temperature range -20° to 20° C and frequencies up to 30 THz.
c     July 1990
c     ----------

      subroutine manabe_water(freq,temp,m)
      real*8 freq,temp,theta,e0,ep,fp,es,fs
      complex*16 h1,h2,ea,eb,m

      theta=3.0d2/(2.7315d2+temp)-1
      e0=7.766d1+1.033d2*theta
      ep=5.48d0
      fp=2.009d1-1.42d2*theta+2.94d2*theta**2.0
      h1=dcmplx(freq,fp)
      ea=((e0-ep)*freq)/h1
      es=3.51d0
      fs=5.9d2-1.5d3*theta
      h2=dcmplx(freq,fs)
      eb=((ep-es)*freq)/h2
      m=cdsqrt(e0-ea-eb)
      return
      end
```

A.3 Subroutine for the calculation of the refractive index of ice.

```
c     Program made by A.D.Papatsoris
c     Adapted from Ray [1972]
c     Valid for temperature range -20° to 0° C and frequencies up to 300 GHz
c     July 1990
c     ----------

      subroutine ray_ice(freq,temp,m)
      real*8 freq,temp
      real*8 pi,l,es,s,eoo,a,ls,h,h0,h1,h2,eii,nr,ni
      complex*16 m

      data pi / 3.14159265358979 3d0 /
      l=3.0d1/freq

      h=(temp+2.7315d2)*1.9869d0
      es=2.03168d2+2.5d0*temp+1.5d-1*temp**2.0
      s=1.26d0*dexp(-1.25d4/h)
      eoo=3.168d0
      a=2.88d-1+2.5d-3*temp+2.3d-4*temp**2.0
```

```
ls=9.990288d-5*dexp(1.32d4/h)
h0=(ls/l)**(1.0d0-a)
h1=dsin(0.5d0*pi*a)
h2=1.0d0+2.0d0*h0*h1+h0**2.0
eii=(es-eoo)*ho*dcos(0.5d0*pi*a)/h2+(s*l)/18.8496d10
nr=1.78d0
ni=eii/(2.0d0*nr)
m=dcmplx(nr,-ni)
return
end
```

APPENDIX B

ALGORITHM BASED ON THE C05NCF NAG SUPPLIED ROUTINE TO SOLVE TRANSCENDENTAL EQUATIONS.

B.1 Main program.

```
c     MODES OF FREE OSCILLATION OF A SPHERE
c     Program made by A.D.Papatsoris
c     Main program adapting the NAG supplied C05NCF routine
c     March 1991
c     -------------

c     Declarations and Data
c     ------------------------
      integer n,maxfev,ml,mu,mode,nprint,nfev,ldfjac,lr,ifail
      parameter (n=2, ldfjac=n,lr=(n*(n+1))/2)
      real*8 x(n),fvec(n),xtol,epsfcn,diag(n),factor,fjac(ldfjac,n),
     $r(lr),qtf(n),w(n,4)
       complex*16 m
       common m
       integer*4 k
       common k
       external fcn

c     Initialization of C05NCF
c     ----------------------------
      ifail=1
      xtol=0.0d0
      maxfev=200*(n+1)
      ml=n-1
      mu=n-1
      epsfcn=0.0d0
      mode=2
      factor=1.0d0
      nprint=0
      ifail=1

      do 10,i=1,n
         diag(i)=1.0d0
10    continue

      m=dcmplx(1.78d0,-6.57d-4)
      print *,'Enter the order of the trancedental equation ...'
      read(5,*) k
      print *,'Enter a rough solution z=x(1)+x(2)*i : '
      read(5,*) x(1),x(2)
```

```
      call c05ncf(fcn,n,x,fvec,xtol,maxfev,ml,mu,epsfcn,diag,
     $mode,factor,nprint,nfev,fjac,ldfjac,r,lr,qtf,w,ifail)

      write(6,99) (x(i),i=1,n)
99    format(f30.23,1x,f30.23,'*i')
      end
```

B.2 Subroutine for the calculation of electric modes TE.

```
c     Program made by A.D.Papatsoris
c     March 1991
c     ----------

      subroutine fcn(n,x,fvec,iflag)
      integer n,iflag
      real*8 x(n),fvec(n)

      complex*16 z,zm,cyj(101),cyh(101),tas1,tas3,hx1,jy3
      real*8 fnu
      integer nz,ifail
      character*1 scale
      complex*16 m,m2
      integer*4 k,l
      common m,k

      fnu=0.5
      nz=0
      ifail=0
      scale='u'
      l=1
      z=dcmplx(x(1),x(2))
      zm=z*m
      m2=m*m

      call s17def(fnu,zm,k+1,scale,cyj,nz,ifail)
      call s17dlf(l,fnu,z,k+1,scale,cyh,nz,ifail)

      tas1=zm*cyj(k+1)-k*cyj(k)
      tas3=z*cyh(k+1)-k*cyh(k)
      hx1=cyh(k)*tas1
      jy3=cyj(k)*tas3

      fvec(1)=dreal(hx1-m2*jy3)
      fvec(2)=dimag(hx1-m2*jy3)

      return
      end
```

B.3 Subroutine for the calculation of magnetic modes TM.

```
c     Program made by A.D.Papatsoris
c     March 1991
c     ----------

      subroutine fcn(n,x,fvec,iflag)
      integer n,iflag
      real*8 x(n),fvec(n)
complex*16 z,zm,cyj(101),cyh(101),tas1,tas3,hx1,jy3
real*8 fnu
integer nz,ifail
character*1 scale

complex*16 m
integer*4 k,l
common m,k

fnu=0.5
nz=0
ifail=0
scale='u'
l=1
z=dcmplx(x(1),x(2))
zm=z*m

call s17def(fnu,zm,k+1,scale,cyj,nz,ifail)
call s17dlf(l,fnu,z,k+1,scale,cyh,nz,ifail)

tas1=zm*cyj(k+1)-k*cyj(k)
tas3=z*cyh(k+1)-k*cyh(k)
hx1=cyh(k)*tas1
jy3=cyj(k)*tas3

fvec(1)=dreal(hx1-jy3)
fvec(2)=dimag(hx1-jy3)

return
end
```